vol 21 / 2021

JOURNAL OF ELECTICAL ENGINEERING

University "Politehnica"
Timișoara Romania
Faculty of Electrical and Power Engineering

"Politehnica" Publishing House
ISSN 1582-4594

No 3

PERFORMANCE COMPARISON OF CSC CONVERTER BASED ACS

Shubham MISHRA Shikha SINGH
[1,2]Shri Ramswaroop Memorial University, Lucknow
226005 Uttar Pradesh, India, +919305056663
shubhammishra113@gmail.com,
shikha.ee@gmail.com

Abstract: *The design, operating principle and analysis of an air condition system (ACS) using with bridge and without bridge configurations are presented for power quality improvement. The performance of these ACSs is compared on various parameters such as voltage regulation, input current harmonic spectrum etc to choose the optimal configuration according to user's specifications. Both the input converters are designed in discontinuous mode for simple control as well as inherent power factor correction. The observed performance of both the ACSs is well within the set guidelines of international power quality standards.*

Key words: *ACS, Power Quality, CSC Converter, Power Factor.*

1. Introduction- An Air conditioning system is used to maintain atmospheric conditions such as temperature, moisture etc according to human comfort. As the number of air conditioners increases these days, the demand on the distribution system increases. Due to increased usage of such power electronics load, poor power quality becomes a major concern. Moreover, BLDC motor draws high harmonic current from the input side which does not meet the PQ standard IEC 61000-3-2. Therefore, to adhere to these PQ standards, power factor correction is immensely used and incorporated in power supplies [1-3].

Various power factor correction (PFC) converters have been used at input side for voltage regulation as well as to improve the power quality. Generally, boost converter is used for voltage regulation and to maintain good power factor. Various other buck converter and buck boost converter configurations have been employed as PFC. Buck-boost configurations are widely used to take the advantage of large voltage variation. In single phase applications, a single phase diode bridge is used for ac-dc conversion at input to the power factor corrected converters. However, in now days, without bridge configurations are also becoming popular because of its features such as low voltage drop, high efficiency and low stress [4]. The two stage battery charger utilizes a Canonical Switching Cell (CSC) converter for shaping the supply current and a remote DC-DC converter control the charging current and voltage of an e-rickshaw battery. A power factor corrected two fold parallel connected BLDC motors drive with a single inverter has been presented in [5]. The performance comparison of without bridge CSC and diode bridge rectifier based CSC is carried out for four switch BLDC motor for power quality improvement [6]. The combined control strategy of pulse width modulation and pulse amplitude modulation applied in BLDC motor using without bridge CSC converter in [7]. By this dual method, control can be obtained for fixed as well as variable dc link voltage. For welding applications, switched mode power supply using without bridge CSC is described for power quality improvement in [8]. Here, the converter is operating in DICM to obtain PFC at the supply AC mains.

A pulse train control method for a PFC boost converter in DCM has been described, which can attain almost unity power factor (PF) over a supply voltage choice [9]. For improving the power factor, SEPIC is used which also reduces the harmonics within standard limit. Single phase AC-DC SEPIC with PFC controller has been used for attaining higher efficiency power factor with lesser THD in comparison of conventional converters [10]. In the SEPIC and Cuk converter fed ACS the DC link voltage is utilized to maintain the speed. However, the cost of the system increases due to the use of two sensors [11-14].The critical conduction mode based, light emitting diode (LED) driver using boost converter has been presented in [15].The proposed converter feeds dual output dc-dc converter and provides constant dc voltage for LED. One of the buck-boost converter configurations, also known as CSC converter has been used in early 90's in various applications [16]. The advantages of CSC converter are enhanced performance, good power factor; better light load conditions and small component count. To improve the power quality of ac mains and to maintain the good power factor, a voltage follower technique is implemented using CSC converter for VSI [17]. The CSC converter in LED driver is utilized for high power projection to control brightness and intensity [18]. In one of the configuration, two converters are utilized; one at input side and another at output side [19]. A CSC based PFC off-board charger has been presented in [20], to enhance the power quality of conventional e-

rickshaw battery charger. To eliminate the circulating current and circulating power losses, an improved without bridge SEPIC is presented which also improves the power factor of the input supply [21-22]. To maintain output voltage levels, the switched capacitor has been utilized in SEPIC [23]. The static gain of SEPIC has been increased by utilizing switched capacitor. For constant input and constant output current, a Cuk converter is used but the polarity of output voltage is reversed. The switched inductor Cuk converter for enhanced PQ ac–dc converter has been presented for battery charging application [24]. To reduce the output filter capacitance, the combination of without bridge Cuk/SEPIC is used which increases the system reliability [25]. This control technique uphold the increase of the without bridge Cuk/Sepic PFC rectifier in various different applications. For improving the input current harmonics and power factor a without bridge buck converter is used which is operated by eliminating dead angles in input current using auxiliary flyback circuit [26]. A low voltage LED driver is presented by using without bridge Zeta converter for power quality improvement [27]. The proposed LED driver can control LED brightness, illumination etc. with fine power quality. While compared to without bridge configurations of Cuk and Zeta converters, the without bridge CSC converters have low components and low (number of power electronic devices at each semi cycle for the ac input. Therefore, a single voltage sensor based CSC converter (with and without bridge) based ACS which is cost efficient and suitable for low power applications has been used. The designed and simulated converter configurations have been analyzed to demonstrate the pros and cons of each configuration so that a user can select the optimal converter according to the need.

2. Description of conventional CSC and without bridge CSC based ACS

Fig. 1(a) and Fig. 1(b) show the CSC converter based ACS and without bridge CSC converter based ACS respectively. Both the configurations are fed from single phase ac supply and are operated at high switching frequency and maintaining unity power factor at ac mains. The CSC converter consists of mainly three components i.e. input inductor, middle capacitor and an output inductor. The scheme has shown in Fig. 1(a) and Fig. 1(b) gives a close to unity power factor at input for an output dc link voltage variation.

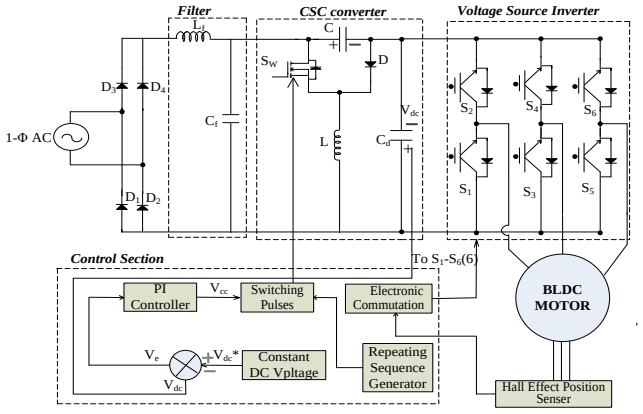

Fig. 1(a). Schematic of ACS using CSC converter

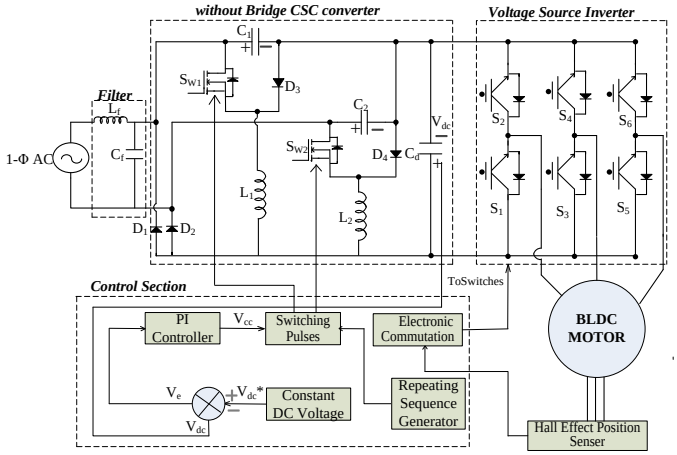

Fig. 1(b). Schematic of ACS using without bridge CSC converter

3. Operating Principle of an ACS using without bridge CSC converter

The operation of without bridge CSC converter is explained in this section. The operating principle of with bridge CSC converter configuration is exactly same as explained in half switching cycle. The without bridge CSC converter is designed to operate in discontinuous mode i.e., the input inductors L_1 and L_2 current are discontinuous in upper half and lower half in each switching cycle. The voltage across the intermediate capacitors C_1 and C_2 are continuous in each switching cycle of upper half and lower half converter configuration. The active circuit of without bridge CSC converter for upper & lower half cycles of input voltage is shown in Fig. 2. When switch turns on in positive half cycle as shown in Fig. 2a, wherein the current flows through the cell, consisting the diodes D_2 ,D_3, inductor L_1,capacitor C_1 and switch Sw_1. And for the negative half-cycle, the cell consisting diode D_1 ,D_4, inductor L_2,capacitor C_2 and switch Sw_2 as shown in Fig 2b [16].

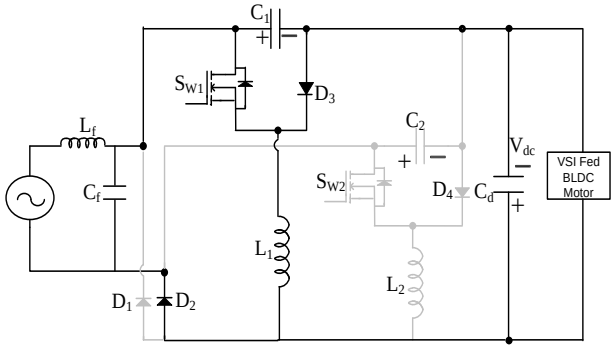

Fig. 2(a). Conduction path of without bridge CSC converter in upper half cycle of supply voltage

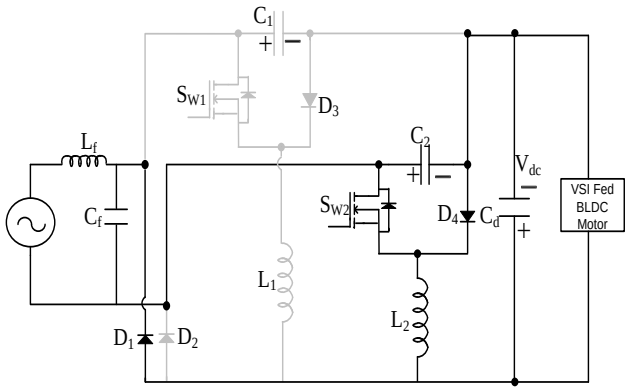

Fig. 2(b). Conduction path of without bridge CSC converter in lower half of supply voltage

Mode I-A: Switch Sw_1 is turned ON shown in Fig. 3a, capacitor C_1 dissipates energy to the capacitor C_d while the inductor L_1 starts storing energy. Hence, inductor current i_{L1} is rising.

Mode I-B: Switch Sw_1 is turned OFF, the inductor L_1 starts discharging to the dc link capacitor C_d, and capacitor C_1 begins charging, shown in Fig. 3b.

Mode I-C: The current on input inductor remains zero until the start of next switching cycle as shown in Fig. 3c. In this mode the capacitor C_1 preserve its energy, and provides the energy necessary for the load is provided by the capacitor C_d.

The operation of the CSC converter follows the same charging and discharging of components for lower half cycle of supply voltage.

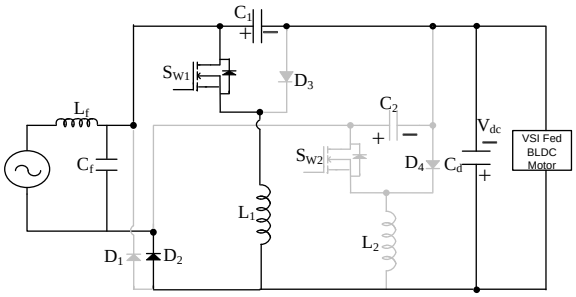

Fig 3. (a)

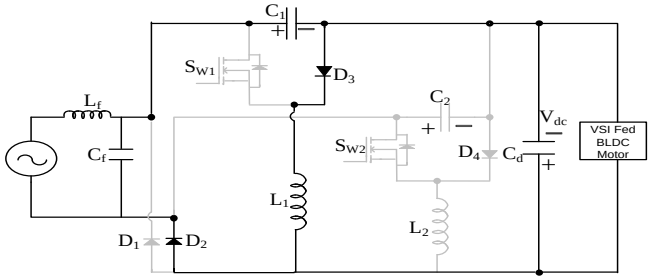

Fig 3. (b)

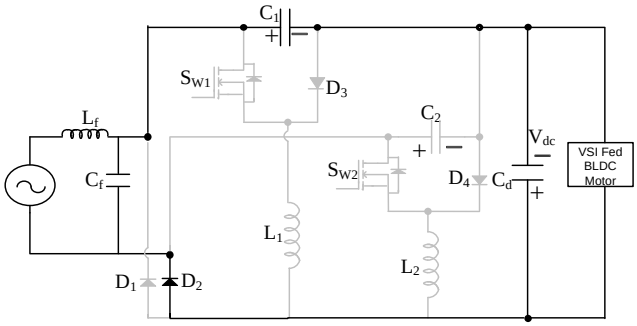

Fig 3. (c)

Fig 3. Various modes of a without bridge CSC converter during (a-c) upper half cycle of supply voltage

4. Design of CSC and without bridge CSC based ACS

A. Design of duty cycle

Both the CSC converter based ACS and without bridge converter based ACS are operated in discontinuous mode for inductor current. The output voltage is related with input voltage by duty cycle is equal for both the converters & is obtained by

$$d_m = \frac{V_{dc}}{V_{dc} + V_{in}} = \frac{300V}{300V + 220V} = 0.58 \tag{1}$$

B. Design of input filter

For minimizing the ripples, the LC filter is designed as follows.

The value of capacitor (C_m) for filter is given by [10],

$$C_m = \frac{I_p}{w_c * V_p}\tan(\theta) = \frac{(\sqrt{2}P_0 / V_{in})}{w_c * V_p}\tan(\theta)$$
$$= \frac{(1000W * \sqrt{2})}{314Hz * 220^2 V * \sqrt{2}}\tan(1^\circ) = 1.15\mu F \tag{2}$$

In this V_p and I_p are the peak value of ac supply voltage and current and θ is the phase angle.

The filter inductor is obtained by [10],

$$L_{req} = \frac{1}{4\pi^2 f_c^2 C_f} = \frac{1}{4 * (3.14)^2 * 4000^2 \times 1.15 * 10^{-6}} = 1.38mH \tag{3}$$

Where f_c is the interrupt frequency ($f_L<f_c<f_s$) in effect as $f_s/10$ .Therefore a value of filter inductor (L_{req}) is selected as 2mH.

C. Designing of input inductors

The value of inductor for discontinuous mode of conduction is measured as

$$L_1 = L_2 = \frac{v_{in} d_m}{2 i_{in} f_s} = \frac{220V * 0.58}{2 * 4.55A * 40000Hz} = 351\mu H \quad (4)$$

Where $$i_{in} = \frac{P_0}{V_{in}} = \frac{1000W}{220V} = 4.55A \quad (5)$$

The inductors (L_1 and L_2) are taken as 255µH.

D. Designing of intermediate capacitors

The design of intermediate capacitors (C_1 and C_2) is as [16],

$$C_1 = C_2 = \frac{d_m V_o}{f_s R_o \Delta V_{C_{1,2}}} = \frac{0.58 * 300}{40000 * 90 * 61.1} = 0.79\mu F \quad (6)$$

The value of intermediate capacitors (C_1 and C_2) is considered as 0.93µF.

E. Designing of output capacitor

Output capacitor is same for both the configuration to moderate the second order harmonics .The design is obtained as,

$$C_{out} = \frac{I_o}{2w\Delta V_o} = \frac{3.33A}{2 * 314Hz * 6V} = 884\mu F \quad (7)$$

5. Simulation Results of Designed ACSs

Both the ACS is modeled in Matlab and various PQ parameters are obtained to observe the performance. The rating of BLDC motor is taken as 1000W. For a supply voltage of 220V and at variable output voltages at dc link, the results have been presented for both the configurations.

A. Performance of CSC converter based ACS at 300V Output Voltage

A single phase input voltage energizes the ACS and the observed performance is shown in Fig. 4.For CSC converter based ACS, the supply current is observed as sinusoidal in nature and of amplitude of 3.962A (rms), while the output voltage is observed as 300V dc which is maintained constant. The electromagnetic torque is observed in the range of 2.4Nm to 3.6Nm. The rotor speed of CSC converter based ACS is obtained as 1472rpm. The THD spectrum of supply current for CSC converter based ACS is shown in Fig. 4(b). It has been observed that the harmonic of ac current is 4.45% which is well within the guiding principle of International standards.

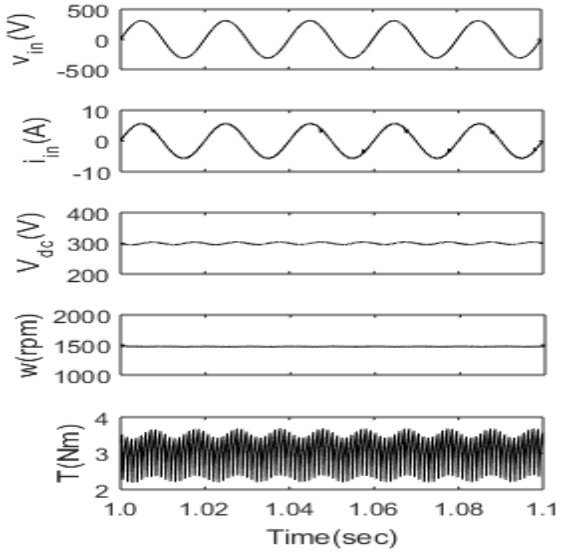

Fig. 4(a)

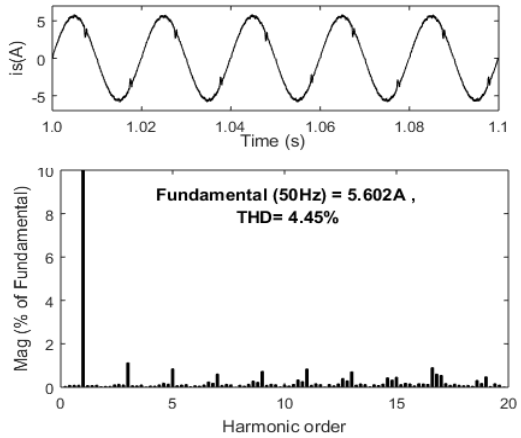

Fig. 4(b)

Fig. 4. Performance of ACS at output voltage of 300V for CSC converter

B. Performance of CSC converter based ACS at 200V Output Voltage

To demonstrate the reliability and design of the ACS, performance of both the ACS has been observed on varying dc voltages. The performance of CSC based ACS has been observed at 200V and is shown in Fig. 5(a). The supply current in this case is observed 2.71 (rms). There is no such significant change in the torque of motor. The rotor speed for CSC converter based ACS is obtained as 1472 rpm. It is clear from the results that there is no change in speed which demonstrates the functioning of ACS even under varying output voltage. The THD spectrum of supply current for CSC converter based ACS is shown in Fig. 5b. For CSC converter based ACS, the harmonics of supply current is recorded 9.55% which is slightly high as compared to 300V dc voltage.

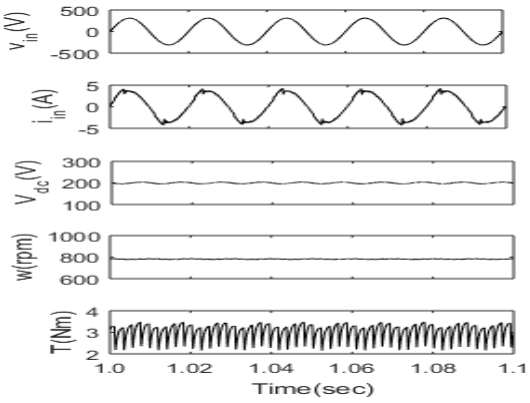

Fig. 5(a)

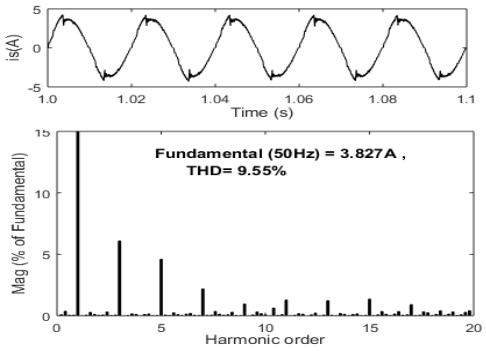

Fig. 5(b)

Fig. 5. Performance of ACS at output voltage of 200V for CSC converter

C. Performance of without bridge CSC converter based ACS at 300V Output Voltage

The performance of without bridge CSC converter based ACS is tested to compare with the performance of CSC converter based ACS. The value of input current in this case is obtained as 3.93A (rms) as shown in Fig. 6(a) whereas the output voltage is maintained constant at 300V. The electromagnetic torque varies from 2.35Nm to 3.66Nm and the rotor speed is almost same 1474rpm as in the case of CSC converter based ACS. Fig. 6b shows the harmonic spectrum of input current which is of the order of 2.31%.

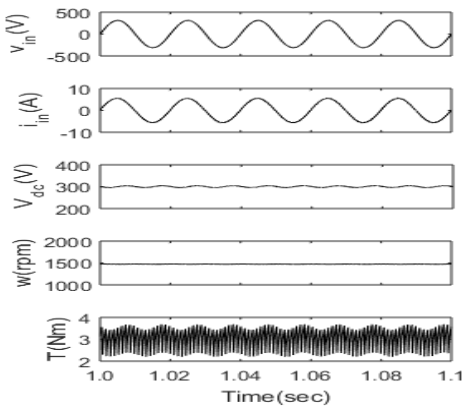

Fig. 6(a)

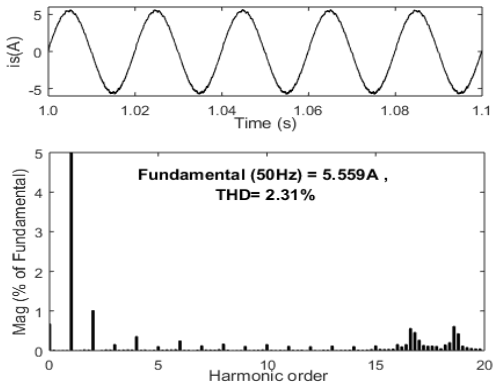

Fig. 6(b)

Fig. 6. Performance of ACS at output voltage of 300V for without bridge CSC converter

D. Performance of without bridge CSC converter based ACS at Variable Output Voltage

To demonstrate the functioning of without bridge CSC converter based ACS, the output voltage is varied from 300V to 200V and performance is shown in Fig 7. As it is clear from Fig. 7 that the output voltage is constant and value is 200V. As compared with 300V, the supply current is less sinusoidal and comes out as 2.69A (rms). The rotor speed is obtained as 1474 rpm. Fig. 7b shows the harmonic spectrum of input current which is of the order of 9.46%.

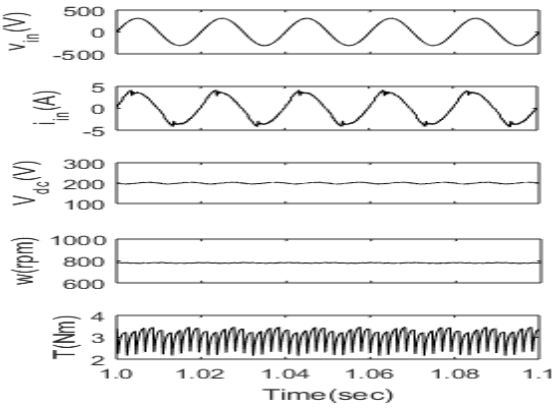

Fig. 7(a)

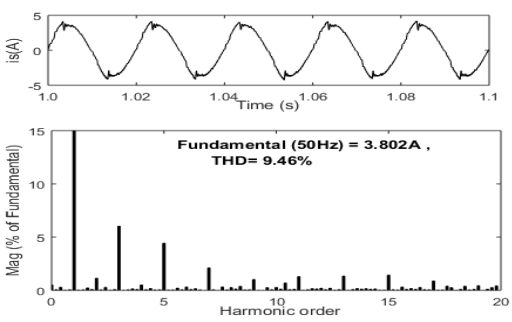

Fig. 7(b)

Fig. 7. Performance of ACS at output voltage of 200V for without bridge CSC converter

At 300V, the supply current is observed slightly high in comparison to without bridge ACS. The output voltage ripple for both CSC converters based ACS and without bridge CSC converters based ACS is observed as 2.67% approximately. There is a slight declination in speed of CSC converter based ACS. The voltage stress and current stress across the switch are approximately 600V and 24A for both the converters at 300V while the middle capacitor voltage and discontinuous inductor current are about 640V and 23.5A respectively for both the converters.

At 200V, the supply current of CSC converter based ACS is high as compared to without bridge ACS. The ripple in output voltage is around 4% for both CSC converter based ACS and without bridge CSC converter based ACS while it is slightly low in case of 300V dc. At 200V the voltage stress and current stress of the switch for both of the converters are 500V and 18A respectively while the middle capacitor voltage and discontinuous inductor current for both the converters are 520V and 18A approximately.

Table 1 shows the comparison of parameters at dc output voltage of 300V and 200V. At output voltage of 300V, the settling time of CSC converter based ACS is 0.84sec, while it is 0.52sec for without bridge CSC converter based ACS. Similarly, the output inductor current for CSC converter based ACS and without bridge CSC converter based ACS are 2.9A and 3.06A respectively. It is clear that the settling time is high in case of CSC converter based ACS while the output inductor current is slightly high in case of without bridge CSC converter based ACS. Likewise, at 200V, the settling times are 0.62sec and 0.5sec for CSC converter based ACS and without bridge CSC converter based ACS respectively. The output inductor currents are 2.85A and 2.8A for CSC converter based ACS and without bridge CSC converter based ACS respectively. Hence, from the obtained results at output voltage of 200V, the settling time and output inductor current are high in case of CSC converter based ACS. The components used in conduction path in one switching cycle for conventional CSC converter are three diodes while without bridge CSC converter are two diodes. The number of capacitors and inductor used in half switching cycle is same for both as shown in Table 1.

Table 2 show the various performance parameters such as THD, DPF, PF, supply current under variation of output dc voltage V_{dc} for CSC converter based ACS and without bridge CSC converter based ACS. As seen from the Table 2, the THD of supply current is low in case of 300V.

Table 1
Comparison of parameters at DC output voltage of 300V and 200V

	CSC converter	**without bridge CSC converter**
At 300V output voltage		
Settling time	0.84sec	0.52sec
Output Inductor Current	2.9A	3.06A
Components used in one half switching cycle	3 diode, 2 capacitor, 1 inductor	2 diode, 2 capacitor, 1 inductor
At 200V output voltage		
Settling time	0.62sec	0.5sec
Output Inductor Current	2.85A	2.8A

Table 2
Performance parameters with variation of output DC voltage (V_{DC}) for CSC converter and without bridge CSC converter

V_{dc}(Volts)	**I_{in}(A)rms**	**THD %**	**DPF**	**PF**
200V CSC Converter	2.71	9.55	0.999	0.995
Without bridge CSC	2.69	9.46	0.999	0.9946
220V CSC Converter	2.93	8.31	0.999	0.9956
Without bridge CSC	2.91	7.13	0.999	0.9965
240V CSC Converter	3.25	7.45	0.999	0.9962
Without bridge CSC	3.19	6.53	0.999	0.9969
260V CSC Converter	3.46	6.67	0.999	0.9968
Without bridge CSC	3.41	5.87	0.999	0.9973
280V CSC Converter	3.74	5.23	0.999	0.9976
Without bridge CSC	3.68	4.31	0.999	0.9981
300V CSC Converter	3.96	4.45	0.999	0.998
Without bridge CSC	3.93	2.31	0.999	0.9987

Fig. 8 (a) depicts the variation of supply current with respect to the variation in output voltage in both the ACS. The variation of supply current THD with the output voltage in both the ACS is shown in

Fig. 8 (b). Thus as seen from Fig. 8 (a), the supply current is slightly high in case of CSC converter based ACS while THD is significantly improved in case of without bridge CSC converter based ACS. Therefore, from the obtained performance of both the ACSs, it is clear that if the settling time and THD are of main concern, without bridge CSC converter based ACS may be a preferable option while if cost, size and heat sink are the main concern than CSC converter based ACS may be preferred.

Further, without bridge CSC incorporates two CSC converters at the front end for ac-dc conversion while CSC converter based ACS uses one converter. Therefore, the component count in without bridge CSC is twice than CSC based ACS. However, the conduction losses are low in without bridge CSC (due to absence of diode bridge at the front end), due to which, it offers higher efficiency than bridge based CSC. Therefore, as per the configuration and simulated performance, a user can select one of the configurations for the optimal operation of ACS according to the priority of cost, size, efficiency, settling time, THD, component count, input current.

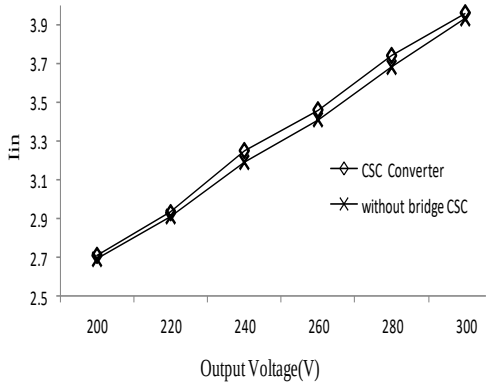

Fig. 8(a). Variation of single phase ac supply current of CSC converter and without bridge CSC converter at various Output Voltage

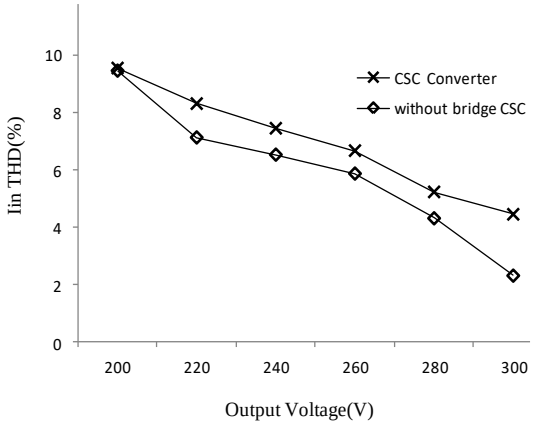

Fig. 8(b). Variation of THD of single phase ac supply current for CSC converter and without bridge CSC converter at various Output Voltage

6. Conclusion- The performances of CSC converter based ACS and without bridge CSC converter based ACS is observed under various parameters to demonstrate the effectiveness of power supply. Both the converters have been designed to function in discontinuous mode of conduction for inductor ensuring unity power factor operation. The major advantages of using CSC converter and without bridge CSC converter as a PFC are low harmonics, high PF at AC mains, low switching losses etc. Under the variation of output dc link voltage the supply current harmonics is obtained below 10%. Thus it is compatible for low power applications as well as recommended by the PQ standard.

References

1. Handershot J. R., Miller T.J.E: *Design of Brushless Permanent Magnet Motors*, Clarendon Press, Oxford, 2010.
2. Xia C. L.: *Permanent Magnet Brushless DC Motor Drives and Controls*, Wiley Press, Beijing, 2012.
3. *Limits for Harmonic Current Emissions*, International Electro technical Commission Standard, IEC-61000-3-2, 2004.
4. Singh B., Bist V.: *A BL-CSC Converter Fed BLDC Motor Drive with Power Factor Correction*, In: IEEE Transactions on Ind. Electron., LXII (2015), No.1, p. 1-12, India.
5. Reshma T. P., Rashmi M. R.: *Power Factor Correction in Brushless DC Motor Dual Drive Using Bridgeless Canonical Switching Cell Converter*, In: Proceedings of the 2nd International Conference on Power and Embedded Drive Control (ICPEDC), August 21-23, 2019, Chennai, India, p. 258-263.
6. Hegde A.R., N A. K., Meenakshi T., Pai M V.: *Power Factor Correction of Four Switch BLDC Motor Drive Using Bridgeless-CSC Converter*, In: Proceedings of the IEEE International Conference on Advances in Electrical Technology for Green Energy (ICAETGT'), September 23, 2017, Coimbatore, India, p. 56-63.
7. Nair A. S., C. A. K. W.: *Dual Mode Control Strategy for BLDC Motor Drive with Bridgeless Canonical Switching Cell Converter*, In: Proceedings of the International Conference on Power Electronics, Drives and Energy Systems (PEDES), December 14-17, 2016, Trivandrum, India, p. 1-6.
8. Narula S., Singh B., Bhuvaneswari G., Chandra A., Haddad K. A.: *Power Quality Improved SMPS Using BL-CSC Converter for Welding Applications*, In: Proceedings of the IEEE Industry Applications Society Annual Meeting, October 2-6, 2016, Portland, OR, USA, p.1-8.
9. Luo H., Xu J., Luo Y., Sha J.: *A Digital Pulse Train Controlled High Power Factor DCM Boost PFC Converter Over a Universal Input Voltage Range*, In: IEEE Trans. Ind. Electron., LXVI (2019), No. 4, p. 2814-2824, China.
10. Akter K., Sarowar G., Hoque M. A. , Ahmed S.F.B.: *Modeling and Simulation of Input Switched AC-DC SEPIC Converter with PFC Control for Optimized Operation*, In: Proceedings of the International conference on Electrical Engineering and information & Communication Technology (ICEEICT), September 13-15, 2018, Dhaka Bangladesh, p. 240-245.

11. Costa P. J. S., Font C. H. I., Lazzarin T. B.: *A Family of Single- Phase Voltage-Doubler High-Power-Factor SEPIC Rectifiers Operating in DCM*, In: IEEE Trans. Power Electron., XXXII(2017), No.6, p.4279 – 4290, Brazil.
12. Singh B., Anand A.: *Power Factor Correction in Modified SEPIC Fed Switched Reluctance Motor Drives*, In: IEEE Trans. Ind. Appl., LIV (2018), No.5, p. 4494-4505, India.
13. Anand A., Singh B.: *Modified Dual Output Cuk Converter-Fed Switched Reluctance Motor Drive With Power Factor Correction*, In: IEEE Trans. Power Electron., XXXIV(2019), No.1, p. 624-635, India.
14. Anand A., Singh B.: *Power Factor Correction in Cuk–SEPIC-Based Dual-Output-Converter-Fed SRM Drive*, In: IEEE Trans. Ind. Electron., LXV (2018), No. 2, p. 1117-1127, India.
15. Jha A., Singh B.: *High power factor and low total harmonics distortion using critical conduction mode boost converter–fed light-emitting diode driver*, In: Int. Trans. Elect. Energy Syst., X (2016), p. 1–11, India.
16. Lakshmi G. R. P.: *Power factor improvement of Canonical switch cell Converter fed BLDC Motor Drive*, In: Proceedings of the International Conference on Computation of Power, Energy Information and Communication (ICCPEIC), April 20-21, 2016, Melmaruvathur, India, p. 624-627.
17. Subramanian A.T.S., Sabarish P., Ali A.N.: *A Power Factor Correction Based Canonical Switching Cell Converter for VSI Fed BLDC Motor By Using Voltage Follower Technique*, In: Proceedings of the International Conference on Electrical, Instrumentation and Communication Engineering (ICEICE), April 27-28, 2017, Karur, India, p. 1-8.
18. Jha A., Singh B.: *Power Quality Improvement Using CSC Converter for High Power LED Driver*, In: Proceedings of the IEEE 6th International Conference on Power Systems (ICPS), March 4-6, 2016, New Delhi, p. 1-6.
19. Litrán S.P., Durán E., Ferrera M.B., Semião J., Barroso R. S.: *A Zeta-CSC Converter Combination for Single-Input and Bipolar Output*, In: Proceedings of the IECON 2019 - 45th Annual Conference of the IEEE Industrial Electronics Society, October 14-17, 2019, Lisbon, Portugal, p. 5721-5726.
20. Pandey R., Singh B.: *A Canonical Switching Cell (CSC) Converter Based Power Factor Corrected Battery Charger for E-Rickshaw*, In: IEEE Trans. Ind. Appl., LVI(2020), No. 5, p. 5046-5055, India.
21. Ma H., Li Y., Lai J. S., Zheng C., Xu J.: *An Improved Bridgeless SEPIC Converter Without Circulating Losses and Input-Voltage Sensing*, In: IEEE Journal of Emerging and Selected Topics in Power Electronics, VI(2018), No. 3, p. 1447-1455, China.
22. Kumar R., Kumar S.S.: *PFC Using Bridgeless SEPIC Converter*, In: Proceedings of the 2nd International conference on Electronics, Communication and Aerospace Technology (ICECA), March 29-31, 2018, Coimbatore, India, p.1620-1624**.**
23. Costa P. J. S., Font C. H. I., Lazzarin T. B.: *Single-Phase Hybrid Switched-Capacitor Voltage-Doubler SEPIC PFC Rectifiers*, In: IEEE Trans. Power Electron., XXXIII(2018), No. 6, p. 5118- 5130, Brazil.
24. Ananthapadmanabha B. R., Maurya R., Arya S. R.: *Improved Power Quality Switched Inductor Cuk Converter for Battery Charging Applications*, In: IEEE Trans. Power Electron, XXXIII (2018), No. 11, p. 9412- 9423, India.
25. Liu Y., Sun Y., Su M.: *A Control Method for Bridgeless Cuk/Sepic PFC Rectifier to Achieve Power Decoupling*, In: IEEE Trans. Ind. Electron., LXIV(2017), No. 9, p. 7272-7276, China.
26. Lin X., Wang F.: *New Bridgeless Buck PFC Converter with Improved Input Current and Power Factor*, In: IEEE Trans. Ind. Electron., LXV (2018), No. 10, p. 7730-7740, China.
27. Jha A., Singh B.: *Bridgeless ZETA PFC Converter for Low Voltage High Current LED Driver*, In: Proceedings of the 6th International Conference on Computer Applications in Electrical Engineering-Recent Advances (CERA), October 5-7, 2017, Roorkee, India, p. 539-544**.**

PERFORMANCE EVALUATION AND ANALYSIS OF RING LOADED PATCH ANTENNAS

K. Mahesh Babu, T.V. Rama Krishna
Research Scholar, Dept. of ECE, KLEF Deemed to be university, Guntur, AP, India.
Professor, Dept. of ECE, KLEF Deemed to be university, Guntur, AP, India.
kmaheshbabu@kluniversity.in tottempudi.rk@gmail.com

Abstract:
The paper presents a detailed investigation on various types of circular ring patch antennas and their importance in Wireless Communications especially under satellite Frequency Applications. The main focus is considered on the typical resonant frequencies, design parameters, theoretical foundations on shape, equivalent circuits, various applications of the ring patch antennas. Simulation and comparison of different structures of patch with annular ring patch was also presented to justify the investigation.

Key Words: *Microstrip Patch antennas, Microwave Frequency, Wireless Communications, Circular Ring patch.*

1. Introduction:

From the past few decades, planar antennas were considered as the best choice of interest to meet the requirements and specifications of microwave frequencies in wireless communications. The main reason for opting the planar microstrip antennas is their weight and compact in size, economic in terms of cost and fabrication [1]. Microstrip Antennas are available in different shapes like ring, rectangle, square circle, triangle, ring, etc. Out of these shapes, ring shape has gained unusual importance for its smaller size, flexible and miniaturization for array structures, wide bandwidth and less stored energy [2]. For Obtaining wide as well as multi-band features, ring structures are included with other geometric elements and one of the interesting features of ring patch antennas is that separation of resonant modes depends on the ring outer to inner radii ratio [3]. The circular polarisation can be easily attained with ring patches related to other shapes by simply making slots or extending the patch dimensions. Although, theoretical analysis of ring patch antennas is not a recent problem but the importance of the analyses for the designs is mandatory to fulfil the conditions and limitations of any application. The theoretical foundations for the ring patches was initiated since the usage of the ring structure has begun. From different ring structures, annular ring is most widely used shape due to its fringing effect at both inner and outer radii and high radiation performance [4]. Ring antennas act as a transitional configuration between a patch and in print loop in both geometrical as well as electrical cases. The ring structure can also be used to determine the material dielectric constant and as a radiator for medical applications [5]. The Ring structures can be of square, triangle, rectangle or circular shapes. The circular or annular ring shape is most widely used as it minimises the open-end loading effect observed in other patch structures. Apart from this, the annular ring which possess several advantages than other structures of microstrip antennas. This paper carries out the investigation of the work done by various authors on annular ring microstrip antennas from the past few decades and the justification of the investigation through simulation and comparison of annular ring patch antenna with other structures of microstrip antennas.

2. Investigation:

In this section, the work carried out by various authors on annular ring patches was presented. In [1] a multiband circular ring patch antenna was proposed on a patch shape configuration method with constant layout dimensions. The applications of the proposed antenna are confined to 4G wireless communications having 3 bands with their centre frequencies at 6.86GHz, 12.37GHz and 13.75 GHz having bandwidths of 270MHz, 460MHz and 480 MHz respectively and the VSWR have been maintained approximately at 1. In [6] the application is focused on C-band satellite communications and X-band under Radar applications with a rectangular patch with two concentric circular ring slots and two diamond shaped patches near the feed line. The designed is made as to obtain circular polarisation using two concentric ring circles and the enhancement of antenna gain by two diamond shaped patches. The proposed antenna provides dual bands having resonating frequencies at 6.6 GHz and 9.4GHz with S_{11} of -14.7dB and -20.9dB respectively. The bandwidths obtained are 6.38- 6.8 GHz and 9.2 TO 9.6GHz with gains of 4.77dB and 6.29dB respectively. In [7] a patch

antenna with concentric annular ring slot was proposed which provides bidirectional circular polarisation radiation with dual bands operating at 2.45 GHz (ISM) and 3.5 GHz (5G) bands. The two-band operation was obtained with tunnelling annular ring slots in the base as well as to maintain circular polarisation two bend structures are loaded on each annular ring inclined at 45^0. In [8] a simple single feed circular patch antenna is proposed with asymmetrical ring-shaped arc slot pairs with extended narrow slots are implanted on both patch and ground which provides dual or multi band circularly polarized radiation. The arc slots embedded increase the impedance bandwidth through the mutual coupling between arc slot resonance and circular patch fundamental resonance and the two extended narrow slots provide circular polarisation. An extensive parametric analysis has been done on each and every parameter dimension to obtain the optimum results. In [9] the importance of a ring structure has been proved by loading a simple co-axial fed conventional circular patch antenna with a ring. This made the antenna configuration to obtain better performance than a conventional patch antenna which includes greater impedance bandwidth, high gain, surface waves excitation reduction with improvement in efficiency. In [10] a novel technique has been implemented using short pins between the patch and ground and loading a circular patch with an annular ring which enhanced impedance bandwidth making the antenna broadband in nature. In [11] full wave analysis of a probe fed spherical circular patch antenna loaded by a circular ring was performed in frequency domain using Galerkin's moment method and vector Legendre transform which provided broadening of impedance bandwidth. In [12] full wave analysis of Circular ring patch antennas on double uniaxial anisotropic substrate were theoretically defined with particular cases of one-layer substrate and adjourned substrate. The observations of analyses include the relation between the resonant frequency and substrate permittivity rather than with its height. The operating frequency and radiation pattern were determined by Hankel Transform domain and Hertz Vector Potentials whose numerical results shown that these depend on antenna geometrical parameters. In [13] different novel and miniaturized ring patch antennas were designed to obtain single and multi-band operations by etching various structures in the patch as well as ground of the patches. The designs have provided very efficient results with variations in the dimensions of the rings patches and cross slot structures. In [14] monopole like broadband omnidirectional radiation characteristics were obtained by centre feeding a coupled annular ring patch. The obtained various parameter results were simulated and measured at 5.8 GHz resonant frequency with gain 5.7 dBi and -10dB S_{11} bandwidth of 12.8%. In [15] a triple band compact size single layer probe fed concentric annular ring patch antenna was designed to provide 6.38, 6.30 and 35% of impedance bandwidths at 1.17GHz, 1.428 GHz and 1.9 GHz respectively. The multiband operation was obtained by etching a cross slot in ground and embedding a simple circular patch to concentric ring patch loaded with dual stub. In [16] a novel UWB circular ring structure antenna was designed and analysed for biomedical applications. The proposed antenna resembles like Ashoka chakra and provides compact size. The design was analysed putting on tri-layered human phantom model examining on arm and head at three different frequencies. In [17] ring patch antenna was designed with frequency independent tunability as peculiar feature for WLAN and WIMAX applications. The Dual-band operation was introduced by loading the patch with a gap. Independent frequency tunability was also obtained by etching peripheral trenches at particular positions on the patch. In [18] an annular ring patch was proposed with DGS to promote multiband operation. The antenna performs at 3 different resonant frequencies of S/C/X bands providing circular polarisation using wave port excitation. In [19] a simple ring-shaped patch antenna was designed operating between 2 to 5 GHz for WLAN, WIFI applications. The frequency tunability was achieved by introducing slots at particular locations.

3. Mathematical Analysis:

The Mathematical analyses regarding the design of annular ring patch has begun around 1980s by James W. Mink [20] providing the theoretical as well as experimental work on a simple ring patch antenna. The paper presents a theoretical expression for the electric and magnetic fields in cylindrical coordinates by using Bessel functions and Taylor's series expansion. The evolution of circular ring antennas was from the ring resonators. The fundamental field expressions were considered based on the ring resonators. The magnetic currents and propagated fields were experimentally verified. The resonator operating frequency was computed with stationary principle and the numerical results were compared with experimental data for testing accuracy [21,22].

Out of numerous mathematical models/methods for the analysis that are followed since from the initial investigation, some important methods were discussed here. The basic mathematical analysis of circular ring microstrip antenna was performed to determine resonant frequency using planar wave guide model, radiation characteristics were derived from the magnetic current equations and radiating fields using electric vector potentials derived from magnetic currents [23]. The development of the annular ring patch improved to obtaining dual frequencies and detailed analysis of patch design and its radiation characteristics were proposed in [24] which include supressing unwanted modes, input impedance model, radiation patterns, etc., providing good agreement between theoretical and measured values. In [25] the methods required for improving the patch characteristics were investigated numerically as well as experimentally stating that the resonant frequency and impedance depend on design geometry. As in [25] was proposed for a printed square ring antenna, the same was implemented for annular ring in [26] through FWSD moment method solution in which the probe feed and ring patch connection was modelled using mode expansion function. Another approach for numerical analysis is done majorly through the Hankel Transform domain [2, 12, 27, 28] and Hertz Vector potentials [2, 12, 28] where the equivalent circuit of the patch and field expressions were obtained. Cavity model analysis [29, 30] can also be used to derive various field expressions and current expressions based on magnetic currents on the peripherals of the wall. The model also determines the design requirements like effective dielectric constant, Mode dependent resonating frequency, effective geometry dimensions.

4. Comparison of Annular ring with other basic Shapes of Patch Antennas:

There are numerous structures available for microstrip antennas like rectangular, Square, Triangular, Circular, Ring, etc. out of these patch shapes, annular ring is most widely used one. To justify this statement, comparison and analysis of annular ring patch with other basic patch shapes like rectangular and circular patch antennas were performed operating at a frequency f_0 = 15 GHz, dielectric medium RT duroid with permittivity value ε_r = 2.2 and depth h = 1.59mm. Inset microstrip feed technique was used for proper impedance matching. The antennas were designed and simulated using CST 2017. The mathematical design equations for each patch antenna are considered from [5, 30, 31]

4.1 Rectangular Patch antenna:

Width $W_o = \frac{c}{2*f_0*\sqrt{\frac{\varepsilon_r+1}{2}}}$ (1)

Length $L_0 = L_{eff} - 2 * \delta l$ (2)

Where

c = 3* 10^{10} is velocity of light in cm/sec.

$L_{eff} = \frac{c}{2*f_0*\sqrt{\varepsilon_{reff}}}$ is the operative length of the patch fringing effect.

$\varepsilon_{reff} = \frac{\varepsilon_r+1}{2} + \frac{\varepsilon_r-1}{2}[1 + 12 * \frac{h}{w}]^{\frac{-1}{2}}$ is the effective dielectric constant.

$\delta l = 0.41 * h * \frac{(\varepsilon_{reff}+0.3)*(\frac{w}{h}+0.264)}{(\varepsilon_{reff}-0.258)*(\frac{w}{h}+0.8)}$ is the normalised extended length.

The substrate and ground dimensions are given by

$Length\ L_g = L + 6 * h$ and

$Width\ W_g = W + 6 * h$

The substrate thickness $h = \frac{0.0606*\lambda}{\sqrt{\varepsilon_r}}$.

By substituting the specified design values, we get the geometry dimensions as W = 0.79 cm, L = 0.59cm, L_g = 1.59 cm, W_g = 1.74 cm, L_{eff} = 0.721 cm.

Fig.1. Rectangular patch antenna structure

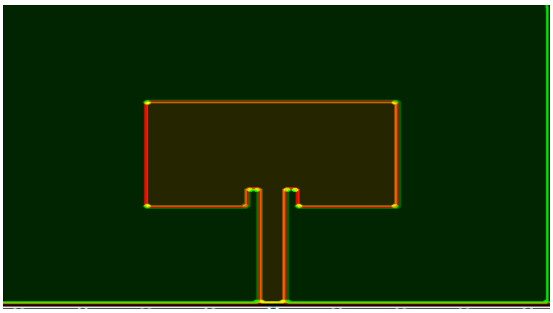

4.2 Circular Patch antenna:

The resonant frequency expression is given by

$f_{rnm} = \frac{\chi_{nm}*c}{2*\pi*a*\sqrt{\varepsilon_r}}$ (3)

Where c = 3* 10^{10} is velocity of light in cm/sec

$a = \frac{F}{\{1+\frac{2*h}{\pi*\varepsilon_r*F}[1.7726+ln(\frac{\pi*F}{2*h})]\}^{\frac{1}{2}}}$ is the radius of the patch

$$F = \frac{8.791*10^9}{f_0*\sqrt{\varepsilon_r}} \quad (4)$$

χ_{nm} is the first order Bessel function root and depends on the mode of the patch. For TM_{10} the value of χ_{nm} = 1.841.

The operative radius with fringing is

$$a_e = a\{1+\frac{2*h}{\pi*\varepsilon_r*a}[1.7726+\ln(\frac{\pi*a}{2*h})]\}^{\frac{1}{2}} \quad (5)$$

The geometric dimension values of circular patch antenna for the specified design are a = 0.35 cm, F= 0.395 and a_e = 0.45 cm.

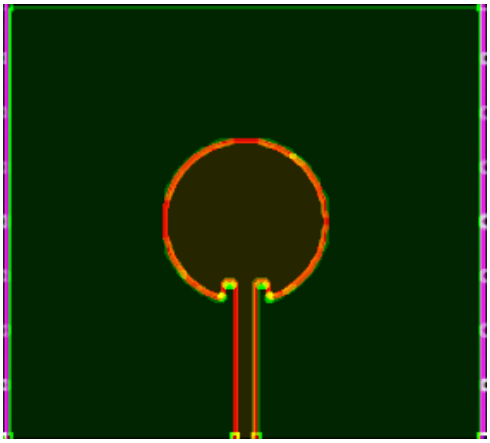

Fig.2. circular patch antenna structure.

4.3 Ring Patch Antenna:

The mathematical analysis of a ring patch was similar to circular patch

Resonant frequency $f_{rnm} = \frac{\chi_{nm}*c}{2*\pi*a*\sqrt{\varepsilon_r}}$ (6)

Where

c = 3* 10^{10} is velocity of light in cm/sec

χ_{nm} is the first order Bessel function root and depends on the mode of the patch.

For TM_{11} the value of χ_{nm} = 0.6773. $\chi_{nm} = K_{nm} * a$

Where n indicates azimuthal variation and
m indicates field variation across the ring width.

The above expressions provide accurate values when $\frac{b-a}{b+a} < 0.35$ and $b = 2 * a$ conditions are met. 'a' and 'b' are the inner and outer radii of the ring.

If the fringing effect is also considered then the resonant frequency is given by

$$f_{rnm} = \frac{\chi_{nm}*c}{2*\pi*a*\sqrt{\varepsilon_{re}}} \quad (7)$$

Here

$\varepsilon_{re} = \frac{\varepsilon_r+1}{2} + \frac{\varepsilon_r-1}{2}[1+10*\frac{h}{w}]^{\frac{-1}{2}}$ is the effective dielectric constant. w = b-a is the width of the ring.

The computed geometrical values from mathematical expressions are b= 0.323 cm and a= 0.1618cm.

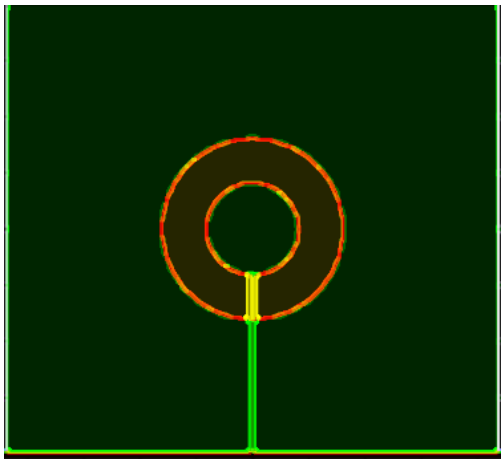

Fig.3. Annular Ring patch antenna structure.

4.4 Ring loaded circular patch:

The performance characteristics of circular patch antenna can be improved through loading an annular ring with a width of annular ring and the separation between the loaded ring and patch are maintained at 0.15 cm. The annular ring is etched away at the feed point. The outer radius and inner radius of the loaded ring are 0.3cm and 0.15 cm respectively.

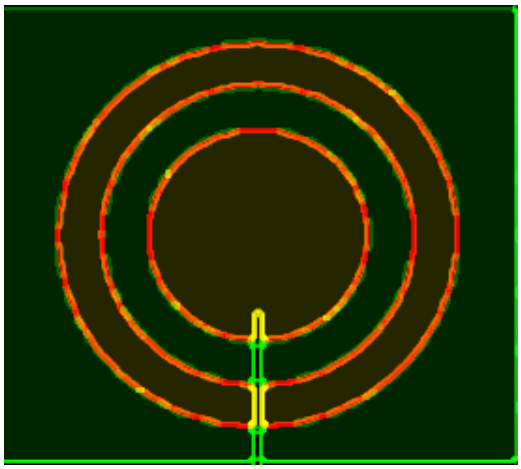

Fig.4. circular patch with loaded annular ring antenna structure.

5. Results and Discussions:

The antenna structures discussed in the above section were designed and simulated using CST 2017. This section provides analysis of the EM fields as well as comparison of the ring patch with other patch antennas. The patches were inset fed for proper impedance matching and examined that width and depth of the microstrip line inset feed decides the impedance matching of feed and patch.

The designed rectangular patch resonated at a frequency of 15.196 GHz having good return loss of -49.369 dB with an impedance bandwidth of 1.46 GHz [(15.951 – 14.505) GHz]. The gain provided by the antenna is 6.48dBi. The 3dB angular beam width is 89.2^0, sidelobe lobe level of -15.4dB and the directivity is 6.39dBi.

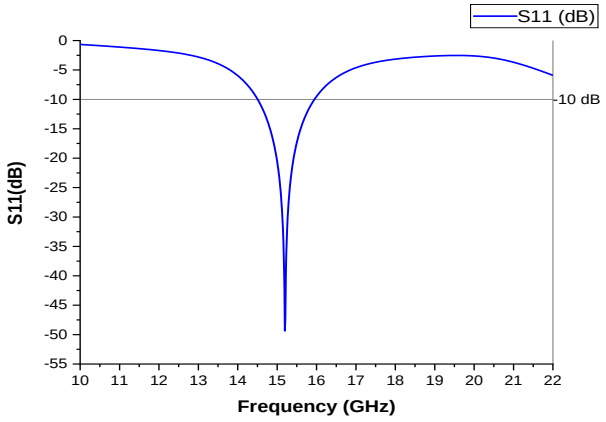

a. Return Loss Vs Frequency

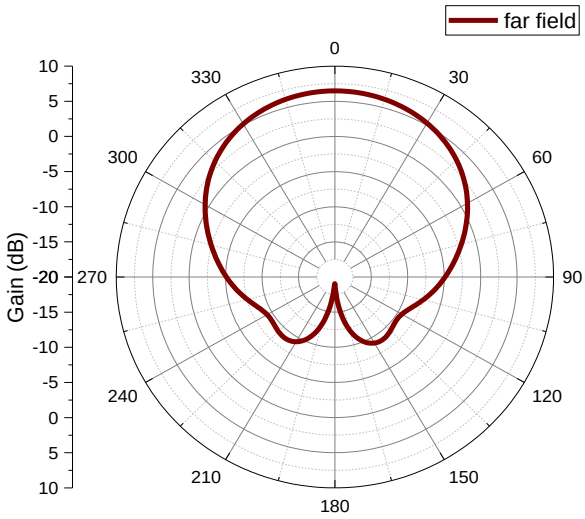

b. Far field Polar Plot

Fig.5. Performance metrics of Rectangular Patch Antenna

The proposed circular patch resonates at 15.28GHz with S_{11} =-38.32 dB and the -10dB bandwidth is 1.357 GHz [(15.965 to 14.608) GHz]. The realized gain is of 6.31dBi, beam width 92.3^0, side lobe level -17.3 dB and 6.27dBi.

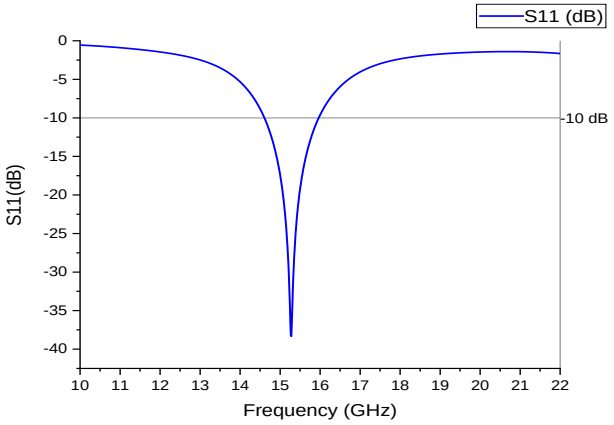

a. Return Loss Vs Frequency

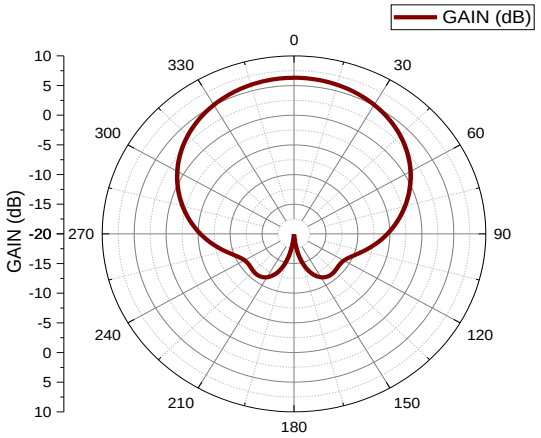

b. Far field Polar Plot

Fig.6. Performance metrics of Circular Patch

The ring antenna provided a return loss of -14.71 dB at an operating frequency of 15.396 GHz with -10dB bandwidth of 1.013 GHz [(15.909-14.896) GHz], gain 6.43dBi, beam width 94.9^0, side lobe level -16.9 dB and directivity of 6.38dBi.

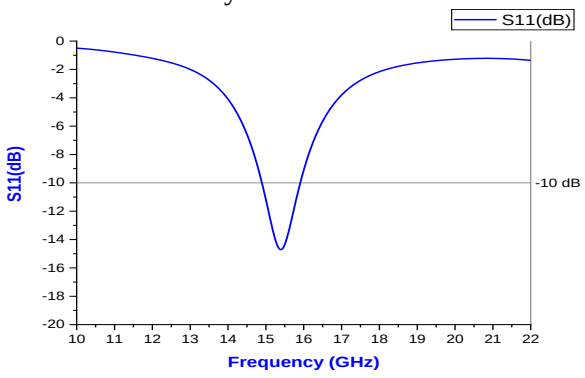

a. Return Loss Vs Frequency

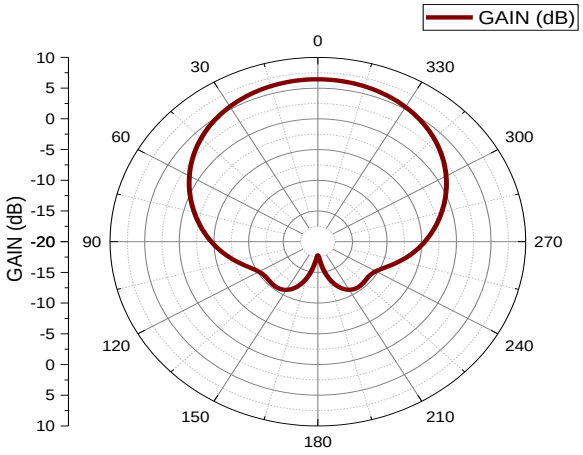

b. Far field Polar Plot

Fig.7. Performance metrics of Annular Ring Patch.

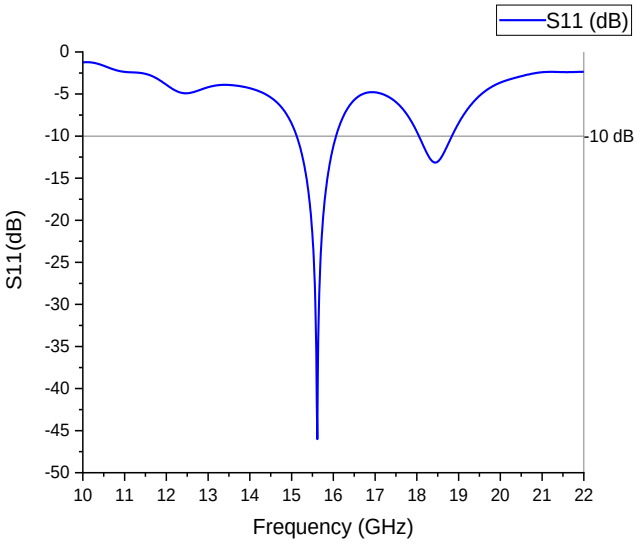

a. Return Loss Vs Frequency

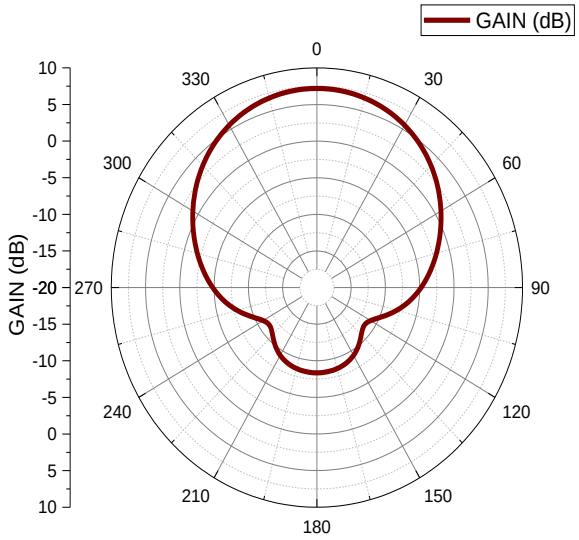

b. Far field Polar Plot at Band1

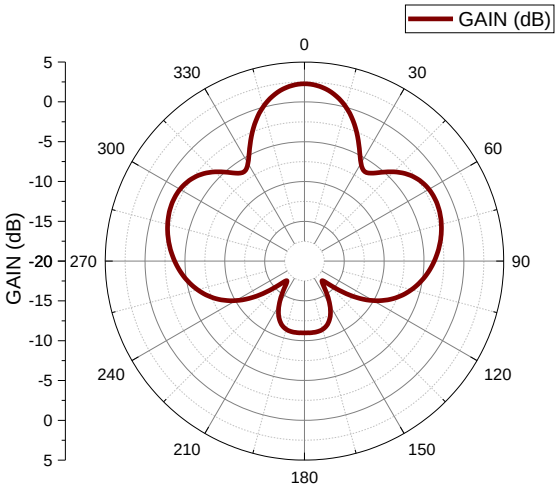

c. Far field Polar Plot at Band 2

Fig.8. Performance metrics of Annular Ring loaded Circular Patch

The ring loaded circular patch has shown tremendous improvement apart from the circular patch antenna. The dual band operation was observed with the resonating frequencies 15.616 GHz and 18.436 GHz with reflection losses of -46. 498dB and -15.431 dB respectively. The impedance band width at band1 is 943 MHz [(16.066-15.123) GHz] and at band 2 is 789MHz [(18.84 – 18.051) GHz]. The gain at centre frequency of band1 is enhanced to 7.19dBi, beam width 81.6^0, side lobe level -15.5 dB and directivity of 7.83dBi. The second band performance metrics are gain 2.26dBi, beam width 34.8^0, side lobe level -4.1 dB and directivity of 4.55dBi.

The parametric analysis was performed on the feed width of the patch(w_f). It is observed that the impedance matching of the patch will be mostly depend on the feed width.

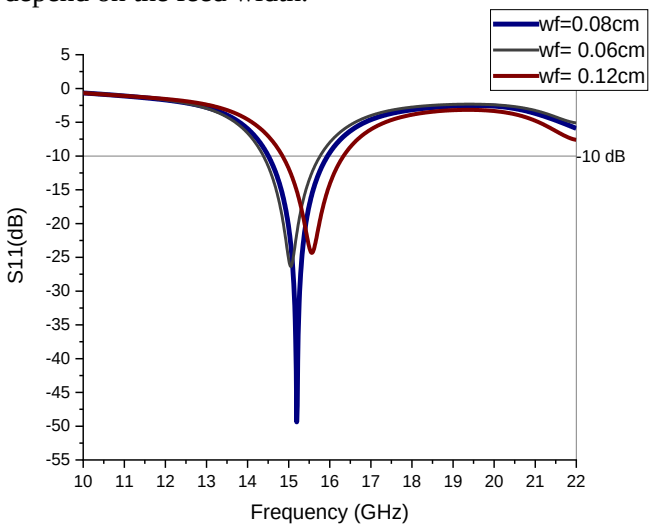

Fig.9. Return loss S_{11} for various feed width values

The table1 illustrates the comparison of different parameters of all the designed patches

Conclusion:

In this paper, the various design of ring Microstrip Patch antenna were studied and surveyed in detail. The mathematical foundations and analyses were also studied which stated that most of the patch analysis used hankel transforms as well as vector potentials. The basic mathematical foundations were also discussed and simulation and analysis of patch antennas were compared. Annular ring loaded circular patch antennas shown better performance were analysed. The inset feeding has shown better performance results when compared with other feeding techniques.

References:

1. Mohamed A. Abdelaal and Hussein Hamed Mahmoud Ghouz, "*New Compact Circular Ring Microstrip Patch Antennas*", Progress in Electromagnetics Research C, Vol. 46, 135-143, 2014.
2. C. F. L. Vasconcelos , S. G. Silva "*Annular Ring Microstrip Patch Antenna on a Double Dielectric Anisotropic Substrate*", Progress In Electromagnetics Research Symposium Proceedings Moscow, Russia, August 2009.
3. Cristian Andriesei, "*Annular-Ring Microstrip Patch Antennas*" Buletinul Institutului Politehnic Din Iasi, Volumul 63 (67), Numarul 4, 2017.
4. Sanyog rawat,kamalesh kumar sharma "*Annular ring microstrip patch antenna with finite ground plane for ultra-wideband applications*", International Journal of Microwave and Wireless Technologies, 2015.
5. Garg R, Bhartia P, Bahl I, Ittipiboon "*A. Microstrip antenna design handbook*". Artech House Inc.; 2001.
6. Ketavath Kumar Naik Pasumarthi Amala Vijaya Sri "*Design of Concentric Circular Ring Patch with DGS for Dual-Band at Satellite Communication and Radar Applications*", Springer, Wireless Personal Communications, Volume 98, Issue 3, 2017.
7. Yong Cheng and Hui Liu "*A Novel Concentric Annular-Ring Slot Dual-Band circularly polarized Microstrip Antenna*", International Journal of Antennas and Propagation, Hindawi, Volume 2018.
8. farzad alizadeh, changiz ghobadi "*A design of ring-shaped dual-band/multi-band circularly polarized microstrip antenna based on slots mutual coupling*", International Journal of Microwave and Wireless Technologies, 2015.
9. D.M. Kokotoff, R.B. Waterhouse, C.R. Birtcher and J.T. Aberle, "*Annular Ring Coupled Circular Patch with enhanced performance*", IEEE Electronics Letters November 1997 Vol. 33 No. 24.
10. D. M. Kokotoff, R. B. Waterhouse, And J. T. Aberle, "*An Annular Ring Coupled To A Shorted Patch*", IEEE Transactions On Antennas And Propagation, Vol. 45, No. 5, May 1997.
11. Hong-Twu Chen, Horng-Dean Chen, And Yuan-Tung Cheng, "*Full-Wave Analysis Of The Annular-Ring Loaded Spherical-Circular Microstrip Antenna*", IEEE Transactions On Antennas And Propagation, Vol. 45, No. 11, November 1997.
12. C. F. L. Vasconcelos, S. G. Silva, M. R. M. L. Albuquerque, "*Annular Ring Microstrip Antennas for Millimetre Wave Applications*", Int Journal of Infrared Millimetre Waves (2007).
13. Ammann, M., Bao, X., "*Miniaturized annular ring loaded patch antennas*", IEEE Antennas and Propagation International Symposium, 2007.
14. Asem Al-Zoubi, Fan Yang, "*A Broadband Centre-Fed Circular Patch-Ring Antenna with a Monopole Like Radiation Pattern*", IEEE Transactions on Antennas and Propagation, VOL. 57, March 2009.
15. X.L. Bao and M.J. Ammann, "*Compact concentric annular-ring patch antenna for triple-frequency operation*", IEEE Electronics Letters, Vol. 42 No. 20, September 2006.
16. B. Prudhvi Nadh B. T. P. Madhav "*Circular ring structured ultra-wideband antenna for wearable applications*", International Journal of RF and Microwave Computer Aided Engineering, October 2018.
17. K. Jhamb L. Li K. Rambabu, "*Frequency adjustable microstrip annular ring patch antenna with multi-band characteristics*", IET Microwaves, Antennas & Propagation, Vol. 5, Issue 12, pp. 1471–1478, 2011.
18. C. R. Prashanth, Mahesh N. Naik, "*Design of Compact Multiband Annular-Ring Slot Antenna*", Integrated Intelligent Computing, Communication and Security, Springer, September 2018.
19. Divyabharathi P, Abirami M, Puvaneshwari S, Vikram N, "*Ring Structured Patch Antenna for wide band Applications*", International Journal of Innovative Technology and Exploring Engineering (IJITEE), ISSN: 2278-3075, Volume-8 Issue-5 March, 2019.
20. James W. Mink, "Circular Ring Microstrip Antenna Elements", IEEE Transactions, 1980.
21. Y. S. Wu, F. J. Rosenbaum, "*Mode Chart for Microstrip Ring Resonators*", IEEE Transactions on Microwave Theory and Techniques", July 1973.

22. Sotirios G. Pintzos, Reinhold Pregla, "*A Simple Method for Computing the Resonant Frequencies of Microstrip Ring Resonators*", IEEE Transactions on Micro wave Theory And Techniques, Vol. Mtt-26, No. 10, October 1978.
23. I.J. Bahl And S.S. Stuchl, "*Characteristic Of Microstrip Ring Antennas*", IEEE Transactions On Micro Wave Theory And Techniques, 1981.
24. N.S. Nurie And R.J. Langley, "*Performnce of Concentric Annular Patches as a Dual Frequency Band Microstrip Array Element*", IEEE Transactions On Micro Wave Theory And Techniques, 1989.
25. L. Shafai, "*Characteristics of Printed Ring Microstrip Antennas*", ANTEM, 1996.
26. David M. Kokotoff, James T. Aberle, and Rod B. Waterhouse, "*Rigorous Analysis of Probe-Fed Printed Annular Ring Antennas*", IEEE Transactions on Antennas and Propagation, Vol. 47, No. 2, February 1999.
27. C . S. Gurel Ä and E. Yazgan, " *Resonant Frequency Analysis of Annular Ring Microstrip Patch on Uniaxial Medium Via Hankel Transform Domain Immittance Approach*", Progress In Electromagnetics Research M, Vol. 11, 37-52, 2010.
28. Ouarda Barkat, "*Full-Wave Spectral Analysis of Resonant Characteristics and Radiation Patterns of High Tc Superconducting Circular and Annular Ring Microstrip Antennas*", Advancement in Microstrip Antennas with Recent Applications, INTECH, 2013.
29. Rajesh Kumar, Dr. D. C. Dhubkarya, "*Design and Analysis of Circular Ring Microstrip Antenna*", Global Journal of Researches in Engineering", Volume 11 Issue 1, February, 2011.
30. Padam Singh, D.C. Dhubkarya, Alok Aggrawal, "*Design and Analysis of Annular Ring Slot MSA for wireless and UHF Applications*", Conference on Advances in Communication and Control Systems 2013 (CAC2S 2013), Atlantis Press.
31. Constantine A. Balanis, "*Antenna Theory Analysis and Design*", Wiley Publications, 2016.

Table.1. Comparison of performance metrics of designed patch antennas

Parameter	Rectangular	Circular	Annular Ring	Ring Loaded Circular
Designed f_r	15 GHz	15 GHz	15 GHz	15 GHz
Obtained f_0	15.196 GHz	15.28 GHz	15.396 GHz	Band1: 15.616 GHz Band2:18.436 GHz
S_{11} (dB) at f_0	-49.369	-38.32	-14.71	Band1: -46.498 Band2: -15.431
Impedance Bandwidth	1.46 GHz (15.951 – 14.505) GHz	1.357 GHz (15.965 – 14.608) GHz	1.013 GHz (15.909- 14.896) GHz	Band1: 934 MHz (16.066-15.123) GHz Band2: 789 MHz (18.84- 18.051) GHz
Gain (dBi)	6.48	6.31	643	Band1: 7.19 Band2: 2.26
Directivity (dBi)	6.39	6.27	6.38	Band1: 7.83 Band2: 4.55
Beam Width	89.2^0	92.3^0	94.9^0	Band1: 81.6^0 Band2: 34.8^0
Side Lobe Level (dB)	-15.4	-17.3	-16.9	Band1: -15.5 Band2: -4.1

Smart DSM to Optimize Residential Load Consumption during Energy Peaks

Rovan Refaat El-Razky, Ahmed Ali Dauod, Kamel El serafy
Department of Electrical Engineering, Faculty of Engineering, Port Said University, Egypt

Abstract. Recently, Demand Side Management (DSM) has played an important role in the smart grid through the optimization of residential load consumption. Smart DSM is a very important tool that permits customers to take right decisions for their energy consumption, it also helps the energy utilities to decrease the over load demand and reshape the load curve.
This paper proposes an optimized DSM technique based on smart metering to minimize load consumption, especially during load peaks. Bat Algorithm technique is proposed to optimize the minimum consumption during peak hours according to load type for three consumers' types whom are classified based on their lifestyles. A control algorithm is applied to the proposed system to achieve load shifting according to the optimization results.

Keywords. Demand Side Management, Smart metering, Load Shedding, Smart Pricing, Bat Algorithm.

I. INTRODUCTION

According to the expectations of International Energy Agency, demand will increase by 12% in 2020, compared to 2010. High peak demands could cause generation outages and blackout. Therefore, to solve this problem smart grid gives benefits to all the following parties; to the utilities as it provides better demand management, to the customer in the picture of saving costs, and to the Environment by granting ability to reduce greenhouse gas Emissions [1].

Demand side management (DSM) is an important function in energy management of the future smart grid; it is a reliable and cost-effective tool to manage the demand according to the available generation. DSM aims at improving the energy efficiency and making less operating cost of the utility [2].

DSM strategies are verified by means of six methods including: peak clipping, valley filling, load shifting, strategic conservation, strategic load growth and flexible load shape. Load shifting strategy encourages customers to shift their peak load to off-peak times. Where, traditional DSM is used to find optimal allocation of resources and on the premise of some effective incentives; smart DSM realizes the effective interaction between the grid and consumers [3, 4].

Smart pricing is a smart tool to encourage users to save energy consumption by using smart metering devices. DSM includes smart pricing will cognize group's central controller about new load schedule and loads that can be reduced for each time step. The control center can place bids in the market such as some loads from the peak demand which will be shifted or shed. Any profits made through this load, DSM will be paid back to customers of the group [5, 6].

In modern smart grid, the controllable devices are needed to be utilized to execute the demand side management algorithm. Furthermore, each type of controllable load can have various characteristics regarding their consumption over few hours. In this paper, the demand side management strategy is proposed for the smart grid which is based on load shifting technique. Moreover, load shedding shall be applied to emergency cases. There is mixture in the proposed strategy between load shifting and load shedding which is used for different devices for different consumer classes.

This paper is organized as follows. Section II, describes the smart grid proposed structure. Section III presents DSM proposed strategy for residential load. Section IV studies smart DSM using bat algorithm for three consumers' classes and for different IEEE distribution test feeder at utility side. Finally, Section VI presents conclusions.

II. SMART DSM MODEL

Smart grid is very essential to create an environment that complies with infrastructure for generation, transmission and distribution, energy, information technology, and infrastructure for digital communications that enables the exchange of procedures and controls information between various segments of the power grid [4].

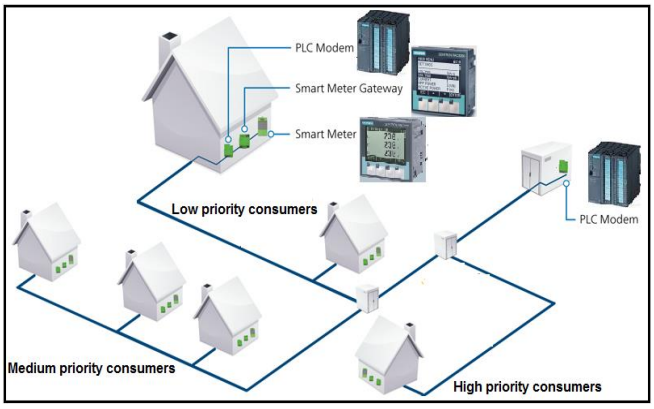

Figure.1. Structure of the proposed system

Figure.1 shows the proposed residential area and illustrates customer's control area which consists of two main parts. The

first part is a programmable logic controller (PLC), which is used to execute the proposed demand response algorithm and provide an interface between the appliances, sensors, and the controller. The second part is smart metering, which is the most important device used in smart grid for obtaining information from the end users' devices and appliances.

Three classes of consumers are proposed within this study, and categorized according to consumers' priorities [7, 8].

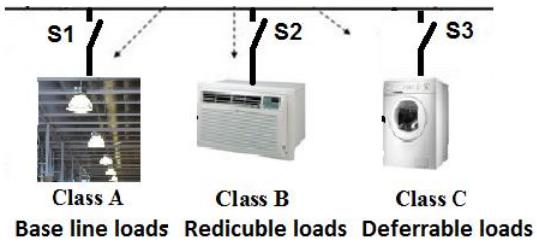

Figure.2. proposed system with control action [10]

In a lower level, Figure.2 shows the categorization of loads inside consumers' home according to loads priority for any of the classes. Loads are categorized into three types: A- Base line loads whose power consumption must be continuous for all time, such as lightning, refrigerator and fans, B- reducible loads, whose power consumption can be decreased for some time periods, such as air conditioning and Water heater, C- deferrable loads, whose operation or charging time can be deferred, such as washing machines, Electrical oven and Microwave oven [12].

III. PROPOSED SMART DSM STRATEGY

The proposed optimization algorithm aims at reshaping the final load curve to achieve the objective of load minimization at peak time using load shifting as the primary technique that can be utilized by the central controller of the smart grid. The DSM strategy is applied to three different levels of consumers which are classified according to consumers' lifestyles and each consumer has three types of loads. The first level is the high consumer level which needs the three types of loads to be operated regardless of the cost. The second level is the medium consumer level which needs at least a base line and reducible loads to be operated. The third level is the low consumer level which needs to reduce electricity bill as much as possible.

I) Problem Formulation

The main objective of each consumer is to minimize his electricity bill. This can be achieved through the following objective equations [9].

$$\text{Minimize: } EC = \sum_{i=1}^{24} a*P_i*E_h + b*P_i*E_m + c*P_i*E_l \quad (1)$$

$$P_i = C\,E_i\,\log(E_i+1) \quad (2)$$

Subject to:

$$a+b+c = 100\% * n \quad (3)$$

$$E_i < \text{Feeder load power} \quad (4)$$

$$a<=.3,\ b<=1,\ c<=1 \quad (5)$$

EC: Electricity cost during a day.

P_i: Energy price in hour i.

E_h: Energy for high priority consumers in hour i.

E_m: Energy for medium priority consumers in hour i.

E_l: Energy for low priority consumers in hour i.

E_i: Energy consumption in hour i.

C: Price parameter is calculated using Egyptian Electric utility and Consumer's Protection. Price parameter in this paper has varied in different periods around the 24 hours as the first period (from 8AM up to 2PM and from 2AM up to 8AM are OFF Peak periods with reduced tariff) and the second period (from 2PM up to 8PM and from 8 PM up to 2AM) are Over Peak periods with another, which applies monthly tariff as an hourly tariff with scaled results [10, 15].

n: no. of consumers connecting to distribution feeder.

a: percentage of high priority consumers = maximum 30% of n.

b: percentage of medium priority consumers.

c: percentage of low priority consumers.

II) DSM Proposed Algorithm

This algorithm allows implementation of features that model the load demand which is based on the lifestyles of the customers, so that the disturbance to the customers can be minimized. Within this paper, Smart DSM model is based on load shifting technique and, load shedding for emergency cases. This can be executed by handling several devices of different load types to minimize consumer's electricity bill. We can find the modeling steps of smart DAM system as follow:

1. Firstly, the data regarding the devices of one consumer, which are used during any normal day of the year, shall be collected. These devices shall be using the smart meters, then to categorize them in three classes: base line loads (lightning, refrigerator and fans), reducible loads (air conditioning and Water heater), deferred loads (washing machines, Electrical oven and Microwave oven).
2. Secondly, three types of consumers shall be determined according to consumers' load priorities, then to calculate the maximum power limit for each consumer type.
3. Thirdly, the total power consumption for each hour is to be compared with the maximum power limit by using PLC device which can control the switches which may occur to the above load types.
4. Fourthly, if total power consumption at any hour is larger than maximum power limit, then the objective function no (1) will be applied. It will calculate the amount of power which can be shifted to the off peak hours by using bat optimization technique.
5. If total power consumption at the same hour during another day is still larger than maximum power limit, the objective function no (1) will be applied once again, and to calculate the amount of power which will be shaded by using bat optimization technique again.
6. Finally, we shall calculate the electricity cost during one day after applying the optimization technique and reshaping consumer's daily load curve.

IV. APPLICATION OF TH E PROPOSED SMART DSM

The system consists of utility and distribution system. IEEE distribution test feeder on one hand and test consumer (1) on the other hand [11].

a) Optimization at Consumer side

In order to simulate real life consumption with accessible data, we concludes average Egyptian consumption throughout the year for one consumer and categorized loads for each consumer according to loads priority mentioned previously in smart DSM model.

Table.1: Daily load consumption for consumer (1):

Time	Class A	Class B	Class C	Total power consumption	Total cost before optimization
8am	455	500	1100	2055	0.77317
9am	455	510	0	965	0.1728
10am	455	10	250	715	0.0904
11am	455	1010	0	1465	0.3755
12pm	455	1010	0	1465	0.3755
1pm	455	1010	0	1465	0.3755
2pm	455	1500	310	2265	1.07
3pm	400	1555	1060	3015	1.966
4pm	470	1000	110	1580	0.4965
5pm	470	1010	10	1490	0.438
6pm	470	1010	10	1490	0.438
7pm	480	40	1440	1960	0.78634
8pm	480	520	810	1810	0.6635
9pm	480	520	1060	2060	0.8743
10pm	480	20	360	860	0.15
11pm	480	20	250	750	0.11173
12am	480	20	250	750	0.1117
1am	340	10	100	450	0.48265
2am	320	0	0	320	0.2305
3am	300	0	0	300	0.2
4am	300	0	0	300	0.2
5am	300	0	0	300	0.2
6am	300	500	0	800	0.1155
7am	300	500	0	800	0.1155
maximum load	480	1555	1440	3015	10.81312

Table.1 shows daily load consumption for an Egyptian customer with base line loads, reducible loads and deferrable loads according to consumer's lifestyle.

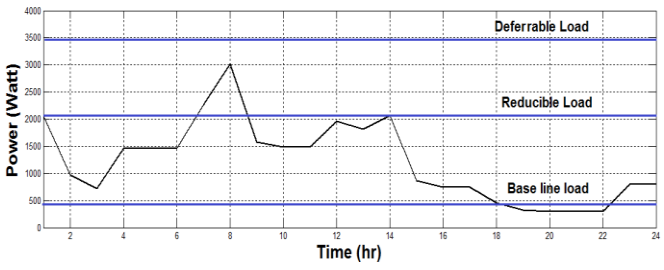

Figure.3 power comsumption for one consumer

Figure.3 shows that Base line load = 480 Watt, Reducible Load = 1560 Watt, and Referable Load = 1440 Watt. Total loads = 3480 Watt.

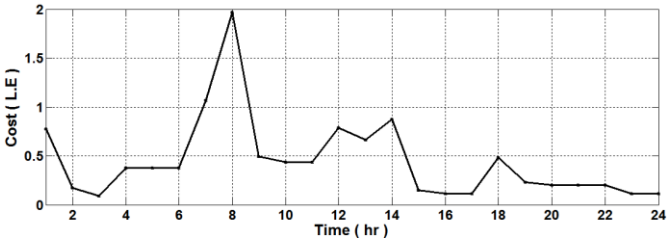

Figure.4 cost before optimization

Figure.4 gives the daily cost of a typical customer according to table number 1. The average cost before optimization = 10.3 L.E/day.

Smart DSM for different consumers' types:

The Bat Algorithm (BA) is a metaheuristic algorithm for global optimization. It is based on the phenomenon of echolocation bat which can find insects and discriminate their different types in full darkness. New studies indicate that this algorithm is very hopeful (Yang 2010) [13, 14].

In simulations, naturally, virtual bats are used. E_i (Total Energy consumption per hour t) is their positions and Pi (Energy price per hour t) is their speeds in a d-dimensional space which are updated. The new solution E^t_i and speed P^t_i at time t are given by

$$EC_i = EC_{min} + (EC_{max} - EC_{min})\,\beta \quad (6)$$

$$P^t_i = P^{t-1}_i + (E^t_i - E_*)\,EC_i \quad (7)$$

$$E^t_i = E^{t-1}_i + P^t_i \quad (8)$$

Where,

$\beta \in [0, 1]$ is a random vector derived from a regular distribution.

E_* is the best presented solution that is found after comparing all solutions.

$$E_{new} = E_{old} + \alpha A^t \quad (9)$$

$\alpha \in [-1, 1]$ is a random number and $A^t = \langle A^t_i \rangle$ is the average loudness of all the bats at this time step.

Bats fly randomly with velocity P_i at position Ei with a fixed frequency EC_{min}, varying wavelength λ and loudness A_o to search for prey. They can automatically adjust the wavelength (or frequency) of their emitted pulses and adjust the rate of pulse emission r $\in$ [0, 1], depending on the proximity of their target; although the loudness can vary in many ways, we assume that the loudness varies from a large (positive) A_o to a minimum constant value A_{min}.

Table.2 Switches Sequence after optimization for different consumer classes in peaks:

Time	**Control Action**		
	Low priority	Medium priority	High priority
8AM: 2PM	Base line Load operates.	Base line and Reducible Load operate.	Base line, Reducible and Referable Load operate.
2PM: 8PM	Base line Load operates.	Base line and Reducible Load operate.	Base line, Reducible and Referable Load operate.
8PM: 2AM	Base line Load operates.	Base line and Reducible Load operate.	Base line, Reducible and Referable Load operate.
2AM: 8AM	Base line Load operates.	Base line and Reducible Load operate.	Base line, Reducible and Referable Load operate.

i. For High Priority Consumers

High priority consumers need the three types to be operated of loads regardless the cost.

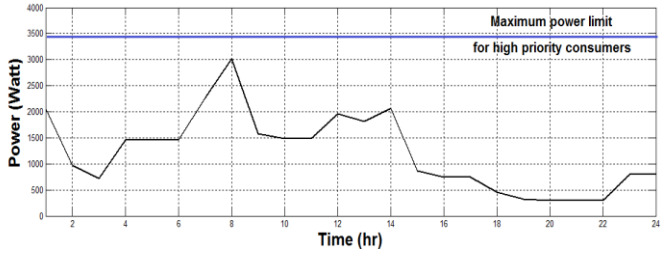

Figure.5. Consumer's load curve for high priority class

Figure.5 shows the consumer's load curve and the maximum power limit which was calculated from table.2. As all switches for different load categories are closed, any power more than power limit line will be shed in peak hours.

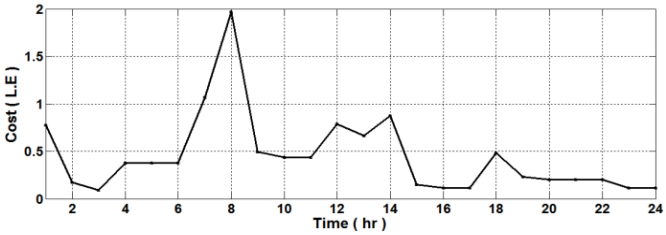

Figure.6. daily electrical price for high priority consumer

Figure.6 shows the total electrical price for one consumer in high priority class = 10.3 L.E/Day.

ii. For medium priority consumers:

To optimize medium priority consumption; load shifting optimization technique will be used to reshape medium priority consumer's load curve in peaks.

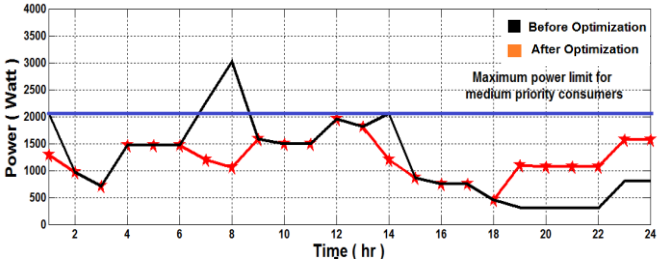

Figure.7. Power consumption before and after optimization

Figure.7 shows the consumer's load curve before and after optimization for one consumer (table.2 and maximum power limit which was calculated from table 1).

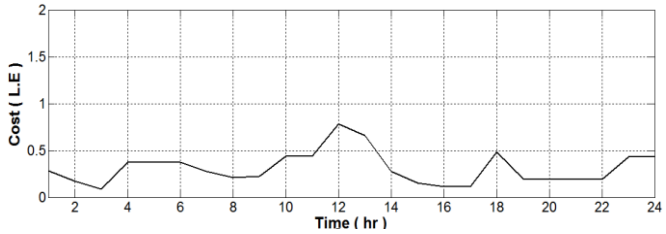

Figure.8. Daily electrical price for a medium priority consumer

Figure.8 shows the total electrical price for one consumer in a medium priority class = 7.22 L.E/Day.

iii. For Low Priority Consumers:

In low priority consumer's load, load shifting and shedding optimization techniques will be used so as not to exceed maximum power limit.

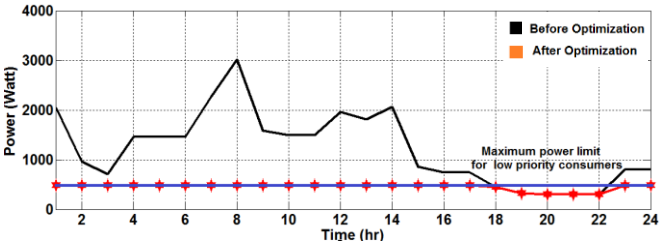

Figure.9 Power consumption before and after optimization

Figure.9 shows the consumer's load curve before and after optimization for one consumer (table.2 and maximum power limit which was calculated from table 1).

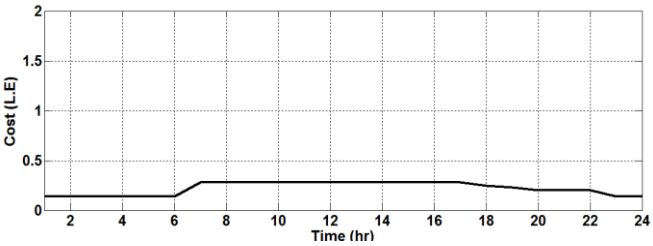

Figure.10 Daily electrical price for low priority consumer

Figure.10 shows the total electrical price for one consumer in a low priority class = 5.3 L.E/Day.

b) Optimization at utility side

The utility side is represented by IEEE distribution standard test systems, these systems were designed to evaluate and benchmark algorithms in solving unbalanced three-phase radial systems. Each of these systems represents reduced-order models of an actual distribution circuit [15].

1. 4-Bus Test Feeder.
2. 13-bus Feeder.
3. 34-bus Feeder.
4. 37-bus Feeder.
5. 123-bus Feeder.

The optimization function will be applied to determine the power capacity of each IEEE distribution test feeder. Moreover, if we have a specific power value for each feeder, then the number of consumers at the different consumer levels could be calculated by evaluating the maximum percentage of consumers in each consumer's priorities level using the linear programming.

Objective function:

$$\text{Minimize } P = P_h*a + P_m*b + P_l*c \quad (10)$$

Subject to:

$$a+b+c = 1, \quad (11)$$

$$a<= 0.3, b<= 1, c<=1 \quad (12)$$

P_h: Maximum power limits for high priority consumers.
P_m: Maximum power limits for medium priority consumers.
P_l: Maximum power limits for low priority consumers.

Firstly, we will determine the power capacity by using the pervious maximum power limit values. The minimum power value that may achieve a suitable number of consumers in each consumer level (a = 0.3 = 30% of n, b = 0.7 = 70% of n, c = 0 = 0% of n) can be calculated through applying the objective

function using the linear programming method, so the minimum power value equals 2472 Watt. It shall be taken into consideration that these percentages are the maximum limits for both the high and the medium priority consumers with the minimum power consumption calculated.

Secondly, we will calculate the maximum percentage of the number of consumers in each consumer's priorities level at each test feeder having a specific power value. Initially, the power consumption of spot loads in each distribution test feeder system shall be evaluated; that shall be executed for 400 consumers then, to determine the maximum percentage limit for the number of high, medium and low priority consumers.

1. For IEEE 4 node test feeders:

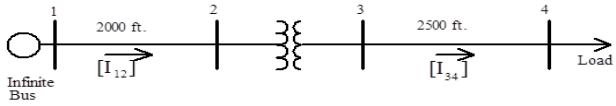

Figure.11 IEEE 4 Node Test Feeder

Figure.11 shows the system to be used in testing transformer models. Loads are connected in grounded wye for four wire line configurations with P=1800KW and connected in closed delta for three wire line configurations with P=1200KW. As the transformer must be loaded with 80%; So Maximum power consumption is 1800KW*80% = 1440 KW (wye load connected), 1200 KW * 80% = 960 KW (Delta load connected) according to load data in the table, if we have 10 buildings, each building has 40 consumers, so power consumption for one consumer in wye load connected = 1440 KW/400consumer = 3600 Watt, however, in delta load connected = 960 KW/400consumer = 2400Watt.

2. For IEEE 13 node test feeders:

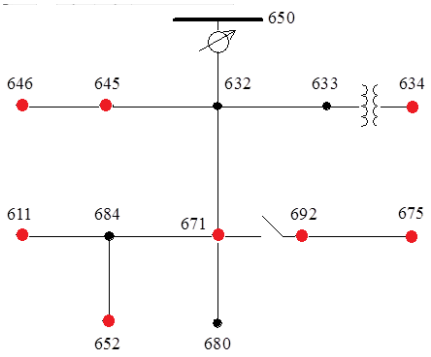

Figure.12 IEEE 13 Node Test Feeder

Figure.12 shows the system which is characterized by being short, relatively highly loaded, a single voltage regulator at the substation, overhead and underground lines, shunt capacitors, an in-line transformer, and unbalanced loading. The figure also shows the spot load points number 646, 645, 634, 652, 692, 675 671, and 611 with power of 1158 KW per phase (1), 973 KW per phase (2) and 1135 KW per phase (3). If we have 400 consumers, so, power consumption for one consumer = 1158KW/400consumers = 2895 Watt per phase (1), 973KW/400consumers = 2432.5 Watt per phase (2), 1135KW/400consumers = 2837.5 Watt per phase (3).

3. For IEEE 34 node test feeders:

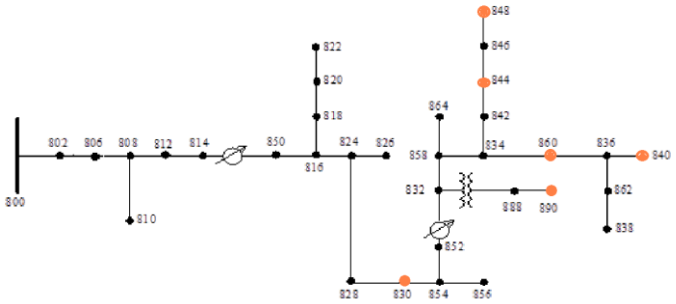

Figure.13 IEEE 34 Node Test Feeder

Figure.13 shows the system which is characterized by being long and lightly loaded, two in-line regulators, in-line transformer for short 4.16 kV section, unbalanced loading, and shunt capacitors. The figure also shows the spot load points number 848, 844, 860, 840, 890 and 830 with 344 KW per phase (1, 2) and 359 KW per phase (3). If we have 400 consumers, so, power consumption for one consumer = 344 KW/400consumers = 860 Watt per phase (1, 2) and 359KW/400consumers = 897.5 Watt per phase (3) [16].

4. For IEEE 37 node test feeders:

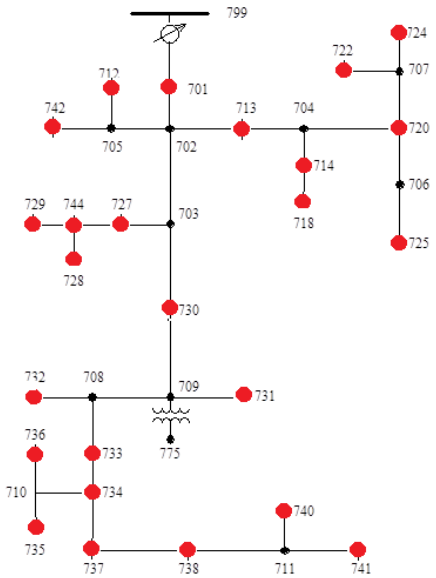

Figure.14 IEEE 37 Node Test Feeder

Figure.14 shows the system which is characterized by delta configured, all line segments are underground, and substation voltage regulation is two single-phase, open-delta regulators. Spot loads are very unbalanced. The figure also shows the spot load points number 724, 722, 701, 712, 742, 713, 714, 718, 720, 725, 727, 744, 729, 728, 730, 731, 732, 733, 736, 734, 735, 737, 738, 740 and 741 with power 727 KW per phase (1), 639 KW per phase (2) and 1091 KW per phase (3). If we have 400 consumers, so, power consumption for one consumer = 727KW/400consumers = 1817.5 Watt per phase (1), 639KW/400consumers = 1579.5 Watt per phase (2), 1091KW/400consumers = 2727.5 Watt per phase (3).

5. For IEEE 123 node test feeders:

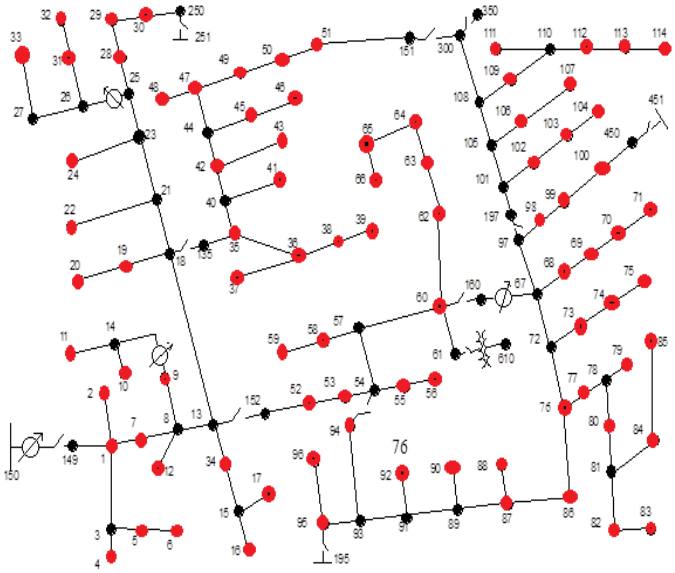

Figure.15 IEEE 123 Node Test Feeder

Figure.15 shows the system which is characterized by being overhead and underground lines, unbalanced loading with current constant, impedance, and power of four voltage regulators, shunt capacitor banks, and multiple switches. The figure also shows the spot load points number 1, 2, 4, 5, 6, 7, 9, 10, 11, 12, 16, 17, 19, 20, 22, 28, 29, 30, 31, 32, 33, 34, 35, 37, 38, 39, 41, 42, 43, 45, 46, 47, 48, 49, 50, 51, 52, 53, 55, 56, 58, 59, 60, 62, 63, 64, 65, 66, 68, 69, 71, 73, 74, 76, 77, 79, 80, 82, 83, 84, 85, 86, 87, 88, 90, 92, 94, 95, 96, 98, 99, 100, 102, 103, 104, 106, 107, 109, 111, 112, 113 and 114 with power of 1420 KW per phase (1), 915 KW per phase (2) and 1155 KW per phase (3). If we have 400 consumers, so, power consumption for one consumer = 1420KW/400consumers = 3550 Watt per phase (1), 915KW/400consumers = 2287.5 Watt per phase (2), 1155KW/400consumers = 2887.5 Watt per phase (3).

Table.3. the maximum percentage limits for three consumers' priorities at spot loads:

	Phase (1)	Phase (2)	Phase (3)
4 Feeders	P=2400W	P=2400W	P=2400W
	a= 30% b= 65% c= 5%	a= 30% b= 65% c= 5%	a= 30% b= 65% c= 5%
13 Feeders	P= 2895W	P= 2432.5W	P= 2837.5W
	a= 30% b= 70% c= 0%	a= 30% b= 67% c= 3%	a= 30% b= 70% c= 0%
34 Feeders	P= 860W	P= 860W	P= 897.5W
	a= 0% b= 0% c= 100%	a= 0% b= 0% c= 100%	a= 0% b= 0% c= 100%
37 Feeders	P=1817.5W	P= 1579.5W	P= 2727.5W
	a= 30% b= 28% c= 42%	a= 30% b= 14% c= 56%	a= 30% b= 70% c= 0%
123 Feeders	P= 3550W	P= 2287.5W	P= 2887.5W
	a= 30% b= 70% c= 0%	a= 30% b= 58% c= 12%	a= 30% b= 70% c= 0%

Table no. 3 shows the maximum percentage limits for a total number of 400 consumers of high and medium priority consumers with the minimum power consumption which can be calculated at spot loads in different distribution systems. The above shows that if P => 2472 Watt, thus the high and the medium priority consumers can load with the power they need, but at 34 IEEE test feeder, the low priority consumers are the only ones who can load as spot load value which almost covers the base line loads.

The main advantage of this objective function and these calculations is that we can re-plan consumers according to their different priority levels at distribution feeders without overload at distribution points.

V. CONCLUSION

This paper presents a comprehensive study of a proposed smart DSM controller. The controller consists of two parts; the first part is smart metering and communication system which consist of smart meters, while the second part is PLC devices and optimization DSM technique. The proposed smart meter has the ability of a two-way communication between customer and utility central control as it enables both customer and utility to take a planned decision based on loading information. The DSM technique allows consumers to control their loads in order to operate the system more efficiently, as this technique supports both customer's and utility's decisions regarding energy management, especially during peak hours.

Throughout the paper, different test systems are used. The proposed smart DSM is applied to three levels of consumers, who are classified according to their life styles. Each consumer has three categories of loads inside his own home. The proposed DSM uses bat algorithm that provides optimized load shifting values according to the preset constraints of the utility. The proposed smart meters receive the optimum values, then apply a control action to consumer's level to achieve the overall purpose of energy management of the whole system. In addition, the proposed smart meters give the opportunity to measure, observe, and control customer's appliances through the central utility control, which is a new concept for smart grid. Based on the above, customers can achieve their target of electricity price saving, taking into consideration the different tariffs during the different operating hours. We shall note that the proposed system proves controllability at the different levels "customer's and utility's" with economic approach.

REFERENCES

[1] Kumara guruparan N., Sivara makrishnan H., and Sachin S. Sapatnekar ECE Department," Residential Task Scheduling Under Dynamic Pricing Using the Multiple Knapsack Method", IEEE PES Innovative Smart Grid Technologies (ISGT), Washington, USA, 2012, PP.1-6.

[2] Mohamed Abo Galeela, Magdy El-Marsafawy, Mohamed El-Sobki, "Optimal Scheme with Load Forecasting for Demand Side Management (DSM) in Residential Areas", Faculty of

engineering Cairo University, Giza, Egypt, Published Online July 2013, PP.889-896 .

[3] Zafar Ali Khan, Saeed Ahmed, Rab Nawaz, Anzar Mahmood, Sohail Razzaq, "Optimization based Individual and Cooperative DSM in Smart Grids: A Review", Power Generation System and Renewable Energy Technologies (PGSRET), Pakistan, 29 October 2015, PP.1-6.

[4] Maria das Neves Queiroz de Macedo, Joaquim Jorge Martins Galo, Luiz Alberto Luz Almeida, Antonio Cezar Castro Lima, "Opportunities and Challenges of DSM in Smart Grid Environment", The Third International Conference on Smart Grids, Green Communications and IT Energy-aware Technologies, Lisbon, Portugal, 2013, PP.156-160.

[5] M. N. Ullah, N. Javaid, I. Khan, A. Mahmood, M. U. Farooq, "Residential Energy Consumption Controlling Techniques to Enable Autonomous Demand Side Management in Future Smart Grid Communications", Eighth International Conference on Broadband, Compiegne, France, 2013, pp1-6.

[6] A. Abaza, Ahmed M. Azmy, "Demand-side management-based dynamic pricing within smart grid environment", International Conference on Smart Energy Grid Engineering (SEGE), Canada, 2013, pp1-6.

[7] Phani Chavali, Peng Yang and Arye Nehorai, "A Distributed Algorithm of Appliance Scheduling for Home Energy Management System", IEEE Transactions On Smart Grid, Vol. 5, No. 1, January 2014, pp 282 - 290.

[8] Soma Shekara Sreenadh Reddy Depuru; Lingfeng Wang; Vijay Devabhaktuni; Nikhil Gudi, "Smart meters for power grid-challenge, issues, advantages and status", Power Systems Conference and Exposition (PSCE), Phoenix, AZ, USA, 23 May 2011, PP. 1-7.

[9] Zubair. M. Fadlullah, Minh. Q. Duong, Nei Kato, and Ivan Stojmenovic, "*A Novel Game-based Demand Side Management Scheme for Smart Grid*" IEEE Wireless Communications and Networking Conference (WCNC 2013), Shanghai, China, Apr. 2013, pp 4677 - 4682.

[10] Rovan R. Elrazky, Ahmed A. Daoud, Kamel Elserafi, "Optimization of Residential Load Consumption during Energy Peaks using Smart Metering," In International Conference on Renewable Energies and Power Quality (ICREPQ'17), ISSN 2172-038 X, No.15, Malaga, Spain, April 2017, pp1-6.

[11] IEEE POWER ENGINEERING SOCIETY, IEEE Node Test Feeder.

[12] G. Rietveld, P. Clarkson, P. S. Wright, U. Pogliano, J. Braun, M. Kokalj, R. Lapuh, and N. Zisky, "Measurement Infrastructure for Observing and Controlling Smart Electrical Grids," 2012 3rd IEEE PES International Conference and Exhibition on Innovative Smart Grid Technologies (ISGT Europe), Berlin, Germany, 2012, PP. 1–8.

[13] Xin-She Yang, "A New Metaheuristic Bat-Inspired Algorithm", Nature Inspired Cooperative Strategies for Optimization (NISCO 2010),Berlin, 23 Apr. 2010, PP.65-74.

[14] Xin-She Yang, Amir Hossein Gandomi, " Bat Algorithm: A Novel Approach for Global Engineering Optimization", Mathematics and Scientific Computing, National Physical Lab, Journal reference: Engineering Computations, Vol. 29, 2012, PP. 464-483.

[15] W.H. Kersting, "Radial Distribution Test Feeders", 2001 IEEE Power Engineering Society Winter Meeting. Conference Proceedings (Cat. No.01CH37194), vol.2, Columbus, OH, USA, 07 August 2002 pp. 908 – 912.

[16] Shammya Saha, Nathan Johnson, " Modeling and Simulation in XENDEE IEEE 34 Node Test Feeder", The Journal of Defense Modeling and Simulation, University of Arizona, USA, volume: 14, pp. 1-12, 2016.

A NOVEL PARTICLE SWARM OPTIMIZATION ALGORITHM FOR MAXIMUM POWER POINT TRACKING BASED PHOTOVOLTAIC SYSTEM

E.MALARVIZHI[1], J.KAMALA[2]
Assistant Professor, Department of Electronics and Communication Engineering,
St.Joseph's College of Engineering[1], Chennai-119, College of Engineering Guindy[2],
Annauniversity, Chennai-25.TamilNadu, India.
malarvizhi0702@gmail.com, jkamalaa06@gmail.com.
A.SIVASUBRAMANIAN[3]
Professor, School of Electronics, VIT University, Chennai-127**,** TamilNadu, India.
shiva_31@yahoo.com.

Abstract: *In recent years, solar energy is effectively utilized as an alternate energy source for generating electricity. Maximum Power Point Tracking(MPPT) is applied to the photovoltaic (PV) system to extract maximum power (MP). Numerous algorithms are developed and implemented to extract the MP under varying environmental conditions. One such algorithm is the Particle Swarm Optimization algorithm(PSO).This article introduces a novel PSO algorithm with Cauchy distribution to track MP from the PV system. It is designed to overcome the drawback of slow convergence rate of conventional PSO. Parameters required for conventional PSO are inertial weight, acceleration coefficients, and a number of particles. In case of Cauchy PSO(CPSO), tuning parameter is the number of particles. In order to increase the convergence speed, Cauchy distribution is used instead of normal distribution function to generate the random numbers. The advantage of this algorithm is that it provides the global best-optimized result at a faster convergence speed. It has the ability to track the MP in extreme climatic conditions with varying loads. The proposed method outperforms the standard PSO and some of the existing methods in terms of quick convergence and also has a simplified structure.*

Keywords: *Photovoltaic(PV) system, Maximum Power Point Tracking (MPPT), Particle Swarm Optimization (PSO) Algorithm, Cauchy PSO (CPSO).*

1. Introduction

These days increased demand for electricity consumption and negative effects on the environment are the major issues [1]. These are due to depleting of fossil fuels at a faster rate. To overcome these issues continuous research is being conducted to seek efficient alternate sources of energy for power generation [2]. Therefore attention is being given to the utilization of Renewable Energy Sources (RES). RES are solar, hydropower, biomass, wind, geothermal energy etc. RES are economical and they also reduce the environmental issues caused by power generation from non-renewable energy sources such as fossil fuels. Because of the merits of RES, these are utilized as best alternate for generation of electrical energy. Nowadays, the generated electricity from various sources is distributed via the centralized grid. Various resources are referred to as Distributed Energy Resources (DER)[3].

Among the RES solar energy and wind energy are currently widely deployed. Compared to solar energy, wind energy has some limitations. The rotatary motion of wind turbine is used to produce electricity. Following are some of the important practical difficulties. Wind turbines are very large machines. It occupies larger area and also wind turbine blades make more noise. Another important fact is that the wind mills are installed near shores, and on high mountain. Site selection also plays a crucial role in several aspects. Financial returns from the project, ease of construction, maintenance and overall safety are the factors that decide the overall design and

implementation of wind power generation systems[4].Therefore solar energy has become widely essential to compensate the energy demand. Its environmental friendly nature, abundance presence on the earth's surface, it being totally free from pollution, low operational cost and also renewable and sustainable characteristics are the merits of solar energy [5]. Although the operational cost is low for the solar energy , the cost of solar modules are high .Still the grid connected PV power generation systems are being commercialized in many countries because of its long term benefits. Further more generous financial schemes for example the feed in tariff and subsidized policies are introduced in various countries resulting in rapid growth of the industry [5].Recently the power generation systems designed using integration of solar and wind energy. The reason is to generate interminable power depend upon the environmental conditions [6].

Conversion of photon energy to electrical energy is called Photovoltaic (PV) effect. PV cells are the smallest element used to produce power. Integration of large number of PV cells produces PV module, large number of series and parallel connected modules produce PV arrays. Nowadays PV arrays are constructed pyramidal like shapes used to upgrade the radiation intensity falling on solar panels.[7]. To extract the MP solar panels are to be operated at Maximum Power Point (MPP). Because of the dynamic environmental conditions such as temperature and irradiance, PV characteristic varies nonlinearly. It is difficult to locate the MPP. Another common issue is Partial Shading Condition (PSC) due to surrounding buildings, trees, passing clouds in the sky etc. Under PSC the PV curve exhibits multiple MPPs with one global and several local peaks [8]. To overcome these issues MPPT controllers are integrated with DC-DC converters.

Conventional MPPT algorithms are Perturb and Observe (P&O), Incremental conductance (INC) and Hill climbing (HC). These are very common MPPT techniques. P&O compares PV array voltage (or current) to the constant reference voltage (or current) at the MPP under specific atmospheric condition. The difference of voltage (or current) is used to decide the direction of tracking. Simply this method perturbs the operating voltage (or current)[9,10]. In INC output conductance is taken for reference. At MPP its magnitude is zero. On either side of MPP, its magnitude has negative and positive increments [9-11]. It is developed to increase the convergence time of tracker. HC approach uses the PV array output current. Change in current is measured before and after a change in duty cycle. Therefore this method perturbs the duty cycle of the converter.

Traditional MPPT techniques have two major difficulties. Under PSC it tracks only the first local MPP.It is unable to track the global MPP and they also suffer from steady state oscillations [12-14].This means after capturing MPP, the operating point oscillates back and forth around MPP. This limits maximum power generation.

Fuzzy based controllers and neural network are another type of controllers. The fuzzy controller uses an ad-hoc technique to handle nonlinearity problems. Its execution is complex with a process of fuzziffication, rule based storage, inference and defuzziffication operations. Implementation requires more knowledge for both user and designer [15]. Neural Network is an Artificial Intelligence (AI) based technique and its implementation process is much complicated. It uses a large amount of data, for tuning. Because of the varying weather conditions, real time implementation needs intelligence processors for better performance [15].

Evolutionary Algorithms (EA) such as PSO , Genetic Algorithm (GA), Ant Colony Algorithm (ACO), Evolutionary Programming (EP), Simulated Annealing (SA) etc. are introduced to improve the performance of MPPT under dynamic atmospheric conditions. In SA, setting of control parameters is a difficult task and convergence speed is slow when applied to a real system. Though the GA techniques have been employed successfully to solve complex optimization problems, its efficiency is degraded due to its premature convergence. EP seems to be good choice to solve multimodal optimization problem. But it takes long simulation time to obtain the optimum solution for this kind of problems [16]. The word optimization broadly refers to locating either the maxima or minima of real functions. It uses a systematic approach to choose real or an integer variable from within the allowed set is called search space.

Among these PSO shows outstanding performance in attaining optimized solutions. The

most suitable and attractive approach to obtain MP from PV array is the PSO algorithm. Merits of PSO are its ability to track the MPP location quickly and accurately irrespective of the climatic conditions. It eliminates the steady state oscillations and produces more stable output unlike the conventional methods [17]. It doesn't require the gradient of the objective function and uses only the values of the objective function. It eliminates complex computational procedures. It also has a simple structure with fast computational ability. Characteristics of Conventional PSO are, it converges quickly and has good search accuracy. Convergence is defined when the particles stop at the desired operating point to provide global optimal result [18, 19]. In practice, the algorithm stuck at local maxima is called premature convergence and it requires larger search space.

To tackle the issue of slow convergence of PSO and Gaussian PSO, CPSO is proposed and implemented. It is an improved version of Gaussian PSO [GPSO] [20] with enhanced convergence speed. Other advantages are reduction in the number of tuning parameters, speedy convergence rate and faster output settling time.

Remainder of this article is organized as follows. Section 2 explains the related work to CPSO Method. Section 3 presents the concepts in conventional PSO. Functional blocks of the proposed method, configuration and implementation of CPSO algorithm are discussed in section 4. In section 5 functional modules are validated through simulation results. Section 6 presents the merits of the proposed method as compared with other techniques and concluding remark on future scope of this work.

2. Related work

Several solutions are dealt in the literature to overcome the PSO convergence issue. These are as follows:

- Introducing variable parameters
- Use of different swarm topologies
- Changing the velocity update formula with the enhancements applied in the inertial weight [21].
- Modifying the particle position and velocity through the mutation operator.
- Modifying the position and velocity update rules, outside the equations, and so on [22,23].

Changes in velocity formula is implemented in improved PSO–MPPT algorithm. Vanxay Phimmasone et al.[24] introduced the fourth term which is called as repulsive term. The repulsive term is given by $c_3 r_3 (cent^k - S_i^k)/(\left|cent^k - S_i^k\right| + d)^3$. Where, $c_3 r_3$ term is same as those used in conventional PSO. Where, cent is the center of all particles. The term'd' is small constant added to avoid divide by zero error for the values of ($cent^k - S_i^k$).

Qing Zhang et al. [25] presented a modified PSO with both mutation and crossover functions to increase the convergence speed and to avoid the trapping of PSO into local maxima. Authors introduced Cauchy random number in velocity and position update expressions.

Venkatesh Kumar et al.[16] introduced the Cauchy mutation in the position update equation of PSO to optimize the results of economic dispatch problems.

Hui wang et al.[26] proposed a hybrid PSO with Cauchy mutation. The inertial weight is modified with the help of Cauchy random number. It is used to enhance the position of best particle to achieve faster convergence.

The difference between the above mentioned methods and the proposed method is faster convergence is achieved using minimum number of tuning parameters.

3. Conventional PSO

PSO is a population based optimization algorithm. It is one of the metaheuristic methods and it follows the random search techniques. Tuning parameters required for the execution of the conventional PSO algorithm are acceleration coefficients (c_1,c_2), inertial weight(ω) and maximum velocity as given by equations(1) and (2) [17,27]. Equation (1) is the velocity update equation and (2) is the positions update equation.

$$v_i(k+1) = \omega v_i(k) + c1 r1((p_{best,i} - x_i(k) + c2 r2(g_{best} - x_i(k))$$

(1)

$$x_i(k+1) = x_i(k) + v_i(k+1) \quad (2)$$

Where r_1, r_2 are uniformly distributed random numbers, p_{best} and g_{best} are particles individual and global best positions respectively from the target position and k is number of iterations.

4. Proposed Cauchy PSO method

Existing methods have complex computational structure. Proposed method has less complex computational structure with faster convergence.

In the proposed method the velocity update formula is modified. Velocity equation is constructed by without inertial weight, maximum velocity and acceleration coefficients (cognitive and social parameters) to achieve the convergence. Gaussian and Cauchy probability distributions are very effective for updating the velocity equation.

Cauchy PSO is also stochastic, population based swarm intelligence evolutionary algorithm. Equations (3) and (4) present the velocity and position updates of the proposed PSO.

$$v_i(k+1) = v_i(k) + r1((p_{best,i} - x_i(k) + r2(g_{best} - x_i(k)) \quad (3)$$

$$x_i(k+1) = x_i(k) + v_i(k+1) \quad (4)$$

Here r_1 and r_2 are the Cauchy distributed random numbers. Cauchy random numbers possesses the long jump ability. It enhances the velocity of the particles. Also this property helps the particles to get best position [3]. Another useful property is that, it is capable of providing huge search space for the particles. This is due to its tail decay very slowly. This yields better result for the search.

The proposed method and the conventional PSO are similar except that the initialization of the tuning parameters. Importance of tuning parameters in PSO is that, it greatly influences the algorithm performance. It is often referred to as exploration and exploitation tradeoff. Exploration is the ability to check the test space and provide global optimal results. Exploitation is the ability to concentrate on the optimization precision.

Important property of Cauchy distribution is that it has heavier tail [28]. This means its probability distributions are not exponentially bounded. That is, its distribution is greater than exponential distribution. Some of the other properties of this distribution is it has no expected value and other moments also. Its median and mode are equal. Probability Density Function (PDF) of Cauchy distribution is given in equation (5) [29].

$$f(x; x_0, \gamma) = \frac{1}{\pi\gamma\left[1 + \left(\frac{x - x_O}{\gamma}\right)^2\right]} \quad (5)$$

x_0 - Location parameter specifies the location of the peak of distribution. γ - Scale parameter or probable error. Its value is half the width of PDF at the half maximum height. Amplitude of Cauchy PDF is $\frac{1}{\pi\gamma}$ located at $x = x_0$. γ=1, x_0=0, the Standard Cauchy distribution with PDF[30] ,

$$f(x;0,1) = \frac{1}{\pi(1+x^2)} \quad (6)$$

In this work , the random numbers are characterized by standard Cauchy distribution. It is a special case of the student's t-distribution. Student's t-distribution is looks almost identical to normal distribution but it possess heavier tail like Cauchy distribution [31].

PDF of student's t- distribution is given in equation (7).

$$f(x) = \frac{\Gamma\left(\frac{n+1}{2}\right)}{\sqrt{n\pi}\,\Gamma\left(\frac{n}{2}\right)\left(\frac{x^2}{n}+1\right)^{\frac{(n\pi)}{2}}} \quad -\infty < x < \infty ; \quad (7)$$

Where, 'n' is called degrees of freedom. If Student's t-distribution has degree of freedom as 1 its PDF is same as that of the standard Cauchy distribution. It is presented in equation (8).

$$f(x) = \frac{1}{\pi(1+x^2)} \quad -\infty < x < \infty \text{ ; for n=1.} \quad (8)$$

Now it is seen that the Equations (8) and (5) are the same.

Figure 1 shows the flowchart of the proposed method. The implementation starts with three different duty cycles. These are referred to as the particles, di, (i=1, 2, 3). Selection of initial duty cycles are based on the MP output of the system. First duty cycle value (d_1) is chosen such that the duty cycle value required generating 80% of the MP of the system. The subsequent duty cycles (d_2, d_3) are 65% and 50% of MP outputs respectively [13]. In the first iteration these are considered to be the personal best ($P_{best)}$ values of the algorithm. For each duty cycle, the current and voltage are sensed and the corresponding power is calculated. This power is the objective function of the system [32]. Its mathematical relationship is given in equation (9). It is compared for different duty cycles. Depending on the received power, the P_{best} value is modified. It is presented in the flow chart.

$$P\begin{pmatrix} k \\ di \end{pmatrix} > P\begin{pmatrix} k-1 \\ di \end{pmatrix} \quad (9)$$

$P\begin{pmatrix} k \\ di \end{pmatrix}$-New power and $P\begin{pmatrix} k-1 \\ di \end{pmatrix}$-Old power

The G_{best} value is computed based on the maximum output power. The value of P_{best} corresponds to the maximum output power is taken as G_{best}. The duty cycle corresponding to the MP is applied to the power converter for each cycle.

Efficiency of the system is computed using equation (10). Where, P_O is the output power and P_{in} is the input power of the system.

$$\text{Tracking efficiency: } \eta = \frac{P_o}{P_{in}} \times 100\,\% \quad (10)$$

4.1 Block diagram of the proposed system

PV system consists of PV array, controller unit and load called Power Conditioning System [5]. Figure 2 shows the block diagram of the proposed system. Buck-Boost converter is designed to transfer the regulated DC output to the load. The output voltage and current of PV array are the inputs of the digital controller to perform iterative tracking for the MPP. The controller decides the operating voltage for the PV array by adjusting the duty cycle of the buck boost (BB) converter.

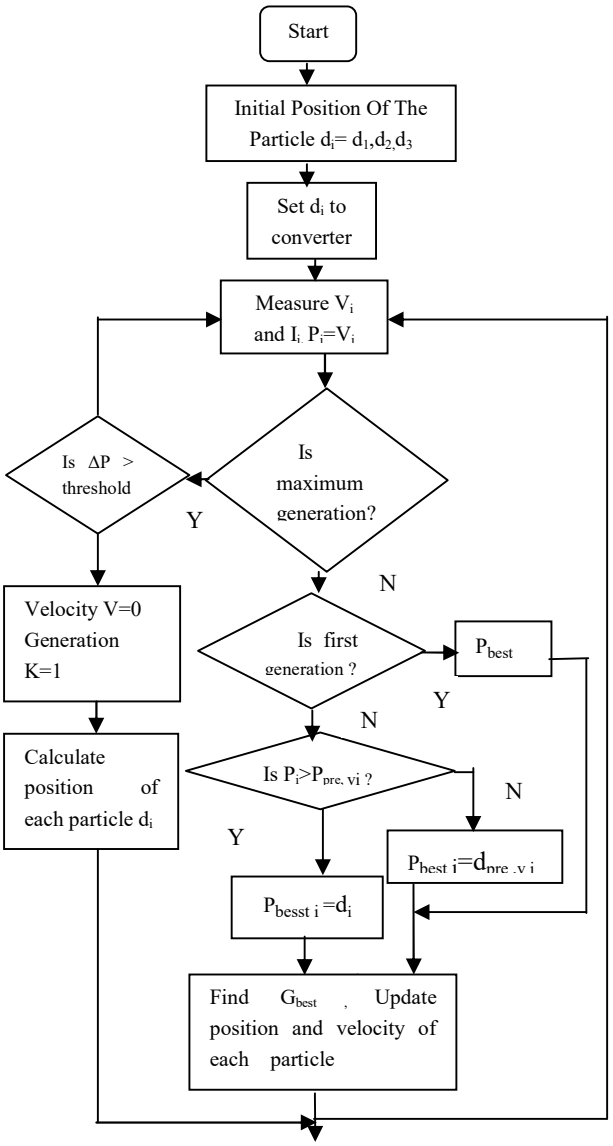

Fig.1.Flow chart of CPSO algorithm [33].

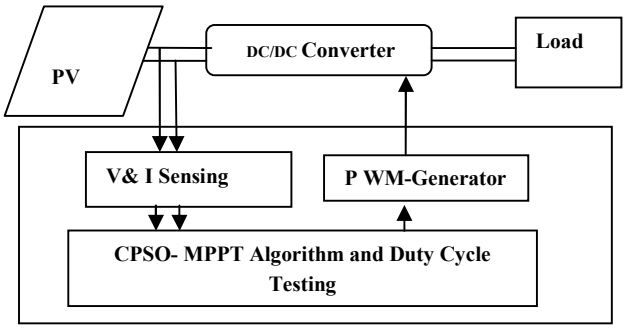

Fig.2. Block diagram of MPPT based PV system [11]

A. System Configuration and Implementation using CPSO

Figure 3 shows the MATLAB/SIMULINK simulation model for the PV system used in this discussion. As per the block diagram the simulation model consists of PV panel, converter and the MPPT control circuitry. PV array consists of series connection of 44 solar cells. Each cell has open circuit voltage, V_{oc} = 0.6V and short circuit current I_{sc} = 2.1 A. The sampling period (or time interval) for sensing voltage and current from the PV panel is 0.01 seconds to obtain the input power. Input power is the objective function. The next important block is a CPSO function block. Inputs are panel voltage and current. Based on the power product, the algorithm computes duty cycle for the converter to obtain the MP. Third section is converter section and the system is implemented with a BB converter.

Table 1 shows the specifications of solar panel at 25°C, temperature and insolation of 1000 W/m2.

Table 1 Parameters of PVpanel

Peak Power(W)	P_{MPP}	42.7
Peak power voltage(V)	V_{MMP}	21.7
Peak power current(A)	I_{MMP}	1.97
Open circuit voltage(V)	V_{oc}	26.4
Short circuit current(A)	I_{sc}	2.1
Number of series cells	Ns	44

Table 2 shows the specifications of the BB converter. It is designed with the help of BB converter design equations [34].

Table 2 Specifications of BB Converter.

Input Inductor	5mH
Output capacitor	25µF
Output ripple voltage	0.05 V
Output ripple current	0.1A
Switching frequency	25kHz

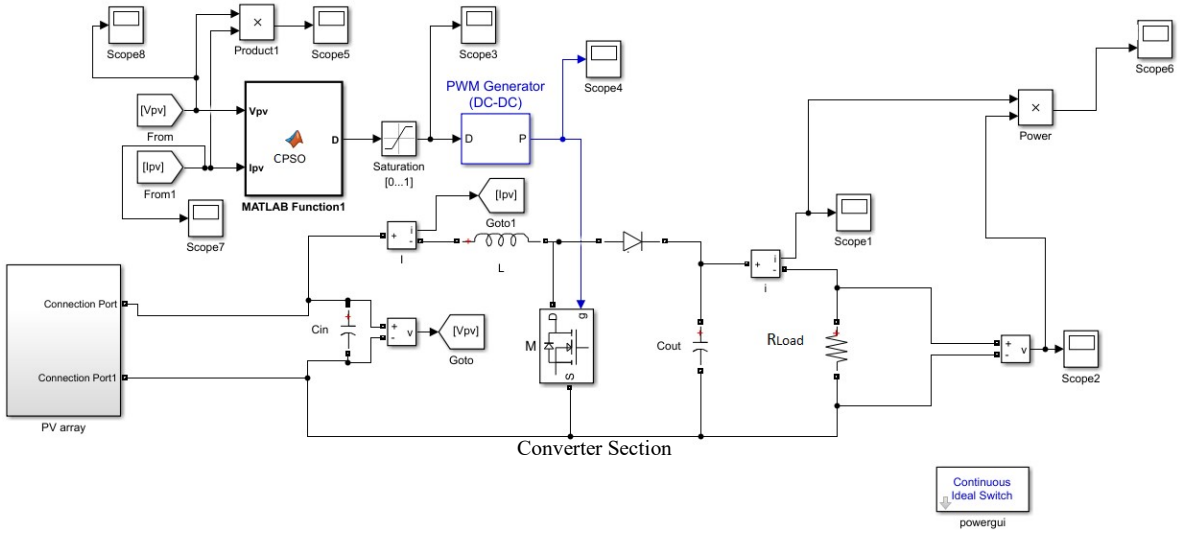

Fig.3.Simulation circuit for CPSO based MPPT system

5. Results and Discussion

In order to evaluate the effectiveness of the algorithm and to validate the results of the proposed method, two different existing algorithms "conventional PSO and Deterministic PSO (DPSO)[17]" are implemented and analyzed. The following parameters of the proposed method are compared,

- Output settling time and
- Convergence time of particles.

Apart from that the system response is analyzed for,

- Varying load conditions
- Varying irradiance conditions.

5.1 Output settling time

The output settling time of conventional PSO is presented in Figure 4 .The settling time is around 1.2s. Figure 5 shows output of DPSO. Output settling time is nearly 0.35s and Figure 6 is output wave form of CPSO. It shows the output settling time as 0.25s.

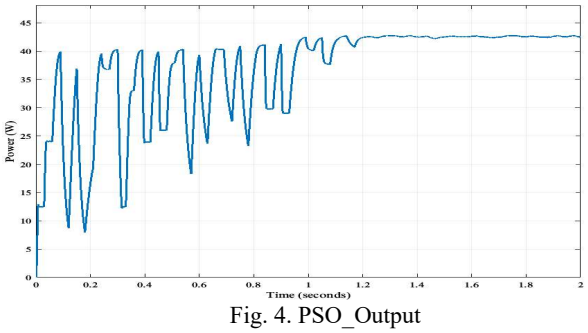

Fig. 4. PSO_Output

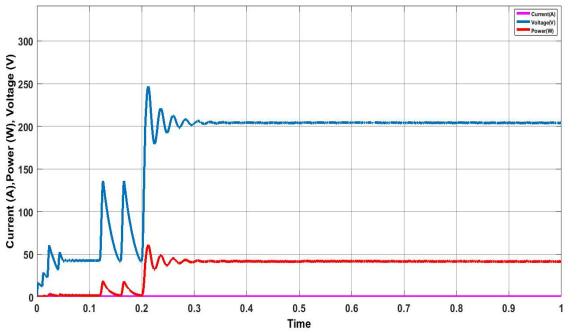

Fig. 5.DPSO_Output

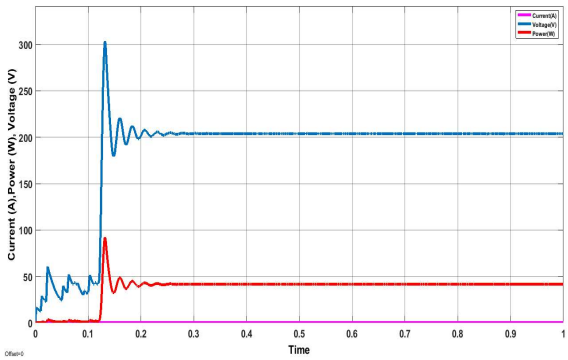

Fig. 6. CPSO_Output

Figure 7 is the comparison chart between the output settling time of all the different implemented versions of PSO discussed in this work. Ratio between the output settling time of PSO ,DPSO and CPSO are analyzed. From the figure CPSO is 4.8 times faster than PSO and 1.4 times faster than DPSO. Therefore from the results it is seen that the proposed method has the fastest settling time.

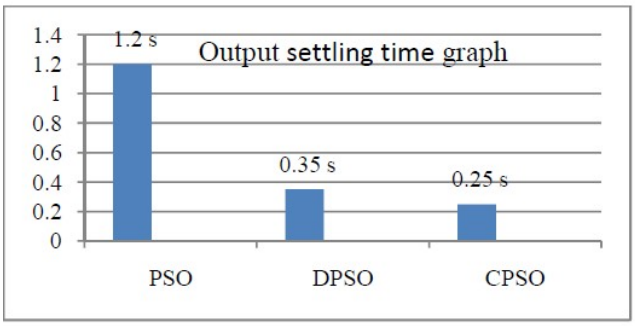

Fig. 7. Comparison chart for output setting time

5.2 Particles converging time of PSOs

Figure 8 shows the duty cycle exploration of standard PSO for 0.2s. All the particles are converged around 0.65s. Figure 9 is for DPSO algorithm. Particles converged at nearly 0.2s. Figure 10 is duty cycle exploration of CPSO. Convergence of particles takes just 0.12s.Among these algorithms DPSO technique doesn't use any random numbers to avoid randomness of PSO. It is designed such that the particles follow deterministic behavior to speed up the operation. Though the proposed method uses the random numbers it still converges earlier than DPSO.

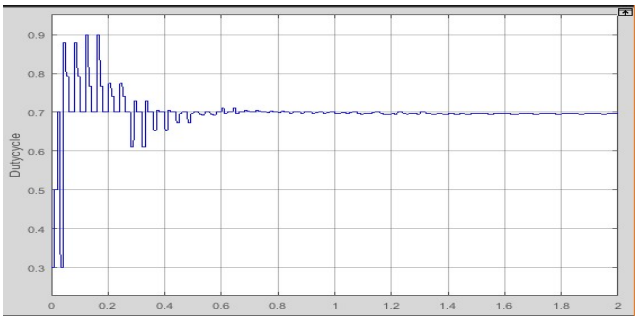

Fig. 8. Duty Cycle exploration of PSO

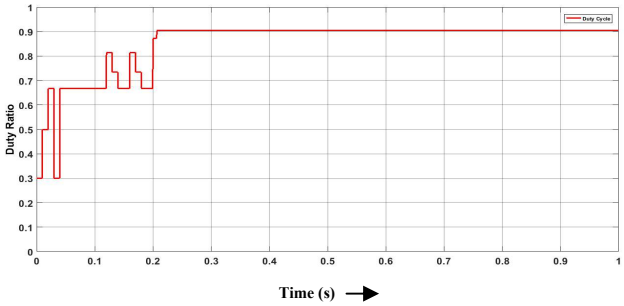

Fig. 9.Duty cycle exploration of DPSO

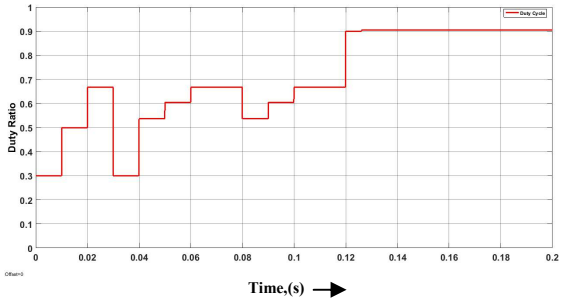

Fig. 10.CPSO duty cycle exploration

Figure 11 shows the converging time of all different PSOs. From this chart it is seen that the in CPSO algorithm particles converged quickly. It is 5.41 times faster than PSO and 1.66 times faster than DPSO.

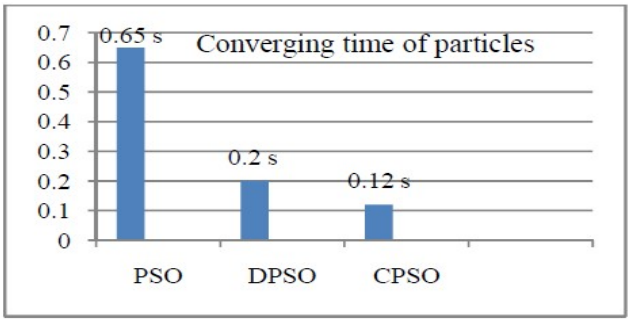

Fig.11. Comparison chart for particles converging time

5.3 Response to load resistance variations

Figure 12 and 13 are plot between load resistance and output power of the proposed system. The output power of the BB converter using CPSO algorithm is recorded for various loads. It provides maximum output power irrespective of load variations.Output power fluctuates approximately by only 1W from minimum load value to maximum load.

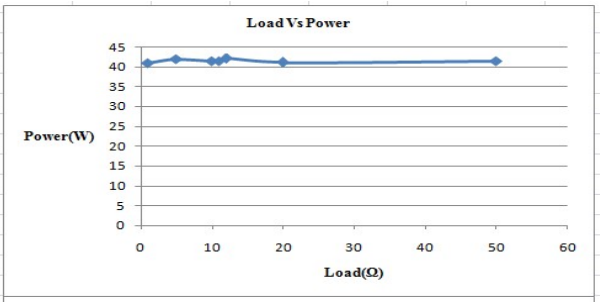

Fig. 12.Load resistor and CPSO P_out for low range of loads

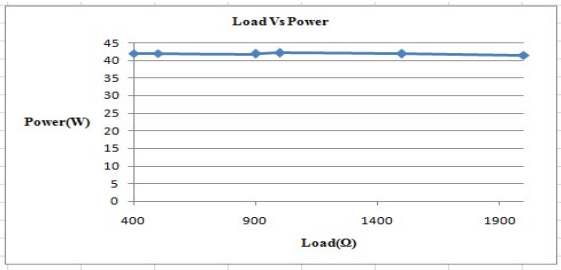

Figure13.Load resistor and CPSO P_out for high range of loads

Figure 14 shows the load versus duty cycle (duty ratio) curve for the proposed method. For the load fluctuations, the algorithm gradually expand the duty cycle to track the maximum panel power.

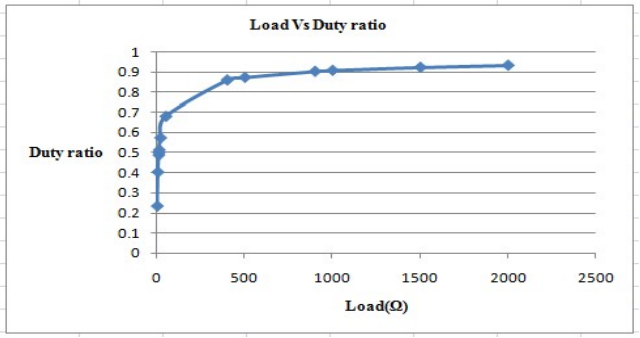

Fig. 14. load resistance Vs Duty cycle of CPSO

5.4 Respose to Irradiance changes

Figure 15 is the plot between irradiance versus power. As we know these two quantities are directly propotional with each other, for lower irradiance(Irs) the power output is low and is increases linerly.

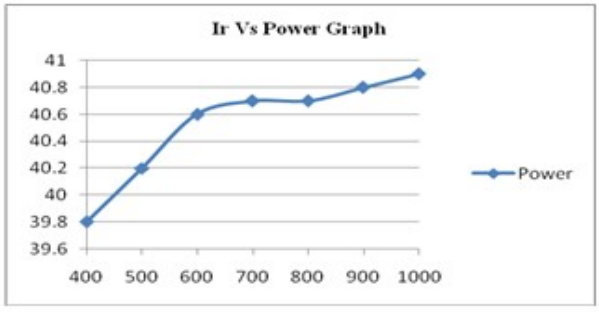

Fig.15.IrradianceVs P_out of CPSO

Figure 16. is a plot between duty cycle versus power for the proposed method.This duty ratio

variations are obtained for various load resistances of the system. Due to the load variations duty ratio is expanded with the help of the proposed PSO method.The system provides the almost constant output power with very slight variations.

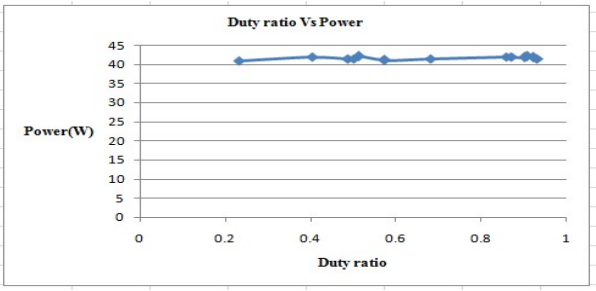

Fig.16.Duty cycle Vs P_out of CPSO

Simulation results illustrate the proposed method outperforms the existing methods in terms of convergence speed and output settling time. Merits of CPSO are (i) It converges quickly than other PSOs (ii) It requires only the number of particles and no other tuning parameters.

6. Conclusion

In this article, a novel Cauchy PSO based MPPT technique is implemented for PV system. The proposed method is designed to overcome the drawback seen in conventional PSO. The enhanced feature of the proposed Cauchy PSO is its less susceptibility of getting stuck at local optima. This is achieved with the help of its long jump ability. It provides rapid convergence rate with high convergence precision. The positive trait of the algorithm is its fast convergence. It is a good thing because it helps to find faster solutions. Hence it can be applied for time critical applications. Though the efficiency of all PSOs are same, CPSO's major advantage is its simplified control structure due to the reduced number of tuning parameters. Therefore the system is economical and less complex. Compared to other algorithms it possess fast convergence rate. The results proved that this algorithm performs better and extracts the maximum power irrespective of load fluctuations. It delivers a wide range of duty cycle output for a low and high range of loads. It provides global maximum power even for uneven insolation.

In future, the proposed system can be used in the hybrid MPPT systems. The hybrid system uses more than one renewable energy sources, combination of wind energy and solar energy. Furthermore it is useful for supplying uninterrupted power to the commercial buildings and industries.

References

1. Yi-Hwa Liu ,Shyh-Ching Huang, Jia-wei Huang,Wen Cheng- Liang,:*AParticle Swarm Optimization-Based Maximum Power Point Tracking Algorithm for PV Systems Operating Under Partially Shaded Conditions.* In:IEEE TRANSACTIONS N ENERGY CONVERSION, VOL. 27, NO. 4, (2012), pp. 1027-1035.

2. Moacyr Aureliano Gomes de Brito, Luigi Galotto,: *Evaluation of the Main MPPT Techniques for Photovoltaic Applications, In:* IEEE Transactions on Industrial Electronics, Vol.60(2013),No.8, pp.1156-1167.

3. Anna Rita Di Fazio, Mario Russo et al.,: *Sensitivity-Based Model of Low Voltage DistributionSystemswithDistributedEnergyResources*.In:Energies,Vol.9(2016),No.10,801:https://doi.org/10.3390/en91001.

4. Independent statistics & Analysis U.S.Energy Information Association. https://www.eia.gov/energyexplained..

5. Kashif Ishaque, Zainal Salam,Muhammad Amjad, sad Mekhilef.:*An Improved Particle Swarm Optimization (PSO)–Based MPPT for PV With Reduced Steady-State Oscillation.* In: IEEE TRANSACTIONS N POWER ELECTRONICS, VOL. 27 (2012), NO. 8, pp. 3627-3638.

6. M.Talaat,Abdullaziz,S.Alsayarri,Mohamand A Essa, M.A.Yousef,: *Investigation of transparent pyramidal covers effect to PV power output using detected wireless sensors incident radiation.*In:Measurement, Elsevier.Vol.136(2019),pp.775-785.

7. M.Talaat, M.A.Farahat,M.H.Elkholy,:

*Renewable power integration: Experimental and simulation study to investigate the ability of integrating wave, solar and wind energies.*In:Energy,Elsevier,Vol.170(2019),pp.668-682.

8. Duy Huynh,C, Tuong Nguyen,M, Matthew Dunnigan,W. Markus Mueller,A,: *Global MPPT of Solar PV Modules using a Dynamic PSO Algorithm under Partial Shading Conditions.*In:IEEE Conference on Clean Energy and Technology (CEAT), 2013, 134-139.

9. MacIsaac, L, Knox, A,:*Improved Maximum Power Point Tracking Algorithm for Photovoltaic Systems*,In: International Conference on Renewable Energies and Power Quality (ICREPQ'10), 2010.

10. Gomathy, S, Saravanan,S,Thangavel,S,:*Design and Implementation of Maximum Power Point tracking (MPPT) Algorithm for a Standalone PV System*, In:International Journal of Scientific & Engineering,,Vol.3(2012),No.3.

11. Saravanan Selvan.D,:*Modeling and Simulation of Incremental Conductance MPPT Algorithm for Photovoltaic Application*. In: International Journal of Scientific Engineering and Technology, Vol. No.2, (2013), No.7,PP.681-685.

12. Ramadan B.A.Koad, Ahmed. F.Zobaa.:*Comparison between the Conventional Methods and PSO Based MPPT Algorithm for Photovoltaic System.*, In: International Journal of Electrical, Computer, Energetic, Electronic and Communication Engineering, Vol:8,(2014), No:4, pp.691-696.

13. K.L.Lian,J.H.Jhang,.I.S.Tian.:*A Maximum Power Point Tracking Method Based on Perturb-and-Observe Combined With Particle swarm optimization*.In:IEEE JOURNAL OF PHOTOVOLTAICS,Vol.4(2014),No.2.pp.626-633.

14. QiangFu, Nan Tong,: *A new Fuzzy Control Method Based on PSO for Maximum Power Point Tracking of photovoltaic System.*In: 2011 International Conference on Computer Science and Network Technology,pp.1488-1491.

15. Trishan Esram, PatricL.Chapman..:*Comparison of PhotovoltaicArrayMaximumPower PointTracking Technique.In:* IEEE TRANSACTIONS ON ENERGY CONVERSION, Vol.22(2007),No.2, pp. 439-449.

16. Venkatesh Kumar, C, Ramesh Babu, M,: *Application of Cauchy Mutated Memetic Particle Swarm Optimization Algorithm to Economic Dispatch Problem with Practical Constraints*,In:WSEAS,Transactions on Systems and Control, Vol.13(2018),pp.80-87.

17. Kashif Ishaque, Zainal Salam.: *A Deterministic Particle Swarm Optimization Maximum Power Point Tracker for Photovoltaic System n Under PartialShadingCondition.In:*,IEEEANSACTIONS ON INDUSTRIAL ELECTRONICS, Vol. 60(2013), No. 8,pp.3195-3206.

18. Xueming Yang, Jinsha Yuan, Jiangye Yuan, Huina Mao.: *A modified particle swarm optimizer with dynamic adaptation.* In: Applied Mathematics and Computation, Vol. 189,(2007) PP. 1205–1213.

19. Po-Chen Cheng,Bo-Rei Peng ,Yi-Hua, Liu, Yu- Shan Cheng, Jia- Wei Huang.:*Optimization of a Fuzzy-Logic-Control-Based MPPT Algorithm Using the Particle Swarm Optimization Technique.* In:Energies, Vol.8,(2015), pp.5338-5360.

20. S. Komsiyah et.al.:*Computational methods of Gaussian Particle Swarm Optimization (GPSO)and Lagrange Multiplier on economic dispatch issues (case study on the electrical system of Java-Bali IV area)*. In:EPJ Web of Conferences, Vol. 68,(2014), No.00014.

21. M.Abdulkadir, A.H.M.Yatim, S.T.Yusuf.: *An Improved PSO-Based MPPT Control Strategy for Photovoltaic Systems.*In: International Journal of Photoenergy, Hindawi Publishing Corporation, Vol. 2014.pp.1-12.

22. Vytautas Jancauskas et.al.:*Empirical Study of Particle Swarm Optimization Mutation Operators*. In:Baltic J. Modern Computing, Vol. 2,(2014) No.4, pp. 199–214.

23. Hao Gao, Wenbo Xu.: *.A New Particle Swarm Algorithm and Its Globally Convergent Modification.* In: IEEE TRANSACTIONS ON SYSTEMS,MAN,ANDCYBERNETICS—PARTB: CYBERNETICS, VOL.41 (2011), NO.5, pp.1334-1351.

24. Vanxay Phimmasone,: *Evaluation of Extracted Energy from PV with PSO-based MPPT Against Various Types of Solar Irradiation Change,In:.*International Conference on Electrical, 2010.

25. Qing Zhang,Changhe Li,Yong Liu,: *Fast Multi-swarm Optimization with Cauchy Mutation and Crossover Operation.* Conference,In:2007,DOI 10.1007/978-3-540-74581-5_38.

26. Hui Wang et. al.: *A Hybrid Particle Swarm Algorithm with Cauchy Mutation. In:* Swarm IntelligenceSymposium,(2007) eeexplore.ieee.org.

27. R.Pon Vengatesh, S.Edward Rajan.:*evolutionary optimization approach For finding GMPP Of a PV array system under heterogeneous operating Condition.* In: Journal of Electrical Engineering. ,Vol.17(2017),No.1,pp.1-8.

28. Heavy Tailed Distribution & Light Tailed Distribution: Definition & Examples. https://www.statisticshowto.datasciencecent .com/heavy-tailed-distribution.

29. QiWu,: *Cauchy mutation for decision-making variable of Gaussian particle swarm optimization applied to parameters selection of SVM. Expert Systems with Applications*, , Elsevier,Vol.38 (2011),pp.4929–4934.

30. Wang,H,Yong Liu,:*A Hybrid Particle Swarm Algorithm with Cauchy Mutation*, In: Swarm intelligence Symposium, 2007, ieeexplore.ieee.org.

31. Student t-Distribution , https://en.wikipedia.org/wiki/Student%27s_t-distribution.

32. Seyed Mohsen Mirhassani, Sayedh Zahra Mirhaberi Golroodbari..:*An improved particle swarm optimization based maximum power point tracking strategy with variable sampling time.* In: Electrical Power and Energy Systems, ELSEVIER, Vol.64,(2015), pp. 761-770.

33. Nattawat Jumpasri, Kittapas Pinsuntia, Kaweepoj Woranetsuttikul.:*Improved Particle Swarm Optimization Algorithm using Average Madel on MPPT for Partial Shading in PV Array.* In:Proceedings of the International Electrical Engineering Congress,(2014).

34. Abhinav Dogra et. al.:*Design of Buck-Boost Converter for Constant Voltage Applications and its Transient Response due to Parametric Variation of PI Controller.*In: ternational Journal of Innovative Research in Science , Engineering and Technology. Vol.3,(2014),No. 6.

Effect of Titanium Oxide on Dissipation Factor for the Insulation of Transformer Oil

SOBHY. S. DESSOUKY SAAD A. MOHAMED ABDELWAHAB
Industrial Education, Suez University, Suez, Egypt
sobhyserry@yahoo.com, saad.abdelwahab@suezuniv.edu.eg
Mohammed Shaban
Industrial Education, Suez University, Suez, Egypt
shaban_1983@yahoo.com

Abstract*—In most cases, The electrical insulation of the transformer oil is exposed to different internal problems, such as short circuit , over voltage, over load, over excitation and etcetera. The insulation of transformer is sever decreased into minimum value, that is unacceptable. This requires some treatments of oil liquid ,such as refining or replacing the old oil, which is a very expensive process. In this paper, The old oil is enhanced with nanoparticles (NPs) for reusing in the power transformer again. The NPs enhance the insulation, physical and chemical properties of transformer oil. The breakdown voltage(BDV) and the dissipation factor (DF) are tested for old oil and after addition the NPs according to IEC standard methods. The NPs are many types, Titanium oxide (TiO2) is one of them, which is used in this research. NPs reduce the effect of moisture as it absorb and form hydroxyl groups around. Also, reduce the effect of dissolved carbonate in oil without harmful effects. A comparative study is conducted to identify the effects of using NPs in transformer oil to ensure their effect on electrical insulation, Also to be used again. The results show that adding small amount of TiO2 to transformer oil improves its breakdown strength as well as dissipation factor.*

***Keywords*—**Nanoparticles; dissipation factor test; breakdown voltage test and Titanium oxide.

I. Introduction

Electrical transformer is used to transmission and distribution the electrical power. It is an important electrical equipment, so it is a spirit of the system because it converts voltage and current with stability of power and frequency. The lifespan of transformer is very important that be ranged from 35 to 40 years. Electrical faults are reduced the lifespan and low the level of electrical insulation [1-4]. The insulation test of the transformer is important, It is entering the service or not.

Due to the regular operation of the transformer, thermal stresses are exposed. This heat causes severe risk. The oil penetrates between the windings to transfer the heat. There are several ways to transfer heat either; pregnancy, conduction or radiation. Therefore, fans, pumps and radiators are used to expel heat from the transformer body. The normal operating temperature of the transformer should not exceed 60 ° C. If the heat increases, the transformer will become aged [2].

The transformer oils are used to isolate, cool the coils, extinguish any electrical arc, Prevent the occurrence of chemical processes such as oxidation and give an indication of the internal state; in order to determine its faults in the transformer. Many tests are operated dissolved gas analysis, break down voltage, chemical test, screen tests, furan test and water content. Therefore, if there is a problem in the oil, the treatment must be either by replacing or refining oil and both methods are very expensive [5-7]. Transformer oil is derived from petroleum derivatives, so replacing it is expensive because the transformer may contain tens of tons.

The refining process costs about 70% less than the replacement. The refining process requires several cycles, reduces moisture and acidity then, the transformer can recover again. The refining process is inefficient if there is an internal problem with the transformer. The large number of refining processes lead to the erosion of paper Cellulosic. So many of the transformers after the refining processes are not valid for operation. Refining machines and spare parts have a high price that be increased the process of difficulty. So a new technique is needed to cure this problem.

Nanotechnology is a scientific revolution in the fields of engineering, medical and scientific. It is based on the substitution of the atom material, which produces a new material completely different from the original material has new physical and chemical properties. These materials of NPs are the most commonly used. It is cheaper, more stable and easy to prepare than other metal elementary substance.

Previous studies are pointed to the importance of using nanotechnology to improve the properties of transformer oil. Therefore, nanoparticles have been used to improve the age of limitation of the transformer and can extend its lifespan to double for paper [4]. It is also used in improving electrical insulation, dissolving gases, improving chemical properties and improving viscosity properties [9]. The NPS of the transformer oil have become as important as the medication for its diseases. it was found the kinds of NPs (Fe_3O_4, CuO, ZnO, Al_2O_3 and TiO_2) can increase both positive and negative breakdown voltages under switching impulse voltage [10-15]. Cadmium sulfide and hexagonal crystal structure are added to transformer oil to improve its dielectric and thermal properties, as well as an increase in the breakdown strength by about 81% in comparison to the base transformer oil for paper [16]. the effect of different nanoparticle material types on the DC and AC breakdown voltages of transformer oil nanofluid has been demonstrated, The effect of the external electric field on the charge type (i.e. positive or negative) has been also presented in paper [17]. Huge works for NPs have been deployed to improve the properties of transformer oil.

From this view, this research aims to improve dissipation factor of the transformer using NPs. In this paper, The TiO2

is used. The paper is organized as follows. First, the old oil is processed by adding nanoparticles materials and then shedding ultrasonic waves and infrared ray on this oil. Second, the breakdown voltage test is performed to ensure that the values are improved after the addition of the nanoparticles and then a mini model of the power transformers is immersed in this oil that will be used. Third, the dissipation factor is tested. Finally, the proposed mechanisms are obtained. The results are discussed between new oil , old oil and nano oil.

II. Experiment Method and Test

A. Nanofluid Sample Preparation

Mineral oils are petroleum derivatives, so it contains Hydrocarbons components, which are carbon and hydrogen compounds. These oils are used in electrical transformers, separation and conduction equipment and capacitors. The properties of oil are high viscosity, high electrical strength, high oxidation resistance, have the ability to absorb heat. Shell Diala of transformer oil is many kinds; B,C,D,Dx and F. Shell diala oil D is used in this experiment, That is Conformed to specification IEC 296. This oil is highly refined include a density is 895 kg/ m3. at 20 °C, a viscosity is 12 at 40 °C, a flashpoint is 135 °C, pour point is -40 °C, a breakdown voltage after treatment is 70 kv and a dielectric dissipation factor is 0.005.

The new oil is used as a basis for comparing the results between the nano oil and the old oil that is used. The old oil is taken from the tap changer of the power transformer That, rated power is 40 MVA and the voltage ratio is 66/22 KV, The sample is 2 liters. Nano oil is prepared by using TiO2, It is added into the old oil. TiO2 is obtained from (Alpha Chemika) company as a powder with a particle size below 100 nm , a purity 99.5% and a relative density of 4.26 g/ cm^3. Quantity of titanium oxide is very important, so it is weighed with a sensitive balance of high accuracy. Then the nanoparticles are mixed with the old oil. The mixing machine rotates at low speed to prevent bubbles and gases in the oil. This process takes 20 minutes after, it is stopped. However, the nanoparticles are not fully soluble in oil. This is because the titanium oxide particles are solid materials that are only dispersed at high frequencies. So, the ultrasound is dissolved titanium oxide in oil.

Ultrasound called the audio frequencies exceeding 20 kHz. Ultrasonic waves are a high-frequency wave that the human ear cannot hear. For example, these waves can remove brain tumors and break up kidney stones. At some frequencies, these waves can generate enough energy to weld some metals. In this experiment, The frequency is used at 65 kHz and the waves are concentrated on oil for two hours. So, nanoparticles were melted into the oil.

Despite the benefits of ultrasound, it caused the appearance of moisture and dissolved gases in the oil. To treat these problems, thermal energy must be used. Heat is transmitted by conduction, pregnancy or radiation. In this experiment, The infrared is used for heating the oil, because it distributes the heat on all the atoms of the sample evenly, so complete removal of moisture and full saturation of oil with added NPS.

Infrared radiation is an electromagnetic radiation that comes after visible radiation and before the microwave. The source of infrared radiation must be characterized by a non-fluctuation of the ray and its stability. Philips lamp is used with rated power 250 watt and 230 volt. It has double reflector system to concentrate the rays on the oil. The radiation was given for two hours, with a five minute break every 20 minutes. The oil temperature ranges between (50 - 55 ° C). The oil temperature should not exceed 60 ° C because this increase causes oil aging, which affects the life of the transformer. That is shown from this equation[2]:

$$t_f = t_k * 2^{(\frac{T_k - 60}{7})} \quad (1)$$

Where, T_k refers to the accelerated aging temperature, t_f indicates the equivalent time and t_k shows the aging period under accelerated. It is indicated the aging rate doubles approximately for every 7 °C increase in temperature above 60°C. The steps of preparation the nano oil are summarized as follow in Fig 1.

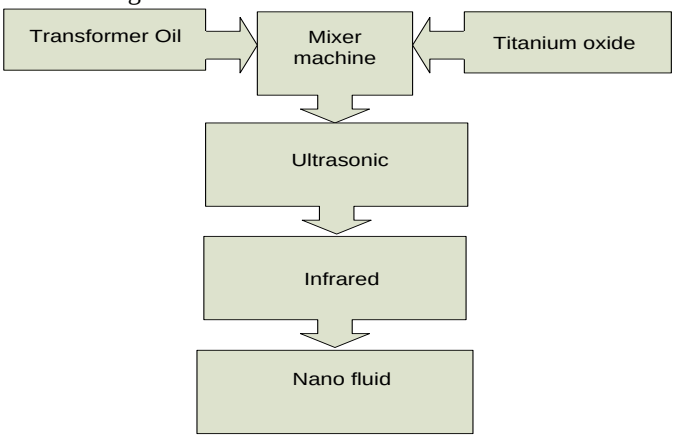

Fig. 1: The Nano fluid preparation steps.

B. Breakdown Voltage Tests

The BDV is measured ability of oil to withstand electrical stress without collapse. The AC breakdown The oil is put in the clean vessel and the gap will be 2.5 mm between the electrodes, now slowly rising voltage is applied between the electrodes. The rate of rise voltage is generally controlled at 2 KV/s and observed the voltage at which sparking starts between the electrodes. The tester gives six values of breakdown were performed. The average value was used as AC breakdown voltage. This test is useful for detecting the presence of insoluble pollutants in oil. such as; moisture, sediment and particulate matter, as it reduces the isolation of oil.

In this search, (BAUR) oil tester model (DPA 75C) is used. The oil breaker contains a magnetic stirrer to stir the sample after each operation. If the magnetic stirrer is not used, the electrons are deposited after each test on the electrodes. Thereby increasing negative charges between electrons. Therefore, the values of breaking oil insulation are incorrect Because the values are raised. The test is done for pure oil, old oil, oil after ultrasonic treatment and nano-oil. Results are compared discussed.

C. The Dissipation Factor Test Methods

The DF is called tan(δ) test. This test shows the leakage of current in oil. The dissipation factor device was used in this experiment is (BIDDle). It has two units one of them for control and other for injected the power, the rated of voltage injected 10 kV, apparent power 1 KVA and current 0.1 A. The angle between the voltage and current are measured through the insulation. appendix A is shown, The specifications of the transformer that is used in this research.

If the angle between the voltage and current is (θ) that shown in fig.2, therefore the completed angle is (δ) that very small value. Whenever small tan(δ) was better insulation and increased is bad insulation. The typical tan(δ) value shall not

exceed 0.5% at 20 ° C. The capacitor shall be measured to confirm the quality of oil insulation of the windings.

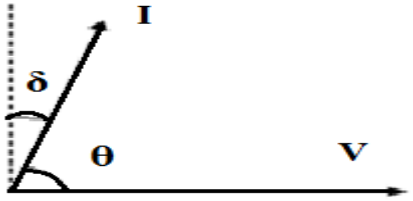

Fig. 2: The angle between voltage and current.

The transformer tank is filled with new oil at first and then tested the DF. After that, it is replaced the new with old oil and nano oil. The procedures of DF test are connected the high voltage cable to the primary side and sensor cable to the low side and tested in these sequence; for measuring (CHG+CHL), for measuring (CHG) and for measuring (CHL).The connection of test in fig.3.

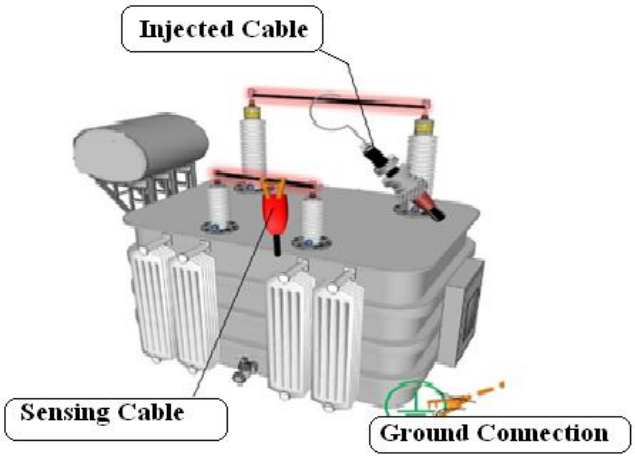

Fig. 3: The injected from HV side.

After that the test will be returned but the injected cable will be at LV side and the sensing at HV side. That be shown in fig. 4.

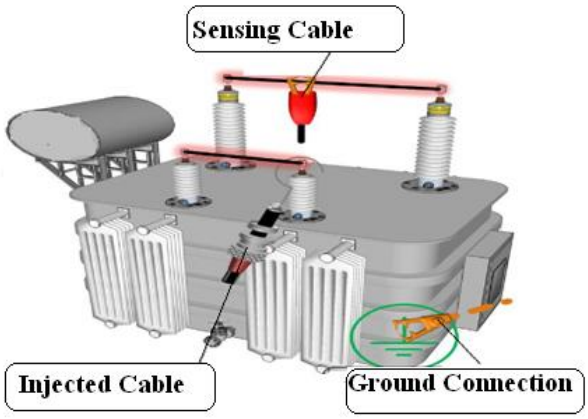

Fig. 4: The injected from LV side.

The purpose of this test is to ensure the quality of internal insulation between windings and ground. The ground of the transformer expresses the iron heart and the transformer tank. This insulation shall be between low voltage side and ground connection, the insulation between high voltage and low voltage sides and the insulation between high voltage side and ground connection.

III. Experiment Result

A. Breakdown Voltage Measurement

Initially, the amount of titanium oxide is determined. So the BDV test is done for new oil. Six readings of new oil were taken at room temperature, the average value was 56 kv. Then, TiO2 is added to the new oil with small values, in milligrams per liter. The added values are 0.02, 0.04, 0.06, 0.08, 0.1, 0.12 and 0.14 g / L. At each value, ultrasonic and infrared treatments are performed and the BDV is tested.the results are shown in fig 5.

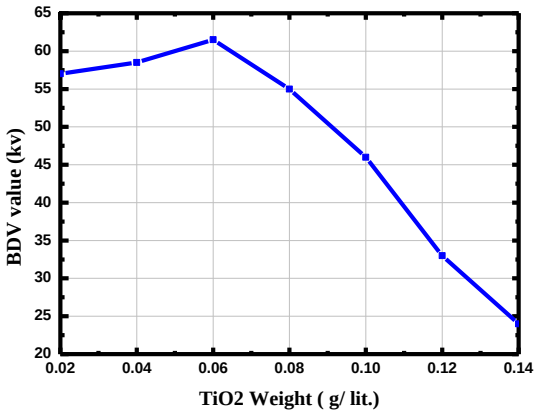

Fig. 5: The amount of TiO_2 nanoparticles in BDV test.

Figure 5 shows the relationship between the amount of (TiO_2) and BDV value. At first, the relationship is positive and then changes to be inverse. the amount 0.06 (g/l) of TiO_2 gives the maximum value of BDV that 61.5 KV for this test. Increasing the titanium oxide particles above that caused a change in the properties of the oil. Viscosity and BDV value are decreased Substantially. So 0.06 g / L of titanium oxide is added to the old oil, to improve the insulation properties. The values of BDV for new oil ,old oil and nano oil are illustrated in fig 6.

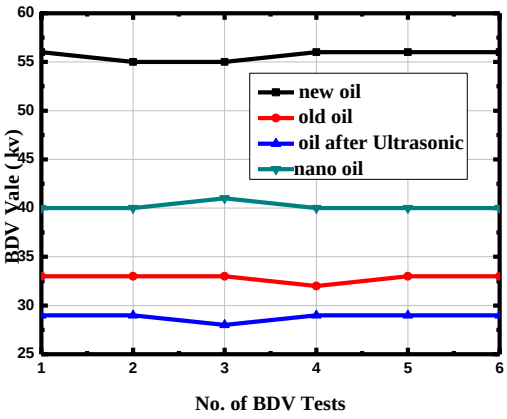

Fig. 6: The BDV measurement for oils.

From the Figure 5, the average values of oils are as follows: new oil is 56 kv, old oil is 33 kv, oil after ultrasonic 29 kv and nano oil is 40 kv. Oil after ultrasonic treatment is decreased the value. This is due to gaps, moisture and bubbles caused by the process. Infrared absorbs foreign matter with organic compounds, that can affect the movement of rotational and vibratory molecules. In the field of organic chemistry is needed short wavelength radiation, which ranges between (30 - 50 cm), leading to high concentration of frequency between (3 - 400 GHz). Therefore, in this research, when using infrared radiation with oil temperature control not to exceed 60 ° C, the

BDV was increased from 33kv into 40 kv. The percentage of enhancement can be calculated according to this equation[19]:

Where, BD_{nf} is the BDV of nano oil and BD_{oil} is the BDV of base oil. The improvement rate is 21%. This corresponds to the values in previous research [2,8,19].

B. Dissipation Factor Measurement

The DF test is essential test in the power transformer. This test ensures the lifespan of overall insulation system of an electrical power transformer. The results of DF are shown in table 1.

Table 1: DF test of the oils.

Injected side	Test volt (v)	Measures	Tanδ %		
			New oil	Old oil	Nano oil
HV side injected	500	CHL	0.22	0.48	0.3
	500	CHL+ CHG	0.28	0.65	0.35
	500	CHG	0.25	0.45	0.29
LV side injected	100	CHL	0.12	0.15	0.12
	100	CHL+ CHG	0.11	0.15	0.12
	100	CHG	0.11	0.16	0.12

From this table The values of Tan(δ) test as follow; new oil is 0.28,old oil is 0.65 and nano oil is 0.35. In the practical life and according to the MPIS (maintenance procedure information system) and IEC:60247 standard, If the DF test is exceeded 0.5 % the transformer is disconnected from the service, Several oil refining cycles are performed. After that, all site-specific tests are done, As well as chemical tests and dissolved gases. If the results are less than the allowed, transformer does not enter the service. After that, an internal detector is made to the transformer. Where, team test are logged through maintenance slots.

The results of DF are enhanced. By Using titanium oxide particles, the values are 0.35 and are within the permissible limits. Effect of applied voltage test on the DF is very important, therefore, it is illustrated in Fig 7.

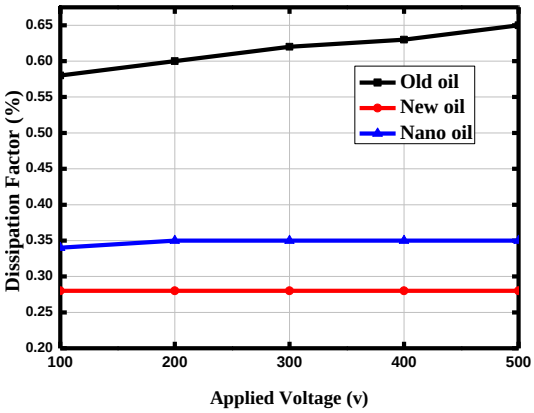

Fig. 7: Relationship between the DF % and applied voltage.

The relationship between the applied voltage and DB is illustreted high stability of the DF in the new oil, as well as in nano oil. DF of the old oil is oscillated in values. This indicates that many atoms of carbon have become semi-conductive, thus affecting insulation. The stability of the nano oil is showen. Transformer oils contain structures of carbon and hydrogen, are systematically correlated that shown in fig. 8.

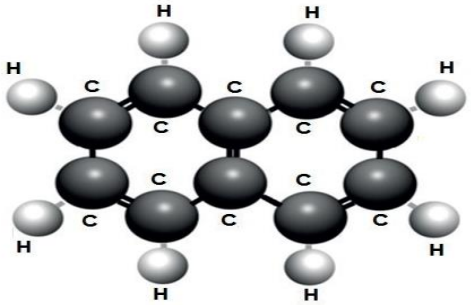

Fig. 8: The structure of transformer oil.

When an electric arc occurs inside the oil, The oil is extinguished the spark, But with frequent recurrence it is decomposited. Carbon atoms appear in oil individually and noticeably. Carbon is a non-metallic substance, Quad parity. Carbon is associated with other elements to be organic compounds. Also found in the inorganic image in carbon dioxide co_2. Carbon of semiconductors, in the normal state is an insulator and when the heat increases the insulation is broken. From (MPIS) instructions, the maintenance of high voltage equipment must not exceed the steps of the tap changer 5000 steps without maintenance or five years, Whichever comes first. Serious maintenance of the tap changer is done by removing it, cleaning the contact points, then returning it and testing the transformer before entering the service. This process in practice is difficult , Sometimes the transformer is damaged due to errors in the maintenance process.

In this research, the sample was taken from the oil of the voltage changer to be practical, So that oil is at the worst conditions. So the BDV was 33kv and after treatment it became 40kv. The basic idea, when attaching a carbon atom with titanium oxide while providing electromagnetic radiation, There is a stirring and interdependence between them, This reaction produces co_2 [20] that shown in equation 3. Fig. 9 shows, Infra-red radiation causes adhesion of carbon atoms to the outer surface of titanium oxide.

$$TiO_2 + C \rightarrow Ti + CO_2 \quad (3)$$

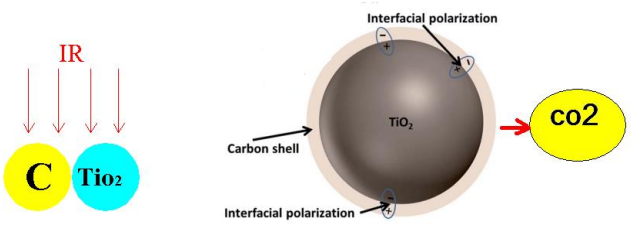

Fig. 9: The effect of IR on carbon and titanium oxide.

From standards IEC 60567 for dissolved gas, the increase in carbon dioxide is not harmful to oil, Allowable 2500 ppm for alarm value and 4000 for trip value. The results are leaded to use this nanoparticles in the electrical field. There is no doubt that using nanotechnology is much better than not using it.

IV. Conclusion

The paper demonstrated the utility of using nanoparticles to enhance the properties of the transformer and improve its efficiency. A model of a transformer similar to power

transformers was made in power grids. Experiments were performed using pure oil and nano-oil. The main conclusions were summarized as follows:

1) The weight of nanoparticles is important and dangerous, so be careful while preparing the oil because the nanometer excess amount reduces the electrical insulation of the transformer and further deterioration.

2) AC breakdown voltage of nanoparticles was higher than pure oil. Also, the dissipation factor is improved.

3) Nanoparticles are enhanced the properties of transformer oil, reduce maintenance risk, Provision of oil change or refining costs and the long life of transformer will be increased also.

Appendix

Table 4: The specification of the transformer.

no.	discriminative	Value
1	No. of phase	Single phase
2	Rated of power	500 VA
3	Voltage on primary	220 volts
4	Voltage on secondary	12 volts
5	Current on primary	2.27 Amps
6	Cooling transformer	ONAN
7	Frequency	50 HZ
8	Mfg. year	2016

REFERENCES

[1] D. A. Mansour, E. G. Atiya, R. M. Khattab and A. M. Azmy, "Effect of titania nanoparticles on the dielectric properties of transformer oil-based nanofluids", IEEE Conf. Electr.Insul.Dielectr.Phenomena (CEIDP), Canada, pp. 295-298, 2012.

[2] X. Zhang and E. Gockenbach, "Determination of the thermal aging factor for life expectancy of 550 kV transformers with a preventive test," IEEE Transactions on Dielectrics and Electrical Insulation, Vol. 20, No. 6, pp.1984-1991, 2013.

[3]Mohammad R. Meshkatoddin, "Aging study and lifetime estimation of transformer mineral oil ", American J. of Engineering and Applied Sciences,vol.1,pp.384-388,2008.

[4]E. G. Atiya, D. A. Mansour, R. M. Khattab and A. M. Azmy, "Dispersion behavior and breakdown strength of transformer oil filled with TiO2 nanoparticles", IEEE Trans. Dielectr. Electr.Insul., vol. 22, no. 5, pp. 2463-2472, 2015.

[5] L.Yuzhen, G.Yang, L. Chengrong, Q. Wang, , Y. Zhou, B. Qi, Y.Kai, X. Chen, and J. Yuan, "Effect of TiO2nanoparticles on streamer propagation in transformer oil under lightning impulse voltage" IEEE Trans. Dielectr. Electr.Insul.,vol. 23,pp.2110-2115, 2016.

[6] D. Yuefan,L. Yuzhen, L.Chengrong, C.Mutian, Z. Yuxiang, Z.Jianquan, L. Xiaoxinand Y. Zhou, "Effect of semiconductive nanoparticles on insulating performances of transformer oil" IEEE Trans. Dielectr. Electr.Insul.,vol. 19,pp.770-776, 2012.

[7]C. Choi, H.S. Yoo and J.M. Oh, "Preparation and heat transfer properties of nanoparticle-in-transformer oil dispersions as advanced energy-efficient coolants" Elsevier, Current Applied Physics, vol. 8,pp. 710–712, 2008.

[8] M.Rafiq, L. Yuzhen, L. Chengrong, Y. Kai, "Effect of different nanoparticle types on breakdown strength of transformer oil" IEEE Conf. on Electr.Insul.andDielectr. Phenomena (CEIDP), vol. 2,pp. 436–440, 2016.

[9] J. A. Mergos, M. D. Athanassopoulou, T. G. Argyropoulos and C. T Dervos, "Dielectric properties of nanopowder dispersions in paraffin oil," IEEE Trans. Dielectr. Electr.Insul., vol. 19, pp. 1502-1507, 2012.

[10] Q. Liu, Z. D. Wang, "Streamer characteristic and breakdown in synthetic and natural ester transformer liquids under standard lightning impulse voltage", IEEE Trans. Dielectr. Electr.Insul, vol. 18, pp. 285-294, 2011.

[11] R. Liu, L. A. A. Pettersson, T. Auletta, and O. Hjortstam, "Fundamental research on the application of nano dielectrics to transformers", IEEE Conf. Electr. Insul.Dielectr.Phenomena, pp. 423-427, 2011.

[12] Y. Torshin, "Schlieren registration of electrohydrodynamics phenomena in dielectric liquids under lightning impulse", IEEE Trans. Dielectr.Electr.Insul, vol. 16, pp. 470-474, 2009.

[13] J. G.Hwang, F. O'Sullivan, M. Zahn, O. Hjortstam, L. A. A. Pettersson, and R. Liu, "Modeling of streamer propagation in transformer oilbasednanofluids", IEEE Conf. Electr. Insul.Dielectr.Phenomena, pp. 361-366, 2008.

[14] M-L. Coulibaly, C. Perrier, M. Marugan and A. Beroual, "Aging behavior of cellulosic materials in presence of mineral oil and ester liquids," IEEE Trans. Dielectr.Electr.Insul.vol.20, no. 6, pp. 1971-1976, 2013.

[15] B.X.Du and X.L. Li "Dielectric and thermal characteristics of vegetable oil filled with BNnanoparticles,"IEEE Transactions on Dielectrics and Electrical Insulation, vol. 24, no. 2, pp. 956-963, April 2017.

[16] Amr M. Abd-Elhady, Mohamed E. Ibrahim, T. A. Taha, and Mohamed A. Izzularab "Dielectric and Thermal Properties of Transformer Oil Modified by Semiconductive CdS Quantum Dots" Journal of Electronic Materials,Vol. 45 , No. 10 , pp. 4755– 4761, october 2016.

[17] Mohamed E. Ibrahim, Amr M. Abd-Elhady, and Mohamed A. Izzularab "Effect of nanoparticles on transformer oil breakdown strength: experiment and theory" IET Science, Measurement & Technology, Vol. 10, No. 8, pp. 839 - 845, 2016.

[18] R. Kochetov, T. Andritsch, P. H. F. Morshuis and J. J. Smit, "Anomalous behaviour of the dielectric spectroscopy response of nanocomposites", IEEE Trans. Dielectr. Electr. Insul., Vol. 19, pp. 107-117,2012.

[19] D. A. Mansour, A. M. Elsaeed and M. A. Izzularab, "The role of interfacial zone in dielectric properties of transformer oil-based nanofluids", IEEE Trans. Dielectr. Electr. Insul., Vol. 23, pp. 3364-3372, 2016.

[20] Anila Ajmal, Imran Majeed, Riffat Naseem Malik, Hicham Idriss and Muhammad Amtiaz Nadeem "Principles and mechanisms of photocatalytic dye degradation on TiO2 based photocatalysts: a comparative overview" Royal Society of Chemistry, Vol 4, pp. 37003–37026, 2014.

Journal of Electrical Engineering ISSN 1582-4594 - Vol 21 No 3 (2021)

Multiport DC-DC converters for renewable energy: an overview with contributions

Aruna Rajendran and Raja Jayamani

Adhiparasakthi Engineering College, Melmaruvathur, Tamilnadu, India

Email: arunarajendran2930@gmail.com, s.t.jayamani@gmail.com

Abstract

The natural energy sources such as oil, coal, natural gas are finite. Also the environmental issues such as global warming have become increasingly serious and require attention. The applications of renewable energy (RE) sources viz. Solar, wind, biomass and tidal power as a major form of clean technology could be the right solution to solve energy crisis ahead with decreasing manufacturing cost. Power electronic converters are used to convert power from renewable sources to cater load demand and/ or grid. Instead of using different DC-DC converters for connecting renewable sources and storage system to the load, Multiport DC-DC converter as single unit can be used to improve efficiency and power density. Many such converters have been proposed in recent times each of which has different topology, reliability and efficiency. The comparison of such different topologies is carried on in this paper which can assist proper selection of suitable topology for any specific requirement. Also, the research extension of the topologies is discussed quoting how the voltage gain can be improved and development of multiport DC-AC inverters.

Keywords: Renewable energy, Storage system, Integration, Multiport converters.

1.Introduction

Photovoltaic energy and wind energy systems have been developed vigorously over recent decade. The cost concerned is also expected to decrease in future along development of technology. A renewable energy source, if works alone cannot satisfy user's requirement of a stable reliable power supply. Hence, there is need of combining or integrating at least two complementary sources like Photovoltaic energy and wind energy along battery storage system leading to the terminology Hybrid Renewable Energy Generation System (HREGS).

For an area near power grid, a Grid connected Renewable Energy system is more appropriate option since the renewable energy sources can supply power both to the local loads and utility grid network, which is termed as Distributed Generation. Renewable Energy systems do not provide pure DC voltage for conversion into AC required by the grid. Hence there is need of a single stage DC-AC-DC conversion. Each source needs a single input DC-DC converter giving rise to a complicated system structure and relative high cost.

The renewable energy source is connected to load through traditional DC-DC converter [4-6] and the energy storage system is connected to either input port or output port through bidirectional DC-DC converter. This traditional solution is of low efficiency as it needs additional converter for energy storage system. Instead of individual converters for each of the renewable energy sources, single Multi-port bi-directional DC-DC converter forms the better choice. The Multiport DC -DC converter in turn is to be connected to an inverter to get the system connected to AC grid and load. The figure 1 depicts the block diagram of Multiport DC-DC Converter where P_{in} is the DC input power, P_b is the DC bidirectional power and P_o is the DC output power.

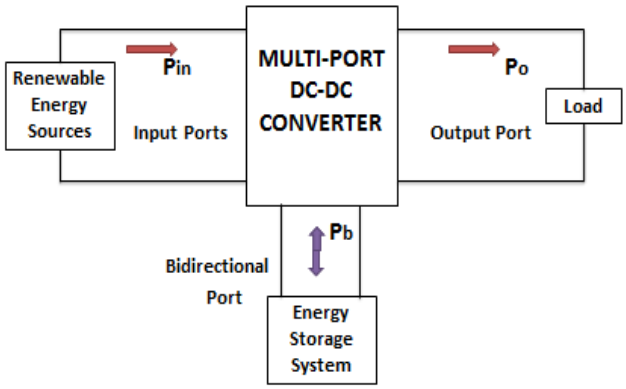

Figure 1 Renewable Energy System using Multiport DC-DC Converter

This paper provides review of Multiport DC-DC converters proposed by different research groups in recent years and compares their features in terms of number of components and reported efficiencies. Few further research areas are also discussed, including the potential application of DC-AC inverters. The organization of the paper is structured as follows: Section 2 presents the reported Multiport DC-DC converters falling under three categories. Section 3 provides brief vivid comparison of these converters and Section 4 puts forth some potential future research in the area. Section 5 concludes the paper.

2. Multiport DC-DC Converters

The Multiport DC-DC converters can be classified depending on connection among ports i.e., including or excluding the use of transformers. They can be broadly classified into three categories viz., Isolated multiport DC-AC-DC converters, Partly-Isolated multiport DC-DC converters and Non-Isolated multiport DC-DC converters. The various topologies of Multiport DC-DC converters were proposed by different researchers in recent years [1-3].

High-frequency transformer is used in Isolated Multiport DC-AC-DC Converter balances well the different voltage levels among different ports. The use of transformer leads to bulky converter and reduces overall power density. Transformer extends voltage conversion ratio but reduces efficiency of conversion. Power loss occurs due to leakage inductance. The number of components is very large since seldom shared. It can be operated with soft switching using appropriate control and modulation methods. The depiction is given in figure 2.

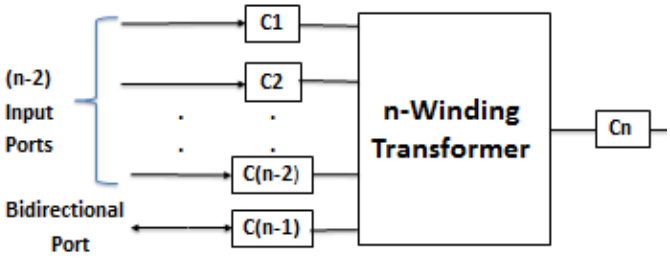

Figure 2 Isolated Multiport DC-AC-DC Converter

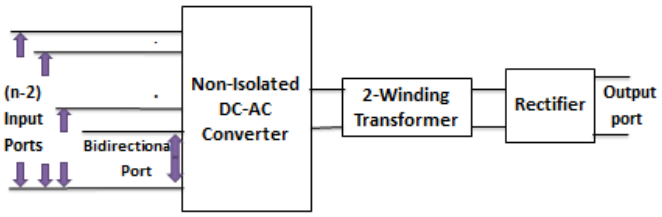

Figure 3 Partly-Isolated Multiport DC-DC Converter

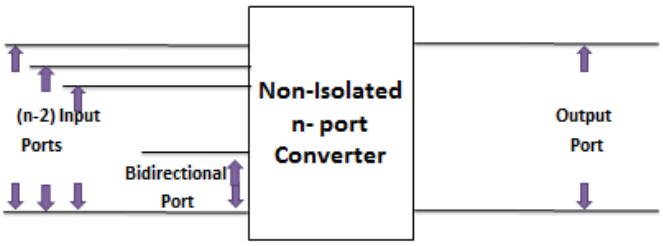

Figure 4 Non-Isolated Multiport DC-DC Converter

In the case of Partly-Isolated Multiport DC-DC Converter given by figure 3, high-frequency transformer is used to isolate one port from other common-grounded ports. Higher voltage gain can be obtained with a larger turns ratio of transformer. Energy storage system operates in all operating modes which can shorten lifespan of the energy system and lower the reliability of system. Disadvantages of having transformer in the circuit imply. The main advantage of Non-Isolated Multiport DC-DC Converter given by figure 4 is reduced number of components. Hence, it has compact structure. It is used only where galvanic isolation is not required. It has limited voltage gain since freedom of modulation of voltage conversion ratio is only the duty cycle. Coupled –inductor can be used to extend voltage conversion ratio to overcome the issue of limited voltage gain. The features are small size and high power density.

2.1. Isolated Multiport DC-DC Converters

The power flow between any two of all ports of Isolated multiport DC-DC converter is realized through multi-winding high- frequency transformer. They have good galvanic isolation and each of the ports has its own components. They are mostly based on the traditional Full-Bridge or Half-Bridge converters or combination of both. The converters proposed in [7-14] have almost similar topology with a high –frequency transformer of three windings interfacing the three ports. An isolated converter formed with three-port triple half–bridge bidirectional DC-DC converter and three-winding high-frequency

transformer is proposed in [7] and that formed with Zero Voltage Switching (ZVS) three-port bidirectional DC-DC converter is studied in [8].

In multiport converters, one port may quit from the system leaving idle port at zero power. Optimal idling control strategy combining Phase –shift control with PWM control is proposed in paper [9]. A hybrid source system made of fuel cell and super capacitor utilizes an isolated three-port bidirectional full-bridge converter [10]. The figure 5 shows the three-port converter with three full bridges, two resonant tanks and three-winding transformer proposed in [11].

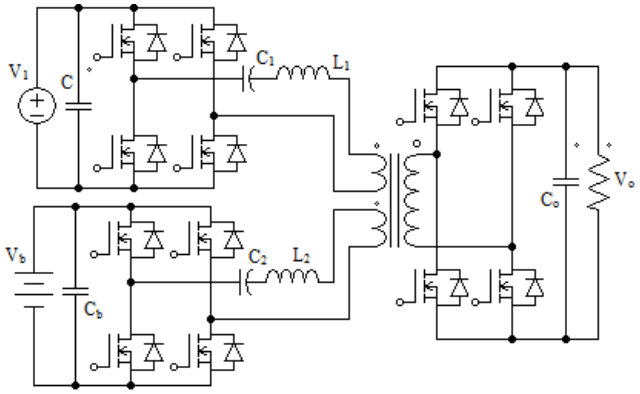

Figure 5 The converter topology in [11]

The converter in [12] has three half-bridges and a three-winding transformer in which bidirectional power flow happens by adjusting phase-shift angles of voltages across two sides of transformer. The analysis of three-port bidirectional converter in soft switching mode is done in [13]. Power switch losses of converters used in hybrid electric systems of [14] are analyzed. The paper [15] explains the topology and control of converter formed of three full-bridge cells and high-frequency transformer whereas a high-frequency magnetic coupled H bridge-double half-bridge three-port bidirectional converter applied in storage battery- ultra-capacitor hybrid energy storage system is explained in [16].

The converters in [17-19] have fuel cell as one of the sources. For safety reasons with galvanic isolation and a high voltage ratio, instead of going for non-isolated types comprising fuel cell, isolated type is considered in [17]. Another converter with current-fed switching topology and multi-resonant circuits is in [18] as given in figure 6. The paper [19] introduces asymmetrical duty cycle control method for the bidirectional converter with two current-fed ports. Three-port converter in [20] based on Cuk topology uses only three power switches along single integrated magnetic core for inductors and windings as shown in figure 7.

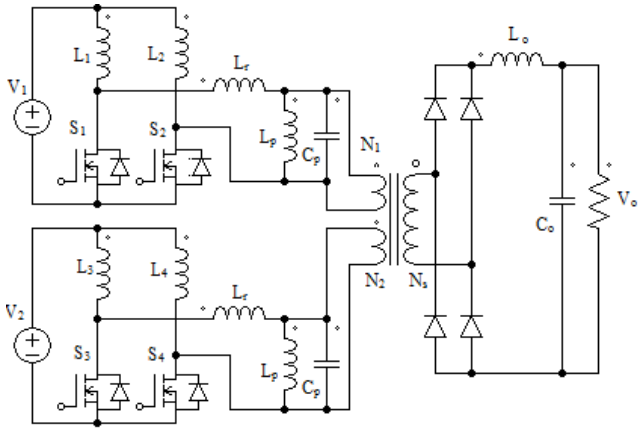

Figure 6 The converter topology in [18]

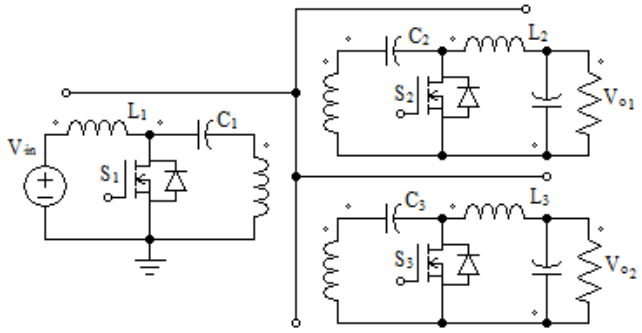

Figure 7 The converter topology in [20]

The converter in [21] uses only one controllable switch in each port. It is used for simultaneous maximum power point tracking control of hybrid system. Multi-input isolated three-level converter adopting high DC link voltage is proposed in [22].

The input inductors are operated in discontinuous conduction mode so that power can be shared between input sources through selection of input inductors. A solid-state transformer has been proposed in [23] to replace regular distribution transformer in future smart grid as depicted by figure 8.

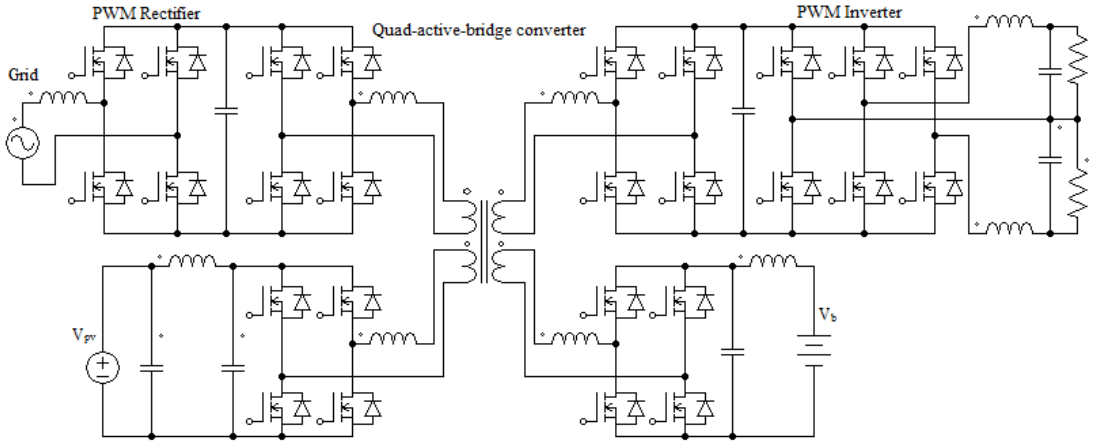

Figure 8 The converter topology in [23]

2.2. Partly-Isolated Multiport DC-DC Converters

Partly-Isolated converters have (n-1) of the n ports directly connected and then these are connected to the third port with galvanic isolation. Input and bidirectional ports are directly connected and are then connected to isolated output port. The paper [24] explains method for deriving soft-switching three-port converters and the circuit is as given by figure 9.

A dual-input interleaved Buck/Boost converter and its power flow control methods are discussed in [25].A three-port converter in [26] is the integration of an interleaved bidirectional Buck/ Boost circuit and a full-bridge LLC resonant circuit for stand-alone PV/Battery system. The converter of [27] given by figure 10 uses least number of switches and soft-switching of main switch is realized by LCL resonant circuit.

A full-bridge three-port converter controlled by PWM plus Secondary-side phase-shift methods is proposed in [28]. A combination of conventional dual active bridge (DAB) and two bidirectional Buck/ Boost circuits is analysed in [30]. A converter involving hybrid battery and super-capacitor applications is given by [29] as depicted in figure 11.

A simple converter derived from full-bridge converter involving a coupled-inductor and diode rectifier is presented in [33]. The paper [34] provides on integrated three-port converter satisfying the requirements of compact and efficient solution. The proposed converter of [35] uses only one switch-mode conversion stage. One port of the three-port converter in [36] is a current source port whose interleaved structure provides the desired small current ripple for the benefit of PV panel.

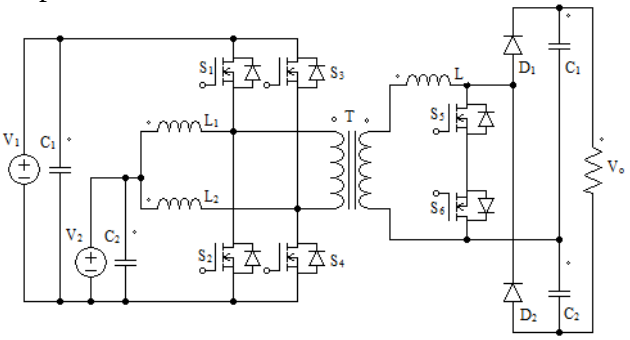

Figure 9 The converter topology in [24]

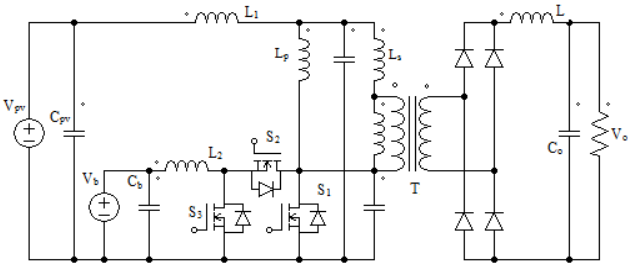

Figure 10 The converter topology in [27]

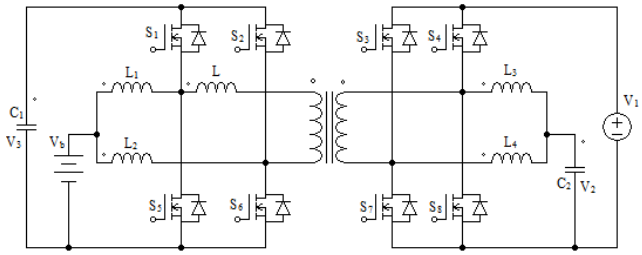

Figure 11 The converter topology in [29]

The paper [31] presents the method of deriving multiport converters from full-bridge converter and bidirectional converter through sharing of parasitized switching legs by both. A method for deriving three-port converters from full-bridge converter is explained in [32]. The schematic depiction of [31] and [32] are given by figures 12 and 13.

Operation of Current-fed dual active bridge converter is studied in [37]. Continuous input current of solar array can be maintained using a magnetic switch obtained from a fourth winding of half-bridge transformer of the converter circuit in [38] which is given by figure 14.

Three-port half-bridge converters are generated by the methods given by [39-40].By adding two switches and two diodes to traditional half-bridge topology, the four-port converter is obtained in [41] which is shown in figure 15. The proposed three-port full-bridge converter in [42] is the integration of two buck-boost converters into primary side of full-bridge topology.

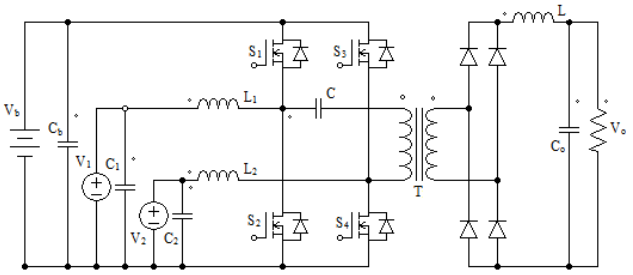

Figure 12 The converter topology in [31]

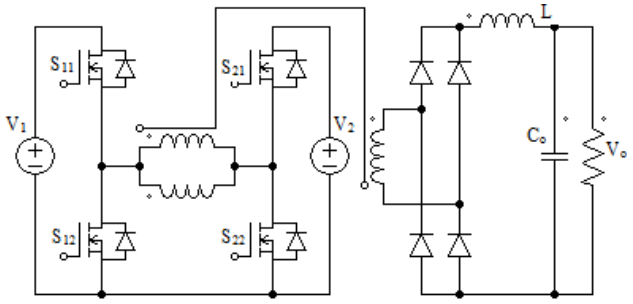

Figure 13 The converter topology in [32]

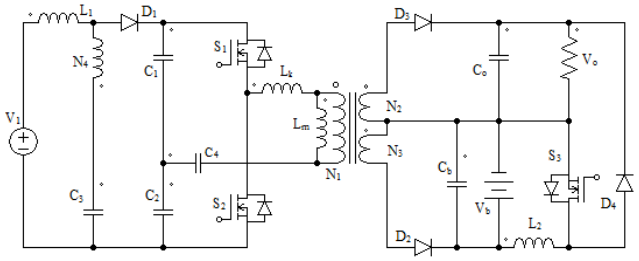

Figure 14 The converter topology in [38]

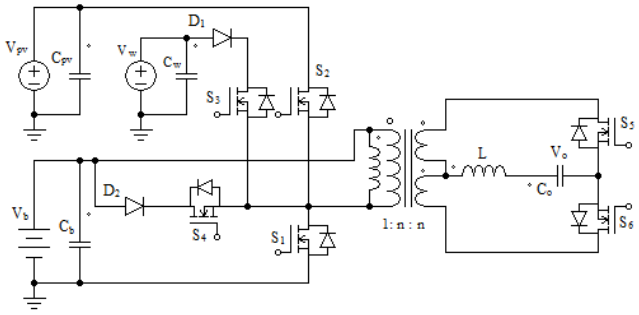

Figure 15 The converter topology in [41]

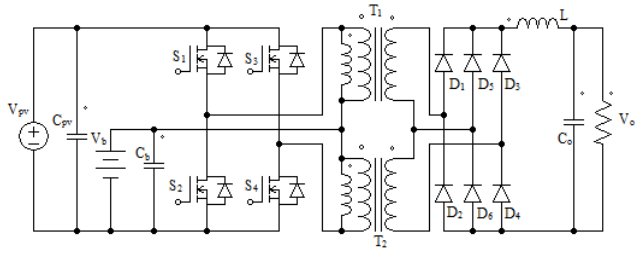

Figure 16 The converter topology in [43]

An interleaved half-bridge three-port converter [44] as an integration of two half-bridge three-port converter modules is presented in [43] as shown in figure 16.

2.3. Non-Isolated Multi-port DC-DC Converters

Non-Isolated multiport converters have been presented in literature with various control and modulation methods. Some use one inductor leading to small size while others use two or three. The gain of these is limited as they are derived from boost, buck and buck-boost converters. In order to cross this limitation, some converters use coupled-inductors to extend voltage conversion ratio. High-voltage gain converter is presented in [45] whose two input sources share only one inductor as shown in figure 17.

A multiport inverter based on DC-link Inductor (DLI) is proposed in [46]. A set of pulsating voltage source cells (PSVCs) are connected in series to derive the converter of [47].A new three-port DC-DC high gain boost converter with bidirectional version of three-state switching cell for battery charging using PV modules in single conversion stage is presented in [48], the circuit of which is figure 18.

High-voltage gain and high efficiency converter based on coupled-inductor, intermediate capacitor and leakage energy recovery scheme handled in [50], is depicted by figure 19.

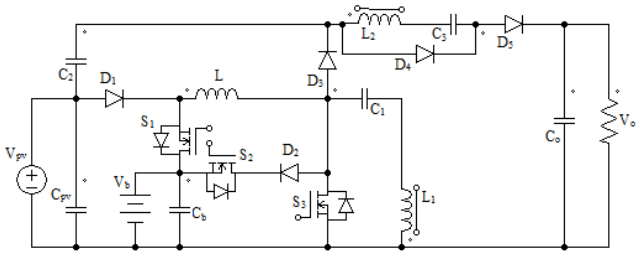

Figure 17 The converter topology in [45]

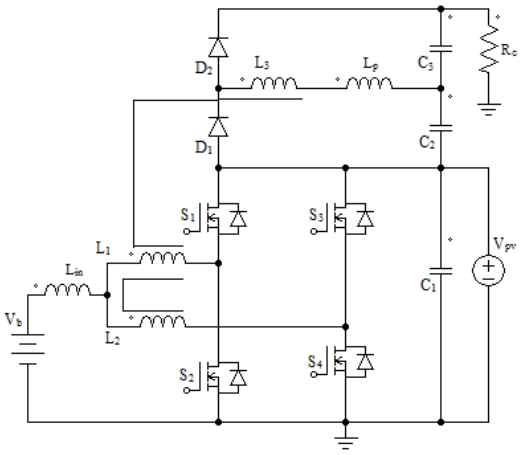

Figure 18 The converter topology in [48]

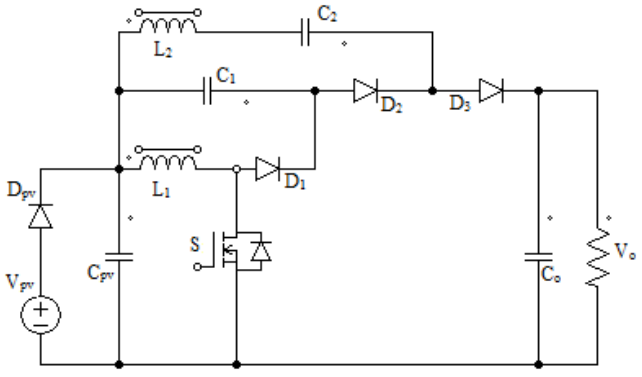

Figure 19 The converter topology in [50]

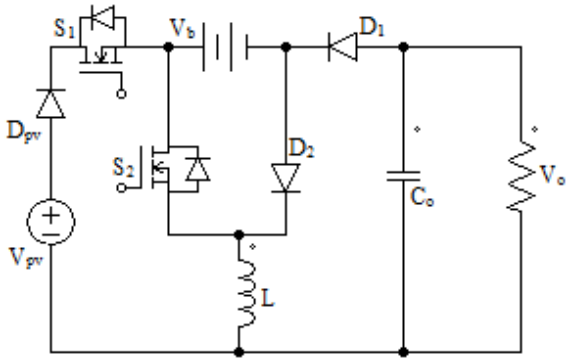

Figure 20 The converter topology in [52]

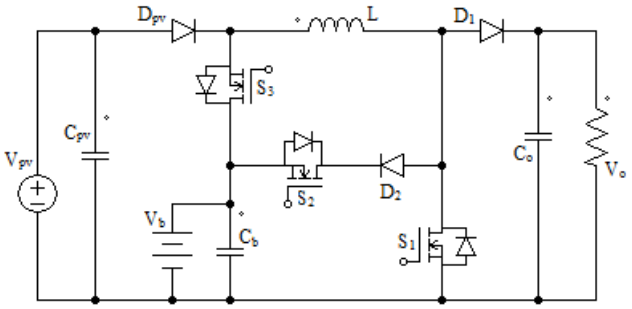

Figure 21 The converter topology in [54]

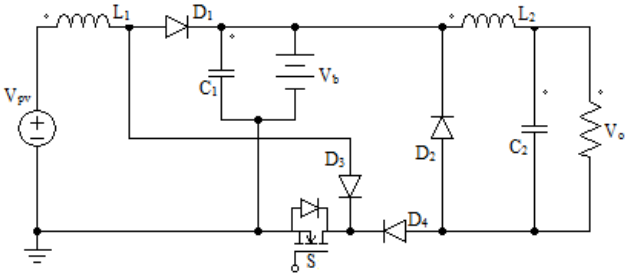

Figure 22 The converter topology in [55]

A simple topology is presented in [51].A new family of three-port converters is proposed in [52] which is obtained by including a general cell into traditional buck, boost and buck-boost converters. The circuit is given in figure 20. Bifurcation analysis of multi-operating mode PV-Battery hybrid system is done in [53].

Systematic method for deriving topologies based on dual-input converters (DIC) and dual-output converters (DOC) is explained in [54]. One of the proposed circuits is presented by figure 21. Design of single-switch three-port converter for stand-alone PV system is proposed in [55] as shown in figure 22.

The paper [56] proposes a bidirectional non-isolated topology for hybrid systems to be used in electric vehicles. The converter in [57] utilizes only four switches independently controlled with four different duty ratios. A family of converters are formed in [58] as shown in figure 23 by introducing a bidirectional cell to basic converter topologies.

The topology of [59] has two sets of parallel boost converters which are controlled to produce two independent output voltage components. The multiport converter of [60] is obtained by interconnection of multiple bidirectional buck/ boost switching cells via DLIs which is depicted in figure 25.

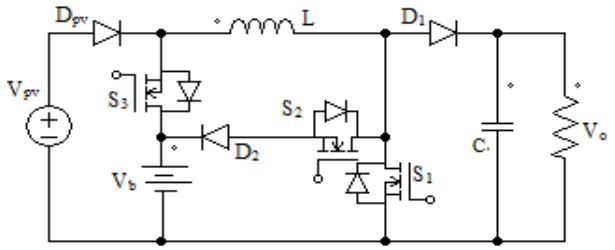

Figure 23 The converter topology in [58]

The converter presented in [61] has traditional buck-boost converters. A multi-input inverter for grid connected system is proposed in [62], which has buck/ buck-boost fused multi-input DC-DC converter and a full-bridge DC-AC inverter as given in figure 24. A converter derived from single inductor dual output converter is proposed in [63].

3. Comparison among the topologies

Many topologies have been proposed in recent times. They have different advantages and disadvantages. In order to provide certain guidance, a comparison is done regarding the structure and features of these topologies.

Isolated and Partly Isolated types provide galvanic isolation whereas the Non-Isolated ones don't provide this. High frequency transformer increases cost. More number of switches in these types leads to lower reliability [64,65].

Comparatively, Non-Isolated types are lower in cost and have less power switching devices along fewer components, but those with higher voltage gain are costlier because of coupled- inductors. These are suitable for small power applications.

The comparison is expressed in the form of tables 1-3 corresponding to Isolated Converters, Partly-Isolated Converters and Non-Isolated Converters respectively. The bar charts depicting the comparison of number of switches and efficiency of Isolated Converters, Partly-Isolated Converters and Non-Isolated Converters are also shown in figures 26-28 respectively.

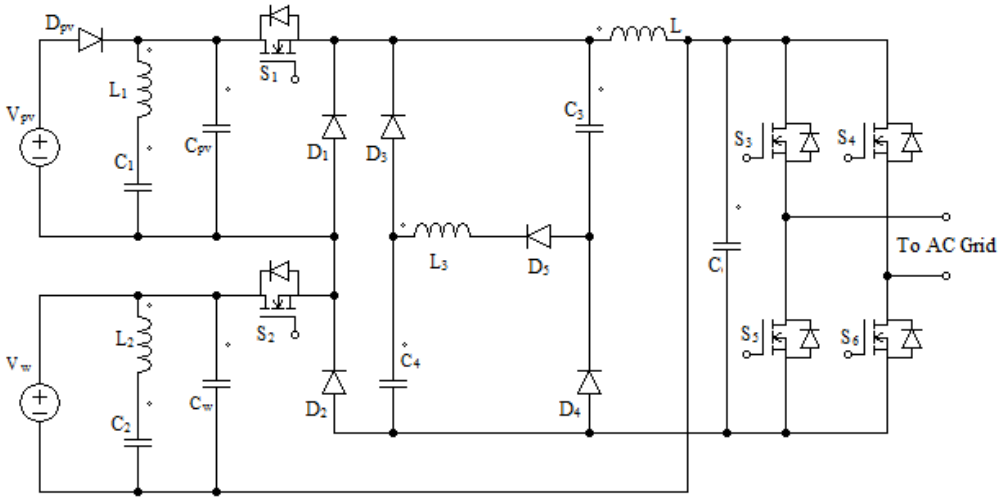

Figure 24 The converter topology in [62]

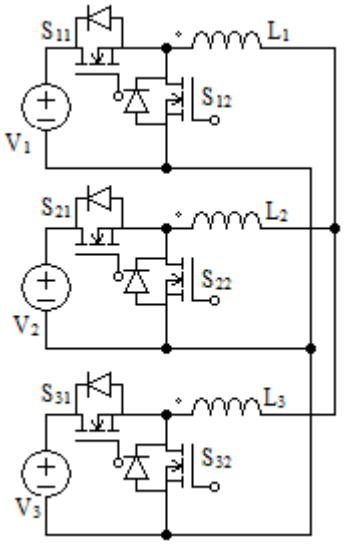

Figure 25 The converter topology in [60]

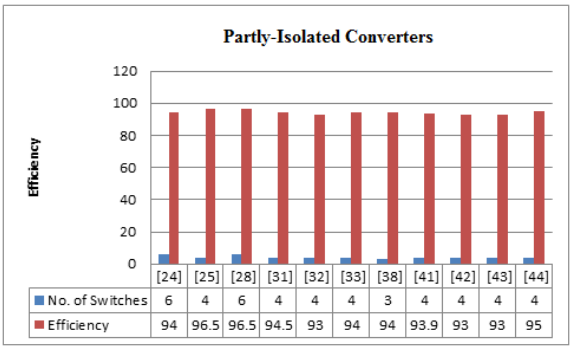

Figure 27 Comparison of number of switches and efficiency of Partly-Isolated Converters presented in papers [24-28], [31-33], [38] and [41-44]

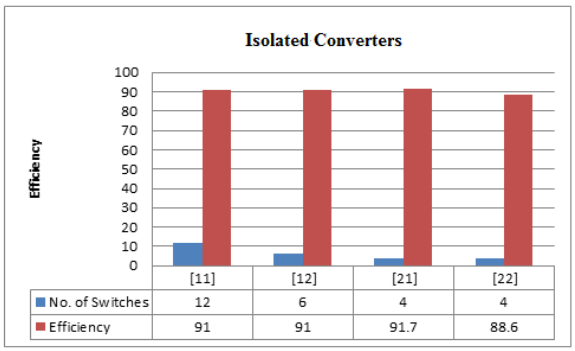

Figure 26 Comparison of number of switches and efficiency of Isolated Converters presented in papers [11], [12], [21] and [22]

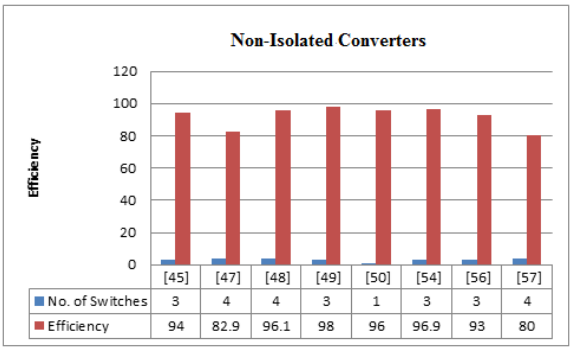

Figure 28 Comparison of number of switches and efficiency of Non-Isolated Converters presented in papers [45], [47-50], [54], [56] and [57]

Table 1 Comparison Table of Isolated Multiport Converters

Serial Number	Reference Number and Features	Number of				Capacity Reported	Maximum Efficiency	Features
		Switches	Diodes	Inductors	Windings of Transformer			
1	7	6	-	4	3	1kW	-	High Voltage conversion ratios; Galvanic isolation for all the ports
2	8	12	-	3	3	1kW	-	
3	9	12	-	3	3	1kW	-	
4	10	12	-	3	3	-	-	
5	11	12	-	3	3	500W	91%	
6	12	6	-	2	3	6kW	91%	
7	13	12	-	-	3	6kW	-	
8	14	12	-	2	3	-	-	
9	15	12	-	3	3	1.5kW	-	
10	16	6	-	3	3	5.7kW	-	
11	17	12	1	-	3	400W	-	
12	18	4	4	3	3	-	-	
13	19	6	-	3	3	2.5kW	-	
14	20	3	-	3	3	-	-	
15	21	m ports	m+4	m+1	2	43W	91.7%	
16	22	4	4	2	1	1.6kW	88.6%	
17	23	20	-	2	4	-	-	

Table 2 Comparison Table of Partly- Isolated Multiport Converters

Serial Number	Reference Number and Features	Number of				Capacity Reported	Maximum Efficiency	Features
		Switches	Diodes	Inductors	Windings of Transformer			
1	24	6	2	3	2	800W	94%	Combination of Interleaved bidirectional converter and Bridgeless Boost rectifier. High frequency transformer. Single stage power conversion. Voltage and power regulated.
2	25	4	4	3	2	1.5kW	96.5%	Total control of power flow from input ports to output ports
3	26	4	4	3	2	500W	-	ZVS realized. Low cost and reduced size. Since Full Bridge unit is shared, input current ripple small.
4	27	3	4	3	2	50W	-	ZVS and ZCS for main switches, Reduced number of switches
5	28	6	2	3	2	600W	96.5%	Improved power devices sharing. Single stage power conversion. Decoupled power control. ZVS realized. No circulating current at free-wheeling stage. Reduced conduction loss, Voltage stresses suppressed.

6	29	8	-	5	2	40W	-	ZVS realized. Current ripples reduced by Interleaved control.
7	30	6	-	2	2	300W	-	Minimised input current ripples, Bidirectional power flow, soft switching.
8	31	4	4	1	2	500W	94.5%	Combination of Full Bridge and Bidirectional converter. Simple topology. Voltage regulation and ZVS realized.
9	32	4	4	2	2	300W	93%	Two switching legs of Full Bridge converter are two switching cells and connected to different sources. ZVS realized. High conversion efficiency. Various similar topologies given.
10	33	4	4	-	2	180W	94%	ZVS realized. Operates over large voltage range.
11	34	5	1	-	3	200W	-	ZVS for all switches, tight load regulation.
12	35	3	1	-	3	60W	-	One switch mode conversion stage. Regulated output.
13	36	12	-	6	6	3kW	-	Three port three phase Interleaved bidirectional DC-DC converter. Voltage boost capability. Soft switching.

14	37	12	-	4	2	5kW	-	High efficiency, step up ratio. Wide input voltage range
15	38	3	4	2	4	500W	94%	ZCS for all main diodes and switches, continuous input current.
16	39	4	-	1	3	200W	-	Integration of Half Bridge converter and a Forward Flyback converter. ZVS realized.
17	40	4	1	-	3	120W	-	Simple topology, high integration, less no.of devices.
18	41	4	2	-	3	-	93.9%	Four ports. Adds two switches and two diodes to half Bridge topology. ZVS realized. Can be extended for additional source.
19	42	4	4	-	4	400W	93%	Single stage power conversion. High power density and efficiency.
20	43	4	6	1	4	500W	93%	Three-leg diode rectifier at Secondary side, hence improved power transfer capability. Extended voltage transfer ratio. Reduced conduction losses. Improved efficiency and high power density. All switches ZVS realized.
21	44	4	6	1	4	400W	95%	Version of two interleaved Half Bridge converter. Soft switching. High efficiency and power density.

Table 3 Comparison Table of Non-Isolated Multiport Converters

Serial Number	Reference Number and Features	Number of				Capacity Reported	Maximum Efficiency	Features
		Switches	Diodes	Inductors	Windings of Transformer			
1	45	3	5	2	NA	300W	94%	Reduced volume, High efficiency, voltage conversion ratio,
2	46	2	1	1	NA	1kW	-	Based on DC link Inductor. Generated by Pulsating Voltage cells(PVC). High efficiency,power density and reliability.
3	47	4	2	1	NA	-	82.9%	Series connection of PVCs. High reliability.
4	48	4	2	2	NA	500W	96.1%	High voltage gain, ZVS over wide range, High efficiency.
5	49	3	3	1	NA	140W	98%	High efficiency, power density, reliability, small size, low cost
6	50	1	3	1	NA	400W	96%	High voltage gain, efficiency.
7	51	3	3	2	NA	100W	-	Simple operation. Easy to control.
8	52	2	2	1	NA	-	-	Cost effective, Compact size
9	53	3	1	2	NA	240W	-	High voltage gain, efficiency.
10	54	3	2	1	NA	1kW	96.9%	High integration, efficiency and power density.
11	55	1	4	2	NA	-	-	Single switch. Reduced component size.

12	56	3	1	1	NA	1kW	93%	Active power sharing. Reduced element count.
13	57	4	4	2	NA	220W	80%	Less no.of inductors, low voltage batteries.
14	58	2	2	1	NA	1kW	96.9%	Good dynamic performance
15	59	4+n	N	2	NA	200W	91%	Minimum no. of switches. High voltage gain.
16	60	2n	-	3n	NA	1kW	98%	Bulky. DC link capacitor eliminated. Reduced size. Low cost.
17	61	1+n	1+n	1+n	NA	-	-	High voltage gain, Reduced semiconductor current stress.
18	62	6	5	1	NA	1kW	-	Large range of input voltage variation. MPPT for both PV and Wind.
19	63	3	3	1	NA	-	-	Compact size, cost efficient. All three ports common ground.

4. Future Research Direction

The applications of multiport DC-DC converters have led to issues like limitation of voltage conversion ratio of Non-Isolated multiport converters and the need of added inverter for AC applications. The following three research topics may be considered for future work.

4.1. Non-Isolated High voltage gain Multiport converters

For the Grid-connected renewable energy generation systems using multiport converters, the voltage conversion ratio, Vout /Vin needs to be high. Traditional Non-Isolated converters does not provide such high step-up gain. Hence, there is need to extend gain using coupled inductors, switched- capacitors, switched- inductors and voltage multiplier circuits.

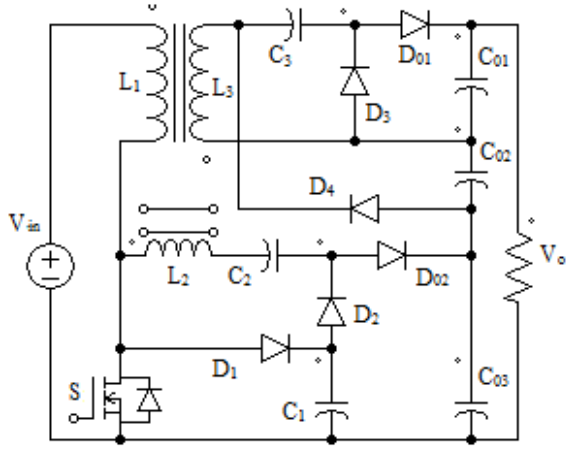

Figure 26 The converter topology in [66]

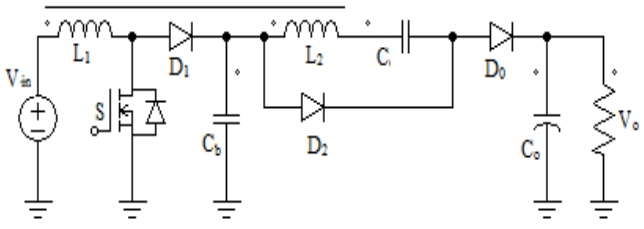

Figure 27 The converter topology in [67]

The utilization of coupled inductors is better than using transformers. The common technique of coupled-inductor circuit has been carried out by researchers in [45, 48, 63]. High step-up converter topologies are proposed with features such as coupled inductor in [66] and additional switched capacitor in [67], the circuits are presented in figures 26 and 27.

4.2. Multiport inverters

To convert power from renewable energy source and provide to the grid, there is a need of DC- AC conversion. This can be done in double stage or single stage configuration. In double stage connection, there are a DC-DC converter and an DC-AC inverter whereas single stage connection needs a DC-AC inverter.

The single stage connection has the benefit ofhaving higher efficiency and a lower cost. Hence, the concept of Multiport converter can be improved as DC-AC Multiport inverter. The papers [68, 69] based on three-level neutral-point-clamped inverter and the circuit of [68] is given by figure 28.

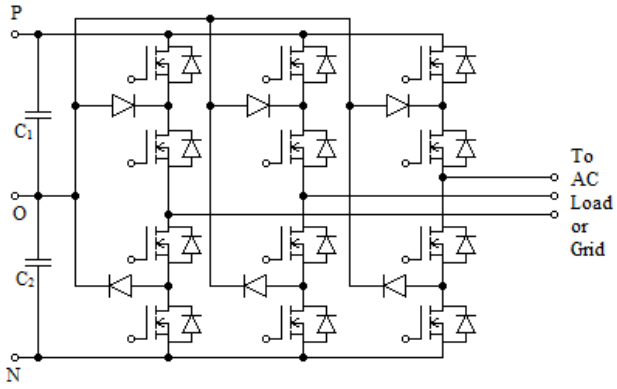

Figure 28 The converter topology in [68]

4.3 Z-source based Multiport inverters

Conventional pulse width modulation inverter needs an additional DC-DC converter to interface the battery and hence, to control state of charge (SoC). Due to the wide voltage range of power sources, the conventional Buck inverter imposes high stresses to the switching devices. DC-DC boosted inverters can suppress these stresses but at high cost and complexity. Both the Buck and Boost configurations use inverter bridge and one DC-DC converter atleast which in turn increases cost and system complexity reducing system reliability.

The Z-source inverter (ZSI) is attractive for the following reasons. ZSI has two independent control freedoms viz., Shoot-through duty cycle and Modulation index against the only control freedom of Modulation index in the case of the conventional PWM inverter. The two control freedoms provide the ability to produce any desired output voltage, regulate (SoC) and control output power/ voltage. The Single stage of ZSI is less complex and more cost effective. ZSI is more reliable as the momentary shoot- through can no longer destroy the inverter i.e., both devices of a phase leg can be On for a significant period of time. ZSI can be used by replacing one of the capacitors with a battery. These facts make the Z-source inverter highly desirable.

By taking advantage of the characteristics of Z-source impedance network such as two capacitors used as energy storage systems, it can be used to derive Multiport DC-AC inverters. Traditional Z-Source inverter as shown in Figure 29, provides both buck and boost operation. The impedance network consists of two inductors (L1 and L2) and two capacitors (C1 and C2) where it couples the main inverter circuit to the DC voltage source. ZSI can operate in boost inverter or buck inverter but not as buck-boost inverter[70].

Quasi-Z-Source Inverter (QZSI) is of new interest in engineering industry and research. Reduction in device rating being the main objective in introducing QZSI, it is feasible in a wide range for high power with medium voltage applications. Continuous input current Quasi-Z-Source Inverter (QZSI) is derived from the original Z-Source Inverter (ZSI) where it can be utilized to all types of power converters.

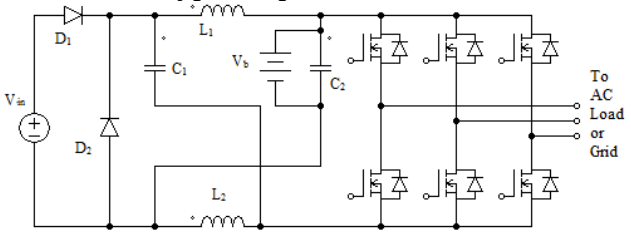

Figure 29 The converter topology in [70]

Some of the disadvantages in traditional ZSI can be overcome by the use of QZSI. The QZSI has the wide range of applicability in the renewable energy system, where it gives a single stage power conversion with buck-boost characteristics and improves the reliability of the inverter. In shoot through states, power switches in a leg are turned on at the same time and it is used to step up the voltage while the output voltage in QZSI can be boost to designed value.

Research based on these QZSI has concentrated on modelling and control, photovoltaic and other electrical applications. The QZSI can buck and boost the input voltage in single stage with two control variables; shoot through and modulation index. New topologies of QZSI derived from original ZSI can be proposed for PV applications, because of continuous input current and reduced capacitor rating. QZSI is combined with renewable energy system for a wide voltage range to distribute for power grid.

Moreover, the voltage stress on capacitors and current stress on inductors and diodes in QZSI are lower than traditional ZSI for same input and output voltage. QZSI avoids initial current inrush, due to which the destruction of the devices can be avoided. Also, these topologies, more viable for solar cell and fuel cell applications, may acquire high voltage gain to match the source voltage difference. For the same input and output voltages as in ZSI, QZSI can use lower duty cycle and higher modulation index, which results in less switching stresses, better output power and lower input current ripple.

The advantage of including inductors in the QZSI network will limit the current ripple through the devices during boost conversion

mode. The inverter draws current with minimal ripple from the Solar PV panel by reducing the size of filtering capacitors. QZSI produce the desired output voltage to the grid, regulate the battery state of charge and control the PV output power to maximize the energy production. An additional input filter can be avoided.

The Quasi Z-Source inverter topologies have one big advantage, such as the DC power supply and the inverter has the same ground connection. This facilitates the design of the driver circuits and current sensing. Also, EMI problems are decreased. QZSI also has added advantage such as higher modulation index with lower component voltage stress. QZSI is obtained from the basic framework of the ZSI. Hence QZSI can be used as a replacement for all the applications in which ZSI is used mainly because of the above mentioned advantages.

Connecting energy storage system to one of the two capacitors in Quasi Z-Source impedance network in parallel is presented in [71] and depicted by figure 30. Conventional structure needs to be oversized to allow wide PV voltage variation derived from changes of irradiation and temperature. The Quasi Z-Source inverter structure can deal such voltage variations without the need for overrating device. Also, shoot – through state helps in reduced component count and system cost along improved reliability. Lower component rating and reduced ripples are added advantages.

Considering more voltage gain, reduce in size of passive components, lesser harmonics and increase in efficiency of the QZSI, it is advantageous and can lead to lower cost when compared to conventional ZSI. Control and modulation techniques for the inverter in [71] are explained in [72-75]. The modified circuit is given in figure 31 [76].

Table 2 Comparison of the three types of inverters

Features/ Type of inverter	**Traditional Buck/ Boost/ Buck-Boost converter based two-stage inverter (Figure 28)**	**Single stage Impedance Source (Z-Source) inverter (ZSI) (Figure 29)**	**Single stage Quasi Impedance Source (Z-Source) inverter (QZSI) (Figure 30 and 31)**
Efficiency %	x	Almost x and in some cases less than x	Greater than x
Size	Not compact	Compact	Compact
No. of Components	Many	Less	Less
Voltage stress on switches	Low	Low	High
Total Harmonic Distortion (THD) %	y	Z less than y	Less than z
Capacitor rating	High	Lower than in Traditional one	Lower than in ZSI
Cost in units	m	n less than m	Less than n

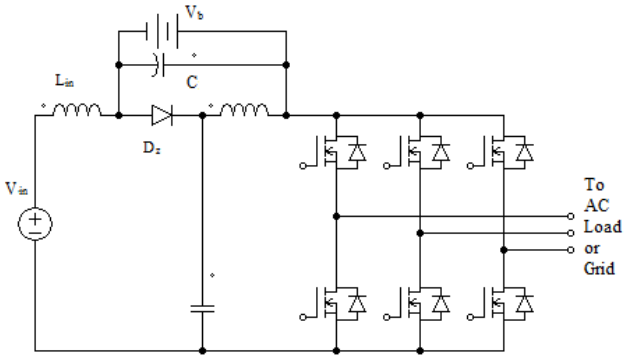

Figure 30 The converter topology in [71]

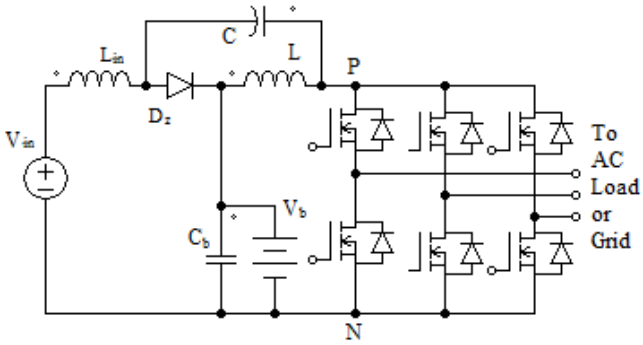

Figure 31 The converter topology in [76]

All of these Z-source based inverters are based on traditional two-level three phase inverter. Application of Z-source impedance network in other inverters such as neutral- point-clamped three- level inverter and single phase inverter can be researched further.

5.Conclusion

A literature review of various topologies used for multiport converters has been presented in the paper. The research in this area has gained substantial progress and also received more attention from researchers in the area of hybrid renewable energy and storage systems. The general working principles advantages and disadvantages of the different topologies are discussed. The comparison among the three kinds of converters has been done in order to pose as guide for practical applications. Conventional inverters, Z source inverters and Quasi Z source inverters are briefly analysed along respective models as well as the comparison is made among them. Further research is to be carried out to increase the voltage of the converter and in the design of novel multiport DC-AC inverters.

REFERENCES

1. H. Tao, A. Kotsopoulos, J.L. Duarte and M.A.M. Hendrix, “Family of multiport bidirectional DC–DC converters” in IEE Proc.-Electr. Power Appl., Vol. 153, No. 3, May 2006, pp.451-458.
2. Haimin Tao, Jorge L. Duarte, and Marcel A.M. Hendrix, “ Multiport Converters for Hybrid Power Sources”, in Proc. IEEE Power Electronics Specialists Conference (PESC’08), Rhodes, pp.3412-3418.
3. Wuhua Li, Xiaodong Lv, Yan Deng, Jun Liu, Xiangning He, “A Review of Non-Isolated High Step-Up DC/DC Converters in Renewable Energy Applications”, in APEC, 2009, pp.364-369.
4. Roberto F. Coelho, Filipe M. Concer, Denizar C. Martins, “A Simplified Analysis of DC-DC Converters Applied as Maximum Power Point Tracker in Photovoltaic Systems”, in Proc. IEEE symposium on Power Electronics for Distributed Generation System, 2010, pp.29-34.
5. Bing Hu, Liuchen Chang, Yaosuo Xue, “Research on a Novel Buck-Boost Converter for Wind Turbine Systems”, in Proc.ICSET 2008, pp.228-233.
6. Alberto Rodríguez Alonso, Javier Sebastian, Diego G. Lamar, Marta M. Hernando, Aitor Vazquez, “An overall study of a Dual Active Bridge for bidirectional DC/DC conversion”, in ECCE 2010,pp.1129-1135.
7. Haimin Tao, Jorge L. Duarteand Marcel A. M. Hendrix, “Three-Port Triple-Half-Bridge Bidirectional Converter With Zero-Voltage Switching”, IEEE Trans. on Power Electronics, Vol. 23 No.2, March 2008, pp.782-792
8. Haimin Tao, Andrew Kotsopoulos, Jorge L. Duarteand Marcel A. M. Hendrix, “Transformer-Coupled Multiport ZVS Bidirectional DC–DC Converter With Wide Input Range”, IEEE Trans. on Power Electronics, Vol. 23 No.2, March 2008, pp. 771-781

9. Jiang Y., Liu F., Ruan X. and Wang L., " Optimal idling control strategy for three-port full-bridge converter", in ECCEASIA 2014, pp.458 - 464.
10. Phattanasak M., Ghoachani R. G., Martin J. P., Pierfederici S. and Davat B, "Flatness based control of an isolated three port bidirectional DC-DC converter for a fuel cell hybrid source", in ECCE 2011, pp.977 - 984.
11. Hariharan Krishnaswamiand Ned Mohan, "Three-Port Series-Resonant DC–DC Converter to Interface Renewable Energy Sources With Bidirectional Load and Energy Storage Ports", IEEE Trans. on Power Electronics, Vol. 24, No.10, October 2009, pp.2289-2297.
12. Danwei Liuand Hui Li, "A ZVS Bi-Directional DC–DC Converter for Multiple Energy Storage Elements", IEEE Trans. on Power Electronics, Vol. 21, No.5, September 2006, pp.1513-1517
13. Oggier G. G., Botalla L. P. and Garcia G. O, "Soft-switching analysis for three-port bidirectional DC-DC converter", in INDUSCON 2010, pp.1 - 6.
14. Botalla L. P., Oggier G. G., Airabella A. M. and Garcia G. O, "Analysis and evaluation of power switch losses for three-port bidirectional DC-DC converter", in ICIT 2012, pp.950 - 955.
15. Chuanhong Zhao, Simon D. Roundand Johann W. Kolar, "An Isolated Three-Port Bidirectional DC-DC Converter With Decoupled Power Flow Management", IEEE Trans. on Power Electronics, Vol. 23 No.5, September 2008, pp.2443-2453
16. Zhixiang Ling, Hui Wang, Kun Yan, Zaoyi Sun, "A New Three-port Bidirectional DC/DC Converter for Hybrid Energy Storage", in IFEEC 2015, pp.1-5.
17. Matheepot Phattanasak,Roghayeh Gavagsaz-Ghoachani, Jean-Philippe Martin, Babak Nahid-Mobarakeh, Serge Pierfederici and Bernard Davat, " Control of a Hybrid Energy Source Comprising a Fuel Cell and Two Storage Devices Using Isolated Three-Port Bidirectional DC–DC Converters", IEEE Trans. on Industry Applications, Vol. 51, No.1, January/February 2015, pp.491-497.
18. Samavatian V., Bathaee S. M. T. and Fereidunian A, "Half-bridge current-fed multi-resonant bidirectional three-port DC converter for flexible distributed generation", in PEDSTC 2014, pp.172 - 176.
19. Wang L., Wang Z. and Li H, "Asymmetrical duty cycle control and decoupled power flow design of a three-port bidirectional DC-DC converter for fuel cell vehicle application", IEEE Trans. on Power Electronics 2012, Vol.27, No.2, pp. 891–904.
20. Biswas S., Dhople S.and Mohan N, "A three-port bidirectional DC-DC converter with zero-ripple terminal currents for PV/microgrid applications", in IECON 2013, pp.340 - 345.
21. Jianwu Zeng, Wei Qiao, Liyan Qu and Yanping Jiao, "An Isolated Multiport DC–DC Converter for Simultaneous Power Management of Multiple Different Renewable Energy Sources", IEEE Journal of Emerging and Selected topics in Power Electronics, Vol. 2, No.1, March 2014, pp.70-78.
22. Serkan Dusmez, Xiong Liand Bilal Akin, "A New Multiinput Three-Level DC/DC Converter", IEEE Trans. on Power Electronics, Vol. 31, No.2, February 2016, pp.1230-1240
23. Sixifo Falcones, Rajapandian Ayyanarand Xiaolin Mao, "A DC–DC Multiport-Converter-Based Solid-State Transformer Integrating Distributed Generation and Storage", IEEE Trans. on Power Electronics, Vol. 28, No.5, May 2013, pp.2192-2203
24. Hongfei Wu, Junjun Zhang, Xiaoqing Qin, Tiantian Mu, and Yan Xing, "Secondary-Side-Regulated Soft-Switching Full-Bridge Three-Port Converter Based on Bridgeless Boost Rectifier and Bidirectional Converter for Multiple Energy Interface", IEEE Trans. on Power Electronics, Vol. 31, No.7, July 2016, pp.4847-4860.
25. Maria C. Mira, Zhe Zhang, Arnold Knott and Michael A.E. Anderson, "Power Flow Control of a Dual-Input Interleaved Buck/ Boost Converter with Galvanic Isolation for Renewable Energy Systems", in APEC 2015, pp.3007-3012.
26. Xiaofeng Sun, Yanfeng Shen, Wuying Li, "A Novel LLC Integrated Three-port DC-DC Converter for Stand-alone PV/Battery System", ITEC Asia Pacific 2014, pp.1-6

27. Zeng J., Qiao W. and Qu L, " An isolated three-port bidirectional DC-DC converter for photovoltaic systems with energy storage", in Industrial Application Society Annual Meeting 2013, pp.1 - 8.
28. Junjun Zhang, Hongfei Wu, Xiaoqing Qin, and Yan Xing, "PWM Plus Secondary-Side Phase-Shift Controlled Soft-Switching Full-Bridge Three-Port Converter for Renewable Power Systems", IEEE Trans. on Industrial Electronics, Vol. 62, No.11, November 2015, pp.7061-7072.
29. Zhihui Ding, Chen Yang, Zhao Zhang, Cheng Wang and Shaojun Xie, "A Novel Soft-Switching Multiport Bidirectional DC–DC Converter for Hybrid Energy Storage System", IEEE Trans. on Power Electronics, Vol. 29, No.4, April 2014, pp.1595-1609
30. Sun X., Liu F., Xiong L. and Wang B, "Research on dual buck/boost integrated three-port bidirectional DC/DC Converter", in ITEC Asia-Pacific 2014, pp. 1 - 6.
31. Hongfei Wu, Peng Xu, Haibing Hu, Zihu Zhou, and Yan Xing, "Multiport Converters Based on Integration of Full-Bridge and Bidirectional DC–DC Topologies for Renewable Generation Systems", IEEE Trans. on Industrial Electronics, Vol. 61, No.2, February 2014, pp.856-869.
32. Hongfei Wu, Kai Sun, Runruo Chen, Haibing Hu and Yan Xing, Member, "Full-Bridge Three-Port Converters With Wide Input Voltage Range for Renewable Power Systems", IEEE Trans. on Power Electronics, Vol. 27, No.9, September 2012, pp.3965-3974
33. Parthiban R.,and Rajammal K, "Performance investigation of three-port converter for hybrid energy system", in ICEES 2014, pp.261 - 266.
34. Qian Z., Rahman O. A., Zhang K., Hu H., Shen J. and Batarseh I, "Design and analysis of three-port DC/DC converters for satellite platform power system", in ECCE 2011, pp.1454 - 1460.
35. Zhijun Qian, Osama Abdel-Rahman, Haibing Hu and Issa Batarseh, "An Integrated Three-port Inverter for Stand-alone PV Applications", in ECCE 2010, pp.1471-1478
36. Zhan Wangand Hui Li, "An Integrated Three-Port Bidirectional DC–DC Converter for PV Application on a DC Distribution System", IEEE Trans. on Power Electronics, Vol. 28, No.10, October 2013, pp.4612-4624
37. Yuxiang Shi, Rui Li, Yaosuo Xue and Hui Li, "Optimized Operation of Current-Fed Dual Active Bridge DC–DC Converter for PV Applications", IEEE Trans. on Industrial Electronics, Vol. 62, No.11, November 2015, pp.6986-6995
38. Zhu H., Zhang D., Athab H. S., Wu B. and Gu Y, "PV isolated three-port converter and energy-balancing control method for PV-battery power supply applications", IEEE Trans. on Industrial Electronics 2015, Vol.62, No.6, pp.3595–3606.
39. Hongfei Wu, Runruo Chen, Junjun Zhang, Yan Xing, Haibing Hu, and Hongjuan Ge, "A Family of Three-Port Half-Bridge Converters for a Stand-Alone Renewable Power System", IEEE Trans. on Power Electronics, Vol. 26, No.9, September 2011, pp.2697-2707
40. Wu H., Xing Y., Chen R., Zhang J., Sun K. and Ge H, " A three-port half-bridge converter with synchronous rectification for renewable energy application", in ECCE 2011, pp.3343 - 3349.
41. Zhijun Qian, Osama Abdel-Rahmanand Issa Batarseh, "An Integrated Four-Port DC/DC Converter for Renewable Energy Applications", IEEE Trans. on Power Electronics, Vol. 25, No.7, July 2010, pp.1877-1887.
42. Wenfei Hu, Hongfei Wu, Yan Xing and Kai Sun , "A Full-Bridge Three-Port Converter for Renewable Energy Application", in APEC 2014, pp.57-62.
43. Hongfei Wu, Kai Sun, Lili Zhu, Yan Xing, "An Interleaved Half-Bridge Three-Port Converter with Enhanced Power Transfer Capability Using Three-Leg Rectifier for Renewable Energy Applications", IEEE Journal of Emerging and Selected Topics in Power Electronics, Vol.4, Iss:2, 2016, pp.1-10.
44. Lili Zhu, Hongfei Wu, Peng Xu, Haibing Hu,Hongjuan Ge, "A Novel High Efficiency High Power Density Three-Port Converter Based on Interleaved Half-Bridge Converter for Renewable Energy Applications", in ECCE 2014, pp.5085-5091.
45. Chien L. J., Chen C. C., Chen J. F., and Hsieh Y. P, " Novel three-port converter with high-

voltage gain", IEEE Trans. on Power Electronics 2014, Vol.29, No.9, pp.4693–4703.
46. Hongfei Wu, Junjun Zhang, and Yan Xing, "A Family of Multiport Buck–Boost Converters Based on DC-Link-Inductors (DLIs)", IEEE Trans. on Power Electronics, Vol. 30, No. 2, February 2015, pp.735-746.
47. Lalit Kumar and Shailendra Jain, "Multiple-input DC/DC converter topology for hybrid energy system", IET Power Electron., 2013, Vol. 6, Iss. 8, pp. 1483–1501.
48. Alves D. B. S., Praca P. P., Oliveira Jr. D. S., Barreto L. H. S. C., and de Freitas L. C. G, " A single-stage three-port boost converter with high voltage gain based on the bidirectional version of the three-state switching cell", in APEC 2015, pp.1934 - 1940.
49. Hongfei Wu, Yan Xing, Yanbing Xia, Kai Sun, "A Family of Non-Isolated Three-Port Converters for Stand-Alone Renewable Power System", in IECON Industrial Electronics Society 2011, pp.1030-1035
50. Moumita Das and Vivek Agarwal, "Design and Analysis of a High-Efficiency DC–DC Converter With Soft Switching Capability for Renewable Energy Applications Requiring High Voltage Gain", IEEE Trans. on Industrial Electronics Vol. 63, No.5, May 2016, pp.2936-2944
51. Vazquez N., Sanchez C. M., Hernandez C., Vazquez E., Lesso R, "A three-port converter for renewable energy Applications", in ISIE 2011, pp.1735 - 1740.
52. Chen Y., Wen G., Peng L., Kang Y., J. Chen, "A family of cost-efficient non-isolated single-inductor three-port converters for low power stand-alone renewable power applications", in APEC 2013, pp.1083 - 1088.
53. Xiaoling Xiong, Chi K. Tse, and Xinbo Ruan, "Bifurcation Analysis and Experimental Study of a Multi-Operating-Mode Photovoltaic-Battery Hybrid Power System", IEEE Journal of Emerging and Selected topics in Circuits and Systems, Vol.5, No.3, September 2015, pp.316-326
54. Hongfei Wu, Kai Sun, Shun Ding and Yan Xing, "Topology Derivation of Nonisolated Three-Port DC–DC Converters From DIC and DOC", IEEE Trans. on Power Electronics, Vol. 28, No. 7, July 2013, pp.3297-3307
55. Junkai Zhao, Herbert H.C. Iu, Tyrone Fernando, Le An and Dylan Dah-Chuan Lu, "Design of a Non-Isolated Single-Switch Three-Port DC-DC Converter for Standalone PV-Battery Power System", in ISCAS 2015, pp.2493-2496
56. F. Akar, Y. Tavlasoglu, E. Ugur, B. Vural, I. Aksoy, "A Bidirectional Non-Isolated Multi-Input DC-DC Converter for Hybrid Energy Storage Systems in Electric Vehicles", IEEE Trans. on Vehicular Technology 2015, pp.1-12
57. Farzam Nejabatkhah, Saeed Danyali, Seyed Hossein Hosseini, Mehran Sabahi, and Seyedabdolkhalegh Mozaffari Niapour, "Modeling and Control of a New Three-Input DC–DC Boost Converter for Hybrid PV/FC/Battery Power System", IEEE Trans. on Power Electronics, Vol. 27, No.5, May 2012, pp.2309-2325
58. Shun Ding, Hongfei Wu, Yan Xing, Yu Fang and Xudong Ma, "Topology and Control of a Family of Non-Isolated Three-port DC-DC Converters with a Bidirectional Cell", in APEC 2013, pp.1089-1094
59. Saeed Danyali, Seyed Hossein Hosseiniand Gevorg B. Gharehpetian, "New Extendable Single-Stage Multi-input DC–DC/AC Boost Converter", IEEE Trans. on Power Electronics, Vol. 29, No.2, February 2014, pp.775-788
60. Junjun Zhang, Hongfei Wu, Jun Huang, Yan Xing and Xudong Ma, "A Novel Multi-Port Bidirectional Converter for Interfacing Distributed DC Micro-Grid", in ISIE 2014, pp.2344-2348
61. Mohammad Reza Banaei, Hossein Ardi, Rana Alizadeh and Amir Farakhor, "Non-isolated multi-input–single-output DC/DC converter for photovoltaic power generation systems", IET Power Electron., 2014, Vol. 7, Iss. 11, pp. 2806–2816
62. Yaow-Ming Chen, Yuan-Chuan Liu, Shih-Chieh Hung, and Chung-Sheng, "Multi-Input Inverter for Grid-Connected Hybrid PV/Wind Power System", IEEE Trans. on Power Electronics, Vol. 22, No.3, May 2007, pp. 1070-1077
63. Zhang P., Chen Y., Zhou Z. and Kang Y, "The cost-efficient, common-ground, non-isolated three-port converter deduced from the single-

inductor dual-output topology", in APEC 2015, pp.2020 - 2025.
64. Song Y., Wang B, " Survey on reliability of power electronic systems", IEEE Transactions on Power Electronics 2013; 28(1): 591–604.
65. Yang S., Bryant A., Mawby P., Xiang D., Ran L., Tavner P, "An industry-based survey of reliability in power electronic converters", IEEE Transactions on Industrial Applications 2011; 47(3): 1441–1451.
66. Mohammad Khalilzadeh, Karim Abbaszadeh , "Non-isolated high step-up DC–DC converter based on coupled inductor with reduced voltage stress", in IET Power Electron., 2015, Vol. 8, Iss.11, pp. 2184–2194.
67. Y. Zhao W. Li Y. Deng X. He , "High step-up boost converter with passive lossless clamp circuit for non-isolated high step-up applications", in IET Power Electron., 2011, Vol. 4, Iss. 8, pp. 851–859.
68. Teymour H. R., Sutanto D., Muttaqi K. M., Ciufo P, " Solar PV and battery storage integration using a new configuration of a three-level NPC inverter with advanced control strategy", IEEE Transactions on Energy Conversion 2014; 29(2): 354–365.
69. Jayasinghe S. D. G., Vilathgamuwa D. M., Madawala U. K, "Diode-clamped three-level inverter-based battery/supercapacitor direct integration scheme for renewable energy system", IEEE Transactions on Power Electronics 2011; 26(12): 3720–3729.
70. Peng F.Z., hen M., Holland K, "Application of Z- source inverter for traction drive of fuel application of Z- source inverter for traction drive of fuel cell –battery hybrid electric vehicles", IEEE Transactions on Power Electronics 2007; 22(3): 1054-1061.
71. Jorge G. C. R., Li Y., Jiang S., Peng F. Z, " Quasi-Z-source inverter with energy storage for photovoltaic power generation systems", in APEC; 2011: 401 - 406.
72. Liu J., Jiang S., Cao D., Peng F. Z, " A digital current control of quasi-Z-source inverter with battery", IEEE Transactions on Industrial Informatics 2013; 9(2): 928–937.
73. Liu Y., Ge B., Haitham A. R., Peng F. Z, " Control system design of battery-assisted quasi-Z-source inverter for grid-tie photovoltaic power generation", IEEE Trans. on Sustainable Energy, Vol.4, No.4, 2013, 994–1001.
74. Haitham A. R., Iqbal A., Ahmed SK. M., Peng F. Z., Li Y., Ge B, " Quasi-Z-source inverter-based photovoltaic generation system with maximum power tracking control using ANFIS", IEEE Trans. on Sustainable Energy, Vol.4, No.1, 2013, pp.11–20.
75. Liu Y., Ge B., Haitham A. R., Peng F. Z, " Modelling and controller design of quasi-Z-source inverter with batterybased photovoltaic power system", IET Power Electronics, Vol.7, No.7, 2014,pp.1665–1674.
76. Ge B., Haitham A. R., Peng F. Z., Lei Q., Almeida A. T. de, Ferreira F. J. T. E., Sun D., Liu Y, " An energy-stored quasi-Z-source inverter for application to photovoltaic power system", IEEE Trans. on Industrial Electronics, Vol. 60, No.10, 2013, pp. 4468–4481.

INDUCTION MOTOR: A NEW STATIC ODEL

Luis AROMATARIS Fabian RINAUDO Juan ALEMANY Marcos GALETTO
Universidad Nacional de Río Cuarto, Rio Cuarto (Cba), Argentina
Ruta 36 km 601, Phone: 543584676495, laromata@ing.unrc.edu.ar

Abstract: *Voltage stability in power system is largely determined by the characteristics of the load. In order to obtain reliable results in voltage stability, the load model must be represented as realistically as possible. The issue is even more challenging with static voltage stability techniques, because dynamic loads must be represented by static models. The commonly used static models are constant impedance, constant current, and constant power. A significant part of the load is made up of induction motors that are usually modeled as static constant power loads. Under variations of terminal voltage of the motor, this static model can approximately represent the active power, but it can commit major mistakes when representing the behavior of reactive power. Therefore, a new motor static model will be developed in this work.*

Key words: *Induction motor, Voltage Stability, Load model, Static Techniques*

1. Introduction

It has been widely recognized that electrical loads have a significant impact on dynamic performances of the wide area power system, and that accurate load models are highly important for power system dynamic simulation and analysis [1]. Hence their behavior has crucial impacts on power system dynamic behavior, especially voltage stability and voltage performance [2]. Specifically, voltage stability analysis and simulation results are greatly affected by the use of different load models [3, 8]. In order to obtain reliable results when studying this problem with numerical simulations, the chosen model to represent the load must represent behavior as realistically as possible. The need for accurate modeling of loads has risen as a result of a number of blackouts that have taken place worldwide [3]. The induction motor loads that are considered dynamic loads account for a great amount of electric loads, especially in large industries and air-conditioning of commercial and residential areas [4].

The modeling issue is even more challenging with static voltage stability techniques [14] because loads with dynamic behavior must be represented by static models. Static loads are represented by algebraic equations using an exponential model, which depends on the load terminal voltage. The commonly used models are referred to as: constant impedance, constant current, constant power, zip model or exponential model [9].

In conventional static voltage stability studies [6, 7, 10], constant impedance and constant current models are considered as allowing the simulation of a large amount of power system loads. Constant power may be reasonable for approximate static analysis when a significant proportion of the load is motors [11]. However, employing a static model for constant MVA loads can lead to erroneous and, often, misleading results [5]. Large motors can also be modeled by an exponential model in which the real power and the reactive power depend on voltage and frequency variation [11]. However, this model has proven not to be accurate in every case.

In this work, a new static model of the induction motor will be developed, and it will have a behavior closer to reality with respect to changes in variables of the network to which it is connected. Thus, a fourth-order algebraic equation system will be solved so as to obtain the motor slip and, from there, the reactive power consumed. To represent its behavior, a plotting method will be used, also proposed in this work. The method relates the power of the motor, the terminal voltage and the slip. This plotting method called non-conventional PV curves will be used in a case study. For the development of this model, data of the steady-state equivalent circuit of the motor is needed.

2. Static model of the induction motor

The static model of the induction motor proposed in this work can be used for any power electric system in which part of the demand consists in induction motors. However, in order to simplify the development of this topic, the work will be based on a small electric system, as shown in figure 1.

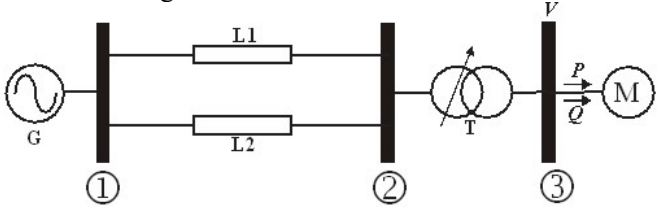

Figure 1. Small Power Systems

The synchronous generator G feeds a motor load M via two lines of transmission L1 and L2, and a transformer T. V is the terminal voltage of the motor, while P and Q are the active and the reactive power consumed by the motor. By calculating a conventional power flow (CPF), the base case for this electric system can be obtained. The data of P and Q are input data in the study of power flow, while the value of V corresponds to the output data.

To calculate the slip in those conditions, it is necessary to know the steady-state equivalent circuit parameters of the motor shown in figure 2.

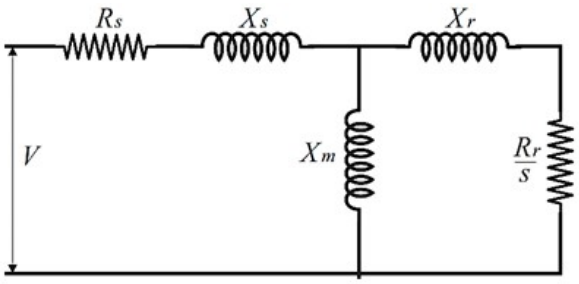

Figure 2. Induction motor equivalent circuit

Where:
R_s = Stator winding resistance
X_s = Inductive reactance of the stator winding
X_m = Magnetizing reactance
X_r = Rotor Reactance
R_r = Rotor Resistance
s = slip

With these parameters, the motor slip can be calculated by solving the following system of equations:

$$0 = a + b\,s + c\,s^2 + d\,s^3 + e\,s^4 \quad (1)$$

where the coefficients are the following:

$$a = P\,R_s^2 + P\,X_m^2 + 2P\,X_m X_s + P\,X_s^2 - R_s\,V^2 \quad (2)$$

$$b = 2P\,R_s\,X_m^2 - X_m^2\,V^2 \quad (3)$$

$$c = P\,X_m^4 + 2P\,R_s^2(X_r + X_m)^2 + 2P\,X_m^2 X_r(X_r + X_m) + 2P\,X_m X_s(X_r + X_m)^2 + 2P\,X_m X_r X_s(X_r + X_m) + 2P\,X_s^2(X_r + X_m)^2 - 2V^2 R_s\,(X_r + X_m)^2 \quad (4)$$

$$d = 2PR_s\,X_m^2(X_r + X_m)^2 - V^2 X_m^2(X_r + X_m)^2 \quad (5)$$

$$e = P\,(R_s^2(X_r + X_m)^4 + X_m^2\,X_r^2(X_r + X_m)^2 + 2\,X_m\,X_r\,X_s(X_r + X_m)^3 + X_s^2(X_r + X_m)^4 - V^2 R_s\,(X_r + X_m)^4 \quad (6)$$

The values of P and V in the equations (2) to (6) are the ones obtained in the base case, which is $P = P_{bc}$ and $V = V_{bc}$., when a subscript bc will be assigned for the base case.

The solution to the system of equations (1) to (6) results in four roots. Two of them are complex conjugate roots and have no physical meaning for this problem. The other two roots represent two possible motor slip values. The highest value represents the slip for a state of unstable balance, so it must be dismissed. The lowest value represents the slip for steady-state conditions, in this case, for the base case.

The value of reactive power used as input data in power flow should be confirmed by the following equations:

$$Z_r = \frac{R_r}{s} + iX_r \quad (7)$$

$$Z_m = \left(\frac{iX_m\,Z_r}{iX_m + Z_r}\right) + R_s + i\,X_s \quad (8)$$

$$Q_{bc} = \frac{imag(Z_m)\ |V|^2}{[real(Z_m)\,]^2 + [imag(Z_m)\,]^2} \quad (9)$$

where i is the imaginary unit, Z_r is the rotor impedance, and Z_m is the motor impedance. If the value of the Q_{bc} obtained matches input data, the next step can be followed; otherwise, input data should be corrected and the base case should be recalculated.

In sum, for the base case, the following variables that correspond to each motor load: P_{bc}, Q_{bc}, V_{bc}, and motor slip, s_{bc} are known.

Now, a fault will be produced on the electric system under study, causing a voltage drop in the network and at the motor terminals. This will produce changes in the active and the reactive power consumed. However, these changes in power will not be reflected in the power flow output applied to the faulty network. This must be corrected by the following equation:

$$P_{pf} = P_{bc}\,V_{pf}^{0.01} \quad (10)$$

where:
P_{pf} = Active power of the post-fault motor
V_{pf} = Terminal voltage of the post-fault motor

This empirical equation reflects the variations in active power of the induction motor when facing voltage variations.

With V_{pf} and P_{pf} values of each load, the new post-fault slip value s_{pf} can be calculated by equations 1 to 6. Then, the new value of reactive power consumed Q_{pf} can be calculated by equations 7 to 9. These equations should be inserted in the iterative process of the CPF, according to the flowchart that outlines the previously described process in figure 3. This modification in the CPF can be

part of a group of additional changes that model other network devices more in detail, so as to achieve a more realistic behavior in the face of problems with voltage stability when using static calculation techniques.

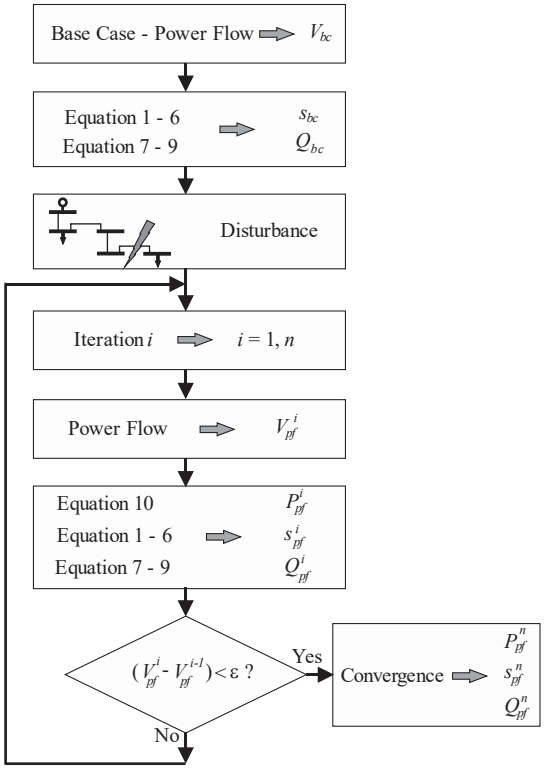

Fig. 3. Flowchart

3. Case study

The electric system shown in figure 4 will be analyzed as case study. The generator feeds a large induction motor via two transmission lines and one transformer. Furthermore, a capacitor bank is also connected to the load bus. The voltage and impedance values are indicated per unit.

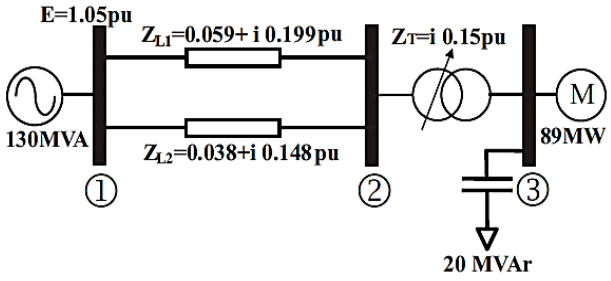

Figure 4. Small power systems

Figure 5 shows the equivalent circuit and the motor parameters expressed per unit.

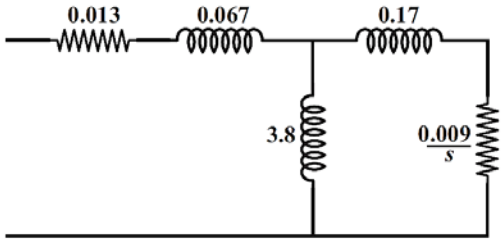

Figure 5. Induction motor parameters

The solution to the base case yields the following results related to the induction motor:

V_{3bc} = Terminal voltage = 1∠–11º
s_{bc} = Motor slip = 0.0088
P_{mbc} = Active power consumed = 89 MW
Q_{mbc} = Reactive power consumed = 45.5 MVAr

A perturbation consisting in disconnecting one of the transmission lines according to the following cases will be applied:

- Case 1: Disconnection without fault of transmission line Z_{L1}
- Case 2: Disconnection without fault of transmission line Z_{L2}

In order to solve the case study proposed, three different calculation techniques will be applied to compare the results obtained, according to the following detail:

a) Conventional static technique, in which the motor is modeled as a constant power load. This technique will be represented by PV curves that relate terminal voltage and the load active power with the factor of constant power.

b) Static technique proposed in this work: This technique will be represented by non-conventional PV curves that relate terminal voltage and the active power consumed by the motor when its slip varies.

c) Conventional dynamic technique, in which the motor is modeled by differential equations. The output curves show terminal voltage variations and the active power consumed versus time. Therefore, the program PSS/E V 32 by Siemens will be used.

3.1 Case 1.

In figure 6, conventional PV curves, load curves at constant pre-fault and post-fault impedance, and the line of *Pcte* = 0.89 pu are shown. The intersection of the pre-fault PV curves, *pre-fault Zcte* and the line of *Pcte* occurs at point A, which indicates a steady state point for the base case. After perturbation, the values move according

to the constant impedance curve until they intersect the post-fault PV curve at point B. Then, the power tends to recover its pre-fault values until it converges at point C. Here, a new steady state point is set at the following values:

$|V_{3pf}|$ = Terminal voltage = 0.9324 pu
P_{mpf} = Active power consumed = 0.89 pu

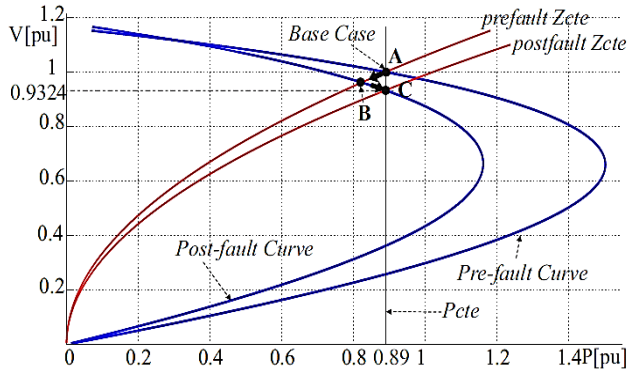

Figure 6. Case 1 conventional PV curve

Figure 7 plots the static technique proposed in this work. Pre-fault and post-fault non-conventional PV curves, constant slip curves, and the motor active power vs terminal voltage curve, obtained by equation 10, can be identified. Point A is the intersection of the pre-fault non-conventional PV curve, the constant slip curve of the base case, and the active power curve of equation 10. After perturbation, the values move according to the constant slip curve until they intersect the post-fault non-conventional PV curve at point B. Then, the power tends to recover its pre-fault values until it converges at point C. Here, a new steady state point is set at the following values:

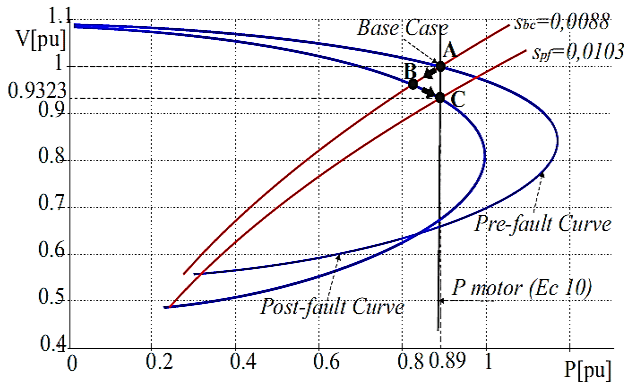

Figure 7. Case 1 non-conventional PV curve

$|V_{3pf}|$ = Terminal voltage = 0.9323 pu
P_{mpf} = Active power consumed = 0.89 pu
s_{pf} = Motor slip = 0.0103

Figure 8 plots the conventional dynamic technique. The output curves indicate the behavior of the terminal voltage and the active power consumed by the motor throughout time. Perturbation is applied to 1 s time. After some oscillations, the power and motor voltage are stabilized at the following values:

$|V_{3pf}|$ = Terminal voltage = 0.9323 pu
P_{mpf} = Active power consumed = 0.89 pu

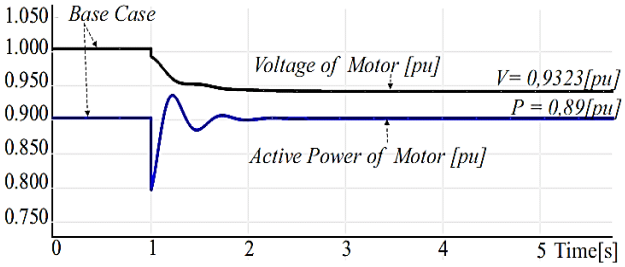

Figure 8. Case 1 Conventional dynamics

As it can be observed, all techniques applied lead to the conclusion that the system is stable, and that the voltage and power values are similar.

3.2 Case 2.

Figure 9 plots the conventional PV curves, load curves at constant pre-fault and post-fault impedance, and the line of *Pcte* = 0.89 pu are shown. The intersection of the pre-fault PV curves, pre-fault Zcte and the line of Pcte occurs at point A, which indicates a steady state point for the base case. After perturbation, the values move according to the constant impedance curve until they intersect the post-fault PV curve at point B. Then, the power tends to recover its pre-fault values until it converges at point C. Here, a new steady state point is set at the following values:

$|V_{3pf}|$ = Terminal voltage = 0.827 pu
P_{mpf} = Active power consumed = 0.89 pu

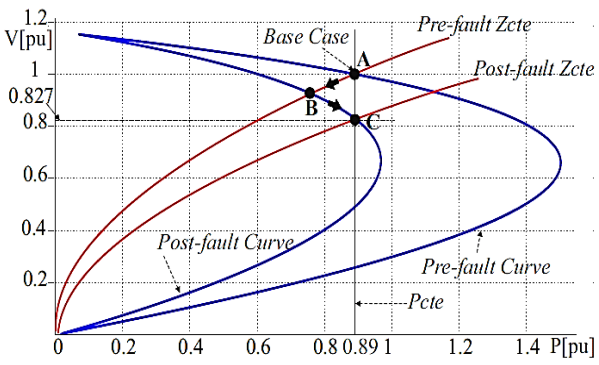

Figure 9. Case 2 conventional PV curve

Figure 10 plots the static technique proposed in this work. As in case 1, pre-fault and post-fault non-conventional PV curves, the constant slip curve, and the motor active power vs terminal voltage curve, obtained by equation 10, can be identified. Point A is the intersection of the pre-fault non-conventional PV curve, the constant slip curve of the base case, and the active power curve of equation 10. After perturbation, the values move according to the constant slip curve until they intersect the post-fault non-conventional PV curve at point B. Then, the power tends to recover its pre-fault values, but it does not converge, as there is no intersection of the post-fault curve and the *Pmotor* curve. Thus, the system loses voltage stability under these conditions.

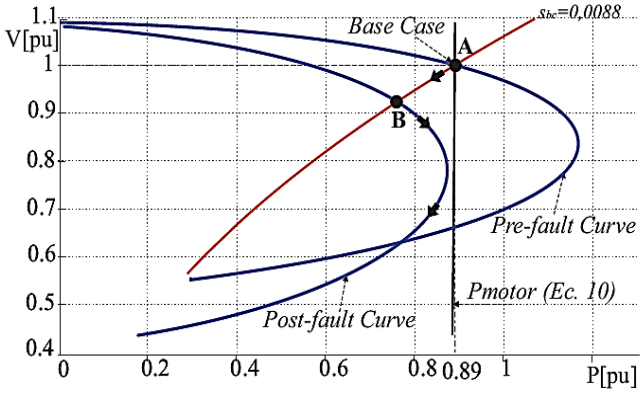

Figure 10. Case 2 non-conventional PV curve

Figure 11 plots the conventional dynamic technique for this case. The output curves indicate the behavior of the terminal voltage and the active power consumed by the motor throughout time. Perturbation is applied to 1 s time. It can be observed that, for this case, system voltage stability is lost because values collapse to unacceptable values.

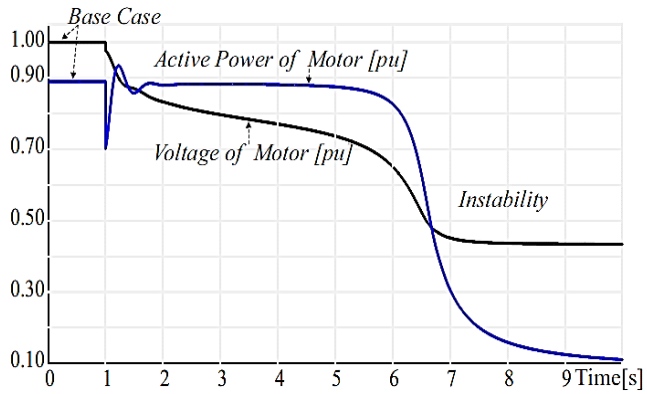

Figure 11. Case 2 Conventional dynamics

In table 1, the results obtained for voltage and post-fault active power for cases 1 and 2 are summarized.

Table 1

Case		PV Curve		Dynamic [pu]
		Conven-tional [pu]	Non-Conventional [pu]	
1	V_{3pf}	0.9324	0.9323	0.9323
	P_{mpf}	0.89	0.89	0.89
2	V_{3pf}	0.827	Non-convergence	Instability
	P_{mpf}	0.89	Non-convergence	Instability

4. Conclusions

We have shown a static model of induction motor which can be applied to any study of static voltage stability in order to improve the accuracy of results. The model proposed indicates a substantial improvement versus the conventional model, as it achieves results highly comparable to the ones obtained by dynamic techniques of calculation.

5. References

1 Ping Ju, Chuan, Qin, Feng Wu, Huiling Xie, Yan Ning: *Load modeling for wide area power system*. Electrical Power and Energy Systems 33 (2011) 909-917.

2 Hao Wu, Ian Dobson: *Cascading Stall of Many Induction*. IEEE Transactions on power systems, vol. 27, Nº4, November 2012.

3 González, E., Guizar, J. G.: *The Effect of Induction Motor Modeling in the context of voltage sensitive: combined loads*. IEEE Latin America Transactions, vol. 10, Nº. 4, June 2012

4 Mahmud, M.A., Hossain, M. J., Pota H., R.: *Effects of large dynamic loads on power system stability*. Electrical Power and Energy Systems 44 (2013) 357-363.

5 Yinhong Li, Hsiao-Dong Chiang, Byoung-Kon Choi, Yung-Tien Chen, Der-Hua Huang, Mark G. Lauby: *Load models for modeling dynamic behaviors of reactive loads: Evaluation and comparison*. Electrical Power and Energy Systems 30 (2008) 497-503.

6 Rajive Tiwari, K. R, Niazi, Vikas Gupta: *Line collapse proximity index for prediction of voltage collapse in power systems*. Electrical Power and Energy Systems 41 (2012) 105-111.

7 Mostafa Eidiani: *A reliable and efficient method for assessing voltage stability in transmission and distribution networks*. Electrical Power and Energy Systems 33 (2011) 453-456.

8 Borghettia, A., Caldonb, R., Nuccia. C. A.: *Generic dynamic load models in long-term voltage stability studies*. Electrical Power and Energy Systems 22 (2000) 291-301

9 Jiajia Song, Cotilla-Sanchez, Eduardo, Brekken, Ted K. A.: *Load Modeling Methodologies for Cascading Outage Simulation Considering Power System Stability*. 2013 1st IEEE Conference on Technologies for Sustainability (SusTech). 78-85.
10 Kundur, P.: *Power System Stability and Control*. McGraw-Hill.1994.
Taylor, C.: *Power System Voltage Stability*. McGraw-Hill.1994.
11 Machowski; J. Bialek; J Bumby. .J.:*Power System Dynamics Stability and Control*. Second Edition. Wiley, 2008.
12 Siemens, PSS/E 32.0.5, Manual
13 IEEE/GIGRE Joint Task Force on Stability Terms and Definitions. *Definition and Classification of Power System Stability*, IEEE Transaction of Power Systems, Vol 19, N.º 2, pp 1387-1401, May 2004.

6 Author names and affiliations

Luis Aromataris. Mechanical Electrical Engineer and Doctor of Engineering. Professor at the Electricity and Electronics Department of the School of Engineering at the National University of Rio Cuarto. Member of the Executive Committee of the Electric Power System Analysis Group (GASEP).

Fabian Rinaudo. Electrical Engineer. Candidate for Doctor of Engineering. Adscript Professor at the Electricity and Electronics Department of the School of Engineering at the National University of Rio Cuarto. Member of the Electric Power System Analysis Group (GASEP).

Juan Alemany. Electrical Engineer and Doctor of Engineering. Professor at the Electricity and Electronics Department of the School of Engineering at the National University of Rio Cuarto. Member of the Electric Power System Analysis Group (GASEP).

Marcos Galetto. Electrical Engineer. Professor at the Electricity and Electronics Department of the School of Engineering at the National University of Rio Cuarto. Member Electric Power System Analysis Group (GASEP).

A NOVEL IMPEDANCE SOURCE INVERTER TOPOLOGY WITH ACTIVE FRONT-END FOR AC DRIVES

D Bensiker Raja Singh
Department of Electrical Engineering, Satyam College of Engineering, Kanyakumari, Tamil Nadu.
Email: benzees003@gmail.com

SujaManimalar R
Department of Electrical Engineering, DMI College of Engineering, Chennai, Tamil Nadu.
Email: sujamonimalar@gmail.com

Abstract: *A unique impedance Source Inverter with an Active Front-End is proposed in this paper, that can be used for controlling AC Drives. There are a number of modulation schemes that may be used with the three-phase impedance source inverters, ultimate reduction in the switching losses makes the discontinuous modulation schemes seem most appropriate. The discontinuous modulation schemes are differentiated into two classes based on the technique used for achieving shoot-through (ST) state: single-phase-leg ST-based and three-phase-leg ST-based (3P) discontinuous modulation schemes. In this paper, we discuss the improvements in Single Phase Maximum Boost Discontinuous Space Vector modulation (1P/MB/DSVM) scheme under similar operating conditions, by simplifying gate signal generation and improving the conversion efficiency. A simulated analysis and comparison of the conventional and the enhanced 1P/MB/DSVM schemes is also discussed using PLECS. Lastly, verification of the simulation outcomes and reported analysis is carried out by making use of a three-phase quasi-Z-source inverter (qZSI) prototype which demonstrates improvement in conversion efficiency, utilizing the refined 1P/MB/DSVM scheme.*

Key words: *Impedance Source Inverter, Active-Front-End, Discontinuous Space Vector Modulation, Quasi-Z-Source inverter.*

I. INTRODUCTION

Interest in the renewable energy sources (RESs) has increased by many folds over the past few decades and they are now rapidly being incorporated into the power systems, stimulating an ongoing improvement in the power conditioning stage (PCS) with respect to the structures being used, their control schemes and modulation [1]–[4]. The boost converter-fed voltage source inverter (VSI) PCS, commonly known as the two-stage PCS, is essential in a few applications like fuel cells and photovoltaic (PV) devices, owing to the un-regulated output dc voltage [5]. A novel alternative to the common two-stage architecture is offered by the single-stage PCSs, demonstrated in the impedance source

Inverters [6]–[10]. The huge amount of attention being given to these impedance source inverters can be attributed to two elementary reasons. First, the acceptance of the boosting capability in the inversion operation, meaning that they can function as buck-boost inverters and second, they can use an additional switching state, the shoot-through (ST) state that does not necessitate dead-time generation. The shoot-through (ST) state is allowed in these kinds of power inverters because of the use of an impedance network existing between the inverter three-phase-leg ST-based (3P) modulation schemes, which achieves the shoot-through state by utilizing the three phase-legs simultaneously; single-phase-leg ST-based (1P) modulation schemes, where the shoot-through state is achieved by using one phase-leg at a time. Moreover , these categories use both the continuous and dis-continuous modulation schemes, however, the discontinuous modulation scheme is deemed more valuable because of the resulting improvement in switching losses [14].

This paper deals with the single-phase-leg discontinuous modulation schemes with maximum boost (MB) capacity [14]– [16], with the proposal of a much improved 1P/MB discontinuous space vector modulation (1P/MB/DSVM). In comparison with the conventional 1P/MB/DSVM scheme, the modified version has the following advantages:

Smooth and easy generation of the gate signals, i.e. reduction in implementation difficulty; the switches alternating at the ST current for a shorter time period during the fundamental period; reduction in switching losses and enhancement in conversion efficiency.

The rest of this paper follows the scheme as given: Section II discusses the general operation of the three-phase qZSI and studies its modulation using the traditional 1P/MB/DSVM scheme. Section III introduces the advanced 1P/MB/DSVM scheme and presents a comparison with the conventional scheme. For verification of the previously reported analysis, Section IV addresses the results obtained by simulation, along with the calculated switching

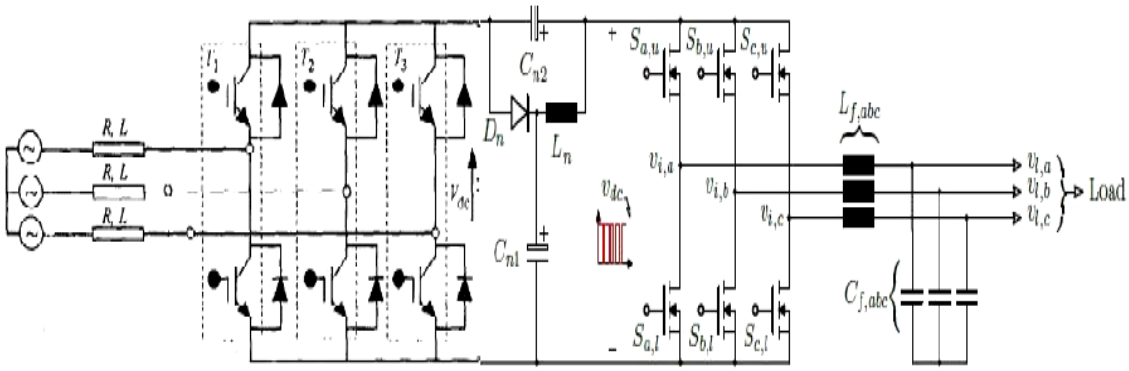

Fig. 1. Circuit diagram of the three-phase quasi-Z-source inverter (qZSI) with an output LC filter.

Losses, for the improved and the commonly used 1P/MB/DSVM schemes using PLECS. The experimental results obtained with a three-phase qZSI prototype are presented and discussed in Section V. The functionality of the modified 1P/MB/DSVM scheme is verified by these results and an improvement in conversion efficiency is demonstrated. Section VI deals with the conclusions drawn from the above results and discussion.

II. REVIEW OF THE THREE-PHASE QZSI OPERATION AND MODULATION

A. Operation of the Three-Phase qZSI

The three-phase qZSI shown in Fig. 1 uses an impedance network that consists of two inductors (2Ln) of exactly the same kind, a diode (Dn) and two capacitors (Cn1 and Cn2) between the input dc source (Vin) and the B6-bridge used [8]. This impedance network makes it possible to use an additional switching state, known as the shoot-through (ST) state, during which the B6-bridge acts as a short circuit as shown in Fig. 2(a).

This B6-bridge, however, functions as a current source in the non-ST states as shown in Fig. 2(b).

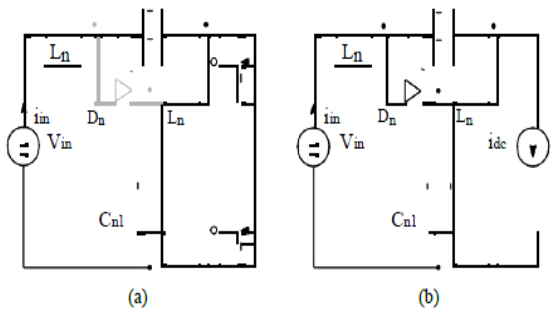

Fig. 2. Equivalent circuits of the qZSI during the ST and the non-ST states.

(a) During the ST state and the B6-bridge becomes equivalent to a short circuit; and (b) during the non-ST states and the B6-bridge becomes equivalent to a current source.

A discontinuous dc-link voltage (vdc) results from such use of the ST state that pulsates between zero and a peak value of v^dc during a continuous conduction mode of operation. The peak value (v^dc) is controlled by monitoring the ST state equivalent time. Another thing to be noted here is that this ST state has to be inserted within the zero states, i.e. the conventional zero states equivalent time is assigned partially or completely to the ST state so that it does not affect the active states and output voltage.

B. Modulation of the Three-Phase qZSI

The qZSI shown in Fig. 1 is modulated under any modulation scheme, to get a three-phase symmetrical output voltage. The output fundamental peak phase voltage is given by:

$$\hat{V}_{\varphi 1} = M \cdot \frac{\hat{v}_{dc}}{2}, \quad (1)$$

where M is the modulation index and v^dc is the peak dc-link voltage given by:

$$\hat{v}_{dc} = \frac{V_{in}}{1 - 2D_{ST}}, \quad (2)$$

Vin being the input dc voltage and DST is the average of the ST duty cycle (dST) that varies from one modulation scheme to another.

With the many different modulation schemes for modulation of qZSI have been mentioned, this paper

deals particularly with the conventionally used 1P/MB/DSVM scheme. The reference signals for said scheme are shown in Fig. 3. According to [14], [16], these reference signals are represented by:

$$v^*_{max,u} = v^*_{max}$$
$$v^*_{max,l} = v^*_{max},$$
$$v^*_{mid,u} = v^*_{mid},$$
$$v^*_{mid,l} = v^*_{mid} - d_{ST},$$
$$v^*_{min,u} = v^*_{min} - d_{ST},$$
$$v^*_{min,l} = v^*_{min} - 2d_{ST},$$

Where

$$v^*_{max} = max(v^*_a, v^*_b, v^*_c),$$
$$v^*_{mid} = mid(v^*_a, v^*_b, v^*_c),$$
$$v^*_{min} = min(v^*_a, v^*_b, v^*_c),$$
$$v^*_{max,u} = max(v^*_{a,u}, v^*_{b,u}, v^*_{c,u}),$$
$$v^*_{max,l} = max(v^*_{a,l}, v^*_{b,l}, v^*_{c,l}),$$
$$v^*_{mid,u} = mid(v^*_{a,u}, v^*_{b,u}, v^*_{c,u}),$$
$$v^*_{mid,l} = mid(v^*_{a,l}, v^*_{b,l}, v^*_{c,l}),$$
$$v^*_{min,u} = min(v^*_{a,u}, v^*_{b,u}, v^*_{c,u}),$$
$$v^*_{min,l} = min(v^*_{a,l}, v^*_{b,l}, v^*_{c,l}),$$

being v*a, v*b , and v*c are given by:

V*a = 1;

$$v^*_b = 1 - M \cdot \{\frac{3}{2}sin(\omega_1 t) - \frac{\sqrt{3}}{2}cos(\omega_1 t)\},$$
$$v^*_c = 1 - M \cdot \{\frac{3}{2}sin(\omega_1 t) + \frac{\sqrt{3}}{2}cos(\omega_1 t)\},$$

Finally, the ST duty cycle (dST) is variable during the fundamental period and it is given by:

$$d_{ST} = 1 - \frac{\sqrt{3}M}{2}sin(\omega_1 t + \frac{\pi}{6}), \quad (4)$$

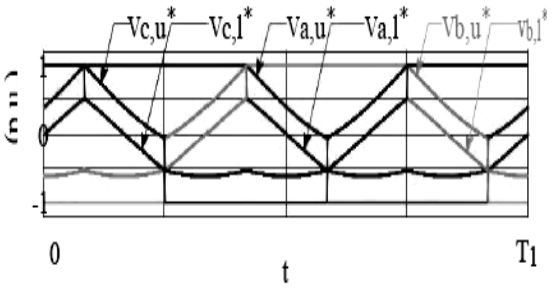

Fig. 3. Reference signals of the conventional single-phase-leg ST-based maximum boost discontinuous space vector modulation (1P/MB/DSVM) scheme, where the modulation index (M) is equal to 0:7 and T1 is the fundamental period. Note that for any phase-leg x, vx;u is used to modulate Sx;u, while vx;l is used to modulate Sx;l.

III. MODIFIED DSVM SCHEME

It can be concluded from the prior discussions that the conventional 1P/MB/DSVM scheme, as shown in Fig 3, has the difficulty in generating the gate signals due to the complex calculation of the reference signals; despite the fact that the ST state is being inserted three times during the course of each switching cycle, effective switching frequency of the impedance network changes between one to three times the carrier frequency. This is because of the variation of the active states equivalent time. Thus, the impedance network must be designed based on the lowest value of the effective switching frequency. In addition, to the following disadvantages, for the upper switches,commutation at ST current takes place for around two-thirds of the fundamental period. In order to overcome these disadvantages, this paper proposes a modified and enhanced 1P/MB/DSVM scheme as given in Fig. 4. The modified 1P/MB/DSVM scheme uses

three reference signals that are commonly used with the traditional three-phase VSIs as shown in Fig. 4, and are given by (4). The three-phase qZSI can be modulated as follows using the improved 1P/MB/DSVM scheme: for any phase-leg x, Sx;u is switched ON when v*x is larger than the carrier signal, while Sx;l switches ON when v is smaller than the carrier signal or is the smallest reference signal as shown in Fig. 4. Hence, the ST is attained through phase-leg x when vx is the smallest reference signal.

As a result of the improved 1P/MB/DSVM scheme, the lower switches never commutate at the

ST current, while the upper switches commutate at ST-current for one-third of the fundamental period. The impedance network effective switching frequency is fixed at the carrier frequency. Whereas, the modified modulation scheme the same variable ST duty cycle (dST) as the conventional scheme. Where, dST and its average (DST) are given by (5). So, Vin is related to V φ1 using the previous equations (1) and (2) for the conventional scheme (1P/MB/DSVM. To design the impedance network properly based on the improved 1P/MB/DSVM scheme, the process followed in [8] can be used here also.

The estimated value of inductor and capacitor can be found by:

$$L_n \approx \frac{\sqrt{3}M \cdot V_{in}}{70\pi(3\sqrt{3}M - \pi) \cdot f_1 \cdot \Delta I_L} + \frac{3\sqrt{3}M \cdot (\pi - 3\sqrt{3}M) \cdot V_{in}}{4(3\pi\sqrt{3}M - \pi^2) \cdot f_s \cdot \Delta I_L},$$

$$C_{n1} \approx \frac{\sqrt{3}M \cdot I_{in}}{35\pi^2 \cdot f_1 \cdot \Delta V_{C_{n1}}} + \frac{(2\pi - 3\sqrt{3}M) \cdot I_{in}}{2\pi f_s \cdot \Delta V_{C_{n1}}},$$

$$C_{n2} \approx \frac{\sqrt{3}M \cdot I_{in}}{35\pi^2 \cdot f_1 \cdot \Delta V_{C_{n2}}} + \frac{(2\pi - 3\sqrt{3}M) \cdot I_{in}}{2\pi f_s \cdot \Delta V_{C_{n2}}},$$

where fs is the switching frequency, Iin is the average input dc current, ΔIL is the peak-to-peak inductor current ripple, and ΔVCn1 and ΔVCn2 are the peak-to-peak capacitor voltage ripples across Cn1 and Cn2 respectively.

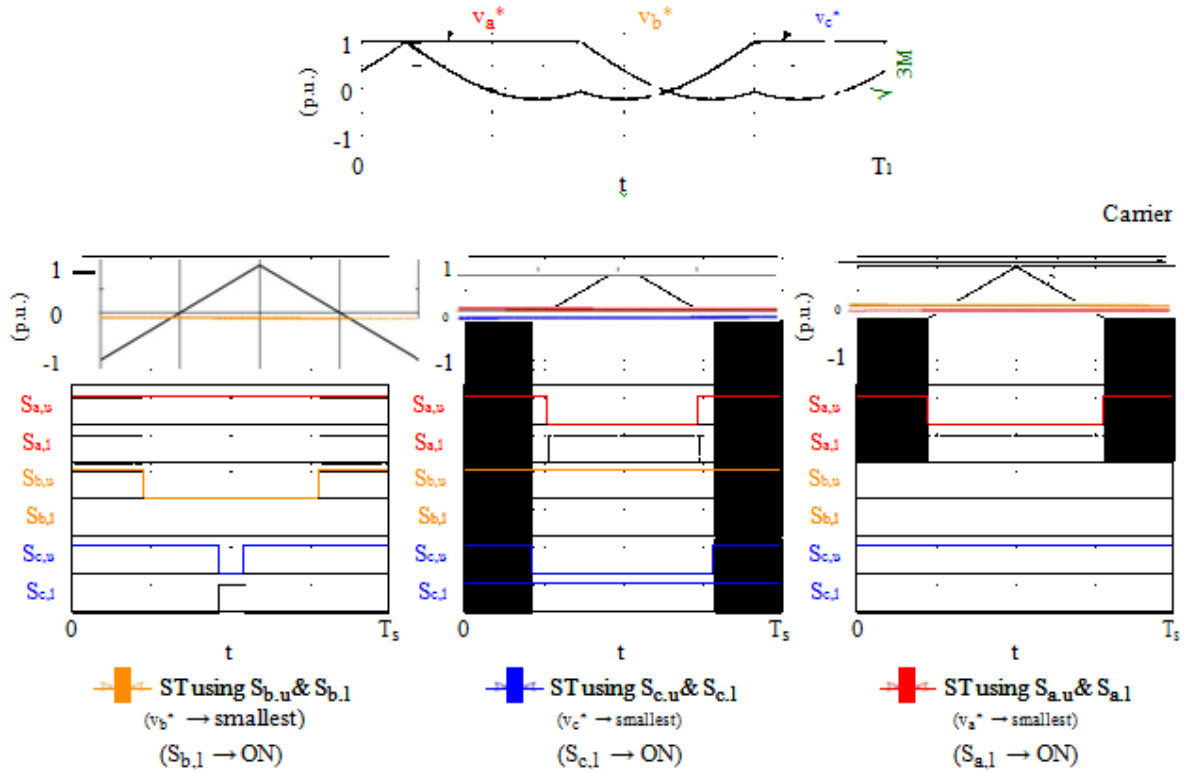

Fig. 4. Reference, carrier, and gate signals of the improved 1P/MB/DSVM scheme (M = 0-7):7. Note that Sa;lis ma

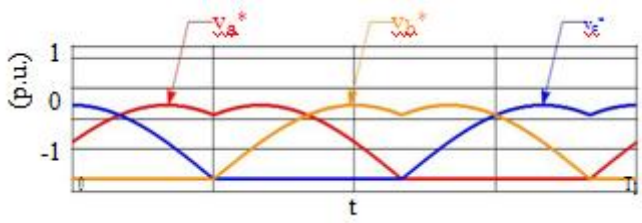

Fig. 5. Reference signals of the improved 1P/MB/DSVM scheme with negative dc clamping.

The fact that the improved 1P/MB/DSVM scheme is conceptually similar to the modulation scheme proposed in [11].Whereas, the modified version proposed in [11], is not an discontinuous one.

The DSVM scheme may be attained with positive dc clamping that is used in this paper, or by negative dc clamping [14]. Taking into account the reference signals of the modulated 1P/MB/DSVM scheme with negative dc clamping, this can be clarified. Fig. 5 showsthis scheme in which the three-phase qZSI is modulated as follows: for a phase-leg x, Sx;lis turned ON when vx is smaller than the carrier signal, while Sx;uis turned ON when Vx is larger than the carrier.

Table 1
Comparison between the Conventional and the Improved DSVM schemes

	Conventional	**Modified**
Ref. signals	Fig. 3	Fig. 4
Num. of ref. signals	6	3
Complexity	High	Low
Sabc;unormalized ST duration (TST;u/T1)	2/3	1/3
$S_{abc;l}$ normalized STduration ($T_{ST;l}=T_1$)	1/3	0

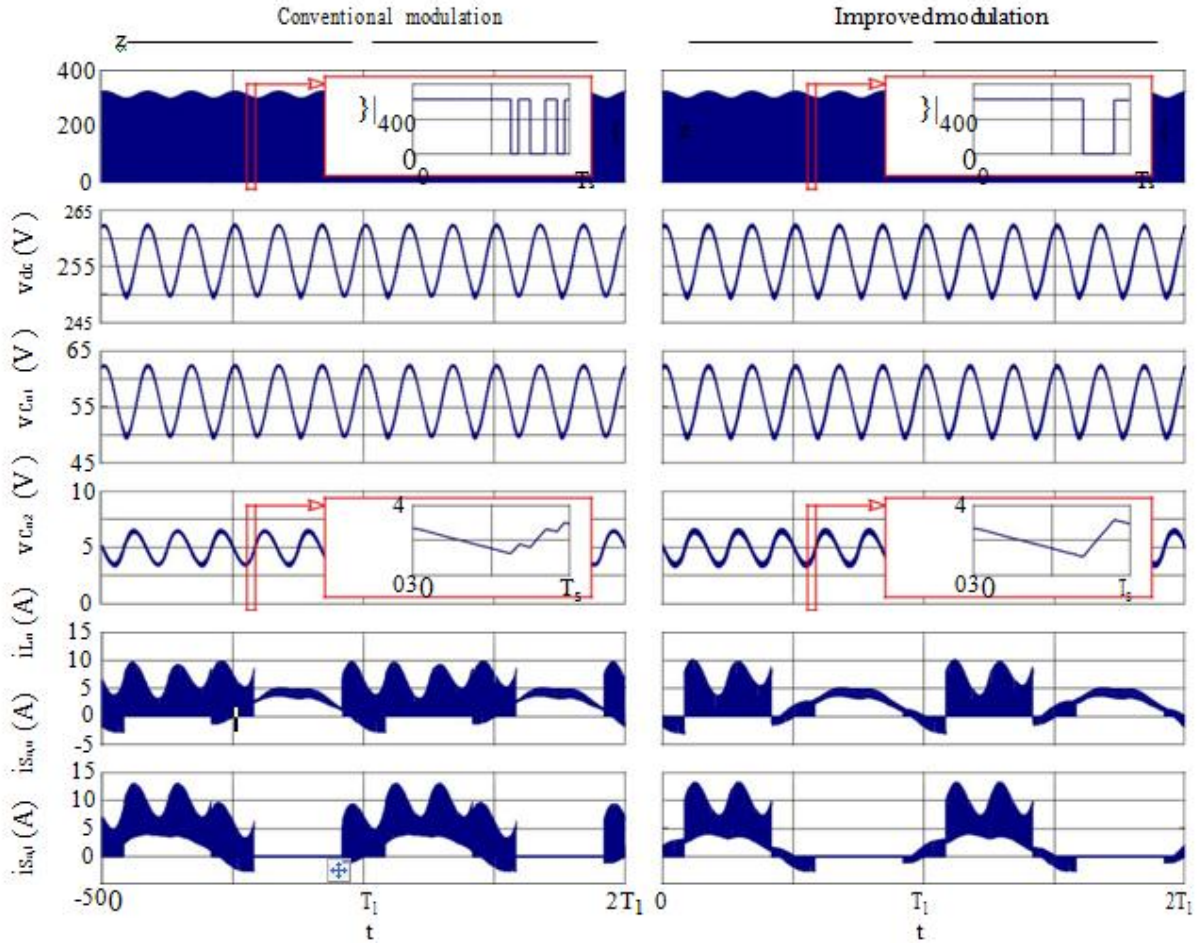

Fig. 6. Simulation results of the 1 kVA qZSI using the conventional and the improved 1P/MB/DSVM schemes. For each modulation scheme, the dc-link voltage (vdc), impedance network capacitors voltages (v Cn1 and vCn2), impedance network inductor current (iLn), and upper and lower switches currents of phase a (iSa;u and iSa;l) are shown from top to bottom.

Table 2
Simulation Parameters (1000 VA Three-Phase QZSI)

Vin	200 V	V'_1	110 V (RMS)	M	0:8564
f_s	60 kHz	L_n	1:6 mH	Cn1;2	20 F
f_1	200 Hz	Lf;abc	0:35 mH	Cf;abc	4:7 F

v_x is greater than the carrier signal, or is the largest reference signal,.

A. Comparative Study

Table I presents a comparison of both schemes from various different aspects, including number of reference signals, , normalized peak dc-link voltage (v^dc=Vin), ST duty cycle (dST) variation, average ST duty cycle (DST), implemen-tation complexity, normalized ST duration for the upper switches (TST;u=T1) normalized output fundamental peak phase voltage (V'1=Vin) and and normalized ST duration for the lower switches (TST;l=T1). It highlights and summarizes the complete difference between the conventional and improved scheme.

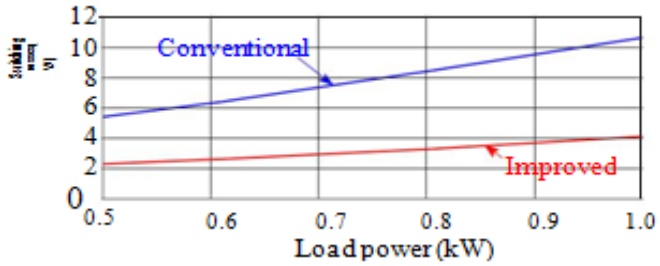

Fig. 7. Simulated total switching losses of the B6-bridge using PLECS for both the conventional and the improved 1P/MB/DSVM schemes. Note that the utilized switch model is C2M0025120D from CREE.

Table Imakes it evident that the improved 1P/MB/DSVM scheme does in-fact enhance the performance of the three-phase qZSI, which is attributed to the smaller ST duration of the various switches, reducing the overall switching losses for the same point of operation.

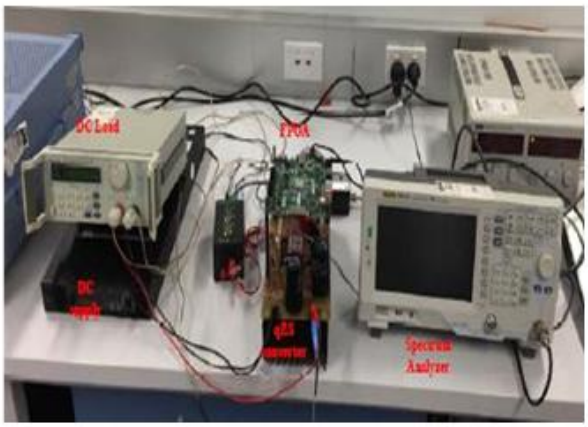

Fig. 8. Experimental prototype of the three-phase ZSI with an output LC filter.

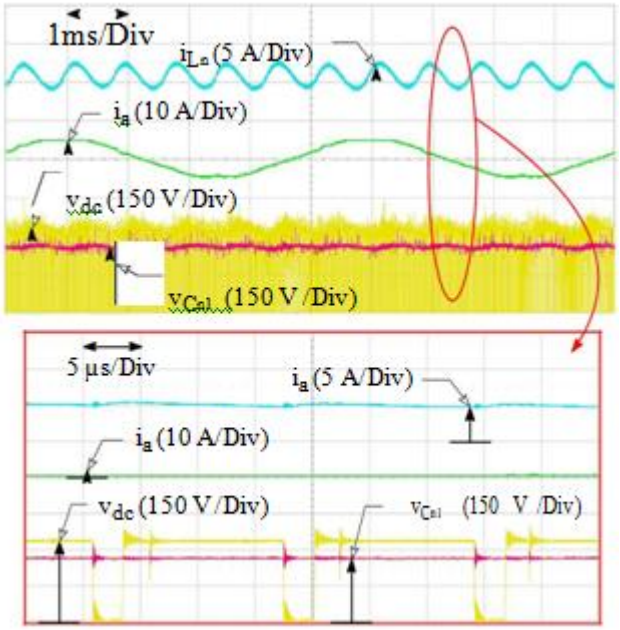

Fig. 9. Obtained experimental results using the proposed modulation scheme using a resistive load of 1 kW, where the dc-link voltage (vinv), voltage across Cn1 (vCn1), inductor current (iLn), and load current (ia) are shown with a zoom for three switching cycles.

IV. SIMULATION RESULTS

For verification of the previous analysis and discussions, a 1 kVA qZSI, the parameters of which are enlisted in Table II, was simulated using PLECS. A resistive load (Rl) was fed by this qZSI via an LC filter as depicted in Fig. 1. The value of M was set to 0:8564 toget a fundamental RMS output phase voltage (V'1) equivalent to 110 V .

Fig. 6 depicts the simulation based data results using both the conventional and the improved 1P-ST/MB/DSVM schemes,

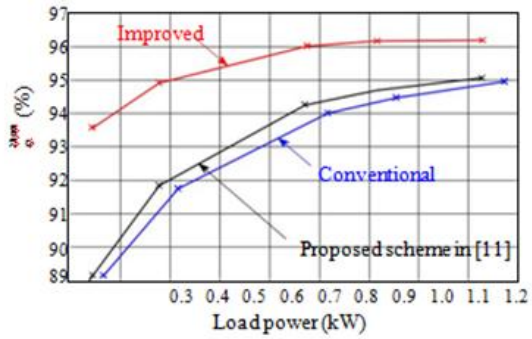

Fig. 10. Measured experimental efficiency of the three-phase qZSI for the conventional and the improved
1P/MB/DSVM schemes, and the introduced modulation scheme in [11].

where theimpedance network inductor current, dc-link voltage (vdc), impedance network capacitors voltages (vCn1 and vCn2),

(iLn), as well asupper and lower switch currents of phase a (iSa;u and iSa;l) are shown for both schemes.

The prior analysis is confirmed by these results and the effective functionality of the proposed modulation scheme is supported. Studying the difference in resulted for both kinds of schemes (Fig. 6) shows that the modified 1P/MB/DSVM scheme works the same way as the conventional 1P/MB/DSVM scheme with an overall improvement in performance.

This performance improvement can be attributed to the simplicity of the different switches and the reduction in commutationperiods at the ST current, which is evident from the represented switch currents(iSa;u and iSa;l) in Fig. 6. Additionally, it is evident from thethe inductor current (iLn)and dc-link voltage (vinv) using both schemes, that effective switching frequency for the1P/MB/DSVM scheme commonly in practice varies between one to three times the frequency of the carrier, while for the modified 1P/MB/DSVM scheme it remains constant and it is equivalent to the carrier frequency.

Finally, the switching losses have been calculated using PLECS for both modulation schemes at different load con-ditions, where the obtained results are shown in Fig. 7. This figure, i.e. Fig. 7, shows that the switching losses under the improved scheme has been significantly reduced due to the shorter periods of commutation at the ST current.

V. EXPERIMENTAL RESULTS

Verification of the improved 1P/MB/DSVM schemefunctionality was carried out using a three-phase ZSI prototype, shown in Fig. 8. The prototype parameters are as listed in Table II.

The prototype was tested at 1 kW using the modified 1P/MB/DSVM scheme and the recorded results are shown in Fig. 9, in which the inductor current (iLn), dc-link voltage (vdc), voltage across Cn1 (vCn1), and load current (ia) are shown along with a zoom for three switching cycles. These results validates the functionality of the modified 1P/MB/DSVM scheme and verify the given simulation results.

The conversion efficiency of the three-phase ZSI prototype was measured under both the conventional and modified 1P/MB/DSVM schemes, using a KinetiQ PPA5530 power analyser and the measurements obtained are shown in Fig. 10. This figureconfirms the advantage of enhancing the converter efficiency due to the shorter commutation period at the ST current. Moreover, the conversion efficiency under the introduced improved modulation scheme in [11] was measured and showed in Fig. 10, which shows that the improved 1P/MB/DSVM scheme exhibits higher efficiency owing to the smaller voltage stresses of the MB as well as the discontinuity of the modulating the switches. This prototype was based on a CCS050M12CM2 SiC power module and a C4D40120D SiC diode from CREE.

VI. CONCLUSION

This paper introduces a unique Z-Source with active front-End, that is validated by simulation and experimental setup.

The conventional (1P/MB/DSVM) scheme has been studied and improved upon to increase the conversion efficiency andenhance the performance of the three-phase impedance source inverters. The improved 1P/MB/DSVM scheme has the following benefits over the conventional scheme: easier to implementbecause it uses three reference signals, the switches commutatefor shorter period at the ST current during the fundamental period, thereby achieving reduced switching losses and consequently better efficiency.

The modified 1P/MB/DSVM scheme has been introduced and analyzed in compared to the conventional scheme. The switching losses werecalculated using PLECS for both kinds of schemes, with the modified scheme exhibiting an effective reduction inswitching losses. Finally, experimental results verify the reported analysis by making use of a three-phase quasi-Z-source inverter (qZSI) prototype, and the results showed an increase in the conversion efficiency with the usage of the improved 1P/MB/DSVM scheme under the same operating conditions.

References

[1] F. Blaabjerg, K. Ma, and Y. Yang, "Power electronics - the key Technologyfor renewable energy systems," in Ninth Int. Conf. on EcologicalVehicles and Renewable Energies (EVER), Mar. 2014, pp. 1–11.

[2] F. Blaabjerg, Y. Yang, D. Yang, and X. Wang, "Distributed powergenerationsystems and protection," Proc. of the IEEE, vol. 105, no. 7,pp. 1311–1331, July 2017.

[3] Abdelhakim, P. Mattavelli, D. Yang, and F. Blaabjerg, "Coupledinductor-based dc current measurement technique for transformerlessgrid-tied inverters," IEEE Trans. on Power Electron., vol. 33, no. 1, pp.18–23, Jan 2018.

[4] Abdelhakim, P. Mattavelli, V. Boscaino, and G. Lullo, "Decoupledcontrol scheme of grid-connected split-source inverters," IEEE Trans.on Ind. Electron., vol. 64, no. 8, pp. 6202–6211, Aug 2017.

[5] J. M. Carrasco, L. G. Franquelo, J. T. Bialasiewicz, E. Galvan, R. C.PortilloGuisado, M. A. M. Prats, J. I. Leon, and N. Moreno-Alfonso,"Power-electronic systems for the grid integration of renewable energysources: A survey," IEEE Trans. on Ind. Electron., vol. 53, no. 4, pp.1002–1016, June 2006.

[6] Abdelhakim, P. Mattavelli, and G. Spiazzi, "Three-phase splitsourceinverter (ssi): Analysis and modulation," IEEE Trans. on PowerElectron., vol. 31, no. 11, pp. 7451–7461, Nov. 2016.

[7] Abdelhakim, P. Davari, F. Blaabjerg, and P. Mattavelli, "Switchingloss reduction in the three-phase quasi-z-source inverters utilizingmodified space vector modulation strategies," IEEE Trans. on PowerElectron., vol. PP, no. 99, pp. 1–1, 2017.

[8] M. Shen, A. Joseph, J. Wang, F. Z. Peng, and D. J. Adams, "Comparisonof traditional inverters and z - source inverter for fuel cell vehicles," IEEETrans. on Power Electron., vol. 22, no. 4, pp. 1453–1463, July 2007.

[9] Abdelhakim, P. Mattavelli, P. Davari, and F. Blaabjerg, "Performanceevaluation of the single-phase split-source inverter using an alternativedc-ac configuration," IEEE Trans. on Ind. Electron., vol. PP, no. 99, pp.1–1, 2017.

[10] Abdelhakim, P. Davari, F. Blaabjerg, and P. Mattavelli, "An improvedmodulation strategy for the three-phase z-source inverters (zsis)," inIEEE Energy Conv. Cong. and Expo. (ECCE), Oct 2017, pp. 4237–4243.

[11] M. Zdanowski, D. Peftitsis, S. Piasecki, and J. Rabkowski, "On thedesign process of a 6-kva quasi-z-inverter employing sic power devices,"IEEE Trans. on Power Electron., vol. 31, no. 11, pp. 7499–7508, Nov2016.

[12] Y. P. Siwakoti, F. Z. Peng, F. Blaabjerg, P. C. Loh, G. E. Town, andS. Yang, "Impedance-source networks for electric power conversion partii: Review of control and modulation techniques," IEEE Trans. on PowerElectron., vol. 30, no. 4, pp. 1887–1906, April 2015.

[13] P. C. Loh, D. M. Vilathgamuwa, Y. S. Lai, G. T. Chua, and Y. Li,"Pulse-width modulation of z-source inverters," IEEE Trans. on PowerElectron., vol. 20, no. 6, pp. 1346–1355, Nov. 2005.

[14] F. Z. Peng, M. Shen, and Z. Qian, "Maximum boost control of the z-sourceinverter," IEEE Trans. on Power Electron., vol. 20, no. 4, pp.833–838, July 2005.

[15] Y. Zhang, J. Liu, X. Li, X. Ma, S. Zhou, H. Wang, and Y. Liu,"An improved pwm strategy for z-source inverter with maximum boostcapability and minimum switching frequency," IEEE Trans. on PowerElectron., vol. PP, no. 99, pp. 1–1, 2017.

Proportional Resonant Controlled Interleaved CUK Converter Space Vector Modulated Inverterfed Induction Motor Drive System with Improved Torque Response

T.ArunSrinivas
Research Scholar, Faculty of Electrical Engineering, Anna University, Chennai, India
Email: arunsrinivas1984@gmail.com

G.Themozhi
Professor, Department of Electronics and Communication Engineering, Tagore Engineering College, Chennai, India

Abstract *This work presents the simulation and application of a Proportional Resonant (PR) controlled Interleaved Cuk Converter Inverter fed Induction Motor Drive (ICCIIMD) system. This work recommends Photo Voltaic (PV) fed interleaved cuk converter to fabricate essential DC voltage in the input of the inverter. The output of the PV system is boosted utilizing an interleaved cuk converter. The output of the interleaved cuk converter is inverted and fed to a three phase induction motor. Closed loop PR controlled ICCIIMD system is simulated and the torque ripple along with time domain parameters are* ***compared*** *with a Proportional Integral (PI) controlled ICCIIMD system. The hardware is contrived and the investigational outcomes are related with the simulation outcomes. The PR controlled drive system has benefits like decreased torque ripple and enhanced time domain response.*

Keywords: *Interleaved Cuk Converter, Photo Voltaic System, Proportional Resonant Control, Torque Ripple and Voltage Source Inverter.*

I. INTRODUCTION

Solar Photo Voltaic (SPV) System is the most preferred power supply system in recent years due to the increasing price of non-renewable resources like hydrocarbon. Industries largely prefer SPV system to sustain their development by meeting the increase in energy demand.Farming sector prefers induction motors as they are rugged, reliable and relatively inexpensive when compared to synchronous motors and direct current motors.The speed of the motor can be controlled as per the mechanical load demand by using power electronic circuits and control systems. Apart from effectively controlling the speed of the motor, power electronic circuits can also improve the motor's dynamic and steady state characteristics.

A voltage controlled cuk converter based Permanent Magnet Brush Less DC (PMBLDC) drive for air conditioners is given by Singh.The paper [1] manages a cuk dc-dc converter as a solitary stage control power factorrectification converter for a PMBLDC motor sustained through a diode connect rectifier from a solitary stage air conditioning mains. A three stage voltage source inverter is used as an electronic commutator to work the motor driving aeration and cooling system compressor. The speed of the compressor is controlled to accomplish ideal ventilating utilizing an idea of the voltage control at dc connects corresponding to the coveted speed of the PMBLDCM [1].

A bridgeless cuk converter based induction motor drive for PFC applications is presented by Raichel. Another bridgeless topology for power factor adjustment is proposed here. Acceptance engine drives are usually used in mechanical areas on account of their high effectiveness, unwavering quality, yield and so on. They are considered as the significant Prime movers and devour around 70% to 80% of the aggregate power. Thus these drives confront numerous Problems identified with control quality and power factor. The principle reason is the input rectifier bridge. An induction motor drive designed using a new bridgeless topology is used for power factor correction [2].

Hardware of a dual half bridge chopper is implemented and compared with its simulation performance. The bidirectional chopper uses Field Programmable Gate Array (FPGA) based switching control scheme for Zero Voltage Switching (ZVS)[3].

An active snubber circuit is used with a converter to achieve soft switching. It also limits the voltage stress across power switches. The primary windings of two transformers are connected in series in the converter.Current stress on the secondary winding of the transformer is reduced by connecting two half wave rectifiers in parallel [4].

Different topologies of regulators are proposed and compared for power factor correction. Less number of power semiconductor switching devices in the current path and the absence of diode bridge can result in less conduction losses with improved thermal management [5]. Low voltage outputs of ac to dc converter can be managed using a bridgeless boost regulator. Both positive and negative halves of input ac voltage can be conditioned using a topology with boost and buck boost regulator [6].

High power factor can be obtained from a

modified version of a single ended primary inductance converter (SEPIC). High gain at low voltage can be obtained from a SEPIC by applying a voltage multiplier technique. A regenerative snubber can be used for soft commutation and the losses during reverse recovery can be reduced [7].

A cuk converter with SEPIC can be used for power factor correction.Power factor value close to unity can be obtained during discontinuous conduction mode using the combination of cuk regulator and SEPIC [8].

A cuk converter can be used to regulate the dc voltage from solar photo voltaic array and can be inverted to ac using a voltage source inverter (VSI). Maximum power point tracking (MPPT) technique like incremental conductance can be used to extract maximum power from the PV array. A dc link capacitor is designed based on new approach to power a motor used for water pumping application [9]. Torque ripple of a brush less dc motor is compensated by a cuk regulator using ARDUINO [10].

The characteristic of switched reluctance motor which is used in commercial application is improved by reducing the torque ripple content[11]. A single switch cuk regulator is designed and analyzed for lowpower battery charging application[12].A dc to dc converter based on SEPIC topology with increased input range is designed for fuel cell power inversion [13].

The total harmonic distortion (THD) of input current of a rectifier used in power factor correction can be reduced using a cuk converter topology[14].A BLDC motor used in water pumping application is powered using solar PV array and the power is modulated by employing a Zeta Converter [15].

SEPIC Converter is designed for improving power factor in an induction heating system [16]. Torque ripple of a BLDC motor drive fed from solar PV array is reduced using SEPIC converter. This improves the life time of the dc link capacitor used at the input side[17]. SEPIC with a modified topology is proposed for improving power conversion efficiency[18].

The control switch of a boost regulator is replaced by a VSI bridge network to obtain a hybrid converter that provides both dc and ac as output. The hybrid converters require lesser number of switches to provide either dc or ac output. The circuit has a higher reliability due to the inherent shoottthrough protection in the inversion stage [19]. Synchronous reference frame based control ofboost inverter is used in nano-grid applications [20]. Integration control is performed by instantaneous current monitoring in a class D seriesresonant converter [21].

II. RESEARCH GAP

The above literature does not discuss about interleaved cuk converter inverter fed induction motor drive with PR controller. This investigation suggests a PV fed interleaved cuk converter with a PR controller forfeeding an induction motor through a VSI to reduce torque ripples. The speed of Interleaved Cuk Converter Inverter Fed Induction Motor Drive (ICCIIMD) is regulated using PR Controller.

IEC 61000-3-2 emphasizes low harmonic contents and near unity power factor current to be drawn from AC mains by low power motors. Therefore reduction of torque ripple is inevitable for an IMD.The objective of this work is to reduce the torque ripple and moderatethe power supplied to the drive to control its speed. The purpose of this work is also to upgrade the time reaction of ICCIIM drive framework utilizing PR controller. DC from the yield of PV is regulated using an interleaved cuk converter. The dc yield of the interleaved cuk converter is associated with the space vector modulated inverter through a dc interface. The VSI is used to control the speed of the drive by varying the ac voltage. The dc voltage of the interleaved cuk converter is controlled by using PR controller to reduce the torque ripple. The Block diagram of the existing system is shown in Figure 1.

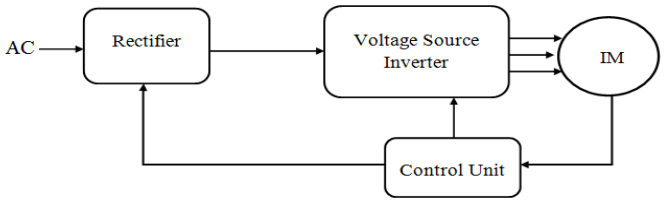

Fig.1 Block Diagram of theConventional System

In the conventional system the AC supply from the grid is rectified to DC using a rectifier the output of which is in turn converted into a controllable AC using a Voltage Source Inverter and then fed to an induction motor. The speed of the motor is controlled by the control unit using pulse width modulation. TheBlock Diagram of Interleaved Cuk Converter Fed IM Drive is shown in Figure.2.

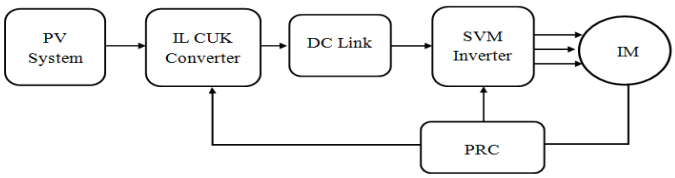

Fig2. Block Diagram of Interleaved Cuk Converter Inverter Fed Induction Motor Drive (ICCIIMD) System

DC from the yield of PV is assisted utilizing aninterleaved cuk converter. The DC yield of the interleaved cuk converter is connected to the VSI through a dc interface. The VSI is then used to control the speed of the drive by varying the ac voltage. The dc voltage of the interleaved cuk converter is controlled by utilizing proportional resonant control to lessen the torque ripple.

Analysis of Proportional Resonant controlled

Interleaved Cuk Converter Inverter fed Induction Motor Drive System

Expression for determining values of inductor and capacitor of cuk converter are as follows

$$L = \frac{V_i\ D}{f\ \Delta I} \quad ---------(1)$$

$$C = \frac{I_o\ D}{f\ \Delta V} \quad ---------(2)$$

Inverter output voltage is given by the following expression

$$V_o = 0.81\ V_d \quad ------(3)$$

In the above expressions V_i, I_o, D and $V_d$are input voltage of cuk converter, output current, duty cycle and dc link voltage respectively. The model of PR controller was developed from fractional differentiation. The response with PR is faster than that of the corresponding PI controlled system. The transfer function of an PR controller takes the form of

$$TF = K_1 + K_r\ w\ /\ (S^2 + w^2)$$

The closed loop control of ICCIIMD is done by regulating load voltage. The actual voltage is measured and compared with reference value. The obtained error signal 'e' and change of error 'ce' are taken as input to the PR controller. From the controller the PWM gating signals are generated by comparing actual and reference signals.

III. SPEED CONTROL SCHEME OF INDUCTION MOTOR

The interconnected structure of the source (Solar Panels), interleaved cuk converter, voltage source inverter and induction motor are shown in Figure 3. The output capacitor and inductor in the interleaved cuk converter act as filter circuit claiming only the dc component and straining the ac component. Here Metal Oxide Semiconductor Field Effect Transistor (MOSFET) is utilized as the switching device for greater switching frequency. The cuk converter can be used in both buck and boost operations. The output-voltage and current can both be simultaneously boosted. The output voltage has a reverse polarity when associated to the input voltage. Hence the terminals are reversed before connecting to the inverter.

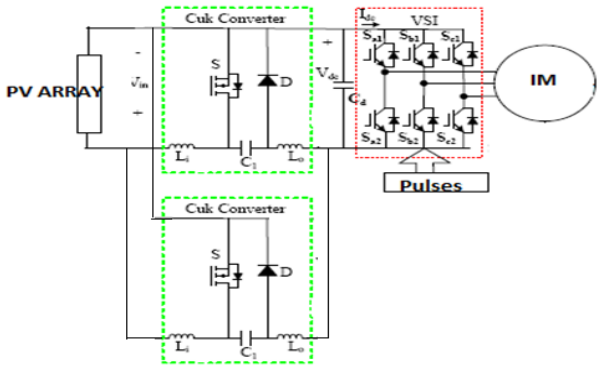

Fig.3 Circuit Diagram of Interleaved Cuk Converter Inverter fed IM Drive (ICCIIMD)

An interleaved cuk type dc to dc converter regulates the dc link voltage depending on the dutyratio (D) of the converter. For rapid and efficient regulation with decreased dimension of magnetic and filters, a greater switchingfrequency is utilized; equally, the switching frequency (f_s) is restricted by the switching device utilized, functioning powerlevel and switchinglosses of the device.

IV. SIMULATION RESULTS

TheICCIIMD system is modeled and simulated using Matlab in open loop and closed loop with PID and PR controllers.

V. Open-loop controlled ICCIIMD system

The open-loop controlled ICCIIMD system with change in insolation is experimented. Two cuk converters are connected in parallel to improve the current proficiency by maintaining the same voltage. The DC input voltage increases because of the variation in the insolation. The input voltage is increased from 150 volts to 175 volts as appeared in Figure5. The output-voltage of the interleaved cuk converter similarly increases from 500 to 520 volts as appeared in Figure6. The speed-response is appeared in Figure7 and the speed subsides at 1380 rpm. The torque-response is appeared in Figure8 and it becomes constant at 0.5Nm. The output voltage of cuk converter increases due to increase in input voltage. The driver pulses applied to the switches M1, M3 and M5 of voltage source inverter are shown in Figure 9.

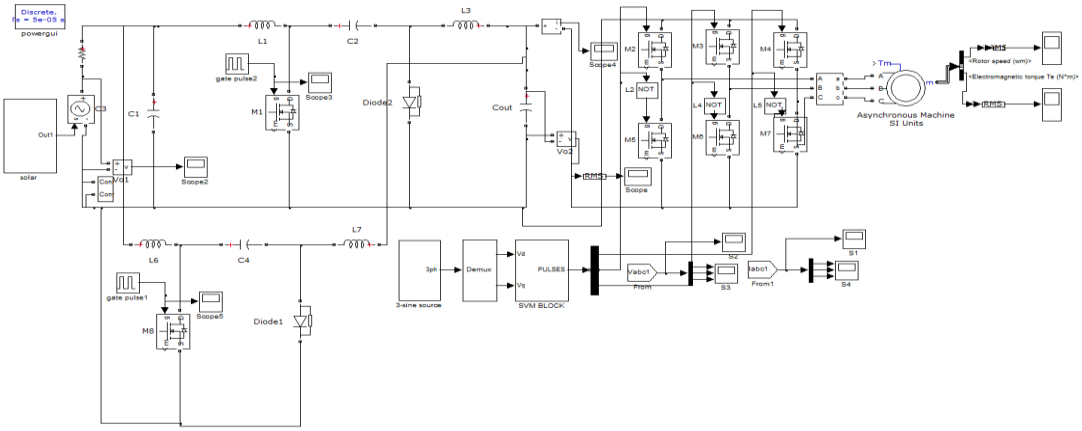

Fig.4 Open loop ICCIIMD system with Measureing Devices

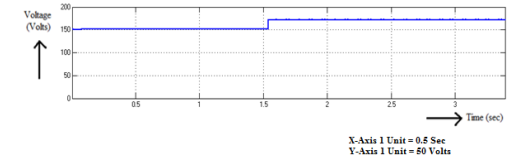

Fig.5 Input Voltage to the interleaved cuk converter in open loop ICCIIMD system

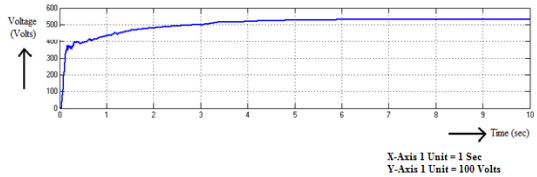

Fig.6 Output voltage of the interleaved cuk converter in open loop ICCIIMD system

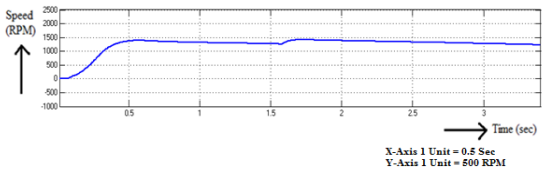

Fig.7 Speed response of the open loop ICCIIMD system

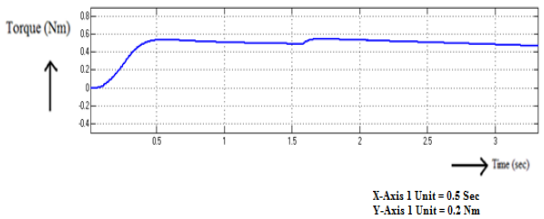

Fig.8 Torque Developed by the open loop ICCIIMD system

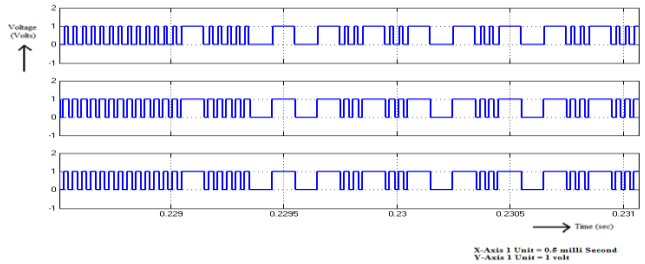

Fig.9 Pulses applied to theswitches M1, M3 & M5 of VSI in ICCIIMD system

VI. CLOSED-LOOP CONTROLLED ICCIIMD SYSTEM WITH PI CONTROLLER

The schematic diagram of the closed loop PI-controlled technique is appeared in Figure 10.The parameters for K_p and K_i used for simulation are K_p = 0.18 and K_i = 4.5. The output-voltage of interleaved cuk converter is related with a reference voltage. The flaw is pragmatic to the comparator across a PI-controller. The output of comparator updates the pulse width applied to interleavedcuk converter. The variation in inputvoltage is appeared in Figure11. The speed response along with its detailed viewand the torque response are appeared in Figures 12, Figure 13 and Figure 14 respectively. The speed inhabits at 1245 rpm. The torque restores at 0.5 Nm . Staring torque is higher due to the increased starting current.

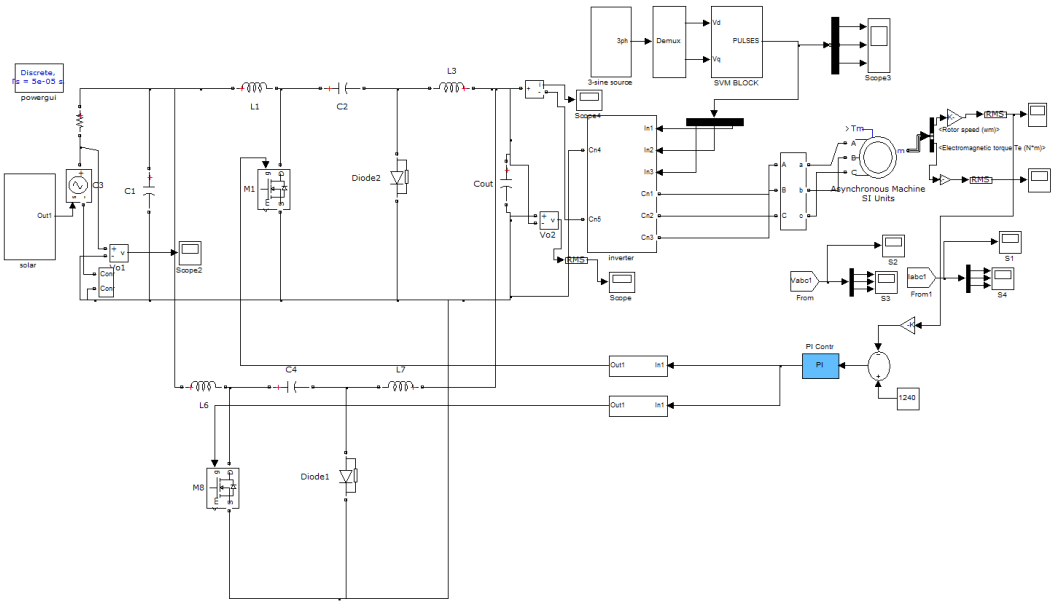

Fig.10 Closed loop PI controlled ICCIIMD system

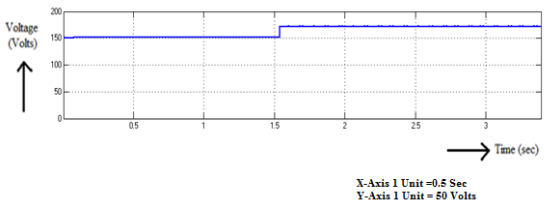

Fig.11 Input Voltage to the PI controlled interleaved cuk regulator

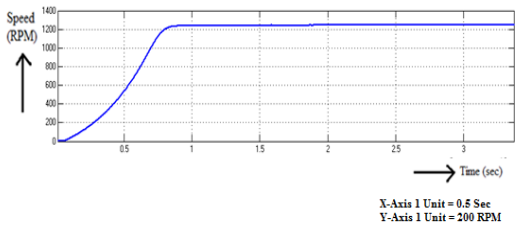

Fig.12 Speed of the PI controlled ICCIIMD system

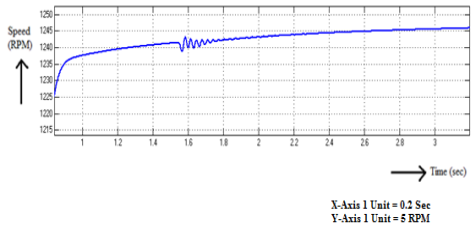

Fig.13 Speed (expanded)response of the PI controlled ICCIIMD system

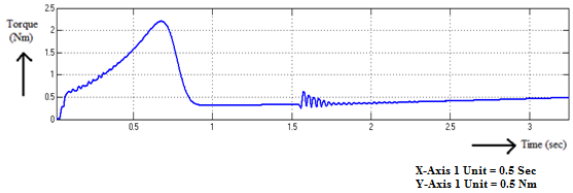

Fig.14 Torque response of the PI controlled ICCIIMD system

VII. Closed-loop controlled CCIIMD system with PR Controller

The closed loop PR controlled ICCIIMD structure is appeared in Figure15. A PR controller substitutes the PIcontroller in the preceding system where as the VSI is kept unchanged to make comparative analysis. The variation in input voltage is appeared in Figure16. The speed response with its detailed view and the torque response are appeared in Figure 17, Figures 18 and 19 respectively. The speed inhabits at 1245 rpm and the speed settles without any oscillations. The torque restores itself at 0.5 Nm and the torque also settles without any oscillations.

The list of components and their ratings used in designing hardware of ICCIIMD system is shown in Table 1. The comparison of time domain parameters for a reference speed of 1240 rpm with PI &PR controllers is given in Table 2. The assessment signifies that the response is faster and steadystate error is reduced utilizing the PR controlled system.

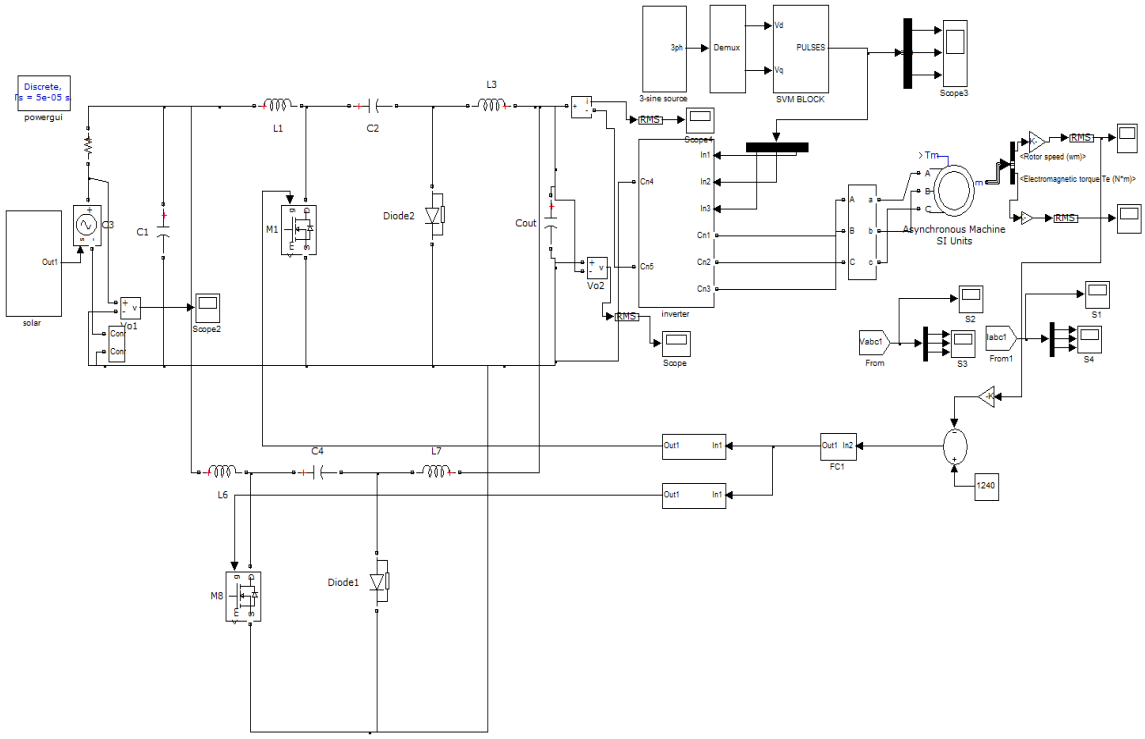

Figure.15 Closed loop PR controlled ICCIIMD system

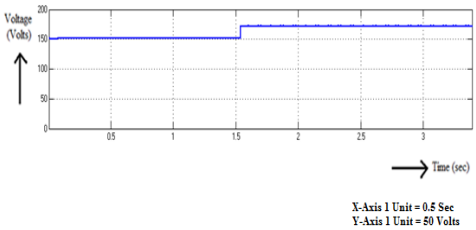

Fig.16 Input Voltage to the PR controlled interleaved cuk converter

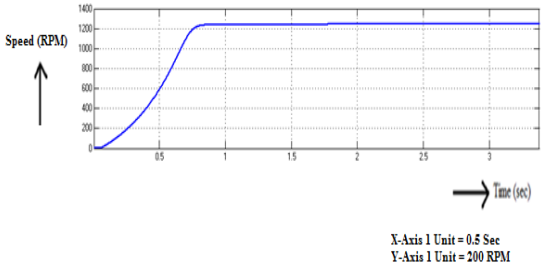

Fig.17 Motor Speed of the ICCIIMD system using PR controller

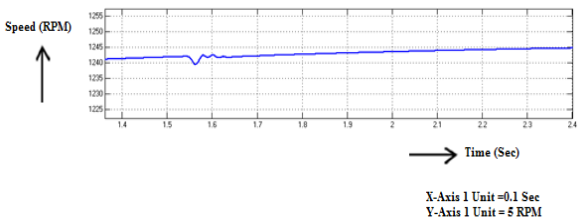

Fig.18 Motor Speed (expanded view) of the ICCIIMD system using PR controller

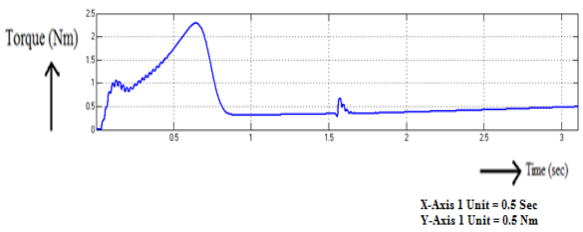

Fig.19 Torque developed by the ICCIIMD system using PR controller

The settling time is as low as 1.65millisecond using PR controller. Settling time is reduced from 1.80 millisecond to 1.65 millisecond. The torque ripple is reduced from 0.15Nm to 0.08Nm using PR controller. Therefore the response of PR controlled

ICCIIMD system is superior to PI controlled ICCIIMD system.

Table 1: List of Components and their Ratings used in Hardware of ICCIIMD system

Sl.No.	Hardware Component	Rating of the Component	Type of Component
1	Capacitor	1000E-03	Electrolytic
2	Capacitor	4.70E-05	Electrolytic
3	Capacitor	3.30E-11	Disc
4	Capacitor	2.20E-03	Electrolytic
5	Diode	1000V ,3A	PN Junction
6	Inductance	10uH	ferrite coil
7	MOSFET (IR840)	600V,8A	N-channel
8	Resistor	1k	Quarter watts
9	Resistor	100E	
10	Resistor	22E	
11	Regulator	12V	L7812/TO3
12	Regulator	5V	L7805/TO220
13	IC	IR2110	Opto-coupler
14	Pic controller	PIC16F84A	RISC
15	PCB	V105	General

Table 2: Comparison of Time Domain Parameters using PI and PR basedICCIIMD Systems (for Nref=1240 rpm)

Type of Controller	Overshoot (Volts)	T_p(ms)	T_s(ms)	Steady state Error (E_{ss})	Torque Ripple (Nm)
PI Controller	1.54	1.60	1.80	2.1	0.15
PR Controller	1.53	1.56	1.65	1.8	0.08

VIII. HARDWARE RESULTS

The hardware arrangement for interleaved cuk converter inverter fed induction motordrive structure has been contrived and verified in the lab. The hardware arrangement for the suggested structure is shown in Figure 20. The hardware consists of a PV-panel, interleaved cuk converter board, inverter board, transformer board and control board. The output-voltage of solar-system is appeared in Figure21 and the output-voltage of interleaved cuk converter is shown in Figure 22. The switching-pulse for interleaved cuk converter is shown in Figure 23. The output voltage of Voltage Source Inverter is shown in Figure 24. The hardware results match with the simulation-results of ICCIIMD system.The spikes in the output of inverter are due to change in switching sequence at every sixty degree interval.

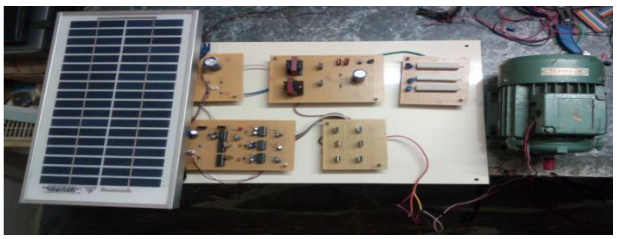

Figure.20 Hardware setup of Solar fed interleaved cuk converter based IM

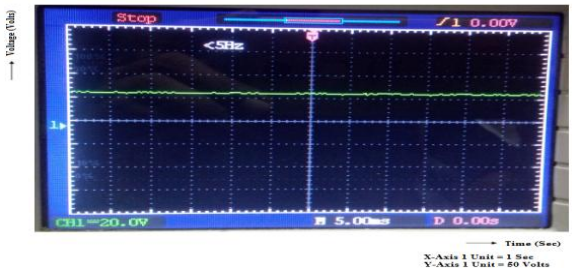

Figure.21 Output Voltage of the Solar Panel

Figure.22 Output voltage of interleaved cuk converter

Fig.23 Switching pulse for interleaved cuk converter

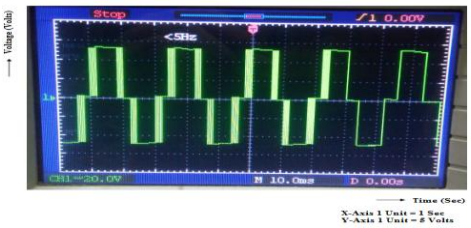

Figure.24 Output voltage of VSI

Complete hardware circuit of the proposed CCIIMD system is shown in Figure 25. PIC16F84 is used to generate pulses. Drivers IR2110 are used to amplify the pulses. The connections from control circuit to power circuit are also presented. The amplified pulses from IR2110 are applied to IRF840 MOSFETs.

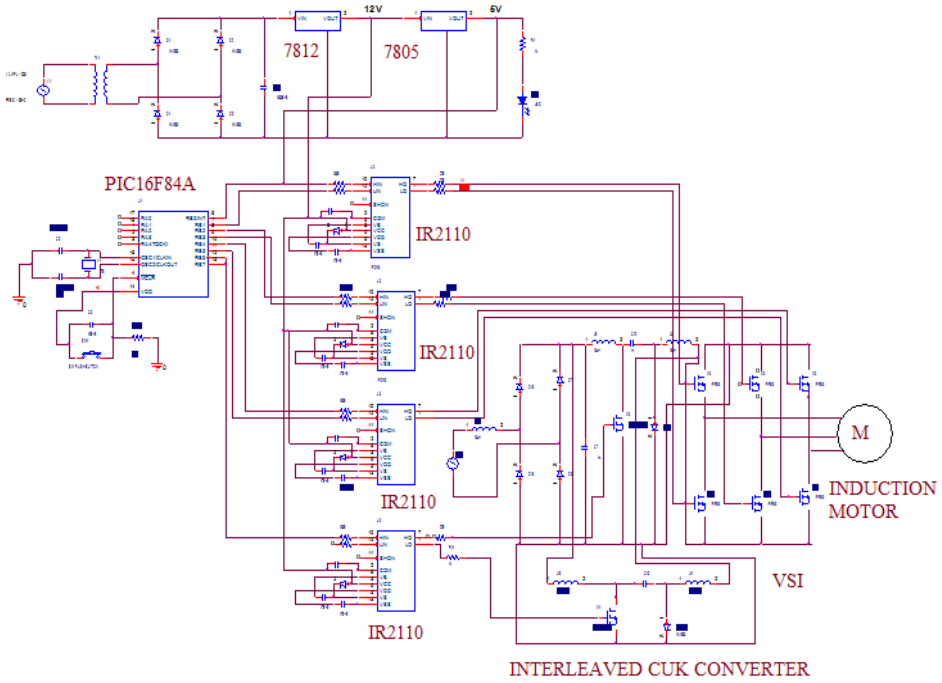

Fig.25 Complete Hardware Circuit Diagram of the proposed ICCIIMD system

IX. CONCLUSION

Simulation studies were done for open and closed-loop systems with PI and PR controllers. These studies were carried out using the Simulink based models for interleaved cukconverter inverter fed induction motor drive. The settling time with PR is reduced by 0.15ms with respect to PI controlled system. The outcomes signify that the PRcontrolled system gave an improved response as compared with PI controlled system. The hardware for 0.5HP induction-motor drive structure is contrived and verified. The investigational outcomes match with the hardware results. The torque ripple is reduced to 0.08Nm using PR controller. The benefits of the recommended ICCIIMD system are decreased torqueripple and enhanced response.

The scope of the current work is the comparison of PR and PIcontrolled open and closedloop systems. The comparison of Artificial NeuralNetwork (ANN) and Fuzzy based systems could be done in the future. The hardware may be implemented using FPGA to enhance the switching-frequency level of interleaved cuk converter.

Funding

The author(s) received no financial support for the research, authorship, and/or publication of this article.

Declaration* of Conflicting *Interests

The Author(s) declare that there is no conflict of interest.

References

[1] Singh S and Singh B. A voltage-controlled PFC Cuk converter based PMBLDCM drive for air-conditioners. *IEEE Trans. Ind. Appl*2012; 48(2):832–838.

[2] RaichelMathew and Aswathy Mohandas P. A Bridgeless CUK Converter Based Induction Motor Drive For PFC Applications. *International Journal of Electrical Engineering & Technology (IJEET)* 2014; 5(12): 191-196.

[3] ThemozhiG and Rama ReddyS.On chop pulse width modulator and dead time controller in bidirectional

DC to DC converter for aerospace applications.*Arab. J. Sci. Eng*2014; 39(2): 957–966.

[4] Lin BR, Huang C and Chiang HK. Analysis design and implementation of active snubberzv switching cuk converter.*IET Power Electron*2008; 1:50–61.

[5] Fardoun A, Ismail EH, Sabzali AJ and Al-Saffar M.A. A comparison between three proposed bridgeless Cuk topologies and conventional topologies for power factor correction. *IEEE Trans. Power Electron* 2012; 27(7): 3292–3301

[6] Wang H, Tang Y and Khaligh A. A bridgeless boost rectifier for low voltage energy harvesting applications. *IEEE Trans. Power Electron* 2013;28(11): 5206–5214.

[7] DeMelo PF, Gules R, Romaneli RF and Annunziato RC. A modified SEPIC converter for high power-factor rectifier and universal input voltage applications. *IEEE Trans. Power Electron*2010; 25(2): 310–321.

[8] Sabzali AJ, Ismail EH, Al-Saffar M and Fardoun A. A new bridgeless PFC SEPIC and Cuk rectifiers with low conduction and switching losses.*IEEE Trans. Ind. Appl* 2011; 47 (2): 873–881.

[9] Rajan Kumar and Bhim Singh. Solar PV Array Fed Cuk Converter-VSI Controlled BLDC Motor Drive for Water Pumping. In: 6thIEEE Power India International Conference, 2014,pp.1-7.

[10] Kannan K, Francis Antony Selvi P and Pushpalatha D. Torque Ripple Compensation Technique Based BLDC Motors using Cuk Converter using ARDUINO.*International Journal of Current Trends in Engineering & Research (IJCTER)* 2016; 2(5): 2455–1392.

[11] Husain I and Ehsani M. Torque ripple minimization in switched reluctance motor drives by PWM current control. *IEEE Transactions on Power Electronics*1996; 11: 83-88.

[12] Singh B, Chaturvedi GD. Analysis, design and development of single switch forward buck AC-DC converter for low power battery charging application. InPower Electronics, Drives and Energy Systems, 2006. PEDES'06. International Conference on 2006 Dec 12 (pp. 1-6). IEEE.

[13] Hua AC, Tsai BC. Design of a wide input range DC/DC converter based on SEPIC topology for fuel cell power conversion. InPower Electronics Conference (IPEC), 2010 (International 2010 Jun 21), pp: 311-316. IEEE.

[14] Fardoun AA, Ismail EH, Sabzali AJ, Al-Saffar MA. A Comparison between Three Proposed Bridgeless Cuk Topologies and Conventional Topologies for Power Factor Correction.*IEEE Trans. Power Electron*2012; 27(7): 3292-3301.

[15] Kumar R, Singh B. BLDC motor-driven solar PV array-fed water pumping system employing zeta converter. *IEEE Trans. Ind. Appl*2016; 52(3): 2315-22

[16] Muthu P, Umayal C, Jagannath M, Adalarasu K. SEPIC Converter for Power Factor Correction in Free Biomass Induction Heating System. *Int. Journal of Bio Sciences and Engg*2016; 3(1):15-36.

[17] Vandana P and VenmaPrabhash. A Torque Ripple Compensation Technique for a BLDC Motor Drive fed from Solar PV Array using SEPIC converter. International Journal of Advanced Research in Electrical, Electronics and Instrumentation Engineering 2016; 5(6): 5436-5443.

[18] Song MS, Oh ES, Kang BK. Modified SEPIC having enhanced power conversion efficiency.*Electron.lett*2012; 48(18):1151-3.

[19] Ray O, Mishra S. Boost-derived hybrid converter with simultaneous DC and AC outputs. IEEE transactions on Industry applications. 2014 Mar;50(2):1082-93.

[20] Adda R, Ray O, Mishra SK, Joshi A. Synchronous-reference-frame-based control of switched boost inverter for standalone dc nanogrid applications. *IEEE Trans. Power Electron* 2013; 28(3):1219-33.

[21] Matysik JT. A new method of integration control with instantaneous current monitoring for class D series-resonant converter. IEEE Transactions on Industrial Electronics. 2006; 53(5):1564-76.

WIND GENERATOR DRIVETRAIN PERFORMANCE AND COMPARISON OF PM FLUX SWITCHING MACHINES

Udochukwu B. AKURU
Tshwane University of Technology
Department of Electrical Engineering, Tshwane University of Technology, Pretoria 0183, South Africa
AkuruUB@tut.ac.za

Abstract: *This study is undertaken to highlight the competitive optimal performance of permanent magnet flux switching machines (PM–FSMs) in different wind generator drivetrains—low–speed (LS), medium–speed (MS) and high–speed (HS). The three–phase 12–stator slots/10–rotor teeth PM–FSM is selected for the study, for small–scale power applications. The design and optimisation is performed using a 2–D finite element analyses (FEA) tool. Thereafter, important features of the different wind generator drivetrains are evaluated and compared, especially in terms of cost of energy (CoE) versus performance. In the end, the study barely stops short of representing the MS as the best among the three drivetrains; however, it is clearly a preferred solution due to trade–offs in torque density and cost of generator.*

Key words: *cost of energy (CoE), design optimisation, finite element analyses (FEA), permanent magnet flux switching machine (PM-FSM), wind generator drivetrain.*

1. Nomenclature

α	current angle [deg.].
Δ	load angle [deg.].
V_s	phase voltage [V].
E_q	no–load generated voltage [V].
I_s	phase current [A].
λ_d & λ_q	d– and q–axes flux linkages [Wb.].
λ_M	no–load flux linkage [Wb].
L_d & L_q	d– and q–axes inductances [H].
I_d & I_q	d– and q–axes phase currents [A].
Π	a variable to represent phase vector quantities like flux linkages or currents.
d, q, & 0	Park's transformation variables.
a, b, & c	three–phase variables.
θ	Park's transformation angle [rad.].
V_d & V_q	d– and q–axes phase voltages [V].
ω_e	electrical speed [rad/s].
R_s	total phase resistance [Ω].
q	number of phase coils in series connection.
N_{ph}	turns number per coil for the phase windings.
ρ_{Cu}	resistivity of copper wire [Ω.m].
l_{st}	axial or stack length [m].
l_{ϑ}	distance of the phase end–winding from lamination [m].
A_{ph}	area of the phase wire [m^2].
N_r	PM–FSM rotor teeth number.
τ_e	electromagnetic torque [Nm].
κ_δ	torque ripple [%].
$\tau_{e(\max)}$ & $\tau_{e(\min)}$	upper and lower peaks of τ_e [Nm].
C_m, σ and β	Steinmetz coefficients for core loss estimation.
$\dot{B}_k$	peak flux density measured in k iron core part [Wb].
M_k	mass of k iron core part [kg].
N	number of iron core parts.
f_e	frequency [Hz].
$\mathcal{P}_{\text{out}}$	real power [W].
Q	reactive power [W].
P_{Cu}	copper loss [W].
P_{Core}	core losses [W].
η	efficiency [%].
PF	power factor.
M_{PM}	mass of the PM [kg].
M_A	total active mass [kg].
M_{FeS}	mass of the stator iron [kg].
M_{FeR}	rotor iron mass [kg].
M_{Cu}	copper mass of phase windings [kg].
$x^{(L)}$ and $x^{(U)}$	lower and upper boundary limits of designated design variable.
Λ_0	split ratio.
κ_L	aspect ratio.
J	phase current density [A/mm^2].

2. Introduction

In recent times, wind turbine manufacturers have increasingly shifted their focus to geared medium–speed (MS) drivetrains for wind turbine systems because of some challenges encountered in low–speed (LS) and high–speed (HS) systems, such as higher manufacturing and maintenance costs [1]. In addition, the impetus to tap the vast wind energy potential which exists both onshore and offshore is increasing because it guarantees a good return on investment (ROI) for wind turbines that are designed at industrial–scale power levels. Hence, geared MS systems, as shown in Fig. 1, offer a reliable compromise for such industrial–scale wind turbines, in terms of the gearbox and generator sizes. Note also, the presence of the solid state converters (SSCs) as critical components of the proposed drivetrain architecture. Recent trends which show the benefits of geared MS drivetrains over LS and HS drivetrains have already been addressed in [2], based on the drivetrain performance comparison of PMSGs.

Also, studies in [3, 4] regarding MS doubly-fed induction generators (DFIGs) and permanent magnet

synchronous generators (PMSGs), respectively, both portrayed lowest cost of energy (CoE) compared to LS and HS systems. Consequently, to capitalise on these latent benefits, there is need to do further research to highlight important qualities of newer concept of wind generators designed for geared MS drivetrains, while comparing for highest CoE. Such studies appear not to have been documented for permanent magnet flux switching machines (PM–FSMs)—typically, a non–conventional machine—gaining wide usage because of its stator–mounted (and brushless) qualities [5, 6].

In this paper, an attempt is made to compare the optimum design performance of the very popular 12–stator slots/10–rotor teeth (12/10) radial–flux PM–FSM topology in the different wind generator drivetrains, for the first time. To achieve this, 2–D static finite element analyses (FEA) method is employed for both the optimisation and the performance evaluation. Eventually, the design feasibility is established by 3–D FEA process applied to a benchmark design.

3. Electromagnetic modelling of the PM–FSM

The design optimisation and performance evaluation process is to be undertaken by means of an in–house Python script–based non–linear 2–D static FEA program, called SEMFEM [7]. But before the design optimisation process, it is important to set forth, for the PM–FSM, the steady–state d– and q–axes (dq) equations which will be implemented in the FEA package. This way, the speed of the design optimisation process is hopefully enhanced.

Consequently, the steady–state dq equivalent circuits and phase diagram, in generator mode, are shown in Fig. 2. Note that, $V_s > E_q$ and that I_s lags V_s as implied in Fig. 2. To associate the meaning of the variable terms, a list of nomenclature has been provided at the beginning of the paper. Based on the evaluation of the 2–D FEA model, the dq axes flux linkages, from which other machine characteristics are devised, are given as

$$\lambda_d = \lambda_M + L_d I_d, \tag{1}$$
$$\lambda_q = L_q I_q, \tag{2}$$

where all the parameters have been defined accordingly in section I.

The expressions in (1) and (2) are used to facilitate the determination of the dq inductances. In reality, the dq flux linkages are fundamental output variables resulting from the SEMFEM technique which prescribes as input variables, the field excitation source and phase currents of a proposed electrical machine design. To this end, the 2–D FEA program evaluates the dq quantities mainly from their fundamental phase quantities by using Park's dq transformation equation expressed as

$$\begin{bmatrix} \Pi_d \\ \Pi_q \\ \Pi_0 \end{bmatrix} = \frac{2}{3}\begin{bmatrix} \cos\theta & \cos\left(\theta + \frac{2\pi}{3}\right) & \cos\left(\theta - \frac{2\pi}{3}\right) \\ \sin\theta & \sin\left(\theta + \frac{2\pi}{3}\right) & \sin\left(\theta - \frac{2\pi}{3}\right) \\ \frac{1}{2} & \frac{1}{2} & \frac{1}{2} \end{bmatrix}\begin{bmatrix} \Pi_a \\ \Pi_b \\ \Pi_c \end{bmatrix}, \tag{3}$$

where all the parameters have been defined accordingly in section I.

The dq axes voltages are evaluated as

$$V_d = \omega_e L_q I_q - R_s I_d, \tag{4}$$
$$V_q = \omega_e \lambda_M - \omega_e L_d I_d - R_s I_q, \tag{5}$$

where all the parameters have been defined accordingly in section I.

The phase resistance is given as

$$R_s = 2qN_{ph}^2 \rho_{Cu} \frac{l_{st}+l_e}{A_{ph}}, \tag{6}$$

where all the parameters have been defined accordingly in section I.

The magnitudes of the phase output voltage and current are calculated as

$$V_s = \sqrt{V_d^2 + V_q^2}, \quad I_s = \sqrt{I_d^2 + I_q^2}, \tag{7}$$

where all the parameters have been defined accordingly in section I.

The torque and torque ripple are given as

$$\tau_e = \frac{3}{2} N_r \left(I_q \lambda_M + \left(L_d - L_q\right) I_d I_q\right), \tag{8}$$
$$\kappa_\delta = \frac{\tau_{e(\max)} - \tau_{e(\min)}}{\tau_e}, \tag{9}$$

where all the parameters have been defined accordingly in section I.

The real and reactive power, total copper and core losses are given as follows:

$$\mathcal{P}_{\text{out}} = \frac{3}{2}\left(V_d I_d + V_q I_q\right), \tag{10}$$
$$\mathrm{Q} = \frac{3}{2}\left(V_q I_d - V_d I_q\right), \tag{11}$$
$$P_{Cu} = \frac{3}{2}\left(I_d^2 + I_q^2\right) R_s, \tag{12}$$
$$P_{Core} = C_m f_e^\beta \sum_{k=1}^{N} \dot{B}_k^\sigma M_k. \tag{13}$$

In this study, non–oriented fully processed M400–50A gauge magnetic steel grade with mass density 7600 kg/m^3 is the preferred core sheets from which the Steinmetz coefficients (C_m, σ and β) are determined from the core loss-frequency curves.

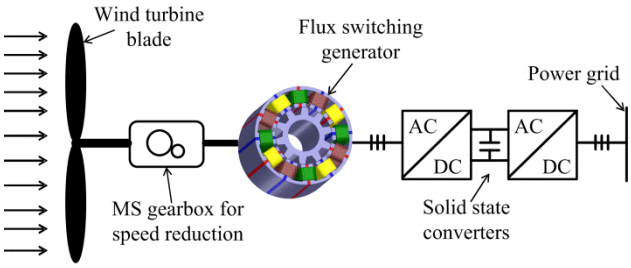

Fig. 1. The proposed wind generator drivetrain.

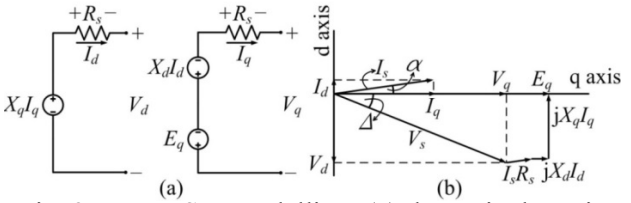

Fig. 2. PM–FSM modelling: (a) dq equivalent circuits, (b) phasor diagram.

Lastly, the efficiency and power factor is given as

$$\eta = \frac{\mathcal{P}_{\text{out}}}{\mathcal{P}_{\text{out}}+P_{Cu}+P_{Core}}, \tag{15}$$

$$\text{PF} = \cos\left(\tan^{-1}\left(\frac{I_d}{I_q}\right) + \tan^{-1}\left(\frac{V_d}{V_q}\right)\right). \tag{16}$$

4. Design optimisation

Although wind generator drivetrain is implied in this study, the focus of the current design is on the wind generator component itself, whereby the conclusions drawn do not take into account the other associated drivetrain components. To this end, the inquiry is mainly on the performance of 12/10 PM–FSM wind generator operated under different drivetrains, with the CoE being of primary interest. The objective functions are the ratio of the average torque to PM mass and the active mass given as

$$F_1(\bar{x}) = \frac{\tau_e}{M_{PM}}, \tag{17}$$

$$F_2(\bar{x}) = M_A = M_{FeS} + M_{FeR} + M_{PM} + M_{Cu}. \tag{18}$$

The design optimisation process is subjected to the following constraint functions defined as $\mathcal{P}_{\text{out}} \geq 10$ kW, $\text{PF} \geq 0.8$, $\kappa_\delta \leq 10$ % and $\eta \geq 90$ %. To account for the different drivetrains, the mechanical speed of the generator is constrained at 30 r/min, 360 r/min and 1500 r/min which represent the LS, MS and HS drivetrains, respectively, while the airgap length (g) was kept constant at 0.7 mm for the three designs. The use of the same airgap length for the three designs may be considered unfair, especially for the LS design, but as shown in [8], in the manufacturing of a similar–sized wound–field flux switching wind generator prototype, the same airgap length is used. As a matter of fact, it is reported in [9] that for machines with exceptionally large stator outer diameter, e.g., in LS designs, an airgap ratio defined as $g/D_{out} \approx 0.001$ is preferred. Besides, for such LS designs, a small airgap is necessary to subsidize the amount of PM usage. Hence, the uniform airgap size adopted for the three designs appears to mostly favour the LS design.

The initial design is created according to the sizing method presented in [10]. Each drivetrain speed is used generate a reference design to initiate the design optimisation in respect of the design geometry. Reasonable boundary conditions are formulated for the twelve design parameters chosen as itemised in Table 1 based on a methodology formulated in [11] for wound-field FSMs. As reported in [12], the current density and current angle have been included as non–dimensional parameters so as to increase the flexibility of the optimum design considering that PM–FSMs are prone to saturation and magnetic cross–coupling effects. The flowchart outlined in Fig. 3 describes the design optimisation procedure.

The optimisation is based on a non–gradient algorithm called the Non–dominated Sorting Genetic Algorithm II (NSGA–II) [13]. NSGA–II as an adaptive search technique inspired from nature, which works on the principle of Darwin's theory of survival–of–the–fittest, and broadly referred to as evolutionary algorithm. It works with a set of solutions (population) and as the simulation (evolution) proceeds, the individuals (solution) in the population improve. On this premise, each optimisation problem is ascribed 20 individuals while 100 iterations are applied, with the tuneable crossover and mutation index set at 20 and 10, respectively.

5. Results and discussion

The simulation results of the optimisation problems executed for the three different drivetrain solutions are presented in Fig. 4, showing scatter plots of the optimal designs. It is clear that relatively less amount of PM is required to achieve the average torque requirements in the LS drivetrain, but with significant increase in the generator active mass. In reality, what is lost in terms of PM amount is traded off for an increase in the amount of copper and steel. As for the HS designs, the ratio of the torque requirement to PM mass is highest, while the smallest amount of copper and steel is used. As expected, the geared MS designs presented a tradeoff, with impressively high torque/PM densities as obtained in the LS designs and very low active mass as obtained in the HS designs.

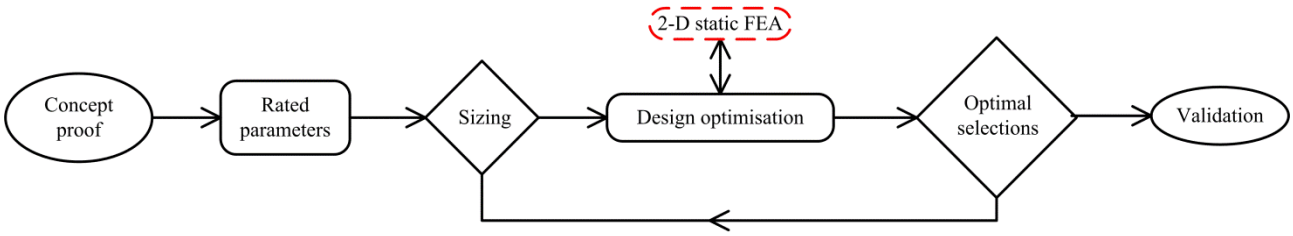

Fig. 3. PM–FSM design optimisation workflow.

Table 1
Boundary conditions defined for design parameters

Design variables	$\bar{x}$	Drivetrain					
		LS		MS		HS	
		$x^{(L)}$	$x^{(U)}$	$x^{(L)}$	$x^{(U)}$	$x^{(L)}$	$x^{(U)}$
Current angle (deg.)	α	0	90	0	90	0	90
Current density (A/mm^2)	J	1	5	1	5	1	5
Stator outer diameter (mm)	D_{out}	600	700	250	300	170	200
Stator inner diameter (mm)	D_{in}	388.5	500	162	180	120	140
Shaft diameter (mm)	D_{sh}	225	300	80	85	50	60
Stack length (mm)	l_{st}	250	500	90	180	70	140
PM length (mm)	b_{pm}	10	20	5	10	5	10
Rotor pole width (mm)	b_{pr}	20	40	10	20	7.5	15
Slot opening width (mm)	b_{sls}	12.5	25	7.5	15	5	10
Stator yoke height (mm)	h_{ys}	12.5	25	7.5	15	5	10
Rotor yoke height (mm)	h_{yr}	10	20	7.5	15	7.5	10
Rotor tooth tapering factor	t_0	0.5	1	0.5	1	0.5	1

Furthermore, the average values of the active mass for each optimal drivetrain design candidates are plotted as shown in Fig. 5. As indicated, the average active mass for the LS designs is highest compared to both the HS and MS options, given that all machines were designed for the same power levels of about 10 kW. Thus, it is perceived that the potential incorporation of gearboxes in both the MS and HS designs, while satisfying the optimum design requirements, gave rise to huge mass discrepancies of these designs compared to the LS one. But considering the generator costs, it is clearly noted that best CoE is achieved in the MS drivetrain, because unlike the HS option, its PM utilisation factor is more attractive.

To further evaluate the performance versus CoE, a representative design is benchmarked from each optimal drivetrain solution, with the baseline power requirement set within the 10 kW limit. The key performance indices for each drivetrain solution are displayed as shown in Table 2, leading to further discussions. The cost estimations are based on price quotations sourced from [14] in US dollars (USD).

As observed in Table 2, the torque–mass densities have similar trends with respect that of the torque–PM densities. Moreover, it is clearly shown that the generator costs are proportional to the torque. Hence, for the estimated total material costs, the LS generator is over 10 times the cost of the MS generator and 27 times that of the HS generator. However, between the MS and HS generators, the cost margin only differs by 250 %.

Consequently, as implied in [15], should a gearbox cost ratio of 183 % between the HS gearbox and single–stage MS gearbox be adopted, then the MS generator drivetrain costs is improved to 136 %. But with higher operation and maintenance costs accruing to the HS gearbox, the cost of the MS system is anticipated to be improved further.

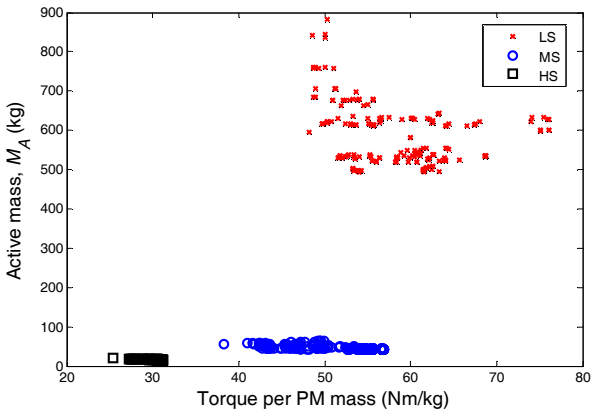

Fig. 4. Optimisation results for different PM–FSM wind generator drivetrains.

Table 2
Benchmark performance comparison of 10 kW PM–FSM wind generator drivetrains

Parameters	Units	Drivetrain		
		LS	MS	HS
Torque, τ_e	Nm	3207.17	260.47	62.33
Torque ripple, κ_δ	%	10.29	9.96	10.28
Output power, $\mathrm{P}_{\mathrm{out}}$	kW	10.24	10.03	10.04
Copper loss, P_{Cu}	kW	1.13	0.42	0.16
Core loss, P_{Core}	kW	0.02	0.09	0.26
Efficiency, η	%	90	95.12	95.95
Power factor, PF	–	0.89	0.8	0.83
Stator steel mass, M_{FeS}	kg	292.56	22.88	7.66
Rotor steel mass, M_{FeR}	kg	91.04	8.03	2.23
Copper mass, M_{Cu}	kg	58.64	6.15	2.52
PM mass, M_{PM}	kg	52.08	4.75	1.99
Active mass, M_A	kg	494.32	41.82	14.40
Torque/active mass	Nm/kg	6.49	6.23	4.33
Torque/PM mass	Nm/kg	61.58	54.83	31.32
Total material cost	USD	4625.48	421.88	169.38
Split ratio, Λ_0	–	0.63	0.57	0.53
Aspect ratio, κ_L	–	0.68	0.69	0.83
Current density, J	A/mm^2	2.673	4.999	4.999

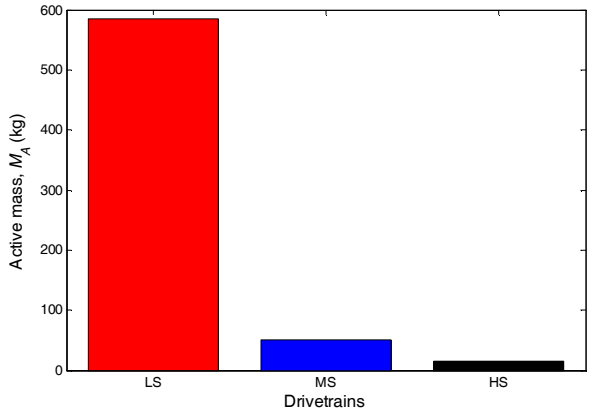

Fig. 5. Comparison of generator mass for different drivetrains.

Also, comparing power factor shows the LS design with the best outcome at 0.89; however, the prescribed power factor limit was achieved in all three drivetrains. The excellent power factor in the LS design is possible only because it incurred the lowest current density after the MDO process. To this end, the LS benchmark potentially yields the cheapest solid state converter (SSC) due to its excellent power factor compared to the rest; because, according to [16], the conduction loss of SSCs depends on power factor, which compounds their power ratings and costs. But such cost rebate might consequently be diminished considering its oversized generator, with implications for very high manufacturing and logistics costs. Or perhaps, the power factor of the LS design could have improved because of the same airgap lengths assumed on the three designs, leading to betterment of the magnetising reactance in the resulting oversized generator. To support such claims, it is reported in [9] that by decreasing the magnetic inductance of a machine, greater amount of reactive current is usually generated to the detriment of the power factor.

Looking at the torque capability of the LS design, one would expect greater torque per PM mass as compared in Table 2. Fig. 4 shows a good proportion of the evolved torque/PM mass of the LS designs in this light, while also portraying a prominent overlap with those of the MS designs.

On the other hand, the copper loss in the LS design is dominant among the three different drivetrains as observed in Table 2. Evaluation of the current values for the reported benchmarks in Table 2 resulted in 24.91 A, 12.24 A and 6.54 A for the LS, MS and HS designs, respectively. Thus, the reduction in the current density of the LS design yields corresponding decrease in the phase current, viz., $I_s^2 R_s$ loss.

The core losses in Table 2 shows the HS design has is highest among the three drivetrains, no thanks to its highest fundamental frequency. Notwithstanding, this increment is dwarfed by the copper loss recorded in the LS design, which apparently resulted in the extremely poor efficiency performance at approximately 90 %. Meanwhile, it is indicated that the efficiency in the MS and HS machines are logged in excess of 95 %. As for torque ripple, the variation among the three drivetrains is not so dramatic, while bearing in mind that each drivetrain solution satisfied the optimum design requirements.

While it may not be a conclusive task to predict

which of the generators give the best drivetrain solution, the MS design is to be acknowledged as the preferred solution because it yields the best tradeoff between CoE and performance. To reach this conclusion, the following are noteworthy:

- The torque densities (with respect to PM and total active mass) of the MS designs is as high as those observed in the LS designs, while its cost remain comparable to that of the HS designs. This should imply a reduction in the size and cost of the wind turbine tower and hub.
- The power factor is lowest for the MS generators, which due to very high current density. This means an increase in the leakage reactance, as well as the losses and cost of the SSC [17]. In any case, the higher cost implications of the LS generator and the HS gearbox should diminish their cost advantage in terms of the SSCs.
- Lastly, considering the baseline power, the MS generators yield comparable torque ripple and efficiency for the benefit of the overall drivetrain reliability and energy yield.

6. 3–D FEA Comparison

In this subsection, the design feasibility of the 2–D static FEA predictions, are compared with 3–D transient FEA solutions executed in ANSYS Maxwell© environment. The MS benchmark design from the preceding subsection is prioritised for the analyses. The magnetic flux density realised on the surface of the 3–D model is as shown in Fig. 11, while the terminal voltage waveforms calculated in 2–D and 3–D FEA are compared in Fig. 12. As can be seen, a good agreement has been obtained. The rough edges observed in the voltage waveform in 3–D FEA are likely due to less accurate meshing.

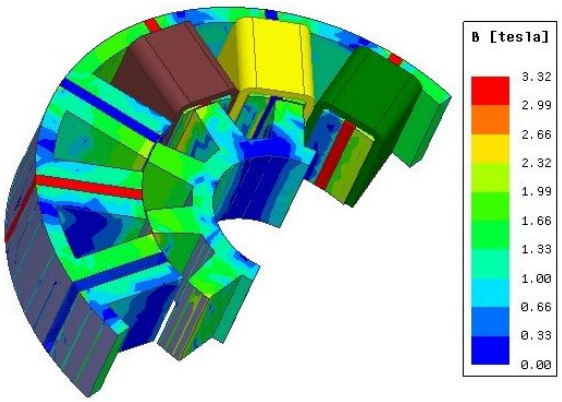

Fig. 11. 3–D FEA model showing the magnetic flux density under rated condition.

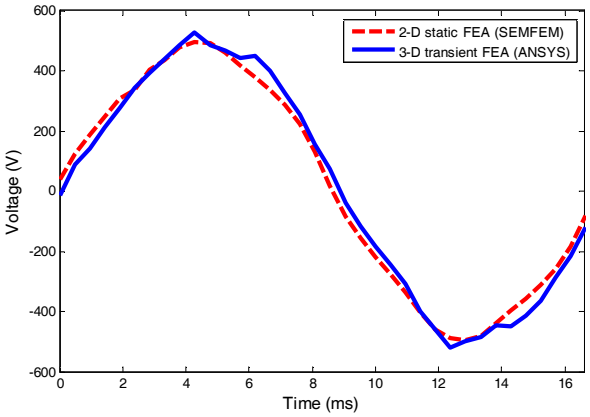

Fig. 12. Phase voltage comparison at 360 r/min.

7. Conclusion

In this study, the optimal drivetrain comparison of 12/10 PM–FSM for 10 kW wind generators has been initiated in FEA. The evaluation is on the CoE versus performance for the identified generator drivetrains—LS, MS and HS. The results show that, in terms of costs, the HS drivetrain presents the cheapest design but at the expense of the highest PM utilisation—torque per PM mass—less than 35 Nm/kg. In addition, the cost of the HS drivetrain increases to maximum due to gearbox installation and maintenance costs. On the other hand, the LS drivetrain uses the lowest amount of PM material—torque per PM mass—between 47 Nm/kg and 67 Nm/kg, but at the expense of an oversized generator. Thus, the LS active material cost is increased, to at least, 10 times the cost of the MS generator and 27 times that of the HS generator. In addition, an oversized LS generator means that the installation and logistic costs is increased. To this end, the MS design is nominated as the preferred solution because of an intrinsic trade–off in the torque/PM densities (37–57 Nm/kg) and generator costs.

Based on some optimal benchmarks from each of the three drivetrain solutions, it is observed that the huge size of the LS generator requires very high amount of copper, such that it results in high copper loss which limits the efficiency target to around 90 %, while benefiting the power factor. On the other hand, the efficiency requirements of the MS and HS designs are both well–exceeded, i.e., beyond 95 %, both with respectable power factor.

In summary, the study focused on the optimal wind generator drivetrain comparison of the 12/10 PM–FSM, showing the MS design as the preferred solution among the three drivetrains. However, a firm conclusion cannot be reached because only the electromagnetic design and performance of the generators are fully addressed in the study, while other

drivetrains components such as gearboxes and SSCs were only considered as estimates.

References

1. E. de Vries, *ABB shifts focus to medium speed drive systems*, WINDPOWER Monthly, 4 September 2012.
2. S. Schmidt and A. Vath, "Comparison of existing medium–speed drive train concepts with a differential gearbox approach," *European Wind Energy Association*, Copenhagen, pp. 179–186, April 2012.
3. W. Cao, Y. Xie and Z. Tan, *Wind turbine generator technologies*, InTech, 2012.
4. D–J Bang, H.P. Under, G. Shrestha and J. Ferreira, "Promising direct–drive generator system for large wind turbines," *Wind Power to the Grid Seminar*, EPE–WECS, 2008.
5. S. E. Rauch and L. J. Johnson, "Design principles of flux–switching alternators," *AIEE Trans.*, 74(III), pp. 1261–1268, 1955.
6. M. Cheng, W. Hua, J. Zhang, and W. Zhao, "Overview of stator–permanent magnet brushless machines," *IEEE Transactions on Industrial Electronics*, 58(11), pp. 5087–5101, 2011.
7. SEMFEM online documentation. [Online]. Available: www0.sun.ac.za/semfem/index.html
8. U.B. Akuru and M.J. Kamper, "Intriguing Behavioural Characteristics of Rare-Earth-Free Flux Switching Wind Generators at Small- and Large-Scale Power Levels," IEEE Transactions on Industry Applications, 54(6), pp. 5772-5782, Nov/Dec 2018.
9. J. Pyrhönen, T. Jokinen and V. Hrabovcova, *Design of Rotating Electrical Machines*, 5th ed., John Wiley & Sons, Ltd: UK, 2008.
10. W. Hua, C. Ming, Z. Q. Zhu and D. Howe, "Design of flux–switching permanent magnet machine considering the limitation of inverter and flux–weakening capability," *Conference Record of the IEEE Industry Applications Conference, 41st IAS Annual Meeting.*, vol.5, pp.2403–2410, 8–12 Oct. 2006.
11. U. B. Akuru and M. J. Kamper, "Formulation and multi-objective design optimisation of wound-field flux switching machines for wind energy drives," *IEEE Transactions on Industrial Electronics*, 65(2), pp. 1828-1836, Feb. 2018.
12. E. Ilhan, M. F. J. Kremers, E. T. Motoasca, J. J. H. Paulides and E. A. Lomonova, "Sensitivity analysis for phase inductances in Flux–Switching PM machines," *XXth International Conference on Electrical Machines*, Marseille, pp. 763–768, 2012.
13. K. Deb, A. Pratap, S. Agarwal and T. Meyarivan, "A fast and elitist multiobjective genetic algorithm: NSGA–II," *IEEE Transactions on Evolutionary Computation*, 6(2), pp. 182–197, Apr. 2002.
14. A. Fasolo, L. Alberti and N. Bianchi, "Performance comparison between switching–flux and IPM machines with rare–earth and ferrite PMs," *IEEE Transactions on Industry Applications*, 50(6), pp. 3708–3716, Nov.–Dec. 2014.
15. H. Polinder, F. F. A. van der Pijl, G. J. de Vilder and P. J. Tavner, "Comparison of direct–drive and geared generator concepts for wind turbines," *IEEE Transactions on Energy Conversion*, 21(3), pp. 725–733, Sept. 2006.
16. E. B. Sulaiman, T. Kosaka and N. Matsui, "Design study and experimental analysis of wound field flux switching motor for HEV applications," *XXth International Conference on Electrical Machines* (ICEM), pp.1269–1275, 2–5 Sept. 2012.
17. I. Boldea, L. Tutelea and F. Blaabjerg, "High power wind generator designs with less or no PMs: An overview," *17th International Conference on Electrical Machines and Systems* (ICEMS), pp.1–14, 22–25 Oct. 2014.

Experimental Investigation on Solar Photovoltaic Driven Cool Thermal Storage System for the Development of Sustainable Micro Grid in Building Sectors

Rajamani NARAYANASAMY[a,*], Gayathri VENKATARAMANI[a], Pandiyarajan VELLAICHAMY[b], Velraj RAMALINGAM[a]

[a]*Institute for Energy Studies, Anna University, Chennai - 600 025, India*
[b]*Department of Chemical Engineering, Anna University, Chennai - 600 025, India*
*Corresponding author: E-mail address: rajamani74@gmail.com

Abstract **- In most of the developed nation, the increase in percentage share of renewable power in the total power generation causes major concerns over the integration of these renewable power with the grid resulting grid instability. Energy storage is a new frontier technology which is considered as the ultimate solution in developing smart micro grid with distributed renewable energy (RE) generation. Most of the hot countries like India spend nearly 24% of the electricity generated on air conditioning and food preservation. Under such scenario, among the various types of storage systems, the cool thermal storage plays a vital role to promote renewable power in an economical way. Considering the importance in the present increasing RE scenario, in the present work, an experimental investigation was performed on a cool water storage integrated with a chiller system driven by solar PV unit which has major advantages in central air conditioning system for demand management strategies and to solve the Grid instability. The results revealed that with the installation of 100 W chiller operated by a 200 Wp solar PV panel it is possible to generate 25 liters of cool brine at – 6°C from 35°C along with the storage of 0.405 kWh and 0.1 kWh of electrical energy in the battery respectively during the months of May and September. In the month of January the temperature was brought down only to a temperature of 1.3°C along with 0.234 kWh of energy stored in the battery. These results will be very useful for the design and development renewable based micro grid for cooling and other applications which are electrically driven in various building sectors.**

Keywords**:** ***DC Compressor, Micro grid, Energy Efficient Building, Solar PV, Cool storage***

1. INTRODUCTION

In the recent years, progress on solar-powered air conditioning has increased and at present air conditioning system is almost a must in every building if there is a requirement for good indoor comfort inside the building. Dauta et al [1] reported that the demand of air conditioning is increasing continuously due to climate change and global warming. If the conventional air conditioning based from fossil fuels, is continued the greenhouse gas emission would continuously worsen global warming; in turn the demand of air conditioning will also increase. In subtropical cities, air conditioning is a standard requirement in all buildings. However, air conditioning would normally consume half of building electricity consumption. In recent years the use of thermal energy storage has become a topic with a lot of interest within

the research community, but also within architects and engineers. It is well known that there is a need to develop technologies to achieve thermal comfort in buildings lowering the cooling and heating demand. The development of renewable energy is on the rise worldwide because of the growing demand on energy, high oil prices, and concerns of environmental impacts.

In order to obtain a feasibility of the air conditioning system using solar, a lot research and testing have been initiated to learn and discover the design and operation of the air conditioning and solar system. Sahoo and Rout [2] reported that with the increase in gas and electricity tariffs, solar energy becomes attractive once the system has been installed. As one of the sources of renewable energy, solar energy is likely the most suitable system for installation in sub-tropical countries. The most common globally, preferred type of thermally driven technology for air-conditioning is absorption cooling. The system, which has simpler capacity control, mechanism, easier implementation, high reliability, silent operation, long life and low maintenance cost was a genuine candidate for efficient and economic use of solar energy for cooling applications. Utilizing solar energy to run the air conditioning system is a practical technique to replace conventional electricity.

Chidambaram et al [3] stated that the power shortage and unstable power supply remain serious problems. Further, they have discussed that the conventional cooling technologies that utilize harmful refrigerants consume more energy and cause peak loads leading to negative environmental impacts.. Also authors highlighted that the thermal storage systems are essential to overcome the disadvantage of the intermittent nature of solar energy and the mismatch in cooling demand. Foster et al [4] experimentally investigated the PV direct drive solar farm milk chillers (FMC) in Kenya with zero failures in the first 2.5 years of operation. The solar FMC technology was introduced to cool about 25 to 40 liters of milk overnight to 4°C. No overnight chilled milk was rejected by milk buyers in the 2-year study (traders and dairy cooperatives) and farmer incomes were significantly increased by over 30%. El-Bahloul et al [5] studied and investigated the performance of 15 ft^3 transportable solar driven DC refrigeration system to be utilized for post-harvest handling of crops at Alexandria, Egypt. The said system comprises, two compartments with different working temperatures of 5 and 0°C to store different types of fruits and vegetables. They have determined cooling loads for the two cold storages are 5.44 and 6.21 kW, respectively. Modi et al [6] studied the performance of domestic refrigerator powered by PV generator and stated that the refrigerator which was designed to operate using R-600a Butane refrigerant of 160 W rating capacity can work smoothly and continually by using a PV generator module of 140 Wp.

Axaopoulos and Theodoridis [7] ensured the successful operation of the refrigeration compressors by the PV panels by using a novel concept dedicated controller, which provides easy start up, power management and maximum power tracking for all the compressors of the system. Ekren et al [8] performed an experimental analysis of a direct current type refrigeration compressor implemented in a 79 litre refrigerator. The authors also investigated the energy usage reduction and operational improvement potential of the direct current compressor via variable speed operation. Further they have performed the experiments at variable speed operation and four different constant speed operation modes of the compressor. Chedop et al [9] presented an assessment of a solar electric-vapor compression refrigeration (SE-

VCR) system in a dry tropical area. They have performed a specific case of the city of Maroua, located in the climatic region of Cameroon. The authors performed an overall evaluation of the hourly cooling loads and the performance of the system by means of energy balance method. The results showed that, for an evaporating temperature of 0°C, the effective power of the compressor in the range of 5.33 kW and 6 kW, the capacity of the condenser in the range of 24 and 28 kW, and the coefficient of performance in the range of 3.28 to 3.74 while the efficiency of the installation is in the range of 17% and 35%. Blas et al [10] centred on the analysis of a direct current permanent magnet motor integrated in a refrigeration facility for milk cooling. They have also estimated the motor parameters by analysis of motor losses, data coming from simple no-load, load and locked-rotor laboratory tests.

The present work focuses to develop and test a prototype DC air conditioning system operated with solar PV system integrated with cool thermal storage for buildings deployed with central air conditioning units. The major advantages of the CTES system used in the solar-based VCR system are: (a) the cool storage system allows 50% reduction in the capacity of the chiller normally used in the central air-conditioning system that particularly reduces the demand cost for the building owner (b) reduces the burden on the power utilities towards the grid management. (c) A high-efficiency direct current motor can be used to run the compressor.

2. EXPERIMENTAL SETUP

A lab scale solar PV operated DC driven chiller unit was developed in the Solar Laboratory of Institute for Energy Studies, Anna University, Chennai, whose latitude and longitude are 13.0827° N, 80.2707° E respectively. The system consists of a 200 W_p PV module, 12 V, 20 Ah Lithium ion battery, a chiller unit with a cooling capacity of 100 W and a cool thermal storage tank of 0.025 m^3. The layout of the experimental setup is shown in Fig.1.

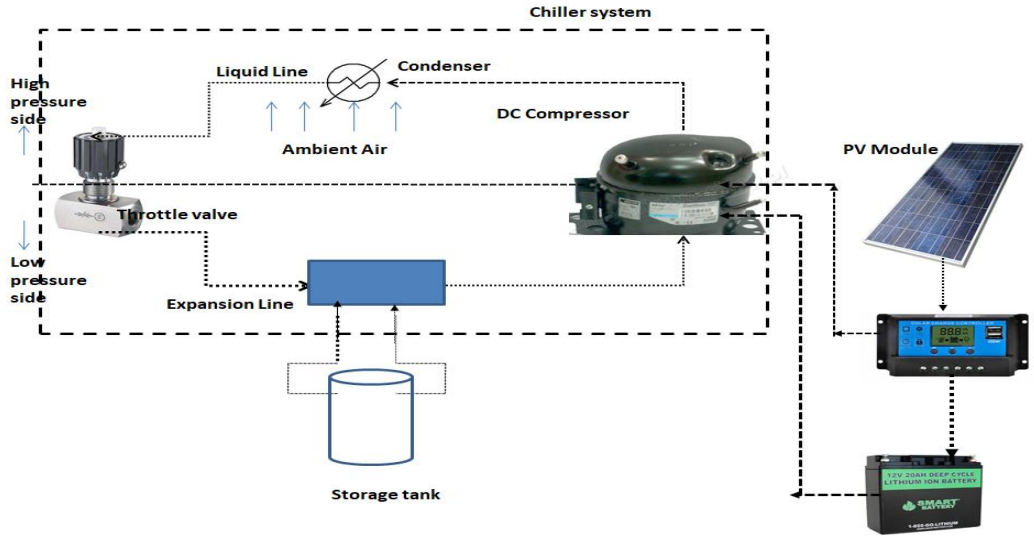

Fig.1 Basic Schematic of Experimental Setup

The detailed specification of the PV module used in the system is given in Table 1. Further, Lithium-ion battery of 12 V, 20 Ah is connected to the PV panel through a charge controller of rating 24 V, 30 A and to the chiller system which is used as a backup to store the excess energy when the intensity of sunlight is high and to provide the required energy for the operation of the compressor in the chiller system when the intensity of the sunlight is not sufficient to drive the compressor.

Table 1 Specification of 200 W_p PV module

Parameter	Values
Wattage (Wp)	200
Voltage at Max Power, Vmp (V)	20
Current at Max Power, Imp (A)	11.12
Open Circuit Voltage, Voc (V)	22
Short Circuit Current, Isc (A)	12.12
Number of Cells	36
Space requirement	14 Sq ft
Panel technology	Poly crystalline
Efficiency	15%
Standard	IEC
Life time	25 years

A DC compressor, evaporator, condenser and the expansion devices are the major components in the chiller unit. A Danfoss BD 35F, 12 V DC compressor particularly designed for the purpose of direct solar application, due to its "soft start" machinery with a minimum starting current of around 4 A to initially start the compressor is the uniqueness in the present setup. A highly efficient variable speed DC brushless motor drives the compressor and it is driven by the PV module directly (or) through discharging the energy from the battery. The rated speed of the motor is 2000 RPM with the maximum of 3500 RPM. The electronic control unit is adjusting the compressor and the motor speed. One advantage of this compressor is the ability to connect it directly to a PV or other source of DC energy supply without an inverter. The compressor is charged with the refrigerant "R134a". The evaporator of the chiller unit has its cooling coil immersed in the brine kept in a stainless steel tank insulated with polyurethane material.

In the evaporator the refrigerant is vaporized at a low pressure and temperature, by absorbing the heat from the brine. From the evaporator, the vapour is drawn by the compressor to a higher condenser pressure level. The superheated vapour enters the air-cooled condenser, where it condenses into the liquid phase while releasing heat to the ambient. Then the liquid refrigerant passes through an expansion valve and returned to the evaporator. In order to bring the chilled water temperature to -6°C, the evaporator temperature was set to -5°C. For the Chennai location the ambient temperature has an average value of almost 30°C and reaching 40°C in late summer. The cool thermal storage unit is used to store the cool energy and to deliver during the cooling demand in the non-sun shine hours. The value of the parameters of the storage unit integrated with the chiller system are shown in Table 2.

The radiation intensity was measured using the pyranometer (Delta Make LP PYRA 02) with a sensitivity of 10 μV/(W/m^2). Three RTDs (PT 100 – class A) with an accuracy of ± 0.1°C were used to measure the temperature of the brine in the storage tank and the ambient temperature. A DC ammeter, Voltmeter and digital DC energy meter were used to measure the generation side and load side electrical

parameters. The accuracy of voltmeter and ammeter are ± 0.02 V and ± 0.023 A respectively.

Table 2 Major parameters of the storage unit integrated with chiller system

Parameter	Value
Chiller capacity	100 W
Evaporator set temperature	-6°C
Evaporator cum storage tank capacity	25 liters
Storage material	Brine (80% Water + 20% mono ethylene glycol)
Storage tank insulation material	Polyurethane foam

Several experimental trials were performed to generate data in order to evaluate the performance of the system. All the trials experiments were conducted between 8 am and 4 pm. Initially the power is drawn from the battery to start the compressor. An on/off control unit is arranged so as to operate the compressor with the priority from solar PV panel directly. During the operation, the ammeter, voltmeter and energy meter readings were continuously monitored on the source and load side. The radiation intensity was continuously monitored through the pyranometer mounted near the solar PV panel that monitors the radiation intensity throughout the day. During this experiment initially the temperature of the brine in the evaporator was around 35°C and the temperature of the brine was decreased continuously with respect to time during the experiment. The temperature of the brine was monitored until the temperature reaches 6°C.

3. Experimental Procedure

In order to evaluate the optimal quantity of refrigerant to be charged in the developed solar powered DC compressor based chiller unit, experiments were performed with various masses of 20g, 25g, 30g, 35g, 40g & 45g of refrigerant R134a charged in the constructed system under other similar operating conditions. During all these experiments, initially the temperature of the brine in the chiller unit was maintained at 35°C and the system is allowed to operate between 11 am to 3 pm. During this time interval the solar radiation received by the solar module and the module power and voltage characteristics were observed to determine the module efficiency. The cooling capacity was evaluated based on the final temperature attained by the brine. The performance of the system under various mass of refrigerant were evaluated.

After evaluating the optimal quantity of charging in the chiller unit, the experiments were performed for the entire day during three different months of January, May & September for the year 2018. These months were selected because the radiation intensity level were highly different. During these experiments, if the solar energy generated by the PV unit is sufficient to run the DC compressor the energy generated will be utilized to produce cool energy in the chiller unit and if the power generated is not sufficient to drive the compressor the generated electricity will be utilized to charge the battery. Further, if the brine in the chiller unit attains –6°C during a day then the additional energy generated also will be utilized to charge the battery. Several experiments were performed to ensure the repeatability of the results.

4. Results and Discussion

Fig. 2 shows the variation of the ambient temperature and the solar intensity measured for a typical day in the months of January, May &

September, 2018 on which the other experimental results obtained from the chiller unit are reported. During the month of May the ambient temperature at 6:30 am is around 28.5°C and it reaches a maximum of 37.5°C at 2 pm, whereas the maximum temperature during the typical day in the months of September and January are only 27°C & 23°C respectively. The peak solar intensity in the month of May is 795 W/m^2 whereas it is 750 W/m^2 & 625 W/m^2 during the months of September and January respectively. Fig. 3 shows the power and voltage characteristics of the PV module used in the present experiment set up. In the month of January the P_{max} occurs at a voltage of 16 V and it delivers a maximum power of 130.6 W. In the month of September the maximum power delivered is 173.1 W at 17 V and during the month of May the maximum power delivered is 185.6 W at 19 V.

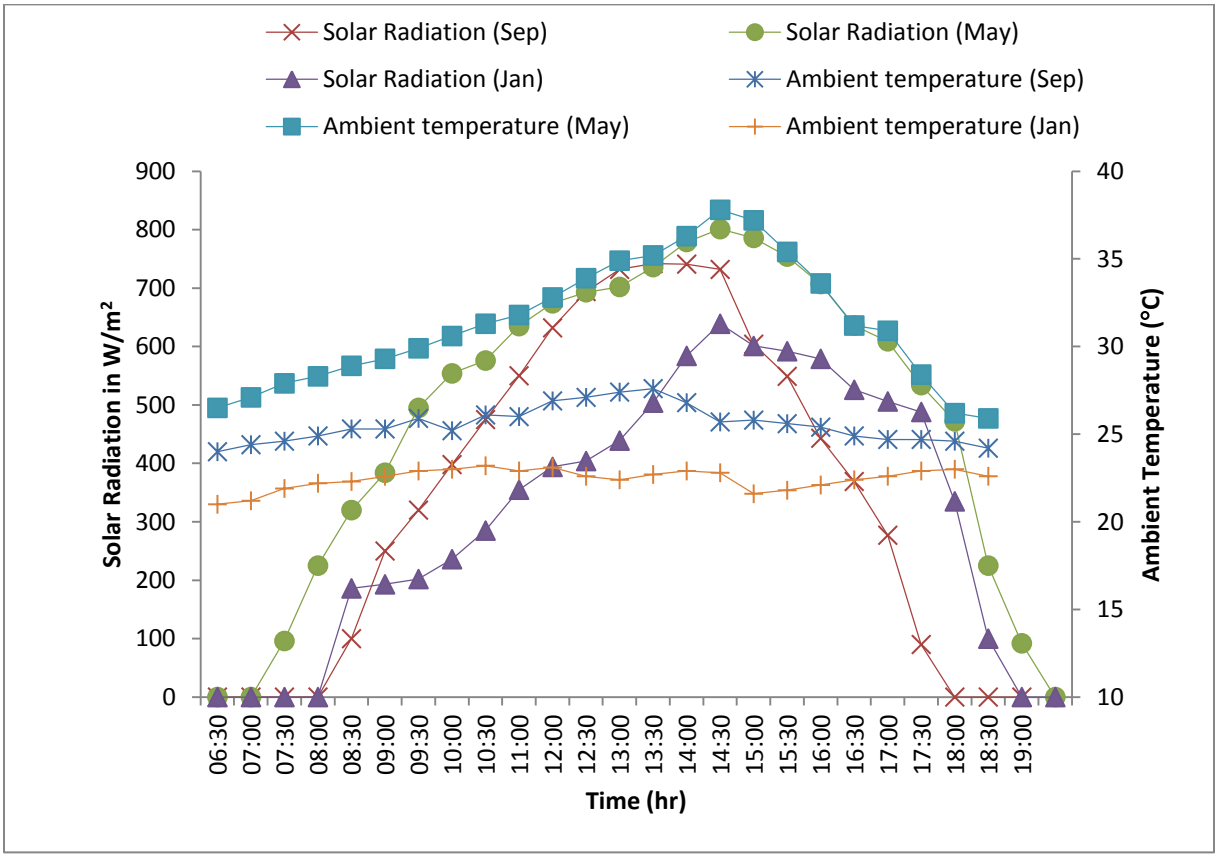

Fig. 2 Variation in Solar intensity and the ambient temperature with respect to time

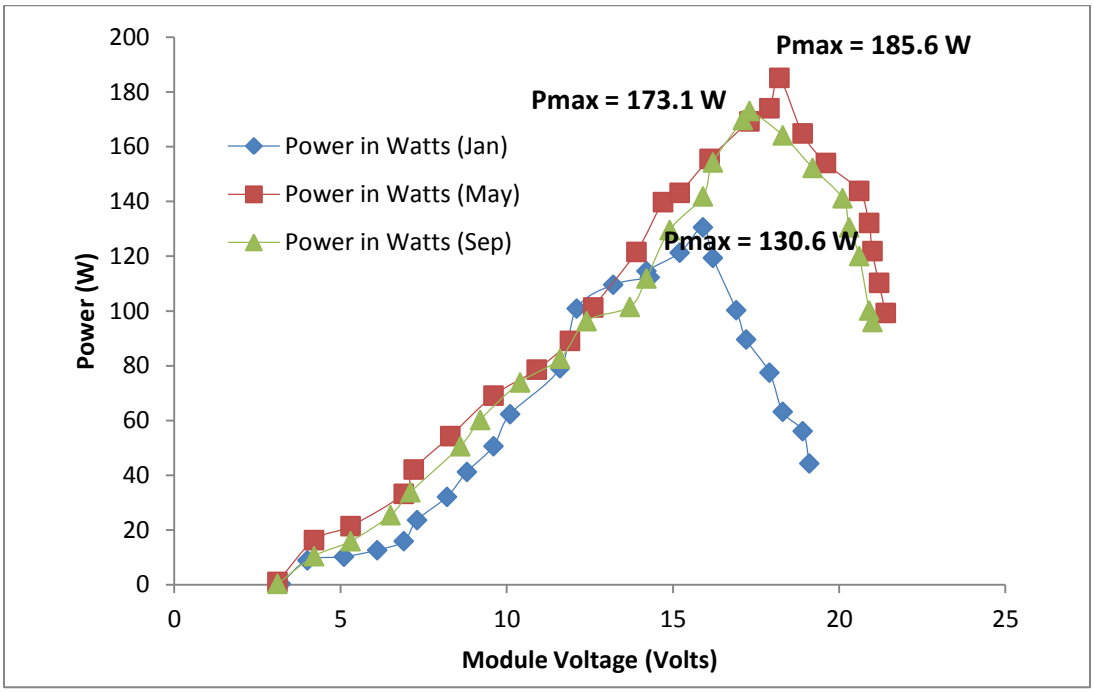

Fig. 3 Power and Voltage Characteristics of PV module

Fig. 4 shows the performance of the solar powered DC chiller unit representing the cooling capacity and the COP along with the power utilized under different mass of the refrigerant charged in the compressor. It is seen from the figure 4 that the average cooling capacity is only 60 W when the mass of the refrigerant is 20 g. Further, it is seen that the cooling capacity increases upto 75 W, when the mass of the refrigerant is increased upto 35 g and increasing the mass of the charge beyond this value does not contribute for further increase in cooling capacity. On the other hand there is a small increase in the average power consumption when the mass of the charge increases from 20 g to 45 g. Though this increase in power requirement is marginal on seeing the COP of the system, the maximum COP is seen when the mass of the refrigerant charged is 30 g. Hence, it is construed to perform the further experiments by charging the system with 30 g of refrigerant.

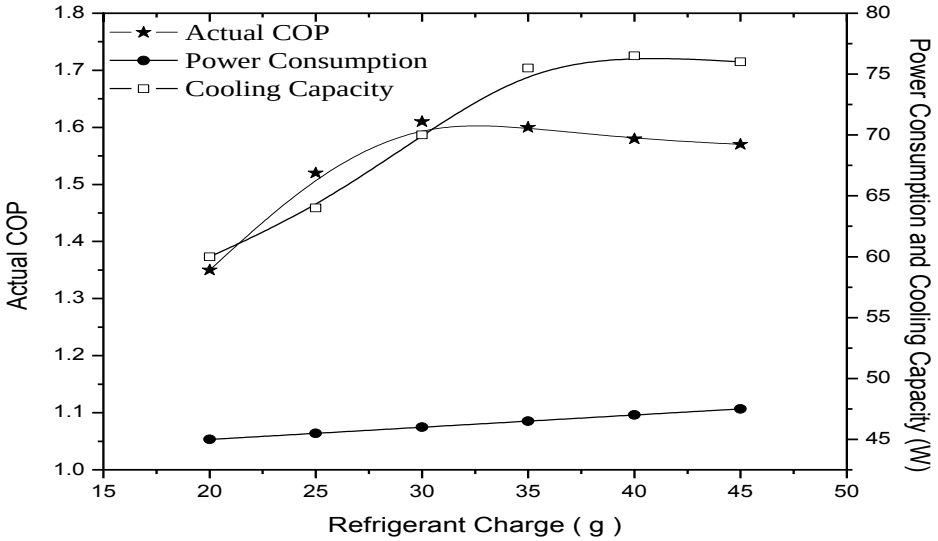

Fig. 4. Performance of the chiller under various mass of the refrigerant charged

Figure 5 shows the temperature variation of the brine in the cool storage tank. Initially the temperature of the brine in the cool storage tank was maintained at 35 °C in all the experiments. Though the experiments were commenced at 8 am, the compressor of the chiller unit was started, when sufficient power was generated from the PV panel to run the compressor. It is seen that during the month of January only after 4 hr the chiller unit was started and the temperature of the brine starts decreasing only after 4 hr from the start of the experiment. Hence, within a day the temperature could not be reduced to -6°C. The final temperature of the brine in the cool storage unit has only reached 1.3°C around 5 pm. In the month of May the brine in the evaporator tank reached -6°C before 3 pm and in the month of September the -6°C was attained by the brine around 4 pm. During these months if the compressor are not in operation the energy generated from the solar PV panel are used to store the energy in the Li-ion battery.

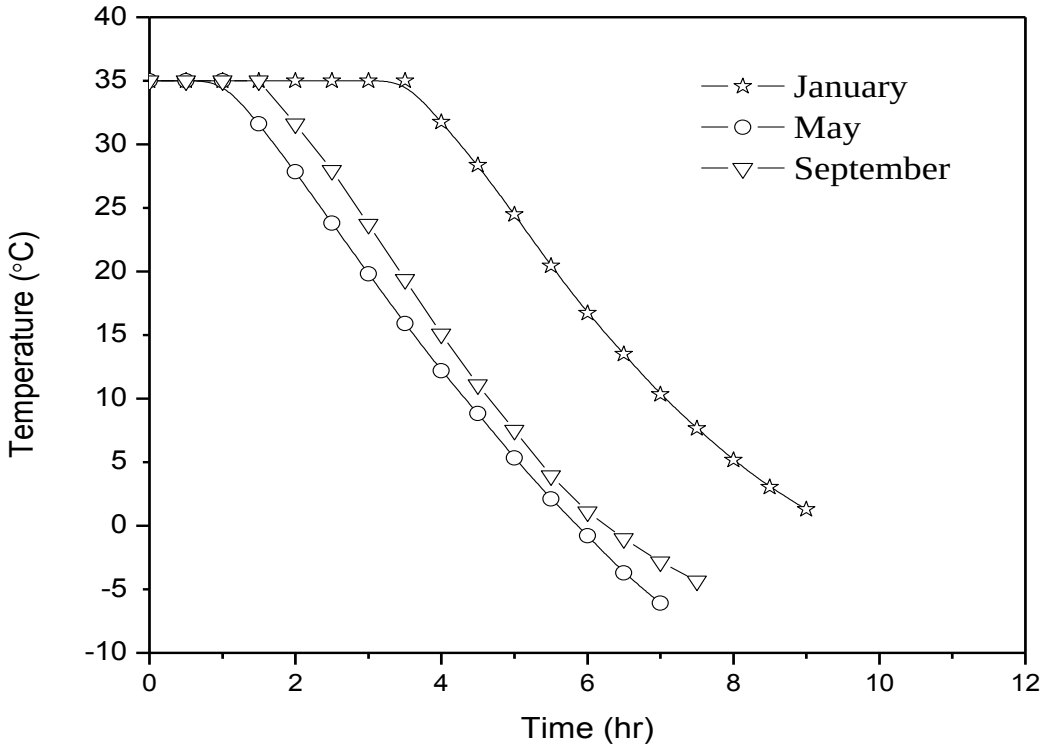

Fig. 5. Temperature variation of the brine in the evaporator during the charging process

The energy utilized to run the compressor for the purpose of cooling and the energy supplied to the battery for charging from the solar PV module are presented in fig. 6. It is seen from the figure that 0.54 kWh of energy is used to run the compressor and nearly 0.23 kWh of energy is used to charge the battery during the month of January. In the month of May, 0.792 kWh of energy generated from PV module is used to run the compressor and nearly 0.405 kWh energy generated is used to charge the battery. In the month of September, 0.738 kWh of energy is utilized to run the compressor and only a very small portion of 0.1 kWh of energy is stored in the battery.

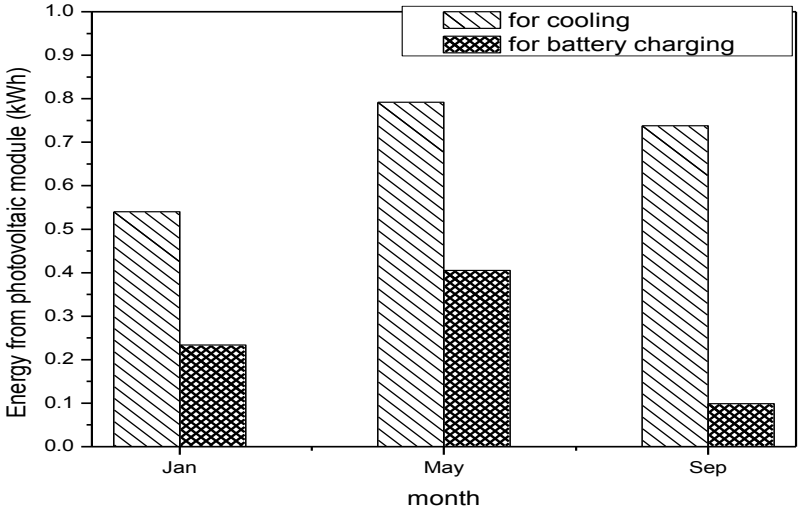

Fig. 6. Energy from PV module used for cooling and battery charging

The total energy generated from the solar PV module during the month of January, May & September are 0.774 kWh, 1,197 kWh & 0.837 kWh respectively. It could be seen that during the month of May & September the contribution by the solar PV module towards the cool energy generated is higher compared to the month of January. Normally during the month of December, the cool energy required for air conditioning also will be lesser and since the duration of the day lighting is lesser the electrical energy for lighting requirement will be more. Hence with the proper selection of the size of the system components such as solar PV module, chiller and the battery storage, it is possible to design a micro grid for various types of buildings.

5. CONCLUSIONS

In the present work a solar operated DC driven cool storage based chiller unit integrated with battery storage unit was constructed and its performance were analyzed. It is concluded that 25 liter of brine could be brought down to -6°C from 35°C using 100 W DC operated chiller and 200 W_p solar PV panel during the month of May & September. In the month of January since the operational duration of the compressor is less the brine was brought down only to a temperature of 1.3°C. In addition to the cool energy generated, 0.234 kWh, 0.405 kWh & 0.1 kWh of electrical energy generated was also charged in the battery during the months of January, May & September respectively. The demonstration of the present set up with the experimental results will be very useful for the solar, air conditioning and building engineers to extend their

services for the design and development of RE based micro grid in the building sector.

ABBREVIATIONS

CTES	:	Cool Thermal Energy Storage
DC	:	Direct Current
ES	:	Energy Storage
FMC	:	farm milk chillers
HVAC	:	Heating Ventilation and Air Conditioning
W	:	watt
kW	:	Kilowatt
hr	:	hour
Li-ion	:	Lithium-ion
PV	:	Photovoltaic
RE	:	Renewable Energy
TES	:	Thermal Energy Storage
V	:	Volt
VCR	:	Vapor Compression Refrigeration

ACKNOWLEDGEMENT

The authors are highly thankful to the RUSA, State Project Directorate, Government of Tamil Nadu and Ministry of Human Resource Development, Government of India, for the financial grant and support rendered.

REFERENCES

1. I. Daut, M. Adzrie, M. Irwanto, P. Ibrahim and M. Fitra, "Solar Powered Air Conditioning System", *Energy Procedia*, vol. 36, pp. 444 – 453, 2013.
2. M. Sahoo & I. S. Rout, "Design, fabrication and performance analysis of solar PV air conditioning system", *International Journal of Scientific and Research Publications*, vol.6, Issue 10, pp.277-282, 2016.
3. L.A. Chidambaram, A.S. Ramana, G. Kamaraj, and R. Velraj, "Review of solar cooling methods and thermal storage options", *Renewable and Sustainable Energy Reviews*, vol.15, pp. 3220-3228, 2011.
4. R. Foster, B. Jensen, B. Dugdill, W. Hadley, B. Knight, A. Faraj and J. K. Mwove, "Direct Drive Photovoltaic Milk Chilling Experience in Kenya," *IEEE Photovoltaic Specialists Conference* 44, Paper #575 Washington DC, June 28, 2017.
5. A. A. M. El-Bahloul, A. H. H.Ali, and S. Ookawara, "Investigation of the performance of solar driven refrigerator for post harvest crops in hot arid remote areas," *New Borg El-Arab*, 2014.
6. A. Modi, A. Chaudhuri, B. Vijay, and J. Mathur, "Performance analysis of a solar photovoltaic operated domestic refrigerator", *Appl. Energy*, vol. 86, Issue 12, pp. 2583–2591, 2009.
7. P. J. Axaopoulos and M. P. Theodoridis, "Design and experimental performance of a PV Ice-maker without battery", *Sol. Energy*, vol. 83, Issue 8, pp. 1360– 1369, 2009.
8. O. Ekren, S. Celik, B. Noble and R. Krauss, "Performance evaluation of a variable speed DC compressor", *Int. J. Refrig*., vol. 36, Issue 3, pp. 745–757, 2013.
9. A. N. N. Chedop, N. Djongyang, Z. Abdelouahab, "Modeling of the performance of a solar electric vapor compression refrigeration system in dry tropical regions", *International journal of Science and Research*,vol. 3, Issue 11, pp. 1066-1076, 2014.
10. M. D. Blas, J. Appelbaum, J. L. Torres, A. Garcia, and A. D. Francisco, "Characterization of an electric motor directly coupled to a photovoltaic solar array in a refrigeration facility for milk cooling", *Biosystems Engineering*, vol. 95, Issue 3, pp. 461-471, 2006.

Stability Analysis of Network Controlled Micro-Grid Systems with Communication Delays and Nonlinear Perturbations

D. Vijeswaran
TANGEDCO
Coimbatore 641012, India
vijeswaran72@gmail.com

V. Manikandan
Department of EEE, CIT
Coimbatore 641014, India

***Abstract*—In this paper, the problem of delay-dependent stability of micro-grid load frequency control systems under networked environment with time-invariant delays and bounded nonlinear perturbations has been addressed using the Lyapunov-Krasovskii functional approach. In the networked control environment, it is observed that transfer of feedback variable from the sensor to centralized controller, and the control effort from controller back to the actuator through communication links introduces time-delays in the feedback path. The time-delays adversely affect the overall performance of the closed-loop system paving way to system instability. In addition, in distributed generation scenario, the uncertainties in the time-delayed micro-grid system brought about by the penetration of fluctuating power generators, viz., solar and wind power combined with perturbations in the system load also affect the performance of the overall system. To assess the impact of these time-varying uncertainties to the closed-loop stability of the micro-grid system, they are included in the mathematical model of the system as a norm-bounded nonlinear perturbation term. Subsequently, the stated problem is solved in a less conservative manner by employing the classical Lyapunov-Krasovskii functional approach combined with Wirtinger inequality. The analysis results in a delay-dependent stability criterion in linear matrix inequality (LMI) framework. In the sequel, the presented stability criterion is validated on a standard benchmark system and supported with extensive simulation results.**

***Index Terms*—Delay-dependent stability, Time-delays, Communication network, Nonlinear perturbations, Lyapunov-Krasovskii functional, Linear Matrix Inequality (LMI).**

I. Introduction

IN the last decade, a paradigm shift in the topology of conventional power system has taken place, and the modern power system has evolved in the form of small pockets of independent entities called micro-grids. A typical microgrid system connected to utility grid encompasses several distributed and interconnected generator units, energy storage units, and loads. Different types of the distributed generation sources include micro-turbine, wind-turbine, solar PV panel, fuel cell with electrolyzer system etc. The load essentially consists of domestic and small/medium-scale industrial loads. The energy storage unit, an optional entity, usually includes batteries, flywheels, super-capacitors, super conducting magnetic energy storage, plug-in-electrical vehicles etc., refer [1], [2]. From the grid perspective of the modern power system, a micro-grid system can be considered as a group of controllable generator units and associated loads; refer [3], and the references cited therein. With increasing penetration of renewable energy sources into the utility grid, given their environment dependent power generation characteristics, design and control of distributed generation in micro-grid environment have become quite complicated; nevertheless, owing to the challenges involved in the process, it has invariably emerged as an active area of research in recent times. The advantages of the micro-grid system include increase in reliability and security of the power system, decrease in the cost of operation by effectively utilizing the micro-sources during peak load condition, base load support and reduction in green house effects.

In this paper, a networked micro-grid closed-loop load frequency control system with time-invariant approximation for delay is investigated for its delay-dependent stability. In this system, wind and PV generators serve as primary sources of electric power. As power from these renewable sources are intermittent in nature, a gas based micro-turbine unit is employed cater the base load. In addition, when unexpected real power imbalance occurs in power system, regulation of grid frequency may not be possible with micro-turbine itself; in such a scenario, for frequency compensation, a fuel cell and electrolyzer system are appropriately integrated into the micro-grid system. This system model is taken from [3].

In micro-grid systems, to compensate for continuous change in load demand, real power generation control is required to keep the frequency constant since incremental frequency variable ($\Delta f(t) = f(t) - f_e$) is an indication of the in-balance that exists between the generation and the demand [4]. To accomplish this objective, load frequency control (LFC) control strategy is employed so that all distributed generation units are operated and controlled cohesively to ensure a stable operation with desirable frequency and voltage profile in the system [5]. This task is facilitated in a micro-grid system through a remotely operated micro-grid central controller (MGCC). The main functions of this centralized control are to obtain measurement from the power system and control information from local controllers, and to decide and implement necessary

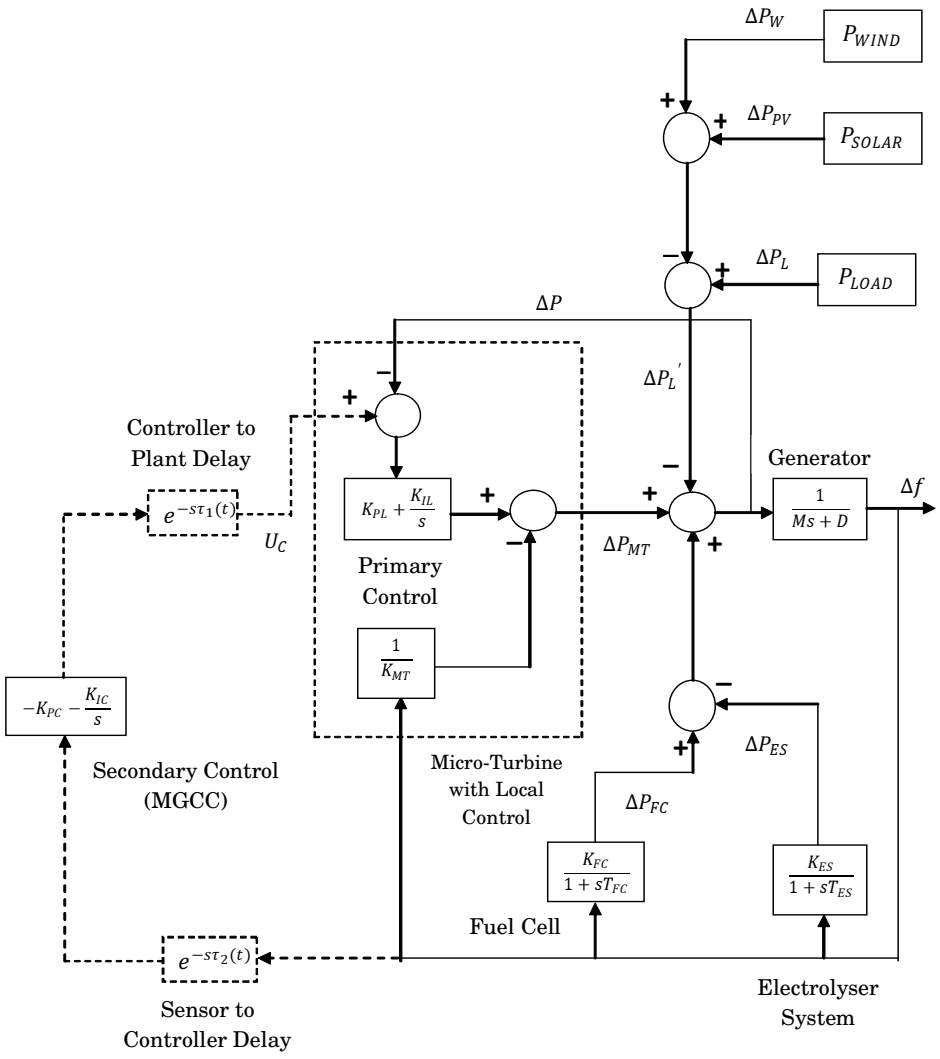

Fig. 1. Block Diagram of Micro-Grid System with Communication Delays.

control actions for regulating the system frequency to the desired value. Since solar and wind power sources constantly generate shortfalls and excesses, MGCC, from the measurement of $\Delta f(t)$, sends appropriate control signal automatically to local controllers in micro-grid to ensure that total amount of power demand at grid is consistently equal the total power supply (i.e. $\Delta f(t) \rightarrow 0, \forall\ t$). This centralized automatic control loop is configured in networked control framework with information exchange carried out through communication channels; this orientation, in turn, introduces time-delays in the feedback path as shown in Fig. 1.

The feedback loop delays are inevitable in such a distributed system scenario where the system to be controlled and the controller that executes the control action are connected through a communication channel in which the measured/controlled data that are realized in the form of discrete pockets of information experience buffering, processing and propagation at various internodes. These network-induced feedback loop delays pose serious limitations to achievable performance of the closed-loop system; in dire situations, when the delay margin exceeds a critical value, the micro-grid system will be driven to instability, and subsequently, it automatically trips from the main grid. The loss of synchronism may sometimes generate low frequency high amplitude power swings in the power system paving way for catastrophic tripping of various generation units connected to the grid leading to islanding of regional power grids, and sometimes, blackouts [6], [7].

Hence, stable delay margin (i.e. maximum allowable delay bound that the networked controlled system can accommodate without losing asymptotic stability) for networked micro-grid systems must be computed for various subsets of controller parameters through a less conservative delay-dependent stability analysis procedure so that they will serve as a practical guideline for fine tuning of controller parameters at the implementation stage even with partial knowledge about network delay size [8]. This, in turn, will enable the operating personnel

to achieve optimal performance from the closed-loop LFC system under delayed control inputs. In this direction, from the perspective of fluctuating power generators, the undertaken study is a capacity management problem; hence, it is significant. Delay-dependent stability criteria are basically sufficient conditions that are employed to compute the stable margin for the network delays within which the power system controlled through a remote MGCC remains asymptotically stable in the sense of Lyapunov.

In this paper, using the classical Lyapunov-Krasovskii functional approach [9] combined with Wirtinger inequality, a less conservative stability criterion is presented for ascertaining delay-dependent stability of the networked micro-grid load frequency control system with time-invariant delays. In the presented analysis, the controller to actuator delay $\tau_1(t)$ and sensor to controller delay $\tau_2(t)$ (see, Fig. 1) are assumed to be time-invariant (i.e., $\tau_i(t) = \tau_i,\ i = 1,\ 2\ \forall t$); hence, they are treated as a single feedback loop delay $\tau = \sum_{i=1}^{2} \tau_i$. Furthermore, the environment dependent power generation from non-conventional distributed sources solar and wind introduces unmodelled time-varying dynamics into the system. In this paper, we have considered these uncertainties by modelling them as bounded nonlinear perturbations with respect to state variables of the system. This is the novelty of the paper.

In literature, there are two results reported in recent times for ascertaining delay-dependent stability of micro-grid systems that involve communication delays [3], [10]. However, in both these results, the impact of load perturbation on system stability is not considered in the stability analysis. The stability analysis presented in [3] and [10] are derived only for nominal systems - systems without any uncertainties. This has motivated the authors to explore the networked micro-grid system for assessing impact of load perturbations on the system performance and stability. In this aspect, to the best of authors$^{'}$ knowledge, we wish to record that the problem of delay-dependent stability of networked micro-grid system with time-invariant delays and time-varying nonlinear perturbations has not been addressed using Lyapunov-Krasovskii functional approach so far.

II. Mathematical Modelling

The mathematical model of various components of the micro-grid control system are presented herewith.

A. Gas-Based Micro-Turbine

The transfer function model the micro-turbine is developed taking into account the linear speed drop characteristics between the power and frequency. This transfer function is given as follows:

$$G_{MT}(s) = \frac{\Delta P_{MT}}{\Delta f} = -\frac{1}{K_{MT}} \tag{1}$$

where Δf, ΔP_{MT} and K_{MT} represent frequency deviation, change in output power and drop characteristics of the micro-turbine, respectively.

B. Fuel Cell and Electrolyzer

A fuel cell with an electrolyzer system is utilized to compensate for real power imbalance when the local controller of the micro turbine becomes less effective for substantial variations in load. A part of the wind power is utilized by the aqua electrolyzer to produce hydrogen for fuel cell. The transfer function model of fuel cell and electrolyzer are given as follows:

$$G_{FC}(s) = \frac{\Delta P_{FC}}{\Delta f} = \frac{K_{FC}}{1 + sT_{FC}}, \tag{2}$$

$$G_{ES}(s) = \frac{\Delta P_{ES}}{\Delta f} = \frac{K_{ES}}{1 + sT_{ES}}, \tag{3}$$

where ΔP_{FC}, K_{FC} and T_{FC} represent the change in output power, the gain, time constant of the fuel cell, respectively, while ΔP_{ES}, K_{ES} and T_{ES} denote similar variables of the electrolyzer.

C. Extended Load

The extended load demand $\Delta P_L^{'}$ consists of housing load, wind power and PV generation; it is expressed as follows:

$$\Delta P_L^{'} = \Delta P_L - \Delta P_{PV} - \Delta P_W. \tag{4}$$

The dynamics of PV and wind power are considered as nonlinear perturbations in the test system employed for study. These uncertainties do substantially affect delay margins results.

D. Local and Central Controller

The local and micro-grid central controller ($G_{LC}(s)$ and $G_{CC}(s)$ respectively) are configured with PI control law. The controller transfer functions are given below:

$$G_{LC}(s) = K_{PL} + \frac{K_{IL}}{s}, \tag{5}$$

$$G_{CC}(s) = K_{PC} + \frac{K_{IC}}{s}, \tag{6}$$

where K_{PX} and K_{IX} represent proportional and integral gains of the controller.

E. Power System

The power system with its connected conventional (high inertia) generators is modelled as a first order transfer function given by

$$G_P(s) = \frac{1}{sM + D}, \tag{7}$$

where M and D are moment of inertia and damping constant respectively.

F. State-Space Model

The overall system including central and local controller encompassing network-induced delay is shown in Fig. 1. The state-space model of the closed-loop system shown in Fig. 1 can be derived in the following autonomous framework:

$$\dot{x}(t) = Ax(t) + A_d x(t - \tau) + \omega(t), \tag{8}$$

$$x(t) = \phi(t), t \in [-\max(\tau), 0], \tag{9}$$

$$\int_b^a \dot{\omega}^T(u)R\dot{\omega}(u)du \geq \frac{1}{b-a}\begin{bmatrix} \omega(b) \\ \omega(a) \\ \frac{1}{b-a}\int_a^b \omega(u)du \end{bmatrix}^T \begin{bmatrix} 4R & 2R & -6R \\ \star & 4R & -6R \\ \star & \star & 12R \end{bmatrix} \begin{bmatrix} \omega(b) \\ \omega(a) \\ \frac{1}{b-a}\int_a^b \omega(u)du \end{bmatrix}.$$

where the system matrices $A \in \mathbb{R}^{5\times5}$ and $A_d \in \mathbb{R}^{5\times5}$ are as follows:

$$A = \begin{bmatrix} 0 & 0 & 0 & 0 & K_{IC} \\ a_{21} & a_{22} & a_{23} & a_{24} & a_{25} \\ 0 & 0 & -\frac{1}{T_{FC}} & 0 & \frac{K_{FC}}{T_{FC}} \\ 0 & 0 & 0 & -\frac{1}{T_{ES}} & \frac{K_{ES}}{T_{ES}} \\ 0 & \frac{1}{M} & \frac{1}{M} & -\frac{1}{M} & \frac{D}{M} \end{bmatrix}, \quad (10)$$

$$A_d = \begin{bmatrix} 0 & 0 & 0 & 0 & 0 \\ d_{21} & d_{22} & d_{23} & d_{24} & d_{25} \\ 0 & 0 & 0 & 0 & 0 \\ 0 & 0 & 0 & 0 & 0 \\ 0 & 0 & 0 & 0 & 0 \end{bmatrix}, \quad (11)$$

with state vector $x(t) \in \mathbb{R}^{5\times1}$ being $x(t) = [K_{IC}\int \Delta f(t)dt \quad \Delta P_{MT}(t) \quad \Delta P_{FC}(t) \quad \Delta P_{ES}(t) \quad \Delta f(t)]^T$. The elements of the matrices (in terms of system parameters) are given below:

$$\begin{aligned}
a_{21} &= 0, \\
a_{22} &= \frac{1}{1+K_{PL}}\Big[-K_{IL} - \frac{1}{MK_{MT}}\Big], \\
a_{23} &= \frac{1}{1+K_{PL}}\Big[\frac{K_{PL}}{T_{FC}} - K_{IL} - \frac{1}{MK_{MT}}\Big], \\
a_{24} &= \frac{1}{1+K_{PL}}\Big[-\frac{K_{PL}}{T_{ES}} + K_{IL} + \frac{1}{MK_{MT}}\Big], \\
a_{25} &= \frac{1}{1+K_{PL}}\Big[-\frac{K_{PL}K_{FC}}{T_{FC}} + \frac{K_{PL}K_{ES}}{T_{ES}} + \frac{D}{MK_{MT}}\Big], \\
d_{21} &= -\frac{K_{IL}}{1+K_{PL}}, \\
d_{22} &= -\frac{K_{PL}K_{PC}}{M(1+K_{PL})}, \\
d_{23} &= -\frac{K_{PL}K_{PC}}{M(1+K_{PL})}, \\
d_{24} &= \frac{K_{PL}K_{PC}}{M(1+K_{PL})}, \\
d_{25} &= \frac{1}{1+K_{PL}}\Big[-K_{IL}K_{PC} + \frac{K_{PL}K_{PC}D}{M} - K_{PL}K_{IC}\Big].
\end{aligned}$$

The time-delay satisfies the following condition:

$$0 \leq \tau \leq \bar{\tau}; \quad (12)$$

where $\bar{\tau}$ is the upper bound of the time-delay.

III. Main Result

The proposed result of this paper is derived by modelling unknown extended power system load disturbance as time-varying nonlinear perturbation in terms of current and delayed state vector. The term $\omega(t)$ represents the uncertainties caused due to the intermittent penetration of solar and wind power to the micro-grid and load perturbation as well. It is treated as a function of state-variables as follows:

$$\omega(t) = \omega(t, x(t), x(t-\tau)), \quad (13)$$

satisfying the following norm-bounded condition:

$$||\omega(\cdot)|| \leq \alpha||x(t)|| + \beta||x(t-\tau)||, \quad (14)$$

where $\alpha \geq 0$ and $\beta \geq 0$ are known scalars. A somewhat restricted version of the condition (14), which is used in this paper, is given by

$$\begin{aligned}
\omega^T(\cdot)\omega(\cdot) &\leq \alpha^2 x^T(t)G^TGx(t) \\
&+ \beta^2 x^T(t-\tau)F^TFx(t-\tau), \quad (15)
\end{aligned}$$

where G and F are known constant matrices of appropriate dimensions. The problem addressed in this paper is stated below:

Problem: *To develop a less conservative robust stability criterion in LMI framework to ascertain delay-dependent stability of the networked micro-grid system described by the state-space model (8) with the load disturbance satisfying the condition (14), and network-induced time-delay (12) using Lyapunov-Krasovskii functional approach.*

For deriving the delay-dependent stability criterion, following lemma is required:

Lemma 1. *For given symmetric positive definite matrix R, and for any differentiable signal ω in $[a,\ b] \to \mathcal{R}^n$, the Wirtinger inequality stated at the top of this page holds.*

The proposed delay-dependent stability criterion is stated in the form of a theorem.

Theorem 1. *For a given delay bound τ, networked micro-grid frequency control system (8) with time-delay (12) and nonlinear perturbation (14) is asymptotically stable in the sense of Lyapunov, if there exist real, symmetric, positive definite matrices P, S and R; symmetric matrix Z and free matrix Q of appropriate dimensions and scalar $\epsilon > 0$ such that following LMIs hold:*

$$\Pi(\tau) > 0, \quad (16)$$

$$\Phi(\tau) < 0, \quad (17)$$

where $\Phi(\tau) = \sum_{i=1}^{4}\Phi_i(\tau)$. The elements of $\Phi_i(\tau)$, $i = 1$ to 4 are given at the top of next page, where $\star$ represents transposed terms in the symmetric matrix.

Proof: The proof of this stability criterion employs the following LK functional (positive definite energy functional):

$$\begin{aligned}
V(t) &= \begin{bmatrix} x(t) \\ \int_{t-\tau}^t x(s)ds \end{bmatrix}^T \begin{bmatrix} P & Q \\ \star & Z \end{bmatrix} \begin{bmatrix} x(t) \\ \int_{t-\tau}^t x(s)ds \end{bmatrix} \\
&+ \int_{t-\tau}^t x^T(s)Sx(s)ds + \int_{-\tau}^0\int_{t+\theta}^t \dot{x}^T(s)R\dot{x}(s)dsd\theta. \quad (18)
\end{aligned}$$

$$
\begin{aligned}
\Pi(\tau) &= \begin{bmatrix} P & Q \\ \star & Z + \frac{1}{\tau} S \end{bmatrix}, \\
\Phi_1(\tau) &= \begin{bmatrix} A^T P + PA + Q + Q^T + S & -Q + PA_d & \tau A^T Q + \tau Z & P \\ \star & -S & \tau A_d^T Q - \tau Z & 0 \\ \star & \star & 0 & \tau Q^T \\ \star & \star & \star & 0 \end{bmatrix}, \\
\Phi_2(\tau) &= \begin{bmatrix} A^T \\ A_d^T \\ 0 \\ I \end{bmatrix} (\tau R) \begin{bmatrix} A^T \\ A_d^T \\ 0 \\ I \end{bmatrix}^T, \\
\Phi_3(\tau) &= -\frac{1}{\tau} \begin{bmatrix} R & -R & 0 & 0 \\ \star & R & 0 & 0 \\ \star & \star & 0 & 0 \\ \star & \star & \star & 0 \end{bmatrix} - \frac{1}{\tau} \begin{bmatrix} 3R & 3R & -6R & 0 \\ \star & 3R & -6R & 0 \\ \star & \star & 12R & 0 \\ \star & \star & \star & 0 \end{bmatrix}, \\
\Phi_3(\tau) &= \begin{bmatrix} \epsilon \alpha^2 F^T F & 0 & 0 & 0 \\ \star & \epsilon \beta^2 G^T G & 0 & 0 \\ \star & \star & 0 & 0 \\ \star & \star & \star & -\epsilon I \end{bmatrix}.
\end{aligned}
$$

By bounding the time-derivative of the LK functional with Wirtinger inequality stated in Lemma 1, and including the constraint imposed on non-linear perturbation term (14), the delay-dependent stability criterion is derived. For detailed derivation, [11] and [12] may be referred simultaneously. □

IV. Benchmark Micro-grid System

The parameters of the standard benchmark system taken from [3] are given in Table I.

TABLE I
NOTATIONS

Parameter	Value
M	10
D	1
K_{MT}	0.04
K_{FC}	1
T_{FC}	4
K_{ES}	1
T_{ES}	1
K_{PL}	1
K_{IL}	1

For this system, the maximum delay bound $\bar{\tau}$ of the time-varying delay for different sub-set of the centralized controller parameters (K_{PC}, K_{IC}) obtained by the delay-dependent stability criterion stated in Theorem 1 is given in Table II. The analytical results are validated using simulation based study. The simulation based study assumes white noise model for intermittent power output from renewable sources viz., wind and solar. Since power electronics based converters are invariably employed for interface with power system grid, this assumption is appropriate. The micro-grid central controller parameters are set at $K_{PC} = 1$ and $K_{IC} = 0.8$. The uncertain extended load demand through out the study is kept

TABLE II
MAXIMUM UPPER DELAY BOUND $\bar{\tau}$ FOR $F = G = 0.1 I_{5\times5}$

K_{PC}	$\alpha = 0, \beta = 0$		$\alpha = 0, \beta = 0.05$		$\alpha = 0.05, \beta = 0.05$	
	K_{IC}	$\bar{\tau}$	K_{IC}	$\bar{\tau}$	K_{IC}	$\bar{\tau}$
1.0	0.2	9.943	0.2	6.753	0.2	5.477
	0.4	5.264	0.4	3.240	0.4	2.408
	0.6	3.664	0.6	2.076	0.6	1.415
	0.8	2.857	0.8	1.511	0.8	0.947
	1.0	2.371	1.0	1.184	1.0	0.684
2.0	0.2	12.688	0.2	10.097	0.2	9.103
	0.4	7.155	0.4	5.347	0.4	4.606
	0.6	5.053	0.6	3.574	0.6	2.957
	0.8	3.949	0.8	2.667	0.8	2.127
	1.0	3.270	1.0	2.122	1.0	1.637

at $P_L' \in [0.4,\ 0.6]$, and time-delay is kept initially at $\tau = 0$; at this condition, the system is assumed to be at the equilibrium state with $\Delta f(t) = 0$. The closed-loop system is introduced with a sudden step change in time-delay at $t = 200secs$. For validating the stable closed-loop operation, the time-delay τ is increased from 0 secs to 2.6 secs. The maximum allowable delay bound, in accordance to Table II, for the chosen MGCC parameters, is $\bar{\tau} = 2.857secs$. Since $\tau = 2.6 < \bar{\tau}$, the incremental frequency variable $\Delta f(t)$ evolves asymptotically towards equilibrium point $\Delta f(t) = 0$ as shown in Fig. 2. If the delay τ is increased to $\bar{\tau} = 2.857$, the system is marginally stable as shown in Fig. 3, and if the delay is further increased to $\tau = 3 > \bar{\tau}$, the micro-grid system becomes unstable with $\Delta f(t)$ variable evolving unboundedly with time t as shown in Fig. 4. These results clearly substantiate the impact of time-invariant delay on the performance and stability of the networked micro-grid load frequency control system, thereby validating the presented stability analysis.

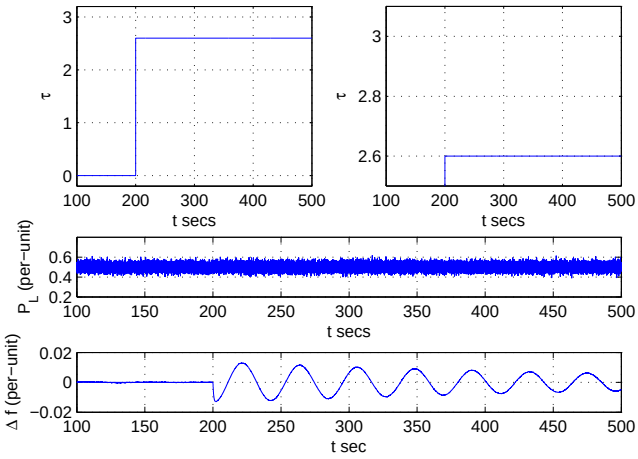

Fig. 2. Time-domain Simulation for $\tau = 2.6$ secs.

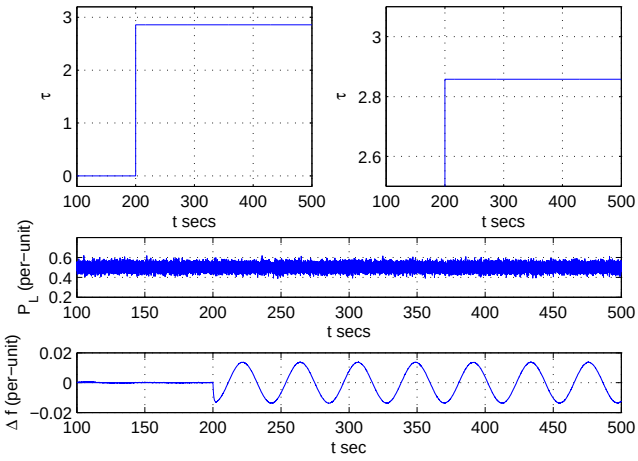

Fig. 3. Time-domain Simulation for $\tau = 2.857$ secs.

V. Conclusions

In this paper, a less conservative stability analysis has been presented for ascertaining delay-dependent stability of networked micro-grid load frequency system with time-delays that emerges due to the communication channels employed in the feedback path, and nonlinear perturbations due to fluctuating power generators connected to the micro-grid system. The presented analysis is based on Lyapunov-Krasovskii functional approach combined with Wirtinger inequality, and the resulting stability criterion is expressed in LMI framework. The nonlinear perturbation term in the mathematical model depicting the uncertainties in the fluctuating power generators is norm-bounded, and they are associated with appropriate scaling factors to quantify the magnitude of the disturbance in the micro-grid system. The proposed stability criterion is illustrated on a standard bench mark system and substantiated with appropriate simulation results. The possibility of alleviating the limitations of the presented results may be explored as a future work.

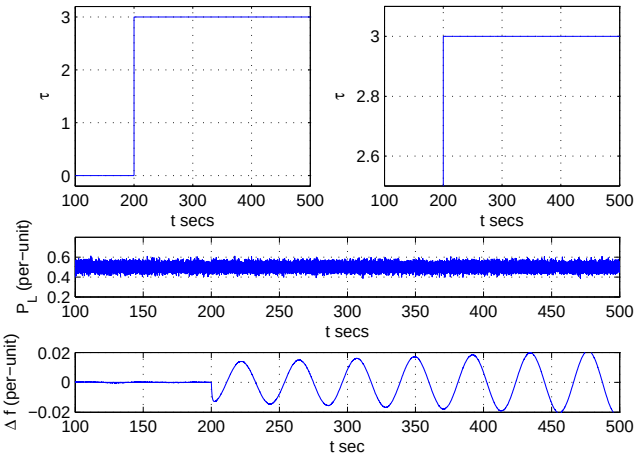

Fig. 4. Time-domain Simulation for $\tau = 3$ secs.

References

[1] M. S. Mahmoud, S. Azher Hussain, and M. A. Abido, Modeling and control of microgrid: An overview, *Journal of The Franklin Institute*, Vol. 351, No. 5 , pp. 2822–2859, 2014.

[2] Ashraf Khalil, Zakariya Rajab, Asma Alfergani, and Omar Mohamed, The impact of the time delay on the load frequency control system in microgrid with plug-in-electric vehicles, *Sustainable Cities and Society*, Vol. 35, pp. 365–377, 2017.

[3] Hakan Gunduz, Sahin Sonmez, and Saffet Ayasun, Comprehensive gain and phase margins based analysis of micro-grid frequency control system with constant communication time delays, *IET Generation, Transmission & Distribution*, Vol. 11, No. 3, pp. 719–729, 2017.

[4] P. Kundur, *Power system stability and control*, McGraw-Hill, 1994.

[5] L. Jiang, W. Yao, Q. H. Wu, J. Y. Wen, S. J. Cheng. Delay-Dependent Stability for Load Frequency Control With Constant and Time-Varying Delays, *IEEE Transactions on Power Systems*, Vol. 27, No. 2, pp. 932–941, 2012.

[6] R. A. Zamora, K. Srivatsava, Control of micro-grids with storage: review, challenges and research needs, *Renewable and Sustainable Energy Reviews*, Vol. 14, No. 7, pp. 2009–2018, 2010.

[7] Olle I. Elgerd. *Electrical Energy Systems Theory: An Introduction*, McGraw-Hill, 1971.

[8] M. Wu, Y. He, and J. H. She, *Stability Analysis and Robust Control of Time-Delay Systems*. Science Press Beijing and Springer-Verlag Berlin Hiedelberg, 2010.

[9] J. P. Richard, Time-delay systems: An overview of some recent advances and open problems, *Automatica*, Vol. 39, pp. 1667-1694, 2003.

[10] T. Jesintha Mary and P. Rangarajan, Delay-dependent Stability Analysis of Microgrid with Constant and Time-varying Communication Delays, *Electric Power Components and Systems*, Vol. 44, No. 13, pp. 1441–1452, 2016.

[11] A. Seuret, F. Gouaisbaut, Wirtinger-based integral inequality: Application to time-delay systems, Automatica 49, Issue No. 9 (2013), 2860–2866.

[12] K. Ramakrishnan, G. Ray, Stability criteria for nonlinearly perturbed load frequency systems with time-delay, IEEE Journal on Emerging and Selected Topics in Circuits and Systems Volume 5, Issue No. 3 (2015), 383–392.

INDIAN RENEWABLE POWER SECTOR: POTENTIAL, POLICIES, BARRIERS, AND ITS PROSPECTIVE

T. BOGARAJ[1], Dr. J. KANAKARAJ[2]
[1]Assistant Professor, Department of Electrical and Electronics Engineering, PSG College of Technology, Coimbatore, Tamil Nadu, India 9443806325, tbr.eee@psgtech.ac.in
[2]Professor, Department of Electrical and Electronics Engineering, PSG College of Technology, Coimbatore, Tamil Nadu, India 9443654496, jkr.eee@psgtech.ac.in

Abstract: *Increasing prices, green house gas emission, and depleting nature of fossil fuel makes the world to think about alternate sources of energy particularly renewable energy sources which are green sources, and freely available. Carbon dioxide emissions can be reduced by replacing the existing fossil fuel based systems with renewable energy sources as far as possible and increasing the energy efficiency of existing systems. Policies of Indian government to adapt more renewable energy sources are rigorous in the last decade. Various strategies taken by Indian government for the last two decades have increased the renewable share in the electricity sector. But the energy demand is increasing at about 10% every year. Renewable energy sources are added in a phased manner into the Indian electricity sector. This paper presents different renewable technologies, developments, potential, and barriers to renewable energy adaption in India. Unused potential of various renewable sources in India are indicated. Also, policies of Government and current, future status of renewable sources are summarised.*

Keywords: *Renewable Energy status in India, Renewable Energy Technology in India, Indian Electricity Sector, Renewable Energy potential in India, Renewable Energy Policies, Barriers for renewable Energy.*

1. INTRODUCTION

Fossil fuels usage cannot be replenished up to two or three decades, due to higher growth of energy needs worldwide. Presently about 80% of energy needs in the world are satisfied by fossil fuels [1]. The surfeit consumption of non-renewable fuels makes emission of greenhouse gases and pollutants into the atmosphere, which leads to global warming and climate change [2]. Also it create huge amount of waste, affect biological systems and accelerate climate change [3]. Extinction of fossil fuels, global warming and pollution etc. lead the scientist and governments to think about alternate energy sources. The world tries to reduce the consumption of fossil fuels, in that too coal & oil. As the gas price is lesser than oil & coal, one-third in carbon emissions, its use is increasing continuously [2, 4].

Renewable energy sources such as wind, solar, biomass, biogas, small hydro, wave, tidal, geothermal etc. are considered as substitute for fossil fuels [3]. Renewable source based energy generations offer an opportunity to reduce green house gases, reduce pollution in the air, and provide sustainable place to living beings. In addition it offers improvement in energy security and economic development to the countries around the world [5].

In 2017 and 2018, a remarkable addition of renewable energy installed capacity was made because of diminishing prices, more capital investments and advances in related technologies. Recently, deployment of renewable energy is impacted by the factors such as low price quotes for renewable power worldwide, considerable increase in electrification of transport, growing digitalisation, decision to convert into pollution-free environment, new policies and partnerships on carbon pricing, new initiatives and targets set by groups of countries at all levels [6].

Many nations and private players are increasing their deployment of renewables and investment in renewables and related infrastructure. Recently in 2017, many nations formulated its renewable energy policies and targets. The total energy consumed worldwide from renewable energy sources had a share of 18.1% in 2017 whereas in 2017 the share was about 10.6%. The year 2017 was an important year for Solar PV, in which capacity addition of solar PV is higher than the cumulative capacity addition of coal, natural gas and nuclear power. Installed capacity of Solar photovoltaic (PV) added in 2017 was remarkably increased than wind power (in second place) also it is more than net installed capacity of coal, natural gas and nuclear power together [6].

Renewables 2019 Global Status Report indicates that total installed capacity of renewable energy sources worldwide account for 1238 GW. If hydro

power also taken into account, the total installed capacity amounts to 2378 GW worldwide. The renewables capacity addition is more than fossil fuel based additions for the last four years 2014 to 2018 globally. At the end of 2018, 181 GW of renewable energy capacity have been added in total. Renewable energy generation contributed a share of 26.2% of global total energy generation in 2018 (Fig.1). Hydropower contributes majority of energy generated which is 15.8% of global total energy generation. Remaining energy has been obtained from wind, solar PV and Bio-power which accounts for 5.5%, 2.4%, and 2.2% respectively of global total energy generation. In 2018, the cost of energy obtained from renewable sources was less than fossil fuel based power plants [6].

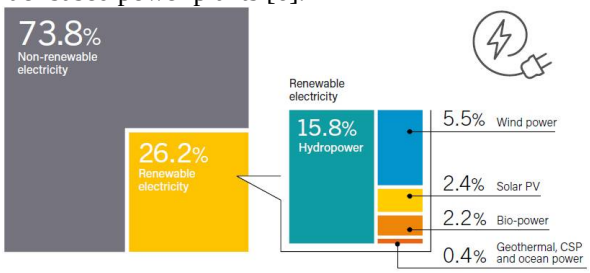

Fig.1. Renewable Energy Generation share out of Total Energy Generation, 2018

2. INDIA'S ELECTRICITY SECTOR STATUS

The total installed capacity of electricity generations in India (Fig.2) is about 369.4 GW at the end of February 2020. Renewable energy installation has a share of 86.8 GW which accounts for 23.5%, excluding large hydro power plants of 45.7 GW which is 12.4% of total capacity. Nuclear Power generation contribute 1.8 % (6.8 GW). Remaining electricity capacity is obtained from fossil fuels accounted for 62.4%, out of which coal and lignite together has a major share of 55.4% (204.8 GW), gas has 6.8% (25 GW) and oil 0.13% (0.5 GW). Installed capacity of renewable energy sources in India at the end of February 2020 are 4683.16 MW of Small Hydro, 37669 MW of Wind, 9861.31 MW of Bio-Power, 139.8 MW of waste to energy and 34405.67 MW of Solar PV [7].

The energy requirement and energy availability of India are shown in Fig.3 for the financial year 2018-19 and 2019-20. The energy demand is around 100000 MU and 110000 MU during the financial year 2018-19 and 2019-20 respectively. Energy availability is less than the requirement in all the months in 2018-19 and is less by 0.1 to 0.7%. But in 2019-20 the energy availability is surplus means that the installed capacities are more than the demand, which is clear from Fig.3. The peak demand and available power are illustrated in Fig.4 for the financial year 2018-19 and 2019-20.

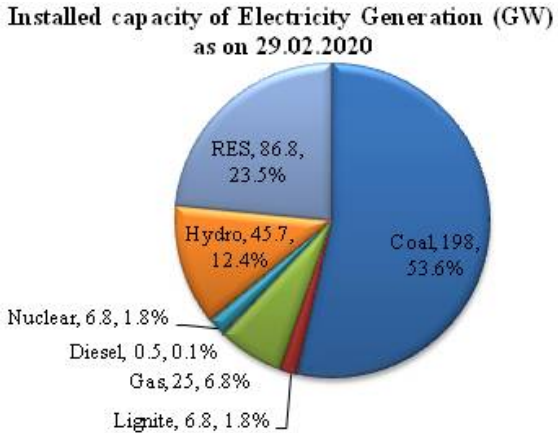

Fig.2. Installed Capacity of Electricity Generations in India (February 2020)

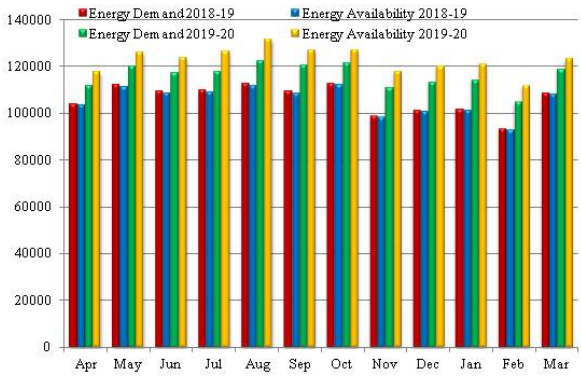

Fig.3. Energy required and Energy generated in India (2018-19 & 2019-20)

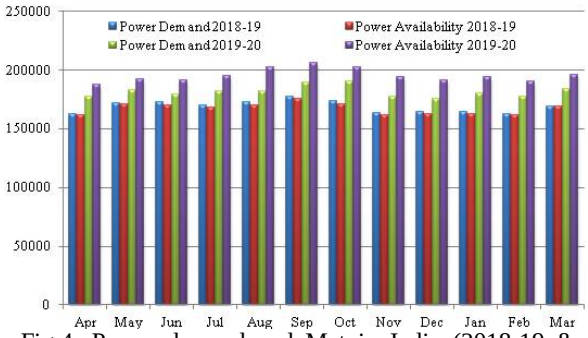

Fig.4. Power demand and Met in India (2018-19 & 2019-20)

The peak demand varies from 162 GW to 177 GW during 2018-19 but in 2019-20, it varies from 176 GW to 190 GW. The power deficit varies in the

range 0.3% to 1.7% in the year 2018-19. So there was a small deficit always exist throughout the year in the power generation. But in 2019-20, it is expected that the demand will be less than the availability of power, because of new generating capacities are added during 2019-20 [8].

3. RENEWABLE ENERGY STATUS IN INDIA

India's future energy growth depends on both International norms on climate control and National development objectives [2]. India's political agenda is to provide electricity and clean cooking to its citizens. International energy Agency (IEA) has highly commended Indian Government's reforms in electricity market and shift in investments towards variable renewable energy (VRE) [9]. According to World Energy Council's report 2018, India is one of the world's renewable growth leaders. Presently, 80 % of India's electricity generation is dependent on coal, oil, and gas [10]. Coal is imported in huge amounts from many countries. In order to increase the self-reliance, energy security and reduce emissions, India has set the renewable energy target of 175 GW by 2022 and 275 GW by 2027 [10]. This will have a share of around 30-40 % of total installed capacity of electricity generations. The target of 175 GW by the year 2022 comprises of 100 GW of solar, 60 GW of wind, 10 GW of biomass and 5 GW of small hydropower capacity [11, 12]. Renewable energy growth in India has many challenges such as i) the sources are available in western and southern parts mostly: ii) Power sector is administered by both State and Central governments iii) Integrating Renewables with existing grid iv) creation of manufacturing and service facilities for Renewable Technologies v) unplanned urbanisation vi) rigid operating nature of base load thermal power stations etc [10, 12].

India's increasing installations of renewable energy generating facilities help to reduce import of expensive fossil fuels [10]. Estimated renewable energy potential in India is about 1096 GW from commercial renewable installations viz., 750 GW of solar power, (assuming 3% wasteland), 302 GW of Wind (at 100-meter hub height); 21 GW of Small Hydro ; 25 GW of Bio-energy [13, 14].

India is one of the larger contributors for the emissions by using fossil fuels for its energy needs. For satisfying international norms and to have clean environment, India is in a position to choose alternatives for the fossil fuels. Renewable energy technologies are providing a solution to this problem and becoming realistic economically and technically because of rapid advancements in that sector and fall of prices. Clean energy transition depends on the rapid adaptation of renewable based power plants and electric vehicles. Uninterrupted electricity to all people by 2022, and electrification of all villages by 2018 are the set goals of Indian Government. India aimed to reduce emissions by 33-35% less than in the year 2005 by the year 2030. Also the renewable energy share of electricity generation in 2030 will be more than 40% [10].

India stands at 5th position all over the world for its installed capacity of renewable energy with a total capacity of 73.35 GW as on 31.10.2018. Wind and Solar power installed capacities reached 4th and 5th positions in the world with wind energy 34.98 GW and Solar energy 24.33 GW respectively. The capacity additions of grid connected Solar, wind, Small hydro power, and Bio-Power during 2014-15 to 2018-19 (Upto October 2018) are shown in Fig.5. In the same duration, other off-grid renewables such as waste-to-energy, biogasifiers, Solar cumulatively have a capacity addition of 1100 MW. During the fiscal year 2017-18, cumulatively 101.83 billion units of electricity were produced from renewable energy sources in India. In 2017-18, out of overall energy generated in the country, renewable energy generated is 8%. The Government has set the target to add 60 GW capacity of solar energy and 20 GW capacity of wind energy by March 2020. As per the target of Indian government, by the year 2022, the solar installed capacity will surpass the wind capacity [15].

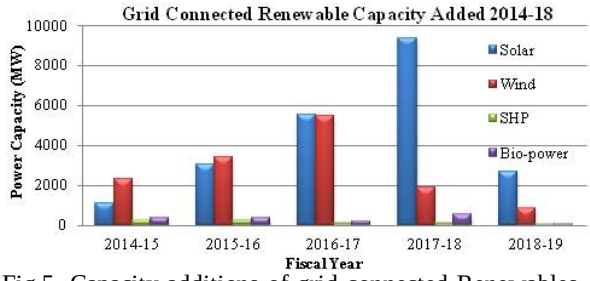

Fig.5. Capacity additions of grid connected Renewables 2014-2018

Government of India to aims to achieve 225 GW of renewable energy capacity by the year 2022, much ahead of its target of 175 GW as per the Paris Agreement. The country stands at fourth and fifth position in the installed capacity of wind and solar respectively as of 2018 [15]. Under National Biogas

and Manure Management Programme introduced in 2014, about 5 million houses are installed with biogas plants for cooking and lighting purpose [16].

The four objectives of India's energy policy are i) Access at affordable prices, ii) Improved security and Independence, iii) Greater Sustainability and vi) Economic Growth [4, 17]. National Energy Policy suggested actions to make energy ready India by 2040. The energy demand in India during 2040 will rose to 270-320% than 2012, because of i) manufacturing sector's share of 30% in GDP ii) 47% people live in urban areas and iii) population of 1.6 billion [4].

India has 86.8 GW of the total renewable power generations till February 2020 which is illustrated in Fig.6. In which the share of sources are: Wind 43.6% (37.6 GW), Solar 39.4% (34 GW), Bio-power 11.4% (9.86 GW), and finally Waste to energy has a least share of 0.2% (0.14 GW) [7].

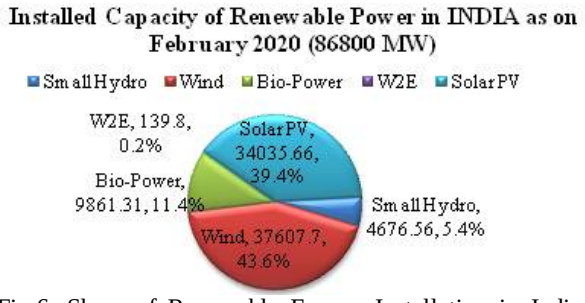

Fig.6. Share of Renewable Energy Installation in India (February 2020)

With the different categories of Renewable energy sources, the electricity generation share by them is increasing year by year. In financial year 2018-19, renewable power including hydro power contributed about 19 % (261,797 GWh) of India's total energy consumption of 1,371,517 GWh [18]. The electricity production from each source in the year 2018-19 is illustrated in Fig.7.

In the next decade, Renewable energy's development in India seems to be very prospective. Hundreds of companies have promised to invest about $350 billion to construct and operate 250 GW Renewable energy power plants primarily of solar, wind, SHP and biomass power. Indian Power sector has opportunities for significant growth with the investments over the next four to five years in power generation, transmission & distribution facilities, and related equipment. Need of energy storage in India will be in huge amounts because of the growth of renewable power and electric vehicles [19].

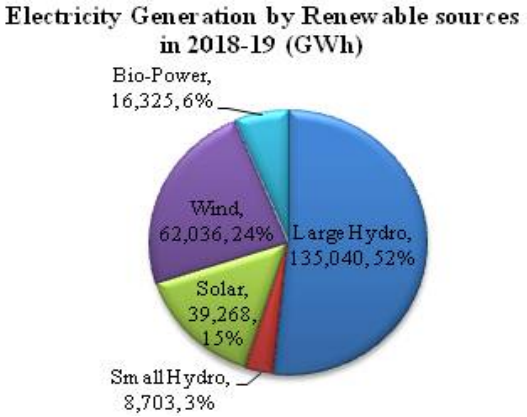

Fig.7. Electricity Generation by Renewable sources in 2018-19

3.1 Solar Energy

In India, yearly solar radiation incident over its land mass is about 5,000 trillion kWh. The daily average of solar energy potential of 4 to 7 kWh/ m^2 is possible with the commercially proven technologies [3]. The total solar potential available in India is 750 GW, out of which only 34 GW is installed at present. The solar power target of 20 GW was achieved four years ahead instead of the year 2022 by the Indian Government. The solar PV power capacities of 3 GW, 5 GW, and 10 GW have been added in the years 2015-2016, 2016-2017 and 2017-2018 respectively. In January 2015, another target of 100 GW up to the year 2022 was set by the government which includes 40 GW of rooftop solar and remaining is large-scale grid-connected solar PV [20].

The generated electricity form solar PV is 39.27 TWh out of 1372 TWh, which is 2.86% of total electrical energy generated in India in the year 2018-19. The installed solar power capacities of top 10 states are listed in Table 1. The Major Solar Power plants which are above 100 MW are listed in Table 2 [20]. The International Solar Alliance is headquartered in India, has the vision to provide clean and affordable energy to people [15].

Table 1
Installed capacity of Solar Power Plants in top 10 states

S.No.	State	Cumulative Capacity as on 31-03-2019 (MW)
1	Karnataka	6096
2.	Telangana	3592
3.	Rajasthan	3227
4.	Andhra Pradesh	3086

5.	Tamil Nadu	2575
6.	Gujarat	2440
7.	Madhya Pradesh	1840
8.	Maharashtra	1634
9.	Uttar Pradesh	960
10.	Panjab	906

Table 2
Major Solar Power Plants in India

Plant	Place	DC peak power (MW)	Commiss -ioned
Bhadla Solar Park	Gujarat	2,245	March 2020
Pavagada Solar Park	Karnataka	2,050	December 2019
Kurnool Ultra Mega Solar Park	Andhra Pradesh	1,000	2017
Rewa Ultra Mega Solar	Madhya Pradesh	750	2018
Charanka Solar Park	Charanka, District Patan, Gujarat	690	2012
Kamuthi Solar Power Project	Kamuthi, Tuticorin District, Tamil Nadu	648	September 2016
NP Kunta	Andhra Pradesh	500	2018
Ananthapura mu - II	Andhra Pradesh	400	2019
Mandsaur Solar Farm	Madhya Pradesh	250	2017
Gujarat Solar Park-1	Gujarat	221	April 2012
Welspun Solar MP project	Bhagwanpura village, Neem -uch District, Madhya Pradesh	151	February 2014
ReNew Power, Niza mabad	Dichpally, Nizamabad District, Telangana	143	April 2017
Sakri solar plant	Sakri, Dhule district, Maharashtra	125	March 2013

3.2 Wind Energy

National Institute of Wind Energy (NIWE), Chennai, is an organization for wind energy research in India under the Ministry of New and Renewable Energy. This institute has installed about 900 wind monitoring stations (WMS) [21] throughout India and 117 WMS are in operating condition as of March 2020 [22]. The wind assessment has been carried out at heights ranging from 20 m to 120 m. In Addition hundreds of private wind monitoring stations is also operational in the country. It was assessed that 237 locations have the wind potential of 200 W/m^2, based on the data collected from WMS. By considering the sites having power density 200 W/m^2 at 100 m hub height and 2% land availability, 302 GW of wind power potential is available to extract. The total installed wind power capacity in India was about 35.6 GW as of 31 March 2019, and becomes the fourth largest in wind power capacity in the world [21].

In India, 10% of total installed capacity is by wind. In 2018-19, 62.03 billion Units of electricity have been generated form wind resources with utilisation factor nearly 19.33%, which contribute 4% of total energy consumption. During Southwest Monsoon, which falls from April to September, 70% of wind energy is generated. The state wise installed capacity of wind turbines and larger wind farms in the country are illustrated in Table 3 and Table 4 respectively [23].

Table 3
Installed wind power capacity by state as of 31 October 2019

S.No.	State	Total Capacity (MW)
1.	Tamil Nadu	9231.77
2.	Gujarat	7203.77
3.	Maharashtra	4794.13
4.	Karnataka	4753.40
5.	Rajasthan	4299.73
6.	Andhra Pradesh	4077.37
7.	Madhya Pradesh	2519.89
8.	Telangana	128.10
9.	Kerala	62.50
10.	Others	4.30
	Total	**37090.03**

Table 4
India's largest wind power production facilities (More than 50MW)

S.No.	Power plant	Producer	Location	MWe
1.	Muppandal windfarm	Muppandal Wind	Kanyakumari, Tamil Nadu	1500
2.	Jaisalmer Wind Park	Suzlon Energy	Jaisalmer, Rajasthan	1064
3.	Brahmanvel windfarm	Parakh Agro Industries	Dhule, Maharashtra	528
4.	Dhalgaon windfarm	Gadre Marine Exports	Sangli, Maharashtra	278
5.	Vankusawade Wind Park	Suzlon Energy Ltd.	Satara District, Maharashtra	259
6.	Vaspet	ReNew Power	Vaspet, Maharashtra	144
7.	Beluguppa Wind Park	Orange Renewable	Beluguppa, Andhra Pradesh	100.8
8.	Mamatkheda Wind Park	Orange Renewable	Mamatkheda, Madhya Pradesh	100.5
9.	Anantapur Wind Park	Orange Renewable	Nimbagallu, Andhra Pradesh	100
10.	Damanjodi Wind Power Plant	Suzlon Energy Ltd.	Damanjodi, Odisha	99
11.	Jath	ReNew Power	Jath, Maharashtra	84
12.	Welturi	ReNew Power	Welturi, Maharashtra	75
13.	Acciona Tuppadahalli	Tuppadahalli Energy India Pvt Ltd	Chitradurga District, Karnataka	56.1
14.	Dangiri Wind Farm	Oil India Ltd.	Jaiselmer, Rajasthan	54
15.	Bercha Wind Park	Orange Renewable	Ratlam, Madhya Pradesh	50

3.3 Small Hydro Power

Another important renewable energy source under the purview of Ministry of New and Renewable Energy is Small Hydro Power (SHP). SHP is chosen to meet the electricity demand mainly in rural and remote areas, which use free water flow for clean electricity generation. The estimated potential for SHP in India is about 21 GW [21]. Numerous of the SHP sites are located in rivers of Himalayan region and rivers & irrigation canals of other parts of the country. Hydro projects up to 25 MW capacities are categorized as Small Hydro Power (SHP) projects, and they are further classified as i) Micro Hydro-Up to 100 kW ii) Mini Hydro-101-200 kW iii) 2001-25000 kW. Alternate Hydro Energy Centre, IIT Roorkee identified 7,133 promising SHP sites with cumulative capacity of 21,133.65 MW according to its report in July 2016. The cumulative capacity of SHP installed is 4593 MW till March 2019. Another 16 GW of SHP potential could be harnessed in the near future [21, 24].

A target of 5000 MW of SHP by the year 2022 was planned by the Ministry of New & Renewable Energy (MNRE). In India, SHP projects are constructed and operated by the Private Investors. SHP projects provide energy at low cost because of no fuel cost, advanced technology with high efficiency systems and operational flexibility. The aims of the SHP scheme are to i) maximise utilisation factor ii) maximise reliability iii) minimize investment for equipment [25].

SHP projects guarantee returns in the long run but involve high capital cost. Living beings and landscape are effected less by the construction of SHP plants. Generally SHP provides good capacity utilization factor than the other renewable energy sources. Hence, Indian government promote SHP by providing financial and technical support. MNRE provides financial support for survey, Project report preparation and Construction of SHP plants [24]. State wise details such as potential identified, installed and under implementation of SHP schemes as of November 2016 are illustrated in Table 5.

Table 5
SHP Potentials in India November 2016

S.No	State	Projects Installed	
		Number	Capacity (MW)
1	Andhra Pradesh & Telangana	72	241.98
2	Arunachal Pradesh	152	104.605
3	Assam	6	34.11
4	Bihar	29	70.7
5	Chhattisgarh	10	76
6	Goa	1	0.05

7	Gujarat	6	16.6
8	Haryana	9	73.5
9	Himachal Pradesh	184	842.11
10	J&K	42	161.03
11	Jharkhand	6	4.05
12	Karnataka	167	1230.73
13	Kerala	32	213.02
14	Madhya Pradesh	11	86.16
15	Maharashtra	65	347.375
16	Manipur	8	5.45
17	Meghalaya	4	31.03
18	Mizoram	19	41.47
19	Nagaland	12	30.67
20	Odisha	10	64.625
21	Punjab	54	170.9
22	Rajasthan	10	23.85
23	Sikkim	17	52.11
24	Tamil Nadu	21	123.05
25	Tripura	3	16.01
26	Uttar Pradesh	9	25.1
27	Uttarakhand	101	209.32
28	West Bengal	24	98.5
29	A&N Islands	1	5.25
Total		**1085**	**4399.355**

3.4 Bio-Energy

Biomass plays a vital role among the renewable energy sources, in particular in rural areas, as it is one of the main energy sources in majority of households in India. Bio-energy is obtained from organic matter derived from trees, plants, crops or from human, animal, municipal and industrial wastes [26]. Biomass resources in India are estimated as 18,000 MW by EAI. Investment of about Rs. 64500 Crores made every year on Biomass related projects, which leads to 5 TWh of electricity generation. MNRE has set 10 GW power generations from biomass as the target by the year 2022. Resources for bio-energy are Biomass, Biogas and Bio-fuel. In India, 450-500 million tonnes of biomass is produced every year. At present Biomass contributes 32% of all the primary energy use [27].

The vision of National Policy on Biofuels 2018 is to augment usage of biofuels in the energy and transportation sectors during the next decade. Increased use of biofuels reduces usage of fossil fuels which warrant National Energy Security, Climate Change mitigation, and new employment opportunities. Also the policy encourages the use of advance technologies for production of biofuels [27]. The primary goal of the policy is to enable market availability of biofuels and increase its blending percentage in petrol and diesel. The proposed goal of the policy is to increase blending of ethanol in petrol to 20% and blending of biodiesel in diesel to 5% by the year 2030. At present blending percentage of ethanol in petrol is around 2.0% and blending percentage of biodiesel in diesel is beneath 0.1%. These goals of the policy [27] are to be achieved by

(a) enhancing supply of ethanol/biodiesel through increasing domestic production

(b) setting up of Second Generation (2G) bio-refineries

(c) development of new raw materials for biofuels

(d) development of new technologies for conversion to biofuels.

(e) creating suitable environment for biofuels and its integration with the main fuels.

3.5 Geothermal energy

Fig. 8. Locations of Major Geothermal Resources in India

Geothermal energy is the natural heat available underneath earth, created from fiery collection of dust and gas more than 4 billion years ago. This energy is renewable in nature, regenerated continuously by the decomposition of radioactive components created in earth layers. The temperature increases by 17 °C to 30 °C for every kilometre depth. In general, the geothermal energy resources are classified as Hydrothermal, Geo-pressurised

brines, Hot dry rocks, and Magma. The estimated geothermal potential of earth up to the depth of 10 km is around 403x106 Quads [28].

India has convincingly high potential of 10,600 MW of geothermal resources. For electricity generation, no geothermal plant is operating at present; but direct usage of heat from geothermal is utilised for drying applications at few places. The installed capacity of such plants accumulates about 203 MW and producing 1606 TJ/year with capacity factor of 0.25 [29].

In India, around 340 geothermal locations have been identified until now by diverse studies and surveys carried out. The regions of geothermal sites are illustrated in Table 6. The majority of geothermal basins are situated in the north-west of the Himalayas and Tatapani fields on the Narmada in central India. Other regions are Godavari Basin Manikaran (Himachal Pradesh), Bakreshwar (West Bengal), Tuwa (Gujarat), Unai (Maharashtra), and Jalgaon (Maharashtra). The important sites of geothermal energy are indicated in the map of India in Fig.8 [28].

Table 6
Potential Geothermal regions/sources in India

Province	Surface Temp ^{o}C	Reservoir Temp ^{o}C	Heat Flow	Thermal gradient
Himalaya	>90	260	468	100
Cambay	40-90	150-175	80-93	70
West coast	46-72	102-137	75-129	47-59
Sonata	60 – 95	105-217	120-290	60-90
Godavari	50-60	175-215	93-104	60

3.6 Ocean Energy Sources

Ocean energy technology is currently under-developed in India. Significant ocean energy sources are such as Tidal energy, Wave energy, Water Current Energy and Ocean Thermal Energy. Government of India looking forward for variety of promising technologies and considers supporting its development. Research and development activities in these fields are to be stimulated in a phased manner to make the ocean energy sources a part of Indian grid. Development of Ocean energy sources provide economic growth, creation of new kind of jobs and help reducing carbon emissions. India's vision named as 'Blue Economy' aims at developing home-grown technologies for extracting ocean energy [30].

3.6.1 Wave Energy

Indian seashore of 7517 km with plentiful estuaries and gulfs makes it suitable for the development of marine energy projects. Indian Wave energy technology developments are in the budding stages. The estimated potential of wave energy is in the range of 40-60 GW with 5-15 MW/m energy densities. IIT Madras and Credit Rating Information Services of Indian Ltd (CRISIL) have made a study and identified many locations along the western coastline in Maharashtra, Goa, Karnataka and Kerala states [31].

Indian Institute of Technology, Madras with the funding from Department of Ocean Development of Government of India established a 150 kW pilot wave energy plant at Vizhinjam in Thiruvananthapuram, Kerala in 1991. This was the world's first Oscillating Water Column (OWC) based technology project but was in operation for few years only. Being out of service for long period it was decommissioned in 2011 [32].

Technological and economical challenges such as low turbine efficiencies, extension of grid connections to potential sites, high turbine costs, lack of experience and stochastic environmental conditions are to be addressed to make wave energy economically feasible. Wave energy doesn't have place in the target of 175 GW by 2022 for renewable energy [32].

3.6.2 Tidal Energy

Tidal energy can be harnessed by utilising the high tide and low tide made in the sea level by the gravitational force of the moon and sun. The energy can be obtained for 6-10 hours a day because the tidal cycle alternates every 12 hours. During high tide, Sea water enters into a barrage constructed across an estuary. During low tide, the collected water made to flow through water-turbine makes use of potential energy to electrical power. At least 5 m height tide is required to acquire the tidal energy. India is one among 20 such locations worldwide. In India, western coastal region has higher tidal height [30]. The Gulf of Cambay has potential of 9000 MW, the maximum and average tidal range of 11 m and 6.77 m. The Gulf of Kutch has the potential of 1200 MW, the maximum and average tidal range of 8 m and 5.23 m respectively. Around 100 MW of tidal energy potential exist in Ganges delta region.

Kalpasar Tidal Power Project located at the Gulf

of Khambhat is a promising site for tidal power generation. For encouraging the private investors, MNRE announced in February 2011 that it offer financial incentive of half of the total project cost [30, 31].

3.6.3 Ocean Thermal Energy Conversion (OTEC)

The temperature difference between the upper surface of sea water and water at deep sea, are used to extract energy is nothing but Ocean thermal energy conversion, or OTEC. A temperature difference of about 20°C could produce usable energy [31]. In general, two types of OTEC concepts are adapted namely closed cycle and open cycle. In the closed cycle system, the temperature difference is used to vaporize a working fluid, like ammonia and the turbine utilize this pressure to rotate. Cold water at the depths of the ocean is condensing the vapour and it is pumped back to the heat exchanger. In the open cycle system, the warm surface sea water is pressurized in a vacuum chamber and converted to steam which is used to run the turbine. The steam is taken to the depth of the sea where it is condensed by cold ocean water and working fluid is pumped to heat exchanger [30].

Indian south coast about 2000 km length has the temperature difference of above 20^{o}C throughout the year. In the Exclusive Economic Zone around the Indian coast of 7500 km long, about 1.5x106 square kilometres of tropical water has the power density of 0.2 MW/km^2. The total estimated OTEC potential in Indian coastal is estimated as 180,000 MW. However, OTEC needs more capital costs and is economically feasible in large scales. Construction of offshore OTEC plants in large scale has many complexities and challenges. Hence a 200 kW land based OTEC plant has been planned at Kavaratti, capital of the Lakshadweep Archipelago supplying power to a thermal desalination plant [33].

4. CHALLENGES FOR RENEWABLE ENERGY GROWTH IN INDIA

In India larger share of Electrical power is obtained from coal based power plants although coal will be available till 2050 and huge amount of CO_2 emission contributing to global warming and are the reason for many health hazards to the people. Promoting renewable energy programs in the rural areas for encouraging distributed hybrid power generations which help to create basic facilities and increase job opportunities. Indian Government has a policy on renewable energy to increase the share of renewable power to 40% in 2030. Even though there is huge scope for development and investment in renewable energy in India, there are many hurdles and constraints make the growth slower [34].

4.1 Political and policy barriers

The multi-layered governance system in India (Central and State Governments) produces a mixed result of fruitful and unfruitful [10]. The policy of Renewable purchase obligation (RPO) compels states to attain a certain amount of energy from renewable sources. Perform, Achieve and Trade (PAT) scheme for industries made the energy demand of industries less. Energy Efficiency Services Limited has achieved considerable progresses in replacing LED lamps for the existing less efficient incandescent lamps and fluorescent lamps. Another achievement of NDA government is provision of LPG gas for cooking purpose for the poor people. Since 2015, through the Pradhan Mantri Ujjwala Yojana scheme, about 50 million LPG stoves and initial refills have been provided freely to poor households [35].

Even though there are encouraging results of many policies and schemes, there are obstacles due to India's multi-layered governance system which prevent the full implementation of policies. Many states are opposing the rational electricity pricing concept formulated during 1970s for political benefit in the state, which provides subsidized minimum price for electricity for agriculture purpose and domestic customers [36].

Industries and business organisations are reluctant in adopting RET because of insufficient and implicit policies of government. Expectations of new ventures such as subsidies for capital investment, tax benefits, power transmission facilities, grid code for interconnection, licensing requirements, environmental clearances from government agencies are lacking [37].

4.2 Technological barriers

Renewable Energy Technology development in India is slower because of many technological factors. Resource assessment, Geographic conditions, distributed and intermittency nature of renewables, and lack of storage technologies are some of the technology issues. Few other obstacles such as i) lack of design and technical standardization of system components ii) nonexistence of long term policies for renewables

which resulted in manufacturing, servicing and maintenance difficulties; iii) inadequate training of personnel; and f) lack of co-ordination between government agencies, renewable industry and research groups in academic and research institutions [37].

4.3 Economic and financial barriers

Indigenous technology developments help to reduce the investment cost and adapt by the investors. Growth of RET demands the economic factors such as small payback periods, subsidies for investment and incentives for production, economic benefits etc. Government decided to introduce performance linked incentives for the power producers instead of the subsidy for capital investment. Provisions in GST to be made included for the existing tax rebate for accelerated depreciation. Feed-in-tariffs will continue to drive the Renewable Energy market. The tariff support to be continued till the renewable energy cost comes down than coal based energy cost [36].

State owned distribution companies (Discoms) have dept over USD2.4 billion. Because of this the Discoms are unable to reach the Renewable Purchase Obligation (RPO) introduced in the Electricity Act 2003. Indebted Discoms are unable to invest on improving grid facilities, which leads to more losses & debt for Discoms and power generated from renewables less viable [36].

4.4 Organizational structure barriers

Inadequate coordination and mutual aid between various central and state ministries, nodal agencies, institutes and other stakeholders delays the progress in RE development. For example, after the acceptance of applications for wind projects under GBI scheme by IREDA, MNRE rejected the applications because the notification was not released in the gazette at that time. In practice, IREDA might have accepted the applications after the gazette notification, so that this confusion might have been avoided. Such implementation gaps among the nodal agencies make investors feared about their investment towards RE [35, 37].

4.5 Technical barriers

Developing countries face technical challenges such as deficient technology and infrastructure to support the growth of RET. Another issue is that inadequate trained manpower to operate and maintain renewable energy systems, specifically in rural areas. Energy cost of renewable power is comparatively higher than fossil fuel power as the technology is matured and resource is readily available. Required Transmission and distribution networks for renewable power projects, is another challenge. Such barriers result loss of investor's confidence in RETs and force them to choose fossil fuels [4].

4.6 Social-cultural barriers

India has lakhs of villages in its geographical structure. The rural people's reluctance to adopt renewable energy due to its unreliability nature and cost involved. Also, awareness and knowledge about renewable energy technologies is lacking in rural communities, which plays a role in restraint growth of RET [4].

4.7 Land rights

Renewable power plants especially solar and wind require larger area of land for its installations even though India has the problem of land scarcity. The previous congress government in order to reinforce rights of the land owners passed a law which made the land price four times the market price, land acquisition complicated and time consuming. The NDA government reformed the law and have paid the same compensation but acquired the land without the consent of farmers and social impact. The opposite parties holding majority in 'Rajya Shaba' opposed the law of land reforms and it was defeated. These shows how difficult are imposing a law in Indian politics [4].

5. RENEWABLE ENERGY POLICIES OF INDIAN GOVERNMENT

5.1 Top Government Programmes in the Solar Sector

5.1.1 Rooftop Scheme

Solar Energy Corporation of India sanctioned 200 MW of rooftop solar projects under the rooftop scheme, in which 45 MW have been commissioned. The projects with 50 MW capacity for the CPWD (Central Public Works Departments) and 73 MW capacity for warehouses have also been sanctioned. As part of MNRE's target of 40 GW rooftop capacity by 2022, SECI initiated a tender which offer 30% subsidy to the residential sector, non-profit private educational institutions, hospitals, social buildings. [38].

5.1.2 Solar Park Scheme

MNRE aims to install number of solar parks under this scheme across the country with a capacity of around 500 MW. This scheme offers financial support to establish solar parks and provide support for acquisition of land, grid facilities, road facilities, water, etc. This policy augurs to construct Solar parks in partnership with the State Governments. The duty of the state governments is acquisition of land and finding private investors/developers of solar park. Local population may get employment opportunities under this scheme. The states may get the benefit of reducing of equivalent carbon emissions. The scheme is implemented by SECI for Government of India [38].

5.1.3 Viability Gap Funding (VGF) Scheme

Viability Gap Funding scheme implemented by SECI supports developing of grid-connected solar PV projects of minimum 2000 MW capacity by the private investors on build, own and operate basis [12, 38]. Under this scheme a budget of Rs. 8580 Crore has been announced by MNRE for the state-run power producers to install 12 GW of grid connected solar PV power projects. Also it is stated that the purchase of equipments should be from domestic manufacturers. This capacity will be added in the years 2019-23 and the power plant may be constructed for self-use or use by government organisations. The bid will be conducted by SECI for allocation of the power capacity [39].

5.1.4 Government Yojana Solar Energy Subsidy Scheme

Government of India announced this scheme for the benefit of power loom and small textile industries which enables to increase textile production. The subsidy for such applicants on capital investment will be provided to the extent of 50 %, 75 % and 90 %. Another benefit of this scheme is reduction of electricity bills of power looms and demand on conventional power plants [38].

5.2 National Wind-Solar Hybrid Policy

Stochastic nature of Solar and wind power makes difficulty in grid connection and introduces stability issues. Due to the complementary periods of availability of wind and solar power during a day, making use of both sources at the same location would provide sustainable power to the loads. Exploitation of both the resources makes possible extension of renewable power plants to new locations and existing locations of solar and wind farms. In the vacant lands of existing wind farms solar PV panels can be installed and similarly wind generators can be added in and around existing solar PV plant [24]. Changes in existing Policies are required to install wind-solar hybrid plants at new locations and also hybridizing existing wind and solar plants. Further, storage facilities may be created to smoothen the wind solar hybrid power [40].

5.3 UDAY Scheme for state distribution Companies

UDAY or Ujjwal Discom Assurance Yojna was initiated by the Government of India in November 2015, with the objective of reforming the power sector, development in renewable energy, reduction in electricity generation cost, energy efficiency, operational improvement, and conservation. This scheme is expected to provide permanent solution to the existing and future issues of electricity industry. The state governments have the option to join the scheme [37].

5.4 National Policy on Biofuels – 2018

This policy targets the increase of blending biofuels in petrol/diesel. The policy aims to substitute fossil fuels which also support for climate change programme, ensures energy security and creates employment opportunities. This policy importantly considers the development of second generation biofuels and pay way for undertaking the Research & Development activities. The areas such as development of new raw material for biofuel production, plantations, processing and conversion technologies will be concentrated in the R&D activities. Primary importance will be given to indigenous technology development in biofuels and patents. At present 2% of ethanol and 0.1% biodiesel are blended jn petrol and diesel respectively. The policy proposed the blending of ethanol in petrol to be 20% and blending of biodiesel in diesel to be 5% by 2030 [27].

5.5 Green Corridor Scheme

Ministry of Power authorised to build transmission lines to enable the integration of large scale renewable energy power plants in various states under the Green energy Corridor Scheme in 2015-16. This project have been adopted in VRE rich states such as Tamil Nadu, Rajasthan,

Karnataka, Andhra Pradesh, Maharashtra, Gujarat, Himachal Pradesh and Madhya Pradesh by the respective transmission companies of states. This scheme provides the option to RE project developers to transmit power through Green Energy Corridors without any charges till the year 2022. In Phase I, 33 GW of RE projects have been integrated by this scheme. In Phase II, it has been planned to install and integrate 100 GW of Solar and 60 GW of Wind within 2022. It is targeted to construct 9400 circuit kilometers of transmission lines and substations with different capacities [9].

5.6 Electric mobility mission of India

The Previous Congress led Indian Government formed 'National Electric Mobility Mission Plan (NEMMP) 2020' in 2011 and subsequently the present government formulated the scheme called, “Faster Adoption and Manufacturing of (Hybrid &) Electric Vehicles (FAME) in India” in the year 2015 [41]. This scheme was introduced with the aim to focus in the areas of Technology Development, Reinforcing the commitment towards the Paris Agreement, Indian Government has planned a major shift to electric vehicles by 2030 ie., 30% of mobility will be by electric. Nodal agency for the scheme is the Department of Heavy Industry (DHI), GoI and is responsible for the planning, implementation and review of the scheme [42].

A Nodal body named Technology Advisory Group (TAG) under the supervision of DHI and Department of Science and Technology (DST) was constituted to look after the technology foresight and road mapping, Project nucleation and proposals. TAG set up two Centre of Excellence (CoE) namely CoE for Battery, Battery Management System, Power Electronics and Vehicle System Integration and Non Ferrous Technology Development Centre (NFTDC). These centres will be acting as bridge between Industry and Academia with an aim to support the prototyping of system components, Validation and commercial applicability [42].

6. ENERGY STORAGE

In present day situation of allowing greater share of Variable Renewable Energy (VRE) sources in the power system require Energy Storage system for flexible operation of grid. As the renewable sources are variable and distributed in nature, in order to achieve stable operation of power system and meet the load demand, electricity is stored in storage systems. Energy Storage System (ESS) is becoming essential part of Renewable energy Systems in the 21st century. India has set a target for the year 2030 of achieving 30-35% reduction in carbon emissions from the 2005 level and also 40% of total electricity generating capacity from Renewable Energy Sources [43]. So it is assessed that Energy storage Systems has massive economic opportunity in India.

Electricity Storage Systems (ESS) enhances decarbonisation as it is utilised in variety of energy utility applications. Electricity storage applications are increasing in usage such as Medium voltage/low voltage (MV/LV) grid-connected, off-grid, e-mobility, Telecom Towers, Data Centres, UPS & Inverter, and DG Replacement applications. The estimates of ESS requirements from different sectors in India for the period 2019-2022, 2022-2027 and 2027-2032 are consolidated in Fig.9 [44].

	Consolidated Energy Storage Roadmap					
	Applications 2019-2022		Energy Storage (GWh)			
			2019-2022	2022-2027	2027-2032	Total by 2032
Stationary Storage	Grid Support	MV/LV	10	24	36	70
		EHV	7	38	97	142
	Telecom Towers		25	51	78	154
	Data Centres, UPS and inverters		80	160	234	474
	Miscellaneous Applications (Railways, rural electrification, HVAC application)		16	45	90	151
	DG Usage Minimization		0.5	3.5	10.5	14.5
	Total Stationary (GWh)		138.5	321.5	545.5	1,005.5
Electric Vehicles	E2W		4	55	496	555
	E3W		26	69	136	231
	E24		8	110	725	843
	Electric Bus		2	13	57	72
	Total Electric Vehicles (GWh)		40	247	1,414	1,701
Total Energy Storage Demand (GWh)			178.5	568.5	1,959.5	2,706.5

Fig.9. Energy Storage Requirement in India

For the estimate of ESS capacity, Stationary storage and Electric Vehicle Applications are considered. Under stationary applications, LV/MV/HV grid support, Telecom towers, Data Centres, UPS & Inverters, Railways, Rural Electrification, HVAC Applications, and DG usage minimisation are taken into account. Two Wheelers, Three Wheelers, Four Wheelers, Buses & Trucks are considered under Transportation Applications. The estimates are listed for each segment for the periods 2019-2022, 2022-2027 and 2027-2032 in Table #. The total energy storage requirement estimate for the periods 2019-2022, 2023-2027, and 2028-2032 for all kind of applications is 178 GWh, 568 GWh and 1960 GWh [44].

Among the variety of storage systems available, commercially viable technologies are Pumped hydro storage, Batteries, Supercapacitors, Thermal storage, Compressed air storage, and Flywheel storage. Lithium ion batteries (LiB) are comparatively cheaper, occupy less space, more energy density,

and provide backup for longer hours than Supercapacitors, Flywheel, and Compressed air storage. So, future trends of Pumped hydro storage and LiB are discussed below.

6.1 Trends of Pumped hydro storage

Pumped hydro storage is globally adapted, commercially matured technology which is having larger share of total storage power capacity (in GW) and the energy storage capacity (in GWh). Presently, Pumped hydro storage system is economic to construct and operate and providing flexibility in operating with the power system. It has a share of 96% of total installed storage capacity of 176 GW in 2017. More than 75% of these kinds of plants are installed in ten countries. Major contribution from three countries as of 2017 – China (32.1 GW), Japan (28.5 GW) and the United States (24.2 GW) – accounting for 48% of global energy storage capacity. India has only 6.8 GW of pumped hydro storage power systems as of 2017 as the water resources are not ample. But there are no significant improvements and flexibility of grid operation is reported and has many issues in its operation. The installation cost of Pumped hydro storage is 1780 USD/kW in 2016 and 1560 USD/kW in 2017. The Levelised cost of energy from Pumped hydro storage is typically ranging between USD 0.04 and 0.06/kWh depending on the location and terrain [45].

6.2 Trends of Battery Storage

Battery storage is other kind of possible electricity storage. Even though the capital cost of batteries are high at present, because of technology advancements and mass production the cost is expected to reduce in future. Battery storage capacity has a share of 1.6 GW and 1.1% of total storage capacity globally in 2017. India's Target of Roof Top Solar PV systems are integrated into LV/MV grids. These integrations have many issues such as voltage, frequency variations and harmonic injection etc. In order to achieve flexilbe and stable operation of power system Battery Energy Storage Systems (BESS) are suggested in India. Energy Storage India Tool (ESIT) has been developed for assessing the battery capacity for different locations/applications [45].

7. ANALYSIS OF RENEWABLE ENERGY COSTS

The capital cost of solar and wind technologies are continuously declining due to deployment of capacity additions worldwide. The Global weighted average total installed cost of various renewable energy sources are listed in Table 7. The installation cost of solar PV, onshore wind, Bio-Power, Hydro Power systems are cheaper than thermal power plants. Even though the installation costs of offshore wind, and Geo-thermal energy systems are comparatively equal or slightly higher than thermal power plants, the energy cost are lesser due to lesser operating and maintenance cost. The installation cost of CSP is higher than thermal power plants presently, but it is expected to fall in future by improvements in technology and more capacity deployment [44].

Table 7
Global weighted average total installed cost of Renewable Energy Sources in 2019

S.No.	Renewable Source	Total Installed Cost (USD/kW)
1	Solar PV	995
2	On Shore Wind	1473
3	Off Shore Wind	3800
4	Concentrated Solar Power	5774
5	Bio-Power	2141
6	Geothermal Power	3916
7	Hydro Power	1704
8	**Fossil Fuel**	3661

Cost of Electricity from renewables is falling in the last decade because of the factors such as technological advancements, large scale installations, increasing supply chain and rising user experience, improvement in capacity factor. The Global average of Levelised Cost of Energy (LCOE) of different renewable energy technologies commissioned in the year 2019 is listed in the Table 8 and also LCOE of fossil fuel power plants at last for comparison. According to this data, except concentrated solar power all kind of renewable energy cost are found to be cheaper than electricity from fossil fuel power plants. Power purchase agreements made in some parts of the world for the year 2021, indicate that there is a fall in the energy costs. LCOE of solar PV could have an average price of USD 0.039/kWh in 2021 which is 42% fall when compared to cost in 2019. Similarly, the auction data indicate that energy cost of onshore, offshore, and CSP will fall to USD 0.043/kWh, USD 0.082/kWh, and USD 0.075/kWh in 2021 which are 18%, 29%, 59% fall respectively from the 2019 prices [44].

Table 8
LCOE of Renewable Energy sources in 2019

S.No.	Renewable Source	LCOE (USD/kWh)
1	Solar PV	0.068
2	On Shore Wind	0.053
3	Off Shore Wind	0.115
4	Concentrated Solar Power	0.182
5	Bio-Power	0.066
6	Geothermal Power	0.073
7	Hydro Power	0.047
8	**Fossil Fuel**	0.05 - 0.177

8. CARBON EMISSION ANALYSIS

It is accessed that the coal based power plants produce an average carbon dioxide emission of 820 gCO_2Eq/kWh. But solar and onshore wind power plants have very less average emission of 48 gCO_2Eq/kWh and 11 gCO_2Eq/kWh respectively during their production process. So by deploying renewable energy sources for electricity, the carbon emissions could be reduced in huge amounts [43].

If solar PV and onshore wind energy systems replaces the least economical 500 GW of existing coal-fired power plants globally, would replace 2170 TWh of coal power generation and reduce emissions by 1.8 Gt of carbon dioxide (CO_2) which is about 5% of global CO_2 emissions in 2019. Replacing coal power plants will reduce the power generation costs and provide an investment stimulus option for renewables worth around USD 950 billion. For replacing 500 GW coal-fired power plants minimum installation of 860 GW of Renewable Energy sources are required, which may pave path for achieving renewable additions for two to three years in compliance with agreement made in UN Climate Conference, Paris 2015 [43].

9. NEEDS AND COST OF DISMANTLING RENEWABLE POWER PLANTS

Recently hundreds of power plants operated for long time become to end of its lifetime and more number of power plants will complete its lifetime in the forthcoming decades. So proper planning is needed to dismantle the facilities and dispose the wastes from these plants. Decommissioning process ensure minimization of negative impacts to local environments, economies, electricity users, and reuse of the land. Fig 10 presents an estimate of decommissioning cost of different power plants [46].

Fuel type	No. of estimates	2016$ (thousands) Minimum	Mean	Maximum
Offshore wind	7	$123	$212	$342
Coal	28	$21	$117	$466
Concentrated solar power (CSP)	5	$24	$94	$138
Solar photovoltaic (PV)	22	–$89*	$57	$179
Onshore wind	18	$2	$51	$222
Petroleum/petroleum + gas	19	$2	$31	$103
Gas (various types)	28	$1	$15	$50

Fig. 10 Decommissioning Cost Estimates per MW of Capacity

Also now because of the technology advancements, new wind turbines are having one to few MW capacities. But the turbines installed earlier to 2012 are having less than 1 MW range having total capacity of 10 GW. A concept called repowering the wind sites was adapted to replace the existing large number of less capacity machines with less number of higher capacity machines. The repowering capacity till 2007 in India for the machines of less than 1 MW capacity is about 4400 MW. In India Solar Systems are installed starting from last decade. So they have life of another 15-20 years. As of now there is no dismantling issue of solar systems [47].

10. CONCLUSIONS

Indian renewable energy developments are steered by the factors such as economic growth, environmental protection by green energy initiatives, and energy security etc. This paper reviews the potential, growth, policies of government, schemes of government, challenges/barriers for the growth of various renewable energy sources in Indian context. Also it presents cost analysis of renewable energy such as their installation and energy cost in comparison with fossil fuel fired power plants. The effect of penetration of renewable power sources on decarbonisation is also presented. Need and cost of dismantling renewable power plants are also discussed. Renewable energy sources such as Solar, Wind, Biomass, Small Hydro, Ocean energy sources, Geo-thermal energy are considered for the analysis. India considers Wind and Solar as the important sources and it is expected that there is significant growth in near future. There is a hope for growth of Biomass, Biodiesel, and small hydro energy sources. But it is noted that the Ocean energy and Geo-thermal energy developments are in its natal stage. Non-availability of Technology, random nature of sources and insufficient funds for investments are the major hurdles for the developments of these sources.

Indian power market provides different options

for the RE generators to sell the energy, such as feed-in tariffs, renewable energy certificates, captive and open access sales. The investors can choose the selling option according to their expected risk-return profile. The financial regulatory terms are formed in such a way to offer cost advantage to generators and buyers. The modified grid norms which include forecasting, scheduling and levy of imbalance cost make an obvious and practical path for the development of the renewable energy industry. Nevertheless, the total share of renewable energy in 2030 would be 30% of total energy consumption in India. Also India targeted 30% of vehicles would be electric in 2030. So, in the next decade there is a huge scope for the growth of Renewable energy & Electric Vehicle industry, related Research & Developments, and Jobs in India.

REFERENCES

1. Farzaneh, H. N. and Hossein, N., *Impact of Renewable Energy Consumption on Economics in India*, International Journal of Energy Engineering, vol.7, no.1, p.32-38, 2017.
2. Navroz, K. D., Radhika, K., Narasimha D. Rao, and Ankit, B., *India's energy and emissions future: an interpretive analysis of model scenarios*, Environmental Research Letters, vol.13, 2018.
3. Ashwani, K., Kapil, K., Naresh, K., Satyawati, S., and Saroj, M., *Renewable energy in India: Current status and future potentials*, Renewable and Sustainable Energy Reviews, vol.14, pp. 2434-2442, 2010.
4. *National Energy Policy: Version as on 27.06.2017*, Ministry of Power, Government of India, 2017.
5. Shahrouz, A., Almas, H., and Jörn, A., *A Review of Renewable Energy Supply and Energy Efficiency Technologies*, Institute for the Study of Labor (IZA), Bonn, Germany, 2014.
6. *Renewables 2019 Global Status Report*, Renewable Energy Policy Network for the 21st Century (REN21), 2019.
7. *Central Energy Agency Report-February 2020*, Ministry of Power, Government of India, 2020.
8. *Load Generation Balance Report 2019-20*, Central Electricity Authority, India, 2019.
9. *India 2020 Energy Policy Review*, International energy Agency, *2019*.
10. *Perspectives on the Grand Energy Transition* World Energy Council, Issues Monitor, 2018.
11. *Renewable energy's transformation of the Indian electricity landscape*, India Environment Portal, 2015. http://www. Indiaenvironmentportal.org.in/content/421814/ renewable-energys-transformation-of-the-indian-electricity-landscape/ (accessed 10 January 2020)
12. Rahul, T., and Samantha, G., *Working to turn ambition into reality: The politics and economics of India's turn to renewable power*, Paper 4, Brookings, 2018.
13. *Year End Review-2017*, Ministry of New and Renewable Energy, Government of India, 2017.
14. Salma, R., and Zaki, H., *Renewable energy governance in India: challenges and prospects for achieving the 2022 energy goals*, Munich Personal RePEc Archive (MPRA), 2017.
15. *Year End Review- 2018*, Ministry of New and Renewable Energy, Government of India, 2018.
16. Karoliina, I., Alexandra, G., and Nicolai, S., *Governing clean energy transitions in China and India: A comparative political economy analysis*, The United Nations University World Institute for Development Economics Research. Working Paper 2016. 28.
17. *Barriers to development of renewable energy in India & proposed recommendations-A Discussion Paper*, Infrastructure Development Finance Company Ltd, India, 2010.
18. *Renewable energy in India*, Wikipedia, 2020. https://en.wikipedia.org/wiki/Renewable_ energy _in _India
19. Gautam, K., *Renewable Energy in India: Current Status and Future Potential*, 2018. https://www.indiary.org/en/legal-advice/ Renewable-Energy-in-India-Current-Status-and-Future-Potential-2-79-429 (accessed 12 January 2020)
20. *Solar power in India*, Wikipedia, 2019. https://en.wikipedia.org/wiki/Solar_power_ in_India. (Accessed 12 January 2020).
21. *Annual report 2018-19*, Ministry of New and Renewable Energy, India, 2020. https://mnre.gov.in/img/documents/uploads/0ce 0bba7b9f24b32aed4d89265d6b067.pdf
22. *Status of Wind Monitoring Stations*, National Institute of Wind Energy. India, 2020. https://niwe.res.in/department_wra_swms.php
23. *Wind Power in India*, Wikipedia, 2019. https://en.wikipedia.org/wiki/ Wind_power_in_ India
24. *Small Hydro Power Programme*, Ministry of New and Renewable Energy, Government of

India, 2017. https://mnre.gov.in/small-hydro (accessed 13 January 2020).
25. BhuvaneshKumar, B., and Sanjay Kumar, S., *Small Hydro Power in India*, 2017. http://www.energynext.in/2017/03/small-hydro-power-in-india/ (accessed 15 January 2020).
26. Darshini, R., and Srinivas, S. N. R., *Bioenergy in India: Barriers and policy options*, United Nations Development Programme, India, 2011.
27. *National Policy on Biofuels – 2018*, Ministry of Petroleum and Natural Gas, Government of India, 2018.
28. *Geothermal*, India Energy Portal, 2017. http://www.indiaenergyportal.org/subthemes_link.php?text=geothermal&themeid=13 (accessed 15 January 2020).
29. *Geothermal Energy*, INDIAN POWER SECTOR.COM, 2014. http://indianpowersector.com/home/renewable-energy/geothermal/ (accessed 16 January 2020).
30. *Ocean Energy*, Ministry of New and Renewable Energy, Government of India, 2018. https://mnre.gov.in/ocean-energy (accessed 20 January 2020).
31. *Ocean Energy*, Energy Alternatives India, 2012. http://www.eai.in/ref/ae/oce/oce.html (accessed 16 January 2020).
32. *Wave Power in India*, Wikipedia, 2017. https://en.wikipedia.org/wiki/Wave_power_in_India (accessed 24 January 2020).
33. *India's first ocean power generation project coming up in Kavaratti, Lakshadweep*, Business Standard, India, *2016*. https://www.business-standard.com/article/news-ani/india-s-first-ocean-power-generation-project-coming-up-in-kavaratti-lakshadweep-116092200284_1.html (accessed 24 January 2020).
34. Vikas, K., Savita, N., and Prashant, B., *Status of solar wind renewable energy in India*, Renewable and Sustainable Energy Reviews, vol.27, pp.1-10, 2013.
35. Nicolò, S., and Margherita, B., *India's Institutional Governance and the Energy Transition*, Sustainable Energy Transition Series, IAI Papers 18/19, 2018.
36. Deepthi, K. D. R., and Binu, B. J., *Indian Progress in the Renewable Technologies: A Review on Present Status, Policies, and Barriers*, International Journal of Renewable Energy Research, vol.8, no.2, pp.805-819, 2018.
37. Sanjeev, H. K., and Anil, T. R., *Renewable Energy in India-Barriers to Wind Energy*, Strategic Planning for Energy and the Environment, vol.38, no.2, pp.40-69, 2018.
38. *The Top Government Programmes in the Solar Sector*, AMplus Solar, India, 2018. https://amplussolar.com/blogs/the-top-government-programes-in-the-solar-sector (accessed 23 January 2020).
39. Uma Gupta, *12 GW 'new' solar with VGF support approved*, PV Magazine-india.com, 2019. https://www.pv-magazine-india.com/2019/03/06/12-gw-new-solar-with-vgf-support-approved/ (accessed 25 February 2020)
40. *National Wind-Solar Hybrid Policy*, Ministry of New and Renewable Energy, Government of India, 2018.
41. *FAME India, The Gazette of India*, Ministry of Heavy Industry and Public Enterprises, Government of India, 2015.
42. *FAME India Scheme*, Ministry of Heavy Industry and Public Enterprises, Government of India, 2018.
43. *Renewable Power Generation Costs in 2019*, International Renewable Energy Agency (IRENA), Abu Dhabi, 2020.
44. *Energy Storage System: Roadmap for India: 2019-2032, Draft*, Indian Smart Grid Forum (ISGF), July, 2019.
45. *Electricity Storage and Renewables: Costs and Markets To 2030*, International Renewable Energy Agency (IRENA), Abu Dhabi, 2017.
46. Daniel Raimi, *Decommissioning US Power Plants - Decisions, Costs, and Key Issues*, Resources for the Future, October 2017.
47. Idam Infrastructure Advisory Pvt. Ltd., *Repowering of old wind turbines in India*, September 2018.

IMPROVED DESIGN OF AN INTELLIGENT CONTROLLER FOR SPEED CONTROL OF BRUSHLESS DC MOTOR (BLDCM)

[1]S. Bagavathy, Assistant Professor, Dept of EEE, Sri Krishna College of Engineering and Technology, Coimbatore. mail: bagavathysp@gmail.com.

[2]Dr.P.Maruthu Pandi, Assistant Professor, Dept of EEE, Government College of Engineering, Coimbatore. mail: maruthugct@gmail.com

Corresponding author: bagavathysp@gmail.com.

Abstract

Brushless Direct Current Motor (BLDCM) drives are progressively prominent in traction as well as in industrial operations. The rheostat of BLDCM in multi quadrants is significant. By utilizing smart controller, the adaptability of the drive mechanism expanded. In this paper, the solar panel is encouraged by the BLDCM, and the for driving the power inverter channel signals of PWM for BLDCM have been effectively executed utilizing a controller with and the motor controlled by all the four quadrants with no consumption of the energy power is preserved through re-forming braking time interval. By using fuzzy with neural network learning the intelligent controller framed. MATLAB /Simulink done by using simulation of the recommended model.

***Keywords**: BLDC Motor, Intelligent Controller, Four Quadrant, Fuzzy, neural network*

1. Introduction

The conventional DC motors, the steady part have the winding field in which rotating part has armature winding along with commutator with brush arrangements. The cost of the motor is high as it needs regular maintenance of the brushes due to wear and tear. While using it in the dirty environment, these brushed motors may cause sparking. This problem can overcome by replacing them by electronic commutation, and with a permanent magnet on its rotor side along with position sensor and stator is a 3- phase winding connected with the inverter. BLDCMs are a kind of synchronous motor that implies that the magnetic field has produced by the stator and rotor created field rotates at a similar frequency. The motors of BLDC drives have better effectiveness, less upkeep and expanded life, simple control with less sound and weight [1][2]. Maximum power point (MPP) operation implemented for DC- DC converter with solar PV based BLDCM Drive with water pump and air blower and with separate shaft arrangement. [3]. A different approach of position sensor less control of brushless DC motors with high-speed with low inductance and non-ideal back electromotive force (EMF) in order to improve the reliability of the motor system is analyzed [4]. BLDC motors with a load angle control algorithm suggested that the measurement of only two current and one voltage signal without speed and position sensors to obtain energy-efficient sensor less control thus saving the energy [5]. The performance of a BLDC motor supplying different types of loads, and at the same

time, deploying different control techniques the jerks produced at the time of load removal also get improved to a large extent with Fuzzy PID controller [6].
In this examination work, an endeavor has made to plan and execute four quadrant controls with re-forming braking of a BLDCM drive with a Position sensor-less Neural-fuzzy controller in both directions. The whole closed loop structure being speed-controlled, four quadrant movement has received using the input of step speed while the sensibleness of the made exhibit has attempted under full stress load during the suffering state. The obtained results satisfy the activity of the four quadrant necessities of cutting-edge drives where control starts and stops are fundamental in both forward and reverse direction. The advance of speed is effortlessness from motoring to recovery energy, which is apparent in the possibility of the following current and torque. By utilizing MATLAB, the outline model of four quadrant control of the BLDCM done. To examine and simulate the task of the motor, a Simulink produced and demonstrated. A BLDC machine displayed as a fixed magnet synchronous machine with trapezoidal back EMF. Accordingly, proposed work finds applications in cutting edge modern drives as energy creative and monetarily insightful another choice to crash the effects of the drop in the voltage and the collection of mechanical load.

2. BLDCM Drive

In this examination, a 3-phase star related BLDCM driven by a 3-phase inverter with 6-stage substitution considered. Figure 1 demonstrates the improved BLDCM drive plot. The BLDC drive plot comprises of a 3-phase inverter, BLDCM, and position sensor. Fig 2.2 demonstrates the perfect current, back EMF, and rotor position motion for a 3-phase BLDCM. Every interim begins when rotor and field lines of the stator are 120° separated and closures when they are 60° separated. The electrical degree of the directing interim of separate phase is 120. The sensors of the hall resolved from the recompense moment mounted on the pole. In an ON method of 2- phase a BLDCM works routinely. For example, at any snapshot of time only 2-stage DC, the partition of the 3-stage which is open and available for evaluating the upcoming EMF. The examination determined by the accompanying assumptions: Protection of the Stator considered by the number of equivalent windings, individual and collective inductances remain consistent, the motor not soaked, iron losses avoided and semiconductor switches are perfect.

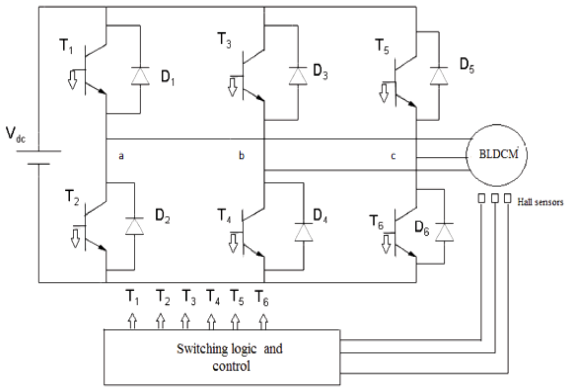

Figure 1. Drive of BLDC motor

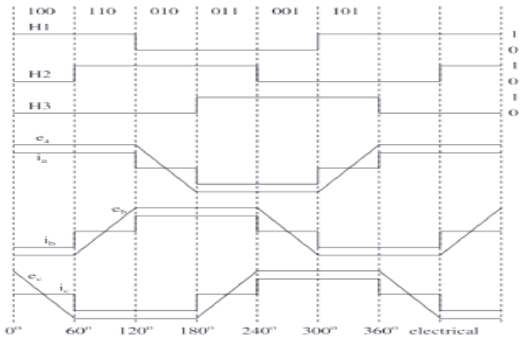

Figure 2. Standard current, upcoming EMF and signals in a hall of 3-phase BLDCM

The voltage equations of the BLDCM shown in figure 1 are given in equations (1) to (3).

$$V_{arab} = sR(i_{spa} - i_{spb}) + L\frac{d}{dt}(i_{spa} - i_{spb}) + (be_a - be_b) \quad (1)$$

$$V_{arbc} = sR(i_{spb} - i_{spc}) + L\frac{d}{dt}(i_{spb} - i_{spc}) + (be_b - be_c) \quad (2)$$

$$V_{arca} = sR(i_{spc} - i_{spa}) + L\frac{d}{dt}(i_{spc} - i_{spa}) + (be_c - be_a) \quad (3)$$

Where,

sR = Stator resistance per phase

L = Stator inductance per phase,

$i_{spa}, i_{spb}, i_{spc}$ = Instantaneous stator phase currents

$V_{arab}, V_{arbc}, V_{arca}$= Instantaneous stator line voltages

be_a, be_b, be_c= Instantaneous phase upcoming EMF

The current relationship is specified by means of,

$$i_{spa} + i_{spb} + i_{spc} = 0 \quad (4)$$

Equation (4) is modified as per,

$$i_{spc} = -(i_{spa} + i_{spb}) \quad (5)$$

Using Equation (5) the voltage of the line are reordered as

$$V_{arca} = sR(i_{spa} - i_{spb}) + L\frac{d}{dt}(i_{spa} - i_{spb}) + (be_a - be_b) \quad (6)$$

$$V_{arbc} = sR(i_{spa} + 2i_{spb}) + L\frac{d}{dt}(i_{spa} + 2i_{spb}) + (be_b - be_c) \quad (7)$$

$$V_{arca} = sR(-2i_{spa} - i_{spb}) + L\frac{d}{dt}(-2i_{spa} - i_{spb}) + (be_c - be_a)$$

Upcoming EMF depends on the rotor of the permanent magnet fluctuation and the rotor speed and specified as in Equation (8)

$$\begin{bmatrix} be_a \\ be_b \\ be_c \end{bmatrix} = \frac{bk_e\omega_m}{2}\begin{bmatrix} MF(\theta) \\ MF(\theta - 2\pi/3) \\ MF(\theta - 4\pi/3) \end{bmatrix} \quad (8)$$

The torque used for the electromagnetic is represented by the equation (9)

$$T_{em}=[\frac{Kt}{2}MF(\theta)isp_a + \frac{Kt}{2}MF(\theta - 2\pi/3)isp_b + \frac{Kt}{2}MF(\theta - 4\pi/3)isp_c] \quad (9)$$

The m otor representation for dynamics and load are given in equation (10)

$$T_{em} = K_f\omega_m + J\frac{d\omega_m}{dt} + LT_L \quad (10)$$

Where, T_{em} = Motor Torque, N- m

J = Moment of Inertia, kg/m^3

bK_e = Back EMF Constant, volts/rad/sec

K_f = Friction Constant, N-m/rad/sec

T_L= Load Torque, N- m

K_t = Torque Constant, N-m/A

ω_m= Rotor Speed rad/sec

3. Sensor less operation of BLDCM using upcoming EMF detection

The BLDCM has utilized for both domestic and mechanical companies inferable limited to its minimized measurements, controllable, and high adequacy. It is used as a vehicle part continuously for example applications of a car taken as a bit of strategy to discard belts and frameworks of hydraulic, to give additional helpfulness and to improve proficiency. The procedure in the magnet expense is decreasing and the required devices for the BLDCM control has added to its usage in a growing number of practices and at advanced power stages. At any rate, one rotor position sensors are ordinarily worked with the BLDCM since the excitation of

the electrical must be synchronous with the position of the rotor. The reliability, mechanic packaging, and the cost reasons especially if the blade runs submerged in liquefied and the motor can permit to run without position sensors, the task which is customarily known as sensor less. It is possible to choose when the drive motor voltages commutate by recognizing the upcoming-EMF current preceding an undriven motor terminal during one of the drive stages. The cost favored the position of sensor less control is prominent exists at the sensors of Hall position at the end. Notwithstanding the way that there are a couple of faults control toward sensor less:

- To create satisfactory upcoming EMF, the motor must move in any minimum rate, and it is detected.
- Sudden changes to the capacity of the motor will affect the loop of the BEMF drive to leave bolt.
- The voltage of the BEMF assessed exactly once the speed of the motor is inside the limited scope of the faultless reward rate intended for the associated power.
- If the Commutation rate is quicker when compared to the perfect rate, then the response of the motor is irregular.
- In case cash is a fundamental concern and low-speed motor undertaking is certainly not an essential, and the motor load isn't depended upon to change rapidly, for application related framework sensor less control may be the better choice.

Since there are particular calculations to conquer every one of the demerits recorded previously, the Sensor less BEMF strategy is rapidly turning into the most prevalent arrangement.

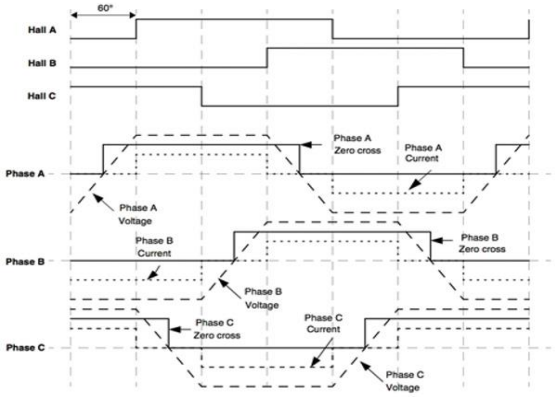

Figure 3. Sensor output for Hall related using upcoming EMF for 3-phase BLDCM

4. Proposed System – Sensor less control strategy for four-quadrant operation

The Simulink model of BLDC drive supplied from a solar panel, fed to the 3-phase inverter, exciting the stator windings based on the gate signals processed through the intellectual controller. The intelligent controller comprises of neural network training algorithm and fuzzy logic and described in figure 4.

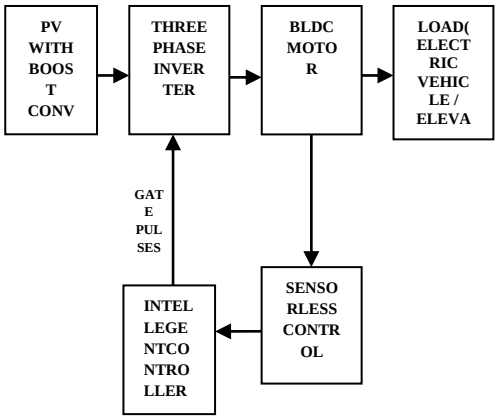

Figure 4. Sensor less BLDCM for neural fuzzy controller

The rotor position of BLDCM identified by BEMF detection and the controller receives signal. The speed of reference achieved by the speed of actual then stays unchanging from there on. Thereby reverse direction invert from left-

right to right-left or the other path around is practiced right away. During the 2nd and 4th quadrant operations, the BLDC machine worked as a generator and developed a soft model of BLDC drive is appeared in figure 5. The operations of the 2nd and 4th quadrant begin, the BLDC machine start working as a generator. The grew delicate model of BLDC drive is showed up in figure 5.1 to figure 5.4.

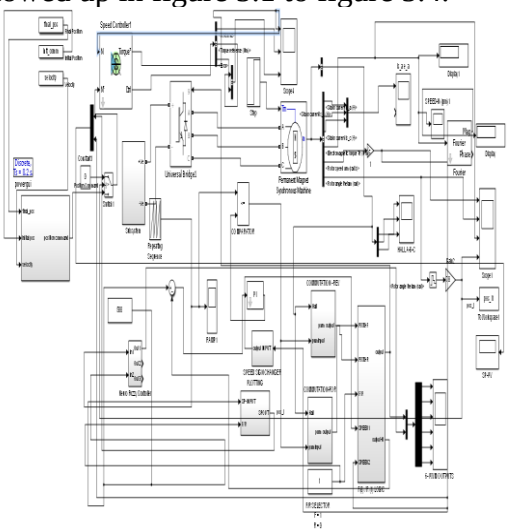

Figure 5. Simulink Model of Neural Fuzzy Controller based Sensor less BLDCM

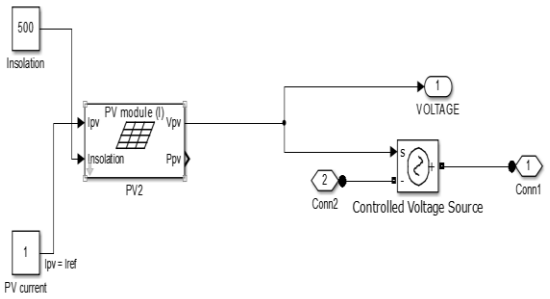

Figure 5.1 BLDCM: Solar panel input

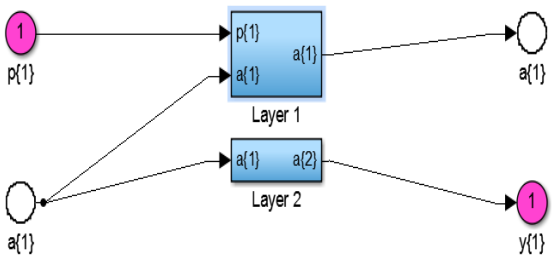

Figure 5.2. Neural Network Model

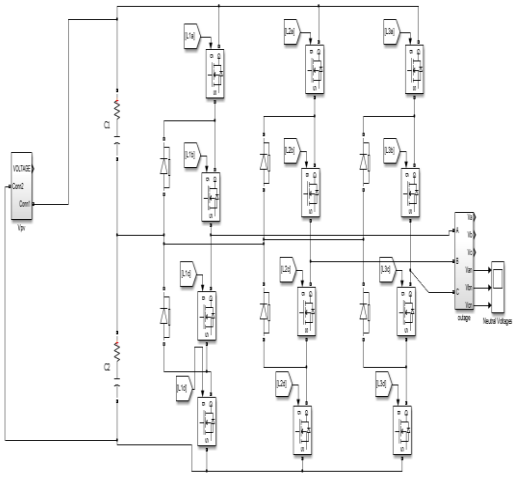

Figure 5.3. BLDCM: BLDCM Inverter

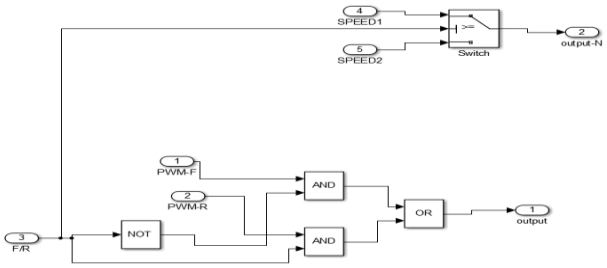

Figure 5.4 BLDCM: Forward Reverse Logic

The distinctive loads to be connected at different moments are additionally displayed. The Hall signals, PWM pulses, stator EMFs and stator currents of the three phases, the actual rotor speed, and the accomplished speed control are caught utilizing the degree. The time of model is 3sec, and the power GUI is ceaseless. The battery attributes, in particular, the battery voltage, the charging current, and the charging status are additionally gotten in the scope.

5. Result and Discussion

For sensor less BLDCM, the control method is proposed to modify the

direction starting with left-right to right-left and control of the speed is accomplished by the assistance of Neural Fuzzy Control. Neuro-Fuzzy is a type of Hybrid Controller, thereby mishandlings of development learning, thereby low computation intensity of neural system for upgrading the execution of fuzzy control structure. Regardless, the perfect topology of network findings strategy of a motor for the drives remains as a test.

From this examination, it explains that fuzzy and neural controller plays a comfort and convenient part in speed control of machines. The investigation explains that the controller of type neural in addition to fuzzy has an advantageous influence in machines for controlling the speed. The simulation output for variation of speed with load changes shown in Fig 6.1 to 6.3.

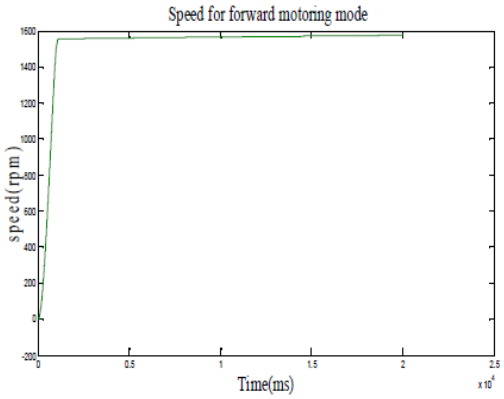

Figure 6.1. Speed for Motoring Forward

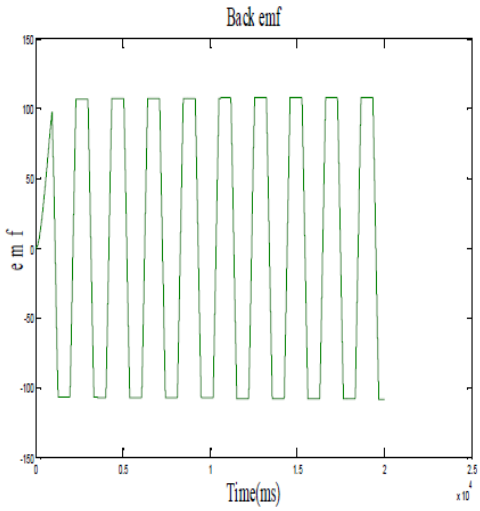

Figure 6.2 Back EMF

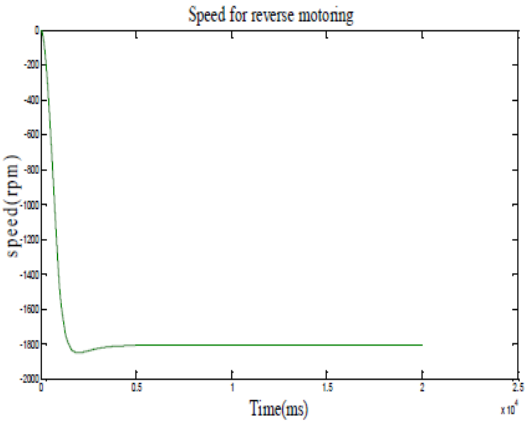

Figure 6.3. Speed for generation mode

In principle case, the motor is on no-load, that is the connected load torque kept up at zero; the reference speed indicated, and the actual speed realized. In another case, the load torque connected at various moments and the execution factors realized. The load and the reference speed, and the reaction of the machine seen, as it works in all the four quadrants.

6. Conclusion

BLDCMs are an engaging possibility for some elite applications, on account of their appealing qualities, for example, power density, torque-to-inertia ratio, power efficiency, robustness, and reliability. A Neural system based fuzzy logic parameters for the execution improvement of the BLDCM drive has

proposed. During the time spent deciding the parameters of the FLC utilizing the Neural, numerous free trials are performed to get ideal esteem. Before beginning the determination procedure, the parameters of the Neural were resolved and proclaimed in the preparation procedure. The reactions of the drive with the Fuzzy based PID instrument contrasted and those of the proposed Neural Fuzzy based control plot for three distinctive speed ranges, and load perturbations for various set speed.

References

[1] A. Ahmed, B.-K. Koh, H. Park, K.-B. Lee, and Y. Lee, "Finite control set model predictive control method for torque control of induction motors using a state tracking cost index,"IEEE Trans. Ind. Electron., vol. 64, no. 3, pp. 1916–1928, Mar. 2017.

[2] H. Shin, S. Kang, and K.-B. Lee, "Torque ripple reduction in direct torque control of five-phase induction motor using fuzzy controller with optimized voltage vector selection strategy,"J. Electr. Eng. Technol., vol. 12, no. 3, pp. 1177–1186, May 2017.

[3] Sreedhar Madichetty, Deepak Pullaguram, Sukumar Mishra, "A standalone BLDC based solar air cooler with MPP tracking for improved efficiency," CSEE Journal of Power and Energy Systems., vol. 5 , no.1,pp.111 – 119, Mar. 2019.

[4] Wenzhuo Li ; Jiancheng Fang ; Haitao Li ; Jiqiang Tang, "Position Sensorless Control Without Phase Shifter for High-Speed BLDC Motors With Low Inductance and Nonideal Back EMF," IEEE Transactions on Power Electronics,vol.31 , no.2, Feb. 2016.

[5] Jasper De Viaene, Florian Verbelen, StijnDerammelaere , Kut Stockman,"Energy-efficient sensorless load angle control of a BLDC motor using sinusoidal currents," IET Electric Power Applications vol. 12 ,no.9 , pp.1378 – 1389,Nov. 2018.

[6] Akash Varshney, Deeksha Gupta, Bharti Dwivedi, "Speed response of brushless DC motor using fuzzy PID controller under varying load condition," Journal of Electrical Systems and Information Technology, vol. 4, no. 2, pp. 310-321,Sept. 2017.

[7] Abdullah JH Al Gizi, Mustafa, MW & Hamid H Jebur," A novel design of high-sensitive fuzzy with PID controller," Applied Soft Computing, vol.24, pp.794-805. Nov.2014

[8] Arulmozhiyal, R & Kandiban, R, "Design of Fuzzy with PID controller for Brushless DC motor," Proceedings of the international conference on computer communication and informatics, pp.1-7. Jan. 2012

[9] Binod Kumar Sahu , Swagat Pati , Pradeep Kumar Mohanty & Sidhartha Panda, "Teaching–learning based optimization algorithm based fuzzy-PID controller for automatic generation control of multi-area power system," Applied Soft Computing, Vol.27, pp.240-249, Feb.2015.

[10]Cheng-Tsung Lin, Chung-Wen Hung, and Chih-Wen Liu, "Position Sensorless Control for Four-Switch Three-Phase Brushless DC Motor Drives", IEEE Transactions on Power Electronics, Vol. 23, No. 1, pp.438-444, 2008.

[11]R. P. Praveen, M. H. Ravichandran, V. T. S. Achari, V.

P. J. Raj, G. Madhu, and G. R. Bindu, “A novel slotless Halbach-array permanent magnet brushless dc motor for spacecraft applications," IEEE Trans.Ind. Electron., vol. 59, no. 9, pp. 3553 - 3560, Sep. 2012.

[12] X. Zhou and J. Fang, ``Precise braking torque control for attitude control flywheel with small inductance brushless DC motor," IEEE Trans. Power Electron., vol. 28, no. 11, pp. 5380 - 5390, Nov. 2013.

[13] Rajesh M Pindoriya ; S Rajendran ; P J Chauhan, “ Field programmable gate array based speed control of BLDC motor,” International conference IEEE Innovative Smart Grid Technologies - Asia (ISGT ASIA), Nov.2015.

[14]C. Jain, B. Singh, "An adjustable DC link voltage based control of multifunctional grid interfaced solar PV system", IEEE J. Emerg. Sel. Topics Power Electron., vol. 5, no. 2, pp. 651-660, Jun. 2017.

[15]P. Vithayasrichareon, I.F. MacGill, "Valuing large-scale solar photovoltaics in future electricity generation portfolios and its implications for energy and climate policies", IET Renew. Power Gener., vol. 10, no. 1, pp. 79-87, 2016.

[16]A. A. A. Radwan, Y. A.-R. I. Mohamed, "Power synchronization control for grid-connected current-source inverter-based photovoltaic systems", IEEE Trans. Energy Convers., vol. 31, no. 3, pp. 1023-1036, Sep. 2016.

[17] X. Zhou, X. Chen, F. Zeng, and J. Tang, ``Fast commutation instant shift correction method for sensorless coreless BLDC motor based on terminal voltage information," IEEE Trans. Power Electron., vol. 32, no. 12, pp. 9460 - 9472, Dec. 2017.

[18] C. Cui et al., "Sensorless drive for high-speed brushless DC motor based on the virtual neutral voltage", IEEE Trans. Power Electron., vol. 30, no. 6, pp. 3275-3285, Jun. 2015.

[19] P. Damodharan, K. Vasudevan, "Sensorless brushless DC motor drive based on the zero-crossing detection of back electromotive force (EMF) from the line voltage difference", IEEE Trans. Energy Convers., vol. 25, no. 3, pp. 661-668, Sep. 2010.

[20]C. Xia, X. Li, "Z-source inverter-based approach to the zero-crossing point detection of back EMF for sensorless brushless DC motor", IEEE Trans. Power Electron., vol. 30, no. 3, pp. 1488-1498, Mar. 2015.

Hand Gesture Recognition using multi-objective optimization-based segmentation technique

*[1]Supriya.S, K.S.R College of Engineering,Tiruchengodu,mail:ssupriyaa85@gmail.com
[2] Dr.Manoharan.C, Sapthagiri College Of Engineering,Dharmapuri,TamilNadu,
mail:c_m_66@yahoo.co.in
*Corresponding author: ssupriyaa85@gmail.com

Abstract:

Hand Gesture Recognition (HGR) software is winding up progressively open with the advances in depth cameras and sensors, however, these sensors are as yet costly and not uninhibitedly accessible. A continuous HGR programming is intended to work with a minimal effort monocular web camera. Skin discovery and skin extraction is a typical type of image handling utilized for motion acknowledgment. The hand gesture image is gone through three phases, preprocessing, feature extraction, and characterization or segmentation. In the preprocessing stage, a few tasks are connected to separate the hand gesture from its experience and set up the hand gesture image for the feature extraction stage. In this paper, Multi-Target Optimization Based Segmentation (MTOBS) has been proposed for HGR. The performance has been analyzed for gesture recognition with and without optimization technique. The outcomes demonstrate that the recognition method without optimization has an exhibition of 85% recognition, while the proposed technique with optimization, has a superior execution of 96% recognition rate.

Keywords: Image Processing, Image Segmentation, Feature Extraction, Gesture and Zernike Moment.

1. Introduction

Gesture recognition is a type of perceptual computing user edge that allows computers to capture and take human gestures as commands. Gesture identification based on computer vision technology has been received great interests recently, due to its natural human-computer interaction characteristics. The advantage is, user can control the devices without touching the keyboard, panel or mouse. Hand gesture method gives more freedom for the user to control the device like television remote control, presentation slide control is some of the applications of this hand gesture. The main drawback is hand motion speed is ever

fast and complicated compared to the computer image processing speed and people may need more training for this version. The general framework is first finding the location of the input image and it's segmented which is depends on the skin color of the image. The second step is finding the motion of the hand.

There are a lot of difficulties in accurate hand gesture recognition. The obstruction could increase the difficulty in pose recognition. The use of hand gestures provides an attractive and natural substitute to these bulky interface devices for human-computer interaction. Using hand as a device can help people to communicate with computers in an inherent way. The most effective tools for capturing hand gesture are electromechanical or magnetic sensing devices. In this, the sensors are enclosed with the hand gloves that transduce finger flexions into electrical signals to define the hand gesture but it has a drawback it hiding the naturalness of the hand. Hand gesture recognition systems detect and segment hands using marker-aided methods. But these methods are difficult when compared with markerless vision-based solutions.

The organization of the paper is as follows; the detailed explanation of hand gesture recognition is given in section.1. Section 2 describes the various linguistic description of the hand. Section 3 presents the proposed method for gesture recognition. Section 4 gives the experimental results. Section 5 described the findings and discussions and finally, the conclusion is given in section.6.

2. Linguistic description of the hand

The regular linguistic description gives data about significant patterns and a normal practice present in datasets, however, they additionally protect data about their representativity, by methods for verb modifiers demonstrating the degree to which the patterns are normal for the entire datasets. The hand arrangement will be characterized by nine phonetic factors. Most commonly, two factors are utilized for the thumb portrayal, they are,

Thumb Configuration-It portrays the extending of the thumb.

Thumb Orientation-It portrays the direction in the hand reference outline.

Four factors are utilized for the portrayal of different fingers called the long fingers: the *finger Configuration*(i=2,3,4,5). They give the shape of the relating long finger and are also named *index, middle, ring, and pinkie.* The last three variables are

utilized for the portrayal of the overall dispersing of fingers 2/3,4/3 and 5/4. They are individually named *finger Abduct$_i$ (i = 2,...,4)* or*list Abduct, ring Abduct, and pinkie Abduct.*. The French communication via gestures Alphabet and Numbers indication of Hand gesture is given in figure.1.

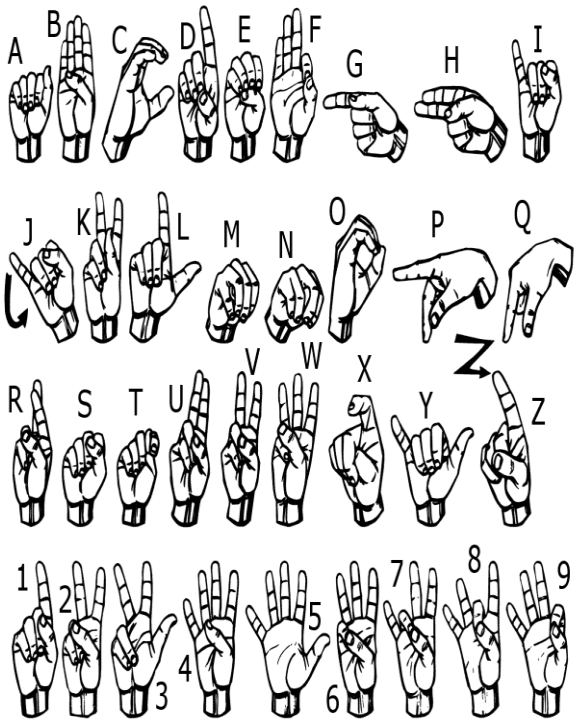

Fig.1 French communication via gestures Alphabet and Numbers

3. Proposed method

The hand gesture recognition using MTOBS is given in fig.2. Here, the gesture images from the standard dataset "BochumGestures1998" has been used as the input for the proposed system. Initially, the gesture images are given to the pre-processing block. Where the required images are subtracted from background and the noise present in the gesture images are filtered by using a median filter. Then, the feature such as Zernike moment has been extracted and optimized using Multi-Target optimization technique. These optimized features are used to recognize the gesture from the hand images.

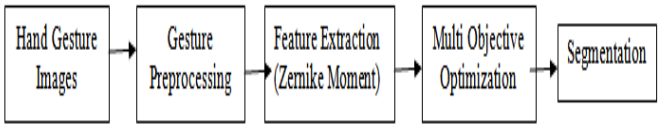

Fig.2. Hand Gesture Recognition using MTOBS method

3.1 Hand Gesture Dataset

In this work, publicly available dataset "BochumGestures1998" has been used. This dataset has static hand gestures, collected at the Institute fuer Neuroin formatik, Ruhr-Universitaet Bochum, Germany. All images from this dataset are 128x128 tiff images. The hand posture is identified by a code "00" to "12" in the filename. The kind of background light, dark, complex) is indicated by a subsequent letter a, b, or c, respectively.

3.2 Gesture Preprocessing

The main objective of this block is to locate and isolate the feature vector points

from the hand gesture patterns. Sachin and Apeksha [14] have demonstrated a moving cursor in PowerPoint slide with the help of hand gestures. Consequently, the Zernike moment is used to determine the feature points of an object within a unit circle with respect to rotation and shift invariant points. It is claimed that the system consists of 100 frames with a difference in its orientation and position.

3.3 Zernike Moment

The displaying of hand portrayal in various measurements depends on the organizing frameworks. In existing procedures, the element can't be perceived appropriately because of its shape depiction, for example, linearity, circularity, and so forth inside a picture. Consequently, the framework utilizes Zernike minute to get higher request highlight focuses in space arrange of request N with various minutes. Give us a chance to consider a mind-boggling set-in Zernike minute polynomial which satisfies the symmetrical property inside the roundabout limit of an article. It is defined as $a^2+b^2=1$, where a and b are rectangular organize tomahawks. Zernike minute an of 'm' request and 'n' dreary stage is given in Eq. (1).

$$A_{mn} = \frac{m+1}{\prod} \oint\oint_{a^2+b^2\leq 1} Z_{mn}(\gamma,\varphi) g(a,b) dadb \quad (1)$$

Where $g\ (a,\ b)$ represents intensity of the image at $(a,\ b)$, m represents positive integer, n is integer, if m-$|n|$ is even integer and |n| =m, $a^2+b^2=1$. ϕ is he angle between a-axis in anti-clockwise direction. $Z_{mn}(\gamma,\phi)$ is a complex conjugate of $B_{mn}(\gamma)$. Radial function is defined as sfollows,

$$B_{mn}(\gamma) = \sum_{c=0}^{m-n/2} \frac{-1^b[(m-b)!\,\gamma^{m-2b}}{b!\,(m+\frac{|n|}{2}-b)(m-\frac{|n|}{2}-b)} \quad (2)$$

When an article is situated concerning focus of circle, some pixel esteem drops out the unit circle which can't be represented figuring. As *Bmn* is the perplexing variable of motion designs. Zernike minute satisfies rotational invariant as a scalar amount. It gives preferable element focuses over other shape descriptor approach. Before extricating highlight focuses, it is imperative to accomplish scaling and revolution invariance by standardization and picture interpretation as recommended by Gholam Reza et al. [15].

3.4 Multi target Optimization Technique

Multi-target optimization considers optimization problems involving more than one target function to be optimized

simultaneously. A solution is called non-dominated or Pareto optimal if none of the objective functions can be improved in value without degrading one or more of the other target values. In multi-objective optimization problem, the goodness of a solution is determined by the dominance. The multi target optimization technique is shown in fig.3. The proposed optimization algorithm has the following steps,

Step-1 Get the hand gesture images from the BochumGesture1998 dataset and the dataset is randomly divided into RGB and SIH subsets.

Step-2 Get the extracted features form a dataset.

Step-3 Initialize the genetic population P 0 of size N and to initialize the threshold value t=0.

Step-4 If *t* is less than maximum iterations, then the threshold value is increased otherwise the Population Q_t of size *N* is obtained from P_t through crossover and mutation.

3.5 Segmentation

Region Growing (RG) based segmentation method has been used to segment the hand gesture images. This method presents some hazy impacts amid segmentation process, so it prompts over segmentation. To conquer this issue, GWO technique has been utilized to optimize the threshold value which is acquired from RG method.

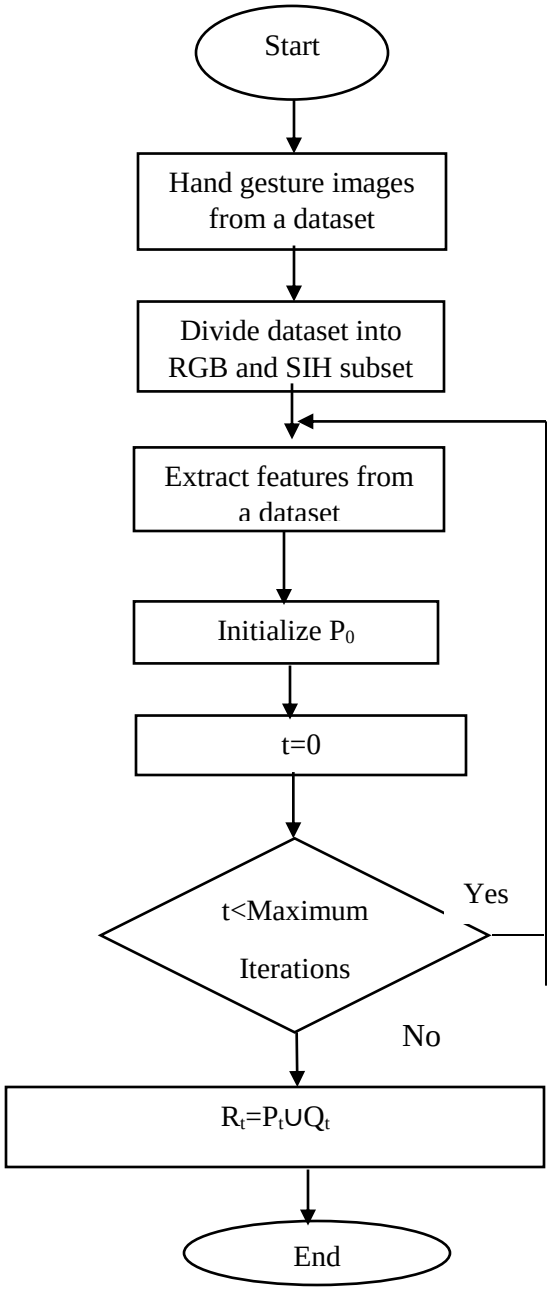

Fig.3 Multi-Target Optimization Technique

3.5.1 Gridding

Gridding is realized to discover a progression of even and vertical lines to isolate one slide image into sub-matrices and individual spots territories. The system of segmentation isolates the spot pixels into closer view, foundation, or commotion. At long last, the intensity extraction is gone for getting the quality articulation levels as per the past operational outcomes.

3.5.2 Seed point selection (Region Centre)

The pixel values of the original image lie in the range of 0 to 255. The most frequently happening pixel value is assigned to be the seed point. Histogram equalization method is used to find the seed point of the image. Then the threshold value of the hand gesture images is calculated. This value is used to segment the hand from the hand gesture images. In order to improve the segmentation accuracy, the obtained threshold value must be optimized. This threshold optimization is performed by using GWO optimization technique. Then, the obtained optimized value is used for segmentation process. So that, we can get the segmented image.

3. Experimental Results

In this paper, only 20 images of the dataset have been shown. Among this, 10 RGB images and the remaining 10 are belongs to SIH images. The images which are used for this experiment is shown in figure.4 and 5. Fig 4 Shows the hand gesture images in RGB domain, and fig.5 shows the input hand gesture images in SIH domain.

(a) (b) (c) (d) (e)

(f) (g) (h) (i) (j)

Fig. 4 Input Hand Gesture Images in RGB domain

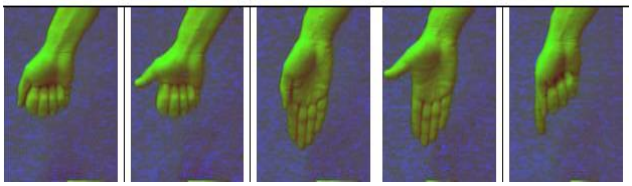

(a) (b) (c) (d) (e)

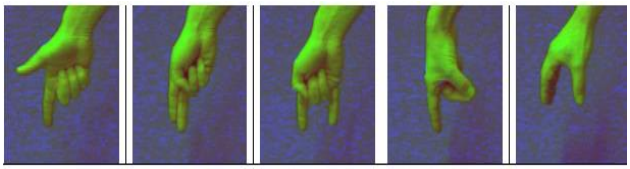

(f) (g) (h) (i) (j)

Fig. 5 Input Hand Gesture Images in SIH domain

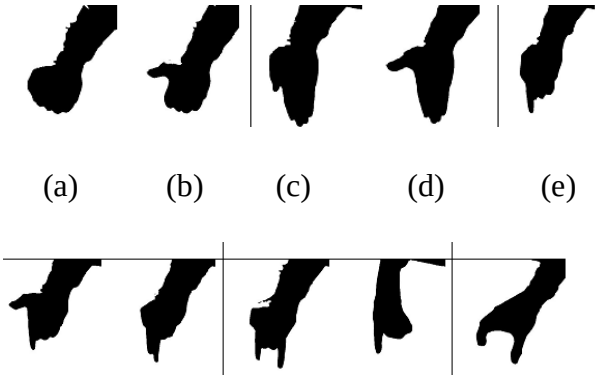

(a) (b) (c) (d) (e)

(f) (g) (h) (i) (j)

Fig.6 Segmented Hand gesture images (RGB) without optimization

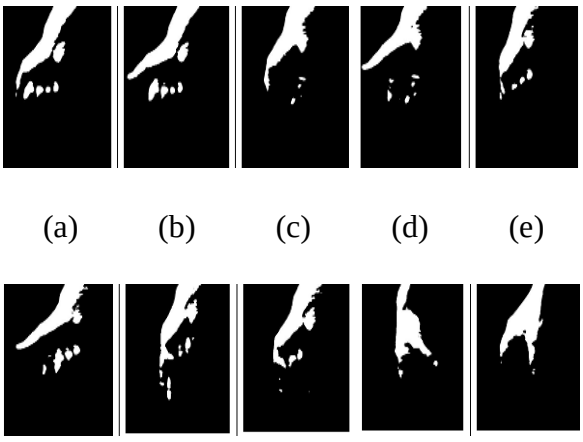

(a) (b) (c) (d) (e)

(f) (g) (h) (i) (j)

Fig.7 Segmented Hand gesture images (SIH) without optimization

The segmented results using proposed method without optimization is shown in fig. 6 and fig.7. Fig.6 shows the segmented hand gesture images in RGB domain and the segmented results in SIH domain is given in fig.7.

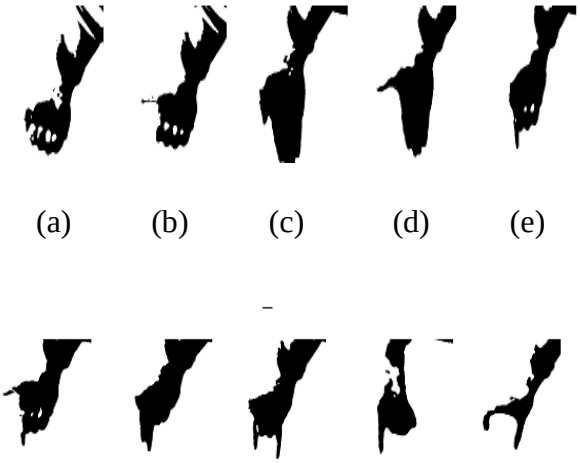

(a) (b) (c) (d) (e)

(f) (g) (h) (i) (j)

Fig.8 Segmented Hand gesture images (RGB) with optimization

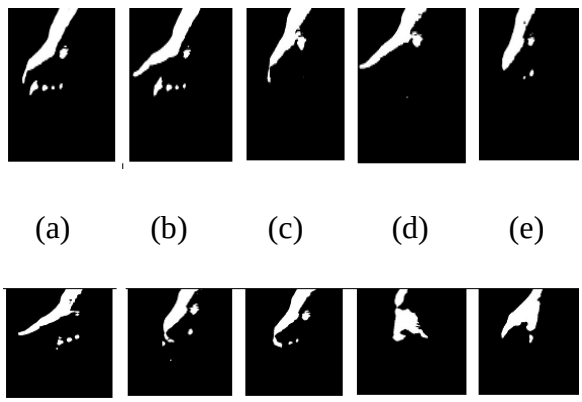

(a) (b) (c) (d) (e)

(f) (g) (h) (i) (j)

Fig.9 Segmented Hand gesture images (SIH) with optimization

The segmented results using proposed method with multi objective optimization is shown in fig. 8 and fig.9. Fig.8 shows the segmented hand gesture images in RGB domain and the segmented results in SIH domain is given in fig.9. By observing the segmented hand gesture images, it is clearly noticed that, the segmented results multi objective optimization technique is better than the segmented results without optimization technique.

5. Performance Evaluation

Due to the dimensional variations of each database images has been independently evaluated to find the accuracy of the proposed method. The output of each dataset has been initially converted to binary images and compared with the ground truth images. Here, the most effectively used evaluation parameters such as accuracy, selectivity and sensitivity has been used for performance evaluation. These values depend on the TP, FN, TN and FP values. The below equations (2-4) has been used to find the parameters, accuracy is given by [16]

$$Accuracy = \frac{TN + TP}{TP + TN + FP + FN} x100 \qquad (3)$$

Another performance metric specificity is calculated by using the following equation [17], the value of specificity must be high for better segmentation.

$$Specificity = \frac{TN}{TN + FP} x100 \qquad (4)$$

The next important parameter is sensitivity, it is expressed as below equation [18]. The segmentation method produces better result when the sensitivity value is high enough.

$$Sensitivity = \frac{TP}{TP + FN} x100 \qquad (5)$$

Where, TP represents True Positive, FN represents False Negative, TN represents True Negative and FP represents False positive respectively The evaluation parameter values for segmentation accuracy, sensitivity and specificity are listed in table.1 and table.2.

Table.1 Evaluation of Segmentation Accuracy, sensitivity and specificity with and without optimization for hand gesture images in RGB domain

Images	Segmentation Accuracy		Sensitivity		Specificity	
	With Opt	Without Opt	With Opt	Without Opt	With Opt	Without Opt
01	0.98	0.92	0.98	0.85	0.96	0.84
02	0.99	0.84	0.98	0.83	0.96	0.87
03	0.9	0.85	0.9	0.84	0.9	0.84

	8		6		5	
04	0.96	0.85	0.95	0.82	0.95	0.83
05	0.94	0.84	0.98	0.82	0.93	0.82
06	0.92	0.83	0.92	0.83	0.92	0.88
07	0.96	0.91	0.94	0.84	0.98	0.87
08	0.94	0.84	0.96	0.85	0.92	0.85
09	0.93	0.81	0.95	0.87	0.96	0.82
10	0.94	0.86	0.95	0.86	0.95	0.83

Table.2 Evaluation of Segmentation Accuracy, sensitivity and specificity with and without optimization for hand gesture images in SIH domain

Images	Segmentation Accuracy		Sensitivity		Specificity	
	With Opt	Without Opt	With Opt	Without Opt	With Opt	Without Opt
01	0.96	0.85	0.98	0.85	0.97	0.84
02	0.96	0.88	0.95	0.83	0.95	0.85
03	0.95	0.86	0.96	0.82	0.96	0.84
04	0.95	0.85	0.94	0.84	0.94	0.87
05	0.92	0.84	0.92	0.85	0.95	0.83
06	0.94	0.82	0.97	0.85	0.98	0.81
07	0.92	0.82	0.98	0.84	0.97	0.82
08	0.94	0.86	0.92	0.83	0.95	0.84
09	0.93	0.87	0.93	0.88	0.92	0.87
10	0.97	0.85	0.91	0.87	0.95	0.88

Table.1 gives the performance values for proposed method in RGB domain, and table.2 gives the performance values of proposed method in SIH domain. This performance evaluation table clearly shows that, the segmentation accuracy, sensitivity and specificity is far better in MTOBS when compared without optimization technique. The proposed MTOBS method produces better segmentation results in terms of average segmentation accuracy of 96%, sensitivity of 95% and specificity of 95%. The segmentation accuracy of proposed method without optimization is 85%. Therefore, the accuracy of the proposed method is increased by 10%.

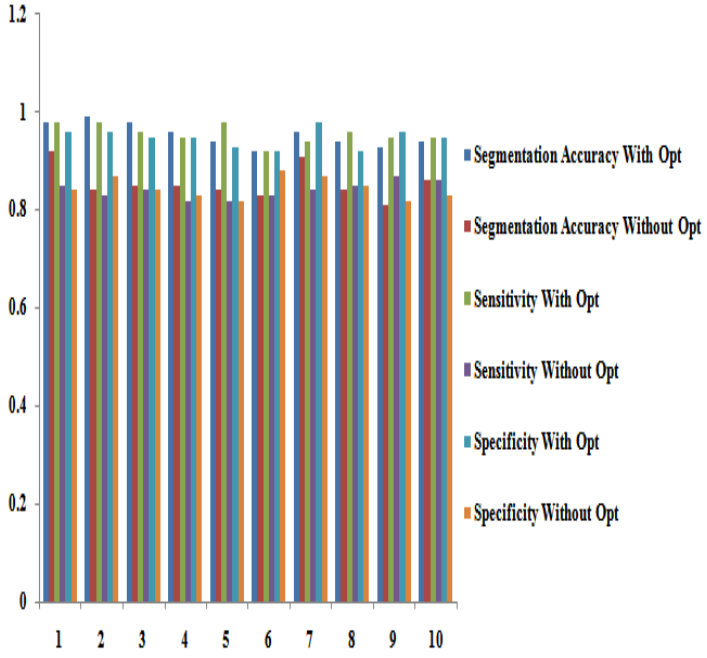

Fig. 10 Comparative Analysis of performance parameters of segmented

Hand gesture images (RGB) with and without optimization

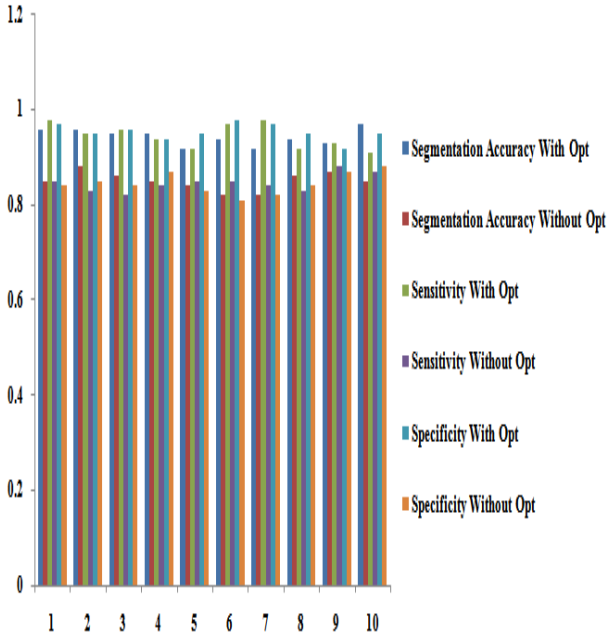

Fig. 11 Comparative Analysis of performance parameters of segmented Hand gesture images (SIH) with and without optimization

The comparative analysis of performance parameters of segmented Hand gesture images (SIH and RGB) with and without optimization is given in fig.10 and fig.11. From the analysis, it is clearly noticed that, the proposed method produces better segmentation results with the segmentation accuracy of 96%. Therefore, it is strongly concluded that, the proposed method is well suitable for segmenting the hand gesture images for hand gesture recognition.

Table.3 Recognition Accuracy of real-time gesture data for various methods.

Methods	Year	Dataset	RA (%)
H. Ragheb et al., [1]	2008	ViHASi	72.00
C. C. Chen & J. Aggarwal, [2]	2009	UT-Tower	90.43
M. S. Ryoo & J.K. Aggarwal [3]	2009	UT-interaction	91.67
J.C. Niebles et al., [4]	2010	Olympic sports	91.10
A. Patron-Perez et al., [5]	2010	TV human interaction	46.00
H. Kuehne et al., [6]	2011	HMDB51	57.20
G. Denina et al., [7]	2011	Video we	72.00
K. Soomro et al., [8]	2012	UCF-101	83.50
K.K. Reddy & M. Shah, [9]	2013	UCF-50	91.20
M.M. Gharasuie, H. Seyedarabi [10]	2014	Numbers (0-9)	93.84
H. Kim & I. Kim, [11]	2015	Kyonggi dataset	95.00
Archana Ghotkar et al., [12]	2016	ISL (20 dynamic signs)	89.25
Pablo Barros et al.,[13]	2017	RPPDI	93.33

Table.3 gives the recognition accuracy of real-time gesture data for various methods. This values has been used to compare the efficiency of the proposed method. The proposed method gives the recognition accuracy of 96%. This comparative analysis is depicted in fig.12

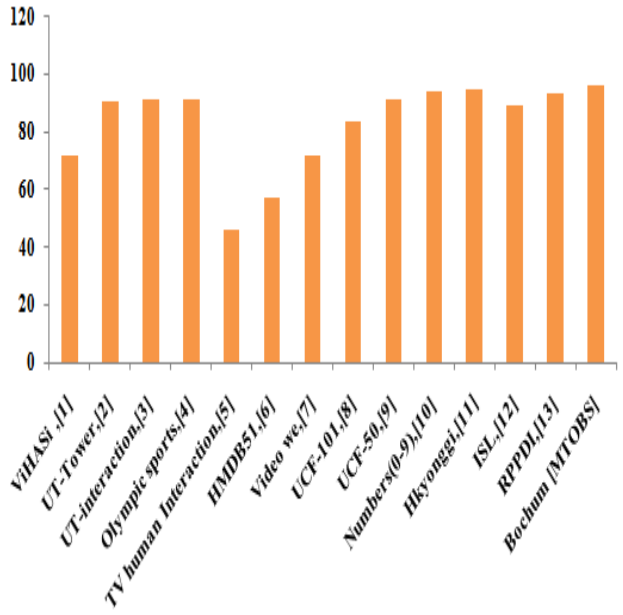

Fig.12 Comparative Analysis of Recognition Accuracy with existing other methods

6. Conclusion

In this paper, an optimization-based segmentation approach is proposed for hand gesture recognition. Multi objective algorithm is used for optimization. The work is carried out for BochumGestures1998 dataset. Experiments are carried out on segmentation with and without optimization. The average value of recognition rate with multi objective optimization has been increased by 10%. The proposed system has also yielded higher recognition rate than the other conventional hybrid techniques used in hand gesture recognition system.

References

[1] H. Ragheb, S. Velastin, P. Remagnino, T. Ellis, Vihasi, Virtual human action silhouettedata for the performance evaluation of silhouette-based action recognitionmethods, 2nd ACM/IEEE International Conference on Distributed Samrt Cameras (ICDSC) (2008) 1–10.

[2] C.-C. Chen, J. Aggarwal, Recognizing human action from a far field of view, Workshop on Motion and Video Computing (2009) 1–7.

[3] M.S. Ryoo, J.K. Aggarwal, Spatio-temporal relationship match: video structurecomparison for recognition of complex human activities, IEEE InternationalConference on Computer Vision (ICCV) (2009) 1593–1600.

[4] J.C. Niebles, C.-W. Chen, L. Fei-Fei, Modeling temporal structure of decomposablemotion segments for activity classification, European Confernce on ComputerVision (ECCV), Springer, 2010, pp. 392–405.

[5] A. Patron-Perez, M. Marszalek, A. Zisserman, I. Reid, High five: recognizing humaninteractions in TV shows, Proceedings of the British Machine Vision

Conference (BMVC) (2010) pp. 50. 1–50.11.

[6] H. Kuehne, H. Jhuang, E. Garrote, T. Poggio, T. Serre, Hmdb: a large video databasefor human motion recognition, IEEE International Conference on Computer Vision (ICCV) (2011) 2556–2563.

[7] G. Denina, B. Bhanu, H.T. Nguyen, C. Ding, A. Kamal, C. Ravishankar, A. RoyChowdhury, A. Ivers, B. Varda, Video web dataset for multi-camera activities andnon-verbal communication, Distributed Video Sensor Networks, Springer, 2011, pp.335–347.

[8] K. Soomro, A.R. Zamir, M. Shah, UCF101: A Dataset of 101 Human Actions Classesfor Videos in the Wild, Technical Report CRCV-TR-12-01, University of CentralFlorida, 2012 November.

[9] K.K. Reddy, M. Shah, Recognizing 50 human action categories of web videos, Mach.Vis. Appl. 24 (5) (2013) 971–981.

[10] M.M. Gharasuie, H. Seyedarabi, Real-time dynamic hand gesture recognition usinghidden Markov models, 8th Iranian Conference on Machine Vision and ImageProcessing (MVIP) (2014), http://dx.doi.org/10.1109/IranianMVIP.2013.6779977.

[11] Hyesuk Kim, Incheol Kim, Dynamic arm gesture recognition using spherical anglefeatures and hidde Markov models, Adv. Hum. Comput. Interact. 2015 (2015) 7, http://dx.doi.org/10.1155/2015/785349 (2015).

[12] Archana Ghotkar, Pujashree Vidap, Kshitish Deo, Dynamic hand gesture recognitionusing hidden Markov model by Microsoft kinect sensor, Int. J. Comput. Appl. 150

[13] (2016), http://dx.doi.org/10.5120/ijca2016911498.[35] Pablo Barros, Nestor T. Maciel-Junior, Bruno J.T. Fernandes, Byron L.D. Bezerra,Sergio M.M. Fernandes, A dynamic gesture recognition and prediction system usingthe convexity approach, Comput. Vis. Image Understanding 155 (2017) 39–149.

[14] Sachin A. Urabinahatti, Apeksha S. Bandekar, Human-computer interaction usinghand gestures, Int. J. Recent Innov. Trends Comput. Commun. 2 (5) (2014)1305–1311.

[15] Gholam Reza Amayeh, Ali Erol, George Bebis, Mircea Nocilescu, Accurate andEfficient Computation of High Order Zernike Moments, ISVC 2005, Springer-Verlag,Berlin, 2005, pp. 462–469.

[16] Godlin Atlas.L,Kumar Parasuraman. "Detection of retinal hemorrhage from fundus images using ANFIS classifier and MRG segmentation" Biomedical Research 2018; 29 (7): 1489-1497.

[17] Yogesh Kumaran, Chandrashekar M. Patil, "A Brief Review of the Detection of Diabetic Retinopathy in Human Eyes Using Pre-Processing & Segmentation Techniques" International Journal of Recent Technology and Engineering, Vol.7 (4S2), 2018, pp. 310-320.

[18]ZeynabMohammadpoory, MahdaNasrolahzadeh, NaghmehMahmoodian,JavadHaddadnia, " Automatic identification of diabetic retinopathy stages by using fundus images and visibility graph method" MeasurementVolume 140, July 2019, Pages 133-141

Proposed Topology of Cascaded Multilevel Inverter Used for Reduced Number of On State Switches

AustinJohnny[1]*, *S.JosephJawhar*[2]

[1]*EEEDepartment, CSIInstituteofTechnology, Thovalai, TamilNadu,India, mail: johnnycsiit@gmail.com*

[2]*ArunachalaCollegeofEngineeringforWomen, Vellichanthai,TamilNadu,India, mail: josephjawahar@gmail.com*

Abstract: This paper presents a novel topology for cascade multilevel inverter. Multilevel inverter is an alternative within the area of lot of power average voltage energy control. This proposed paper analyses a generalized cascaded inverter topology with minimized number of switching devices. In this proposed work of multilevel inverter, the aim is to reduce the number of dc voltage sources and switches to obtain number of voltage levels. The proposed circuit consists of series connected Switching units and it can generate DC voltage levels similar to other topologies. In this paper, six switches are used to generate 9 level inverter output. Topology of the proposed cascaded multilevel inverter considers some factors such as number of switching devices, number of output voltage levels and the standing voltage on the switches. The quality output voltage depends on the number of voltage level in the inverter. This new inverter shows superior capabilities when compared to other existing topologies. To verify the proposed topology, a 9-level inverter has been simulated. In this work the THD value is reduced to 7.58 % which is very low when compared to other existing topologies. The simulation results are carried out using MATLAB/SIMULINK.

Keywords: Multilevel inverter, Cascaded Circuit.

1. Introduction

Multilevel inverters have emerged because of the industry's selection due to their voltage stress reduction, inherent redundancy. They present a set of options that are suited to use in reactive power compensation. Increasing the amount of voltage levels within the electrical converter, while not using higher ratings on individual devices will increase the ability ratings. As the levels of voltage increases, the harmonics of the output voltage waveform decreases. A Neutral-point-clamped (NPC) inverter composed of main switching devices that operate as switches and auxiliary switches to clamp the output potential to the neutral point potential [1]. Flying Capacitance inverters suffer from capacitor voltage imbalance that results in a power quality deterioration and an increase in blocking voltages. The flying capacitor topology needs larger capacitor banks and additional pre-charging electronic equipment [2].

Cascade MLIs has been mentioned on topologies that need a less number of switches, diodes, gate drives and DC sources as the number of voltage levels will increase. This method is used to reduce voltage stress on switches. This inverter has the series connection of the existing unit to generate solely positive levels in the output [3]. Cascade H bridge Multilevel inverter needs

reduced number of elements to generate the maximum number of levels. This inverter will increase the output waveform level and the low order harmonics will be reduced [4]. E-type of cascade inverter module will generate thirteen levels with a reduced range of components. It reduces the stress on semiconductor devices and improves the reliability [5].

A new non-isolated DC supply with symmetric multilevel inverter with the lesser number of switches that reduces the complexity. It is possible to generate an odd range of output voltage levels. Increase the amount of levels that may reduce the distortion of harmonics [6]. Throughout steady-state operation and transient condition, the stability can be verified by capacitor balancing algorithm. It has the ability to generate the voltages from a one dc-link power supply [7]. In a modular multilevel inverter the four discord algorithms is mentioned and calculate an equivalent value of dc sources [8]. This topology has six level inverter consists of the inner flying capacitor and outer two-level inverter. It has reduced the isolated sources and device requirement [9].

By using stacking multilevel inverter, the space vector voltage to be low to generate the higher number of voltage waveform[10]. Low ripple current waveforms is generated with unity power factor. The converter is controlled using the proposed multilevel active rectifier and improved by MPPT algorithms [11]. Topology with a reversing-voltage element is proposed to enhance the performance of multilevel inverter [12]. In this work, modulation is easily extended to three phase, and using the higher level inverters operates with same structure of the module [13]. The performance of current control is improved with voltage delay compensation and therefore the fault tolerance is increased by using unbalance three-phase control [14]. It includes double frequency operation of output inductance and current that flows through power switches and filter inductance to be equal [15].

The Control algorithmic rule is employed to generate the gating signals for the power switches and maintain the natural balancing of all the capacitors [16]. A multilevel DC link employing a fixed DC voltage source and cascaded half-bridge is connected in such a way that the inverter outputs the desired output voltage levels. The staircase modulation technique is definitely used to generate the appropriate switch gate signals [17]. The proposed topology not solely has lower switches and elements compared with another one, however additionally its full bridge converters operate within the lower voltage [18].

The topology needs lesser number of dc sources and power switches and it consists of lower blocking voltage on switches, which ends in reduced complexity [19]. This inverter need less number of switches, whereas capacitor desires less variety of magnitude of dc voltage sources [20]. Symmetric and asymmetric operational modes, are analyzed during this proposed topology [21]. The main aim of optimization was generating the output voltage levels to be maximum with the minimum range of power electronic components and voltage rating on

switches [22]. The proposed technique is robust against the faults in switches of multilevel converter for dc supply [23].

The main contribution of this work is

1. Novel cascade multilevel inverter is designed using reduced number of on state switches, whereas the existing topology are designed for maximum number of switches.

2. Advantage of using Multilevel Inverter in this research is to reduce the harmonics. To validate this, THD analysis is performed.

3. Novel cascade multilevel inverter is proposed in this research to reduce the harmonics and losses.

The paper highlighting the proposed research is organized as follows:

Section 2 presents the block diagram of proposed system with relevant explanations and presents the n basic unit of cascade inverter. It also compares the semiconductor devices and switches in the current path with the existing topologies. Section 3 introduces the simulation results performed using MATLAB/SIMULINK along with relevant discussions. Finally, the concluding remarks and suggestions for further research are given in Section 4.

2. Proposed Topology

The basic unit of the proposed MLI consists of four unidirectional switches (S1, S2, S3 and S4), two bidirectional switches (S5 and S6) and two direct current sources (Va and Vb). This unit is capable of generating nine-level output voltage. This inverter is cascade to get additional voltage levels. If n basic units are cascaded, the inverter will generate up to $(2^{n+1}+1)$and $(2^{n+1}-1)$, (n = 1,2,3,...) voltage output levels for equal and unequal operations. Avoid short-circuiting in the power sources, left-side switches (S1, S3, S5) is ON at a given time and also right-side switches (S2, S4, S6) is ON at a given instant.

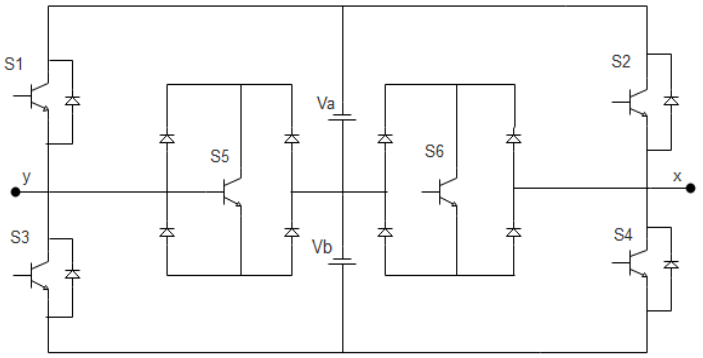

Figure 1 : Basic Block Diagram of Cascade Multilevel Inverter

Where S_j denotes the switching function of switch j (j = 1,2,...,6) and takes the value of 1 when ON and 0 when OFF. Table 1 shows the set of switching states of the fundamental unit and therefore the resulting inverter output voltage. The switching states consist of three null states and six active states. The three redundant null states is used to realize totally different control objectives.

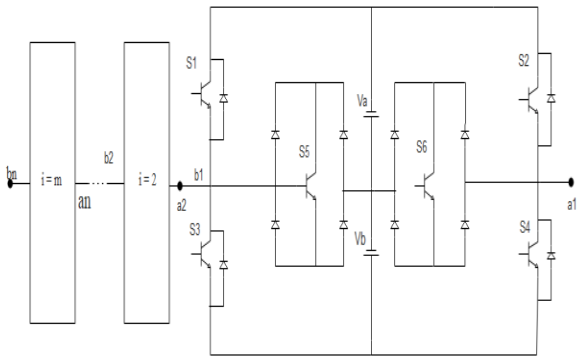

Figure 2: n cascade unit to generate output voltage levels

The bidirectional switches protect the inverter from short-circuit currents when operating in asymmetrical mode. Due to the voltage drop in one of the diodes of the bridge the diodes are forward biased. The bidirectional switches can distort the output wave form at low voltage levels. This topology is not significant in low and medium level voltage applications. Due to drop of voltage in any one of the diode, the bidirectional switches reduce the harmonics in the output voltage waveform.

States	S1	S2	S3	S4	S5	S6	Output Voltage
1	0	0	1	1	0	0	0
2	0	0	1	0	0	1	$+V_b$
3	0	0	0	1	1	0	$-V_b$
4	0	0	0	0	1	1	0
5	0	1	1	0	0	0	$+(V_a + V_b)$
6	0	1	0	0	1	0	$+V_a$
7	1	0	0	1	0	0	$-(V_a + V_b)$
8	1	0	0	0	0	1	$-V_a$
9	1	1	0	0	0	0	0

Table 1 : Switching Topology of Proposed Multilevel Inverter

2.1 Operation of Proposed Topology

It consists of two voltage sources Va and Vb and six semiconductor switches. Every switch consists of a MOSFET/IGBT with anti parallel diode. The output voltage of multilevel is generated on the set of switching states. To produce a nine-level output (Vxy), at least one null state and all the active states are fired in-sequence. For uniform power dissipation among the six switches, two null states are used, wherever State1 is ON throughout the positive half-cycle, whereas State 9 is employed throughout the negative half-cycle. Any PWM method could be used to control the semiconductor switches, tend to choose phase disposition PWM because of its performance.

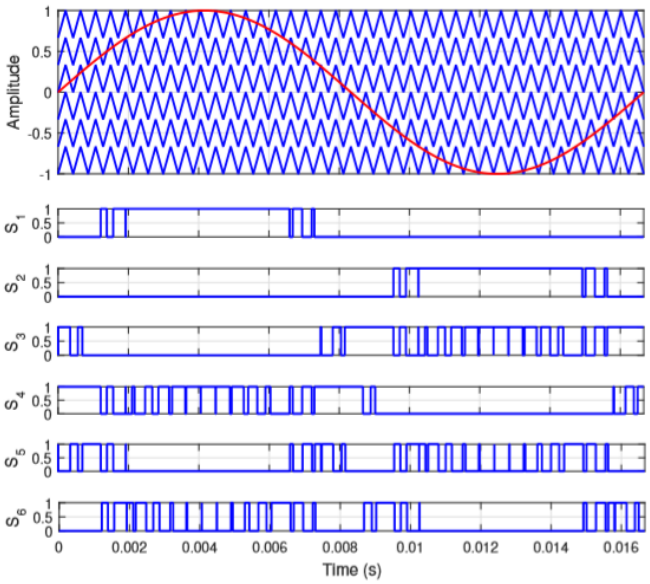

Figure 3 : Phase Disposition Modulation and Gating signals of Nine Level Inverter

The General expression for level number of voltage is

$$l = (2*Sw-3), \quad (1)$$

Where *l* = number of voltage levels in the output

Sw = number of switches

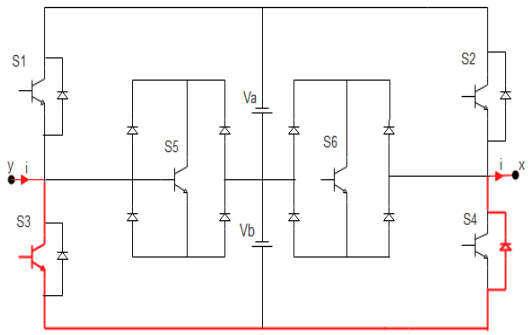

Mode 1: State 1 Vxy = 0, S3 = S4 = 1

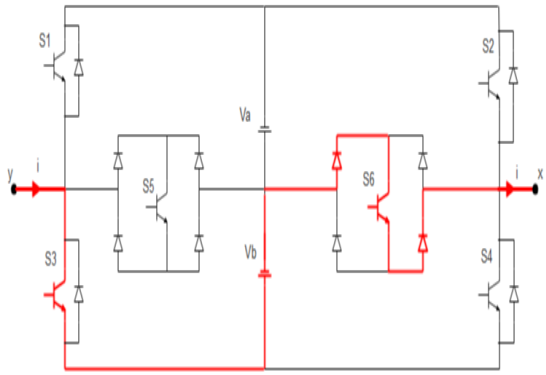

Mode 3: State 2 Vxy = +V2, S3 = S6 = 1,

It requires bidirectional switches with the potential of blocking voltage and current conducting in each direction. The unidirectional switches within the inverter

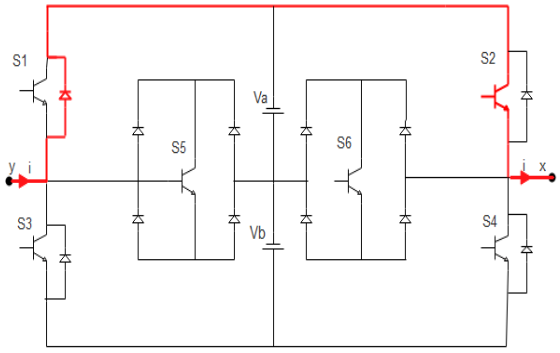

Mode 2: State 9 Vxy = 0,S1 = S2 = 1

and bidirectional switches should operate at the high output voltage and need higher voltage.

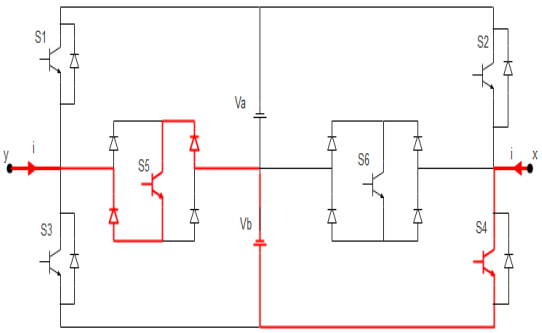

Mode 4: State 3 Vxy = −V2, S4 = S5 = 1

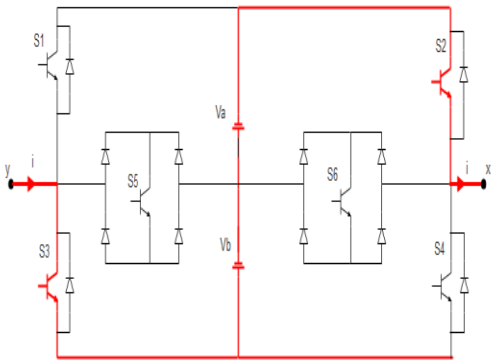

Mode 5:State5 Vxy = + (V1 + V2), S2=S3=1,

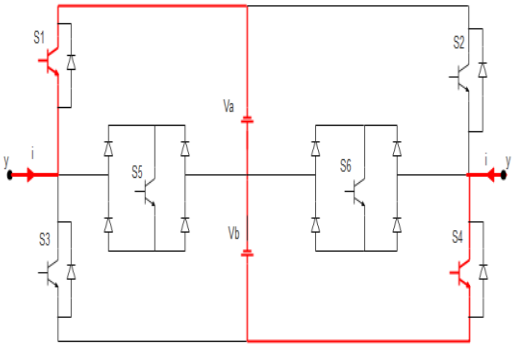

Mode 7: State 7 Vxy = − (V1 +V2), S1=S4= 1

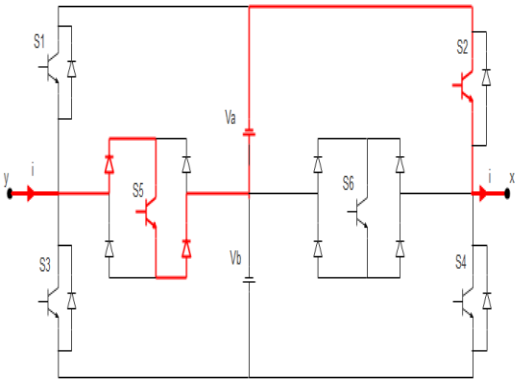

Mode 6: state 6 Vxy = +V1, S2 = S5 = 1

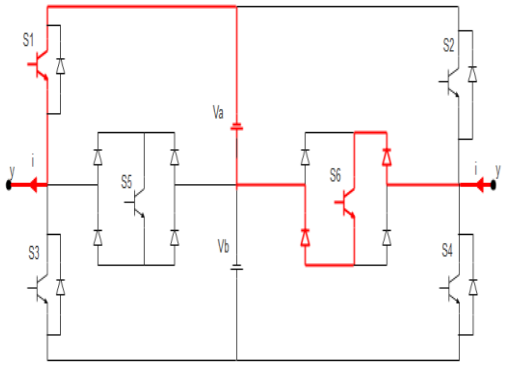

Mode 8: state 8 Vxy = −V1, S1 = S6 = 1

Fig 4 : Switching states for generating voltage level output

2.3 Number of Switching Devices in Proposed Inverter

The number of semiconductor devices has a control on value and size or weight of an MLI unit as a result of the ability to get a similar number of voltage output levels by using reduced switches can each lower a unit's cost and physical size. Figure 5 shows the quantity of switches required to generate a similar number of voltage output levels for various topologies. It's clear that the proposed topology out performs the other topologies with the lowest switch count for a similar voltage level.

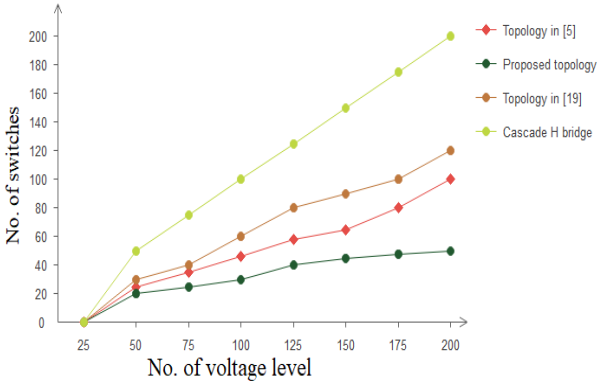

Figure 5: Number of switches versus voltage level of inverter

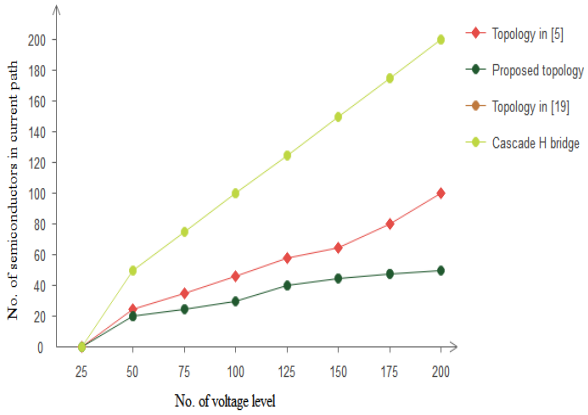

Figure 6: Number of semiconductors in the current path versus output voltage levels

2.4 Number of Semiconductors in the Current Path

When a switch or diode will turn on or off instantly without any power loss, real switches have a finite switching transition time. This finite transition period is accompanied by power loss transients. Hence, a smaller number of needed switches to supply a voltage level implies reduced power losses. Figure 6 shows the number of switches within the current path for identical voltage levels for the various. The proposed topology performs higher than in each modes that can leads to higher efficiency at any output voltage level.

3. Simulation Results and Discussion

Figure 7 shows the schematic diagram of the system with RL load under study. Simulations of six switch 9 level inverter were carried using MATLAB/ Simulink .The semiconductor switches are IGBT with voltage and current ratings of 600 V, 120 A in figure 7.

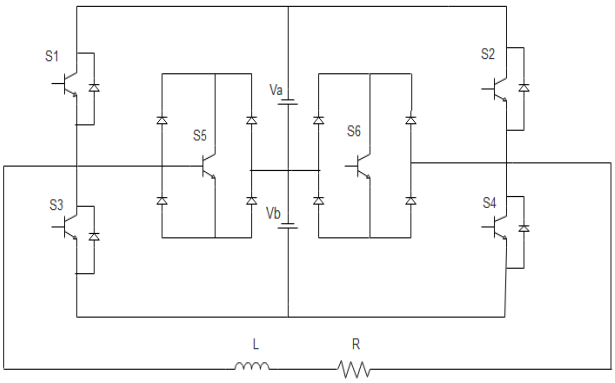

Figure 7: Schematic Diagram with RL load

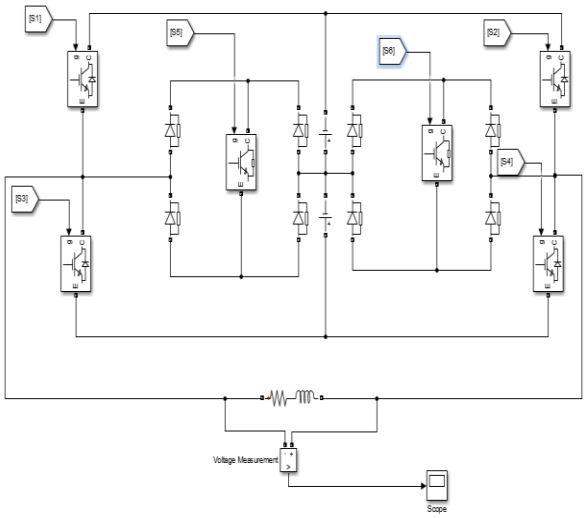

Figure 8 : Simulation circuit of Six-Switch 9 level Inverter

.

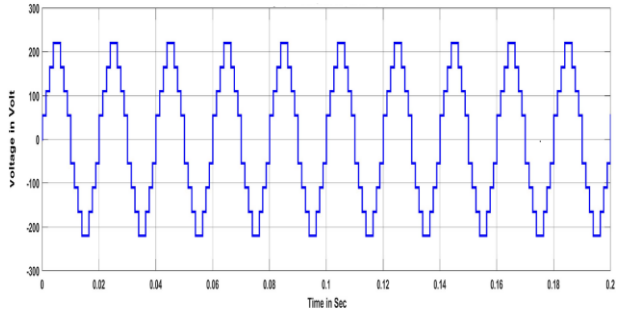

Figure 9 : Simulated 9-level Output Voltage waveform

Figure 9 shows the simulation results of the inverter output voltage waveforms for nine-level operation. Using six switches the nine level output voltage to be determined.

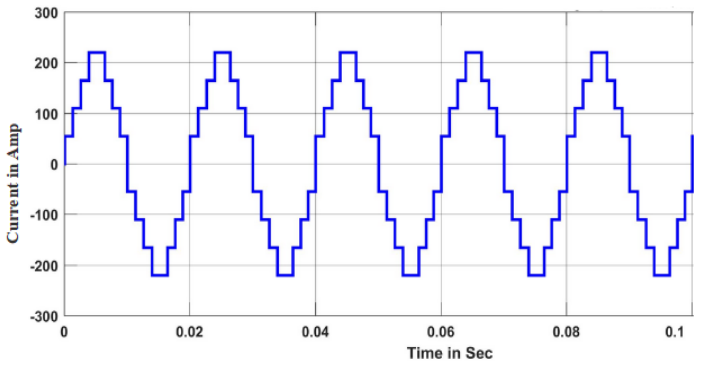

Figure 10: Simulated 9-level Output current waveform

Figure 10 shows the inverter output current waveform for nine level inverter. To generate a desired output with the best quality of the waveform, the number of the voltage steps should be increased.

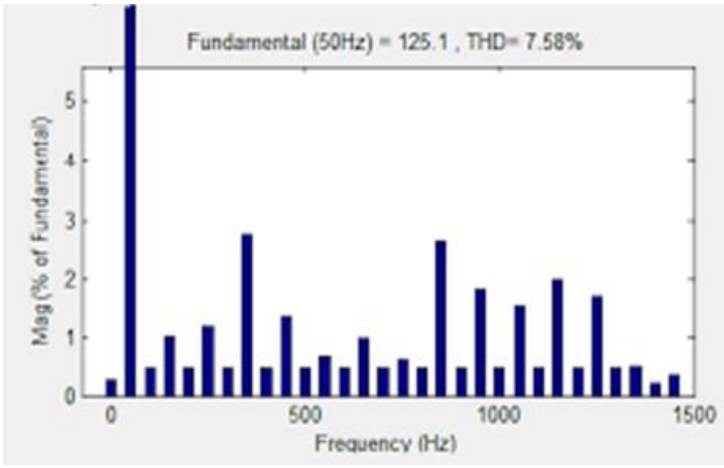

Figure 11 : FFT plot of 9 level Multilevel Inverter

The corresponding THD% are observed using FFT block and the FFT value is shown in figure 11. The THD value is reduced to very low in the proposed topology. It improves the performance of cascaded multilevel inverter.

3.1 Comparative Analysis

Comparative Performance based on THD for 9 level inverter

S.no	Inverter	No.of switches	THD %
1	Proposed work	6	7.58
2	Symmetric Inverter ref no[6]	9	22.27
3	Cascade MLI ref no [21]	8	10.12

4. Conclusion

In this paper, proposed topology for nine level inverter with on state switches to be reduced. The principles of operation of the design are discussed and validated using simulations. The new modulation is compared to two similar modulations in terms of the number of switches needed to generate a voltage level; the number of switches within the current path will be handled by the switches. Here the six switch and 2 dc voltage sources are used to generate the 9 level inverter output. This topology optimization of the proposed cascaded multilevel considering some factors such as number of switching devices, number of output voltage levels is reduced. This topology produces both the positive and negative voltage levels without the necessity for the classical H-bridge circuit and therefore reduces the semiconductor device count. MATLAB/ Simulink simulations are presented for nine level operations of cascade multilevel inverter. In this work, total harmonic distortion value is reduced to very low value when compared to existing topologies.

References

1. Rodriguez, Jose, Steffen Bernet, Peter K. Steimer, and Ignacio E. Lizama. A survey on neutral-point-clamped inverters. IEEE; 2010: 2219-2230.
2. Choi, Hyuntae, Wei Zhao, Mihai Ciobotaru, and Vassilios G. Agelidis. Large-scale PV system based on the multiphase isolated dc/dc converter. In Power Electronics for Distributed Generation Systems (PEDG). IEEE; 2012: 801-807.
3. Babaei, Ebrahim, Sara Laali, and Zahra Bayat. A single-phase cascaded multilevel inverter based on a new basic unit with reduced number of power switches. IEEE; 2015: 922-929.
4. Lai, Y-S., and F-S. Shyu. Topology for hybrid multilevel inverter. IEEE; 2002: 449-458.
5. Samadaei, Emad, Sayyed Asghar Gholamian, Abdolreza Sheikholeslami, and Jafar Adabi. An Envelope Type (E-Type) Module: Asymmetric Multilevel Inverters With Reduced Components. IEEE; 2016 : 7148-7156.
6. Mohammadalibeigy, L., and N. A. Azli. A new symmetric multilevel inverter structure with less number of power switches. IEEE; 2014: 321-324.
7. Kumar, P. Roshan, R. Sudharshan Kaarthik, K. Gopakumar, Jose I. Leon, and Leopoldo G. Franquelo. Seventeen-level inverter formed by cascading flying capacitor and floating capacitor H-bridges. IEEE; 2015: 3471-3478.

8. Barzegarkhoo, Reza, Naser Vosoughi, Elyas Zamiri, Hossein Madadi Kojabadi, and Liuchen Chang. A cascaded modular multilevel inverter topology using novel series basic units with a reduced number of power electronic elements. Journal of Power Electronics 2016; 2139-2149.
9. Le, Quoc Anh, and Dong-Choon Lee. A novel six-level inverter topology for medium-voltage applications. IEEE; 2016: 7195-7203.
10. Nair, Viju, R. Sudharshan Kaarthik, Abhijit Kshirsagar, and K. Gopakumar. Generation of higher number of voltage levels by stacking inverters of lower multilevel structures with low voltage devices for drives. IEEE; 2017: 52-59.
11. Villanueva, Elena, Pablo Correa, José Rodríguez, and Mario Pacas. Control of a single-phase cascaded H-bridge multilevel inverter for grid-connected photovoltaic systems. IEEE; 2009: 4399-4406.
12. Najafi, Ehsan, and Abdul Halim Mohamed Yatim. Design and implementation of a new multilevel inverter topology. IEEE; 2012: 4148-4154.
13. Vijaybabu, S., A. Naveen Kumar, and A. Rama Krishna. Reducing Switching Losses in Cascaded Multilevel Inverters Using Hybrid-Modulation
    Techniques. International Journal of Engineering Science Invention; 2013: 26-36.
14. Park, Young-Min, Han-Seong Ryu, Hyun-Won Lee, Myung-Gil Jung, and Se-Hyun Lee. Design of a cascaded H-bridge multilevel inverter based on power electronics building blocks and control for high performance. Journal of Power Electronics; 2010: 262-269.
15. Hu, Yanshen, Yunxiang Xie, Dianbo Fu, and Li Cheng. A New Single-Phase Pi Type 5-Level Inverter Using 3-Terminal Switch-Network. IEEE; 2016: 7165-7174.
16. Karasani, Raghavendra Reddy, Vijay Bhanuji Borghate, Sidharth Sabyasachi, Hiralal Murlidhar Suryawanshi, and Prafullachandra Madhukar Meshram. Cascaded Multi-level Inverter Topology Developed from a Modified H-bridge. Electric Power Components and Systems ; 2017: 1191-1201.
17. Masaoud, Ammar, Hew Wooi Ping, Saad Mekhilef, and Ayoub Suliman Taallah. New three-phase multilevel inverter with reduced number of power electronic components. IEEE; 2014: 6018-6029.
18. Ebrahimi, Javad, Ebrahim Babaei, and Gevorg B. Gharehpetian. A new multilevel converter topology with reduced number of power electronic components. IEEE ; 2012 : 655-667.
19. Babaei, Ebrahim, Somayeh Alilu, and Sara Laali. A new general topology for cascaded multilevel inverters with reduced number of components based on developed H-bridge. IEEE ; 2014 : 3932-3939.

20. Prayag, Aparna, and Sanjay Bodkhe. Novel Basic Block of Multilevel Inverter Using Reduced Number of On-State Switches and Cascaded Circuit Topology. Advances in Electrical Engineering 2017.
21. Johnny, Austin, and S. Joseph Jawhar. Cascaded Circuit Multilevel Inverter Topology Used for Reducing Number of On State Switches. Journal of Computational and Theoretical Nanoscience ; 2018 : 939-948.
22. Alishah, Rasoul Shalchi, Seyed Hossein Hosseini, Ebrahim Babaei, and Mehran Sabahi. Optimal design of new cascaded switch-ladder multilevel inverter structure. IEEE ; 2017 : 2072-2080.
23. Samanbakhsh, Rahim, and Asghar Taheri. Reduction of power electronic components in multilevel converters using new switched capacitor-diode structure. IEEE; 2016 : 7204-7214.

SFRA Capability for detection of deformation in Transformer windings: A field experience of 400kV 167MVA single phase ICT

Ashok Chavda * **Dr. Vivek Pandya ****

Abstract – Sweep Frequency Response Analysis has become very popular now – a - days due to its ability to provide comprehensive information regarding mechanical as well as electrical condition of power transformers. The SFRA is a signature test and provides better information when evaluation of Transformer condition is done by comparing actual set of SFRA results with reference results. This field experience refers to 400/220/33KV ICT bank, formed with three single phase units – each with capacity of 167MVA. Heavy fault current was fed through ICT due to failure of LA provided on external delta formation of Tertiary winding. Mechanical defects / deformation occur ostensibly due to short circuit current flowing through transformer winding in case of terminal faults i.e. fault adjacent to / on the power transformer. To ascertain mechanical integrity of power transformer, SFRA test is carried out and is supported by other tests i.e. capacitance and tan delta measurement etc. The test results reveal that SFRA is capable of providing more information about mechanical deformation of active parts of power transformers - compared to other tests.

Keywords: Sweep Frequency Response Analysis, Winding Deformation, Inter-connected Transformer ICT, Capacitance and Tan delta, Mechanical integrity.

1. Introduction

Power transformers in service, agonize through excessive electrical as well as mechanical stresses throughout their life span. Power transformers are most costly, substantial and important equipment of power system and their failure may hamper power supply to consumers, especially when sensitive industries are involved. SFRA test provides useful information about mechanical deformation of windings [1]. The most severe and predominant forces arise from system faults taking place adjacent to / on Power Transformer. The electromagnetic forces generated by faults may be axial, radial or assorted, depending on nature of fault. If the forces are excessive, radial buckling or axial deformation may occur [2]. Once a transformer is damaged either enormously or slightly, the ability to withstand further incidents or short circuit withstand ability is reduced proportionate to fault current supplied [3].

In present case- study, overhauling (OH) of single phase ICT unit of B phase was completed on date 07.01.2016 and transformer was put back in service. Subsequent to failure of LA on date 04.07.2016, movement of tertiary winding noticed in SFRA Traces. Same was supported by capacitance and tan delta test results, as change in capacitance value recorded for tertiary winding only. So, inference drawn that - due to failure of LA, heavy fault current was fed through ICT unit, leading to radial displacement in tertiary winding. No deviation noticed indicating any movement – in SFRA traces for other windings.

Other test results were found normal, they didn't indicate abnormality with Tertiary winding, and hence it was recommended to carry out internal inspection of ICT unit. However, nothing was found abnormal during internal Inspection at site.

Tertiary winding couldn't be inspected / visualized – as it was the innermost winding – surrounded by HV-IV winding - covered with hard board insulating cylinder.

Comprehensive SFRA testing and analysis thereof indicated tertiary winding displacement and led suspicion to mechanical integrity of same winding. However, all other test results were found in order; so it was decided to charge the transformer.

*Corresponding Author**:** Dept. of Gujarat Energy Transmission Corporation Ltd. (GETCO) India. (erajchavda@yahoo.co.in)

**Dept. of Electrical Engineering, Pandit Dindayal Petroleum University PDPU India. (Vivek.Pandya@sot.pdpu.ac.in)

Received ; Accepted

After taking all safety precautions and confirming protection checks - transformer was charged. However, Transformer couldn't withstand charging current and tripped immediately on differential protection with buchholz relay. Once again transformer tested meticulously and now SFRA test results clearly indicated turn to turn short in tertiary winding [4]. This was due to development of deformation and reduction of mechanical strength of tertiary winding during heavy fault current feeding at the instant of L.A. failure.

2. Electromagnetic Forces

An electromagnetic force is generated in current carrying conductor when it is surrounded by magnetic flux, and its magnitude and direction depends on magnitude and direction of current flowing through conductor. In power transformer while in service, system faults or faults inside the power transformers cause axial or redial electromagnetic forces and if transformer winding is not capable to withstand such forces then deformation takes place in winding and sometimes immense deformation may lead to transformer failure [5].

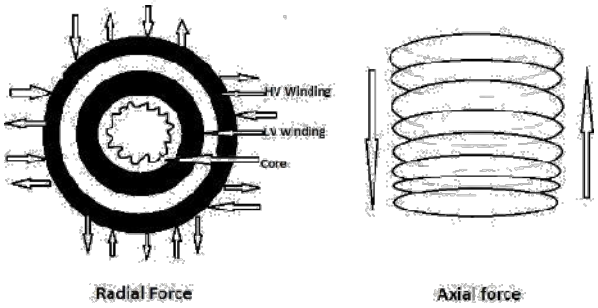

Fig. 1. (a) Radial Force (b) Axial force

Usually, transformer internal short circuits act on the transformer solid insulation system of paper and pressboard, while external through fault short circuits in power networks tends to subject transformer winding through radial electromagnetic forces. It acts on the external winding coil from within, and on the internal winding coil inwards and results in radial movement of the windings. The direction of the forces is perpendicular to the magnetic field lines which may have components that cause both radial forces and axial forces. Radial forces and axial forces cause winding buckling as narrated in figure 1(a) and figure 1(b) respectively.

3. SFRA

The first technical paper published on Frequency Response Analysis by Mr. E.P. Dick and Mr. C.C. Erven in 1978 [1]. Sweep frequency response analysis has been developed to detect winding movement and deformation in power transformers. High voltage power transformer can be represented as a complex electric system consisting bunch of inductances, capacitances and resistances in series and parallel formation. The complex structure of power transformers can be represented in simplified manner with two port network as shown in figure 2.

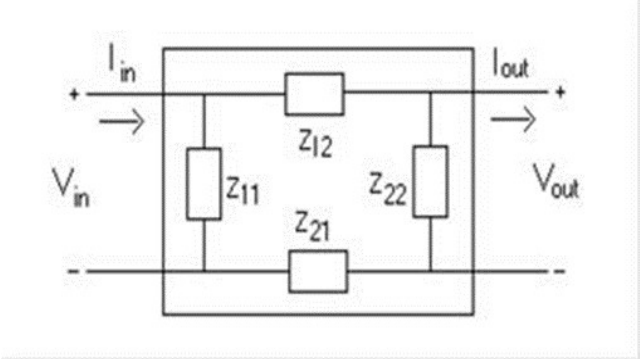

Fig. 2. Power Transformer as a two port network

The two port network, excited by the voltage signal, with variable frequency produces an electrical response which is dependent on the frequency of the input signal, and the value of output voltage depends on impedance of particular winding that have with-stood test at particular frequency.

Output voltage Vo and Input Voltage Vi are compared in the frequency domain, then the gain in dB as under

$$dB = 20\log 10 \ \frac{V_o}{V_i} \quad \text{.....(1)}$$

The values of RLC elements depend on the geometry and material used for each part of the transformer. Any change in geometry or change in material reflect significant change in the response. SFRA analysis involves comparison of two sets of test results: latest results are compared with base results; if base results are not available – comparison can be made with SFRA results of sister unit; and if SFRA results of sister unit are not available – comparison can be made with SFRA traces of other phases of same unit. If base results are available, then sound judgment can be drawn with the help of SFRA test results.

4. Tertiary Winding

It is an additional winding in a power transformer other than primary and secondary winding which is used to connect a synchronous condenser, a reactor and an auxiliary circuit for feeding power at a voltage level different from

secondary voltage is known as a tertiary winding. If auxiliary load connected with tertiary winding then known as a loaded tertiary winding. Delta connected auxiliary winding used particularly in wye-wye connected three phase power transformers as a tertiary winding for following purposes:

1) To stabilize the neutral point of the fundamental frequency voltages.
2) To minimize third harmonics
3) To serve auxiliary load
4) To control the value of zero sequence impedance.
5) Use for testing purpose in Lab

5. Case Study

At one of the 400kv sub-stations, 500MVA interconnected power transformer (ICT) which consists bank of three single phase units, each of 167MVA and tertiary winding with outside delta formation having adequate protection i.e. Lighting Arrestor (LA) and surge capacitor - was in service. Overhauling completed for 167MVA B Ph. unit on date 07.01.2016, transformer was charged and put in to service. On date 04.07.2016, due to failure of B phase LA resulting into heavy fault current feeding - said unit tripped with buchholz relay along with differential protection of ICT-bank. Suspected ICT unit of B phase - kept out of service for further investigation. 500MVA ICT again taken in to service with utilization of spare single phase unit available - instead of suspected B phase unit. For checking healthiness of B phase unit - all diagnosis tests as well all routine tests carried out.

Overall test reports were normal and no any major fault inside the transformer was indicated. It was decided to carry out internal inspection of ICT unit, as in DGA - key gases were observed. During internal inspection, nothing found abnormal inside the transformer. So, transformer oil filtration carried out and transformer was allowed to cool down naturally. Once again all tests carried out. Only SFRA test indicated deviation in tertiary winding graphs and same was support by capacitance and tan delta test showing change in capacitance of tertiary winding. After necessary precautions, checking all protection circuits and logic checks, transformer was charged. But it tripped at the instance of charging - with buchholz and differential relay operation. Outcome of all these test results discussed in following sections.

5.1 Capacitance and Tan delta Test

To ascertain insulating properties of the Transformer - capacitance and tan delta test was carried out. It is one of the most common tests performed on power transformers. The purpose of the test is to determine the capacitances and tan delta values - between the windings and for each winding with respect to earth. The said power transformer was overhauled (OH), and tan delta capacitance measurement carried out after overhauling. Capacitance and tan delta measurement also carried out after tripping of the ICT unit on buchholz relay operation - due to failure of LA. Both results were compared as shown in below table 1. No any major change was noticed and change in capacitance was found particularly in tertiary winding, however it was less than 5 %. No significant change in tan delta value recorded indicating that - there is no flashover occurred inside transformer, though movement of tertiary winding in radial direction could be anticipated as change in capacitance was noticed in CT(capacitance of tertiary winding with respect to earth) and CHT (capacitance between H.V. winding and tertiary winding). This indicates buckling of tertiary winding and same was confirmed by SFRA.

Date of Test	After OH 07.01.2016		After LA fail 07.07.2016		After tripping 12.08.2017	
Test ID	Tan Delta	Capacitance	Tan Delta	Capacitance	Tan Delta	Capacitance
CH+CHT	0.33	7280	0.29	7224	0.44	7323.7
CH	0.36	3651	0.35	3669	0.36	3640.5
CHT	0.3	3624	0.26	3550	0.51	3678.1
CT+CTH	0.35	9469	0.32	9623	0.62	10117
CT	0.38	5834	0.36	6064	0.73	6438
CTH	0.3	3623	0.27	3549	0.52	3678.2

Table 1. Capacitance and Tan Delta Results.

5.2 Measurement of Insulation Resistance (IR) and Polarization Index (PI)

Insulation resistance(IR) taken at one minute and at 10 minutes with application of 5kV DC through insulation tester and Polarization Index (PI) value was derived [6]. Result found normal and no any significant change perceived. Insulation resistance (IR) and Polarization Index (PI) after OH and after tripping shown in Table 2.

IR (G Ohms)	07.01.2016			07.07.2016			12.08.2017		
	1min.	10 min.	P.I.	1min.	10 min.	P.I.	1min.	10 min.	P.I.
HV to Earth	8.3	15	1.8	4.7	8.97	1.9	1.7	2.4	1.4
HV to Tertiary	12	34	2.7	7.6	19.2	2.5	1.6	2.3	1.4
Tertiary to Earth	8.9	26	2.9	6.3	13	2.1	2.3	3.5	1.5

Table 2. Insulation Resistance and Polarization Index.

5.3 Open Circuit and Short Circuit Test

To check electrical functioning of transformer, all routine tests were carried out - with single phase variac to keep supply voltage constant. Three results were noted down which are shown in table no.3, first one was taken after overhauling(OH) of transformer, second one was taken after failure of Lightning Arrestor (LA) and third one was taken after failure of transformer unit. During testing after failure of Lightning Arrestor (LA), magnetizing current was found increased in L.V. winding. However, same was due to residual magnetic flux inside the transformer core, and after de-magnetization of the core, result was found normal. After tripping dated on 12.08.2017, all results were found abnormal – especially magnetizing current increased significantly - indicating turn to turn short inside the transformer winding. Highest magnetizing current noticed for tertiary winding indicating turn to turn short in tertiary winding - same was confirmed by SFRA.

Routine testing	OH 07.01.2016	LA fail 05.07.2016	Tripped 12.08.2017
Open Circuit Test			
Applied voltage across to H.V.and Neutral	220V	220V	220V
Measured Voltage across L.V. -Neutral	123.3V	124V	111.8V
Measured voltage across tertiary (Volt.)	31.7	32.3	23.35
Measured H.V. mag. Current in (mili Amp)	3.47	3.77	450
Short Circuit Test (L.V. and Neutral Short)			
Applied Voltage across H.V. and Neutral	220	220	220
H.V. Current in (Amp)	5.48	5.5	5.51
L.V. Current in (Amp)	10.3	10.3	9.96
Short Circuit Test (HV and Neutral Short)			
Applied Voltage across LV and Neutral	220	220	220
L.V. Current in (Amp)	17.48	17.57	19.6
L.V. Current in (Amp)	10.3	9.86	9.96
Measurement of magnetizing current in tertiary winding (applied voltage 33V)			
Magnetizing current for tertiary (milli Amp)	23.82	12	4560

Table 3. O.C & S.C. Test with magnetizing currents.

5.4 Winding Resistance Test

DC winding resistance test is performed with an application of dc low voltage and high current. The ratio of dc voltage measured across winding and current through winding gives value of DC winding resistance.

In this case, measurement of DC resistance of windings was performed at an ambient temperature of 36 °C, the temperature of winding taken form winding temperature meter and results were noted as shown in table 4. This test was performed with application DC source causing flow of 10 Ampere current through the windings. Only value of DC winding resistance with OLTC tap position number 11 narrated in table for comparison - as transformer was tripped with OLTC tap position at No. 11. Results show that there was not any significant change in winding resistance which means there are no short circuit turns, poor joints, bad contacts or opening of conductor.

Date of Test	Tap Number	H.V.	L.V.	Tertiary
OH 07.01.2016	11	325	155.5	15.35
LA fail 07.07.2016	11	330	154.3	16.62
Trippped 12.08.2017	11	329	170.3	16.7
*H.V.,L.V. and Tertiary winding resistances are in mili Ohms				

Table 4. Resistance Measurements for Windings.

5.5 Dissolved Gas Analysis (DGA)

Dissolved Gas Analysis (DGA) test is performed to measure the amount of dissolved gases' content in transformer oil. Presence and content value of various key gases indicate intensity and severity of fault inside the transformer. Oil samples were taken from the transformer and sent to test laboratory.

DGA was carried out at one of the well-known testing laboratories - ERDA, Vadodara and DGA test results are shown in table no. 5. DGA results for sample drawn after overhauling (OH) is also shown for reference. After failure of Lightning Arrestor, significant increase in key gases was observed- particularly in Hydrogen. It may be due to external fault current fed through ICT unit. However, it was within permissible limit. Oil filtration was carried out before charging transformer and all key gases were found normal. After tripping of date 12.08.17, again DGA test was carried out and it indicates heavy flashover inside the transformer with temperature rise of more than 700 °C - as Acetylene increased significantly.

DGA	OH 07.01.2016	LA fail 05.07.2016	Trip 12.08.2017
Hydrogen H_2	2	152	3058

Oxygen	4969	3998	3058
Nitrogen	13997	20371	9031
Methane	1	42	256
Ethylene	Nil	4	653
Ethane	Nil	4	45
Acetylene	Nil	2	727
Carbon Dioxide	66	554	1194
Carbon Monoxide	2	122	468
Routine Test			
PPM	8	8	12
Tan Delta	0.0015	0.0038	0.0077
Resistivity (Ohm-metre)	$70*10^{-12}$	$70*10^{-12}$	$7.6*10^{-12}$

Table 5. DGA test result comparison table.

5.6 Sweep Frequency Response Analysis (SFRA)

SFRA is a very important test to ascertain the mechanical integrity of transformer winding. SFRA provides valuable information regarding overall mechanical integrity of individual windings for power transformer.

SFRA for each winding was done and compared with its base which was available before overhauling (OH). For SFRA of H.V. winding, signal was injected from H.V. winding and its response was measured at neutral bushing and comparison was done with its base as shown in figure 4.

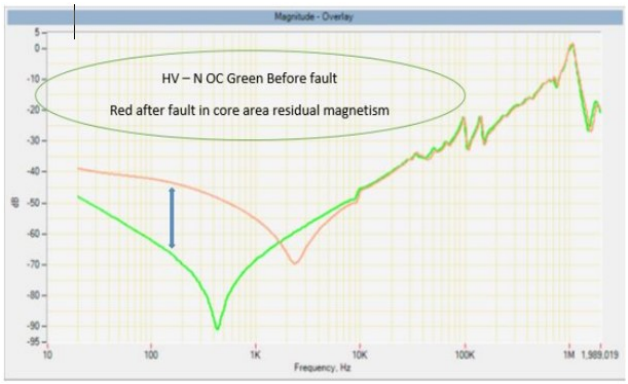

Fig. 4. SFRA of HV winding comparison with base result

In SFRA graphs for HV winding, difference was noticed in core area (low frequency region), while there was no any deviation in winding area (high frequency region). The difference in core area might be due to residual magnetism. SFRA carried out for LV winding with neutral bushing and deviation noticed in low frequency area - same as noticed in HV winding, and it may be due to residual magnetism.

SFRA of tertiary winding also done and compared with base results - similar deviation noticed in SFRA traces of tertiary winding. Residual magnetism might have originated during fault condition. Effect of residual magnetism in LV and tertiary winding is shown in figure 5 and 6

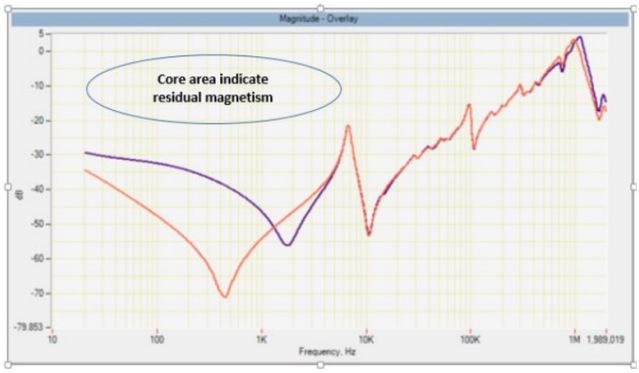

Fig. 5. SFRA of L.V. comparison with base

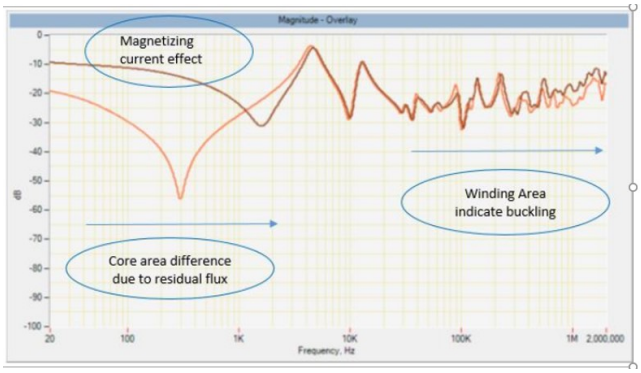

Fig. 6. SFRA of tertiary winding with base

For confirming that – deviation noticed in all three traces are attributed to residual magnetism, SFRA was conducted again for LV winding - after shorting tertiary winding terminals; and the response is shown in figure 5. The results clearly show that there is no any deviation in SFRA results which indicates that H.V. and L.V. both windings are intact.

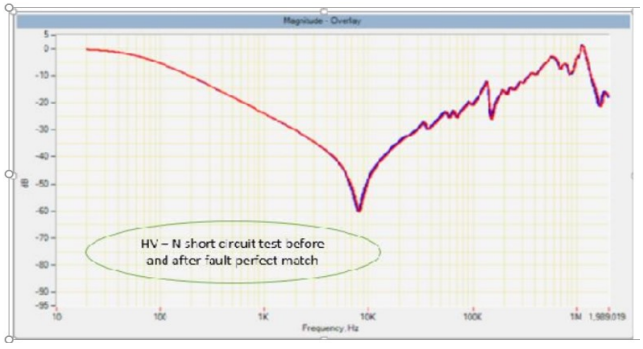

Fig. 7. SFRA of LV winding with tertiary short

For verification the effect of residual magnetism, demagnetization carried out for the transformer and once again SFRA test carried out for all windings individually. After demagnetizing, the SFRA trace of "H.V. – Neutral" in low frequency area almost matched to the base fingerprint as shown in figure 8.

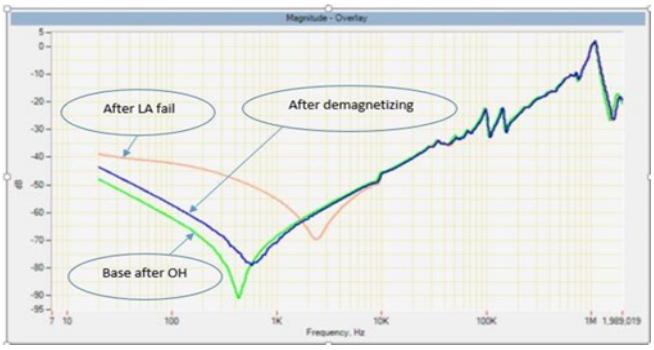

Fig. 8. SFRA of H.V. winding after demagnetization

After demagnetizing, the trace of "L.V.-Neutral" in low frequency area also matched to a great extent - to the base fingerprint as shown in figure 9.

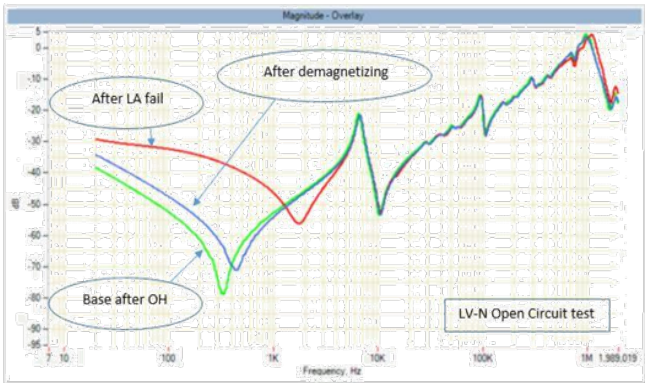

Fig. 9. SFRA of L.V. winding after demagnetization

After demagnetizing, the trace of "L.V.-Neutral" in low frequency area almost matched to the base fingerprint as shown in figure 10.

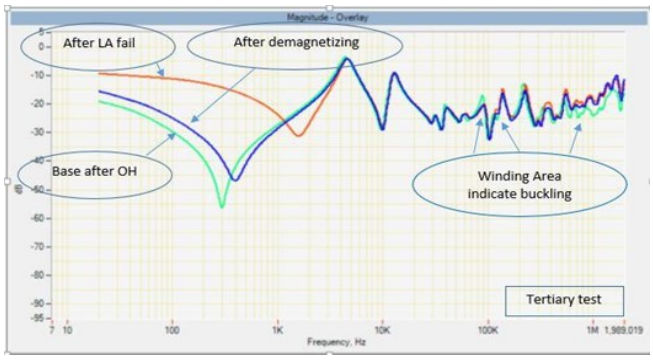

Fig. 10. SFRA of tertiary winding after demagnetization

5.6 Inspection

All test results found normal. Difference noticed in SFRA test results of tertiary winding indicated hoop buckling of tertiary winding, and same supported by capacitance and tan delta test, hence it was decided to inspect the transformer at site by lifting main tank. After removal of oil, thorough inspection of winding was carried out and nothing found abnormal in the transformer. No any black carbon particle or coper particle found inside main tank. After completion of internal inspection oil, filtration and drying out process for power transformer was carried out. All the required tests performed again. All the test results were found satisfactory or within permissible limit. The distortion in tertiary winding indicative from SFRA results - could not be observed / visualized after opening of transformer, as tertiary winding being innermost winding was surrounded by HV-IV winding - covered with hard board insulating cylinder. So nothing can be visualized for tertiary winding in inspection - as shown in figure 11.

Fig. 11. Inspection of active part of transformer

As transformer tank was bell type, huge crane required for lifting of main tank of power transformer. After analysis of all tests results and internal inspection, it was concluded that there was hoop buckling in tertiary winding. The conclusion was drawn from SFRA results and supported Capacitance and tan delta test results. The deviations recorded in SFRA and tan delta test results were within permissible limit, which indicated that the deformation was minor in nature. Deviation in SFRA and tan delta results had led to apprehension, however deviations were within permissible limits. Present available analytical tool of SFRA also didn't indicate any abnormality with Transformer windings.

5.7 Tripping of Transformer

Finally, it was decided to charge the transformer with all necessary safety precautions, as all results found within permissible limit. Transformer tripped at the instant of charging. So, all tests i.e. Tan delta, low voltage routine test, DGA, DC winding resistance and SFRA were performed again. All other test results after tripping shown in respective table. SFRA results of H.V. Winding were compared as shown in figure 12.

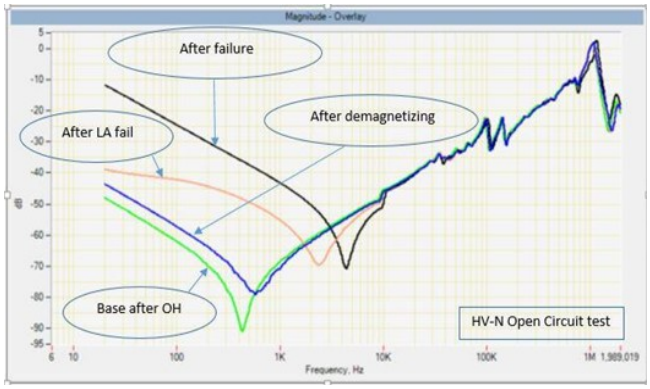

Fig. 12. SFRA of H.V. winding after tripping

As shown in figure 12 dB difference in low frequency area i.e. 10Hz to 100Hz, indicate turn to turn short. However, there was no any deviation in winding area which means that turn to turn short in other winding not in winding under tests i.e. HV winding. SFRA results of L.V. Winding were compared as shown in figure 13.

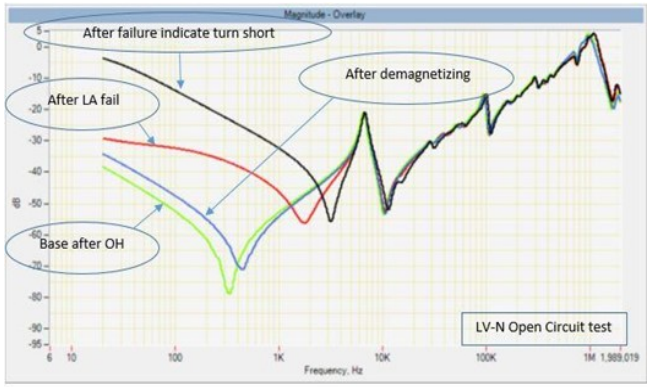

Fig. 13. SFRA of L.V. winding after tripping

As shown in figure 13 all four nos. of SFRA compared, in low frequency area i.e. 10Hz to 100 Hz, indicate turn to turn short. However, there was no deviation in winding area i.e. higher frequency and middle frequency which means that turn to turn short in other winding not in LV winding.

All four results of SFRA results of tertiary winding were compared as shown in figure 14 and deviation in low frequency as well as in middle and high frequency area was Cleary visible, which indicated turn to turn short in tertiary winding.

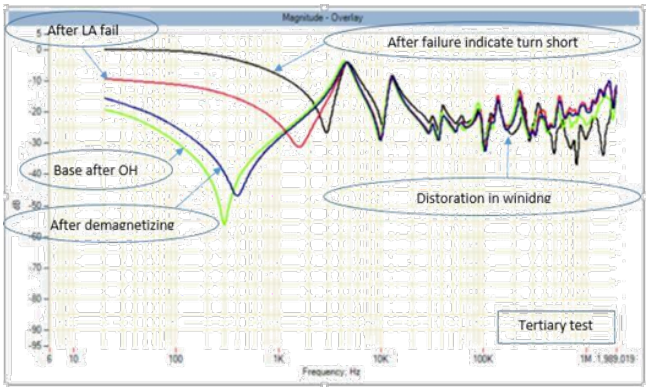

Fig. 14. SFRA of tertiary winding after tripping

Transformer was declared failed with base of SFRA and other test results, for verification of turn to turn shorting in tertiary winding, transformer was decided to open again and inspect the tertiary winding. After opening of transformer at site. H.V. and L.V. windings found intact and turn to turn shorting observed in tertiary as shown in figure 15.

Fig. 15. Buckled tertiary winding with turn to turn short

Transformer scraped and declared fail. To confirmed analysis of SFRA result for turn to turn shorted in tertiary winding proved with physical inspection at field level.

6. Conclusion

Sweep Frequency Response Analysis has proven that it provides valuable information about condition of power transformer windings and their mechanical integrity. SFRA in aid with other tests provides clear information about winding deformation, which cannot be visualize in physical inspection. Present available analytical tool of SFRA didn't indicate any abnormality with Transformer winding. With experience and expertise, proper judgements can be taken as to condition of the Transformer - even from Minor deviations recorded in SFRA traces. Information received with all test carried out will help to decision making authority to take quick and sound decision for transformer for further course of action , like expenditure for inspection, oil filtration required or not. With help of SFRA one can judge the internal condition of power transformer and take sound decision for replacement of transformer, repairing of transformer at site or sent at works etc.

7. Acknowledgement

Authors are very much grateful to the Gujarat Energy Transmission Corporation Ltd. Formally known as GETCO management for kind support, guidance and granting permission to publish this paper. GETCO is a well-known utility in power transmission in India. GETCO is adopting all the new available technology for condition monitoring of equipment. Author work with GETCO for monitoring protection and condition monitoring activity as a Superintending Engineer testing.

8. References

[1] E .P. Dick and C. C. Erven," Transformer Diagnostics Testing by Frequency Response Analysis", IEEE Transaction on Power Apparatus and Systems, Vol.97,pp. 2144 2153,Nov/Dec.1978.

[2] Asif Islam, Shahidul Islam Khan and Dr. Aminul Hoque, "Detection of Mechanical Deformation in Old Aged Power Transformer Using Cross Correlation Co-Efficient Analysis Method" ,Energy and Power Engineering, Vol.3, pp. 585–591,January 2011.

[3] M. Arul Sathya, Usa Savadamuthu," Prediction of Change in Equivalent Circuit Parameters of Transformer Winding Due to Axial Deformation using Sweep Frequency Response Analysis" , Journal of Electrical Engineering and Technology, Vol.10, pp.983–989,May 2015

[4] Hormatollah Firoozi, Nami Mahmoodi, Mohammad Kharrazi and M.I.Ghiyasi, "Frequency response analysis-Low frequency characteristics and fault diagnosis on power transformers", IEEE International Conferences on Solid Dielectrics,Postdam,Germany,July2010.

[5] K. Ludwikowski, K. Siodla and W. Ziomek," Investigation of transformer model winding deformation using sweep frequency analysis", IEEE transaction on Dielectrics and Electrical Insulation, Vol.19. December 2012.

[6] S. D. Mayer, J. J. Kelly and R. H .Parrish, "A Guide to Transformer Maintenance", Transformer Maintenance Institute, USA ,Second printing,1988.

9. Bibliography

Dr. Vivek Pandya received his Bachelor Degree in Electrical Engineering from Sardar Patel University Valabh Vidhanagar Gujarat in 1995. He has completed Master Degree from same university in 2003. He has completed Ph.D. from M.S. University Baroda in 2009. At present Dr. Vivek Pandya work with Pandit Dindayal Petroleum University formally known as PDPU, Gandhinagar, as professor and HOD. Interested and research area of Dr. Vivek Pandya are protection of power system.

Ashok J. Chavda has been employed at Gujarat Energy Transmission Co. since 1989, and currently works as Superintending Engineer, Testing Department at Corporate office, Vadodara. He has worked in many units of Transmission viz. Project, Testing, Operation and Maintenance of Sub-Stations and Lines up to 400Kv. Mr. Ashok received his Bachelor Degree in Electrical Engineering from the Gujarat University Ahmedabad, in 1989.

He has completed M.B.A. from IGNOU in 2001 with specialty in Operation Management and HR. He has completed Master Degree in Power System from R.K. University Rajkot. Mr. Ashok at presently pursuing Ph.D. work in the field of SFRA under guideline of Prof. Vivek Pandya at Pandit Dindayal Petroleum University formally known as PDPU, Gandhinagar. Interested area of Mr. Ashok is Diagnosis of faults in power transformers.

INCIPIENT SHORT CIRCUIT FAULT IMPACT ON SERVICE CONTINUITY OF AN ELECTRIC VEHICLE PROPELLED BY DUAL INDUCTION MOTORS STRUCTURE

S. YAHIA CHERIF[1] **D. BENOUDJIT**[1,2]
[1]LSP-IE'2000 Laboratory, Electrical Engineering department, University of Batna 2
Rue Chahid M[ed] El-Hadi Boukhlouf 05000 Batna, Algeria, Tél./Fax: +213 33 81 51 23

M.S. NAIT-SAID[1] **N. NAIT-SAID**[1]
[2]Health and Safety Institute, University of Batna 2, 53 route de Constantine, Batna, Algeria, Tél./Fax: +213 33 23 01 43

Abstract: *The short circuit is among one of the most dangerous electrical faults in induction motor, which leads to serious implications on the motor operation and its performances. The present paper deals with the influence of the stator short circuit fault in its early stage in terms of performances and service continuity of an electric vehicle (EV) using dual induction motor's structure piloted by Backstepping control. An equivalent induction motor model with turn-to-turn fault on one stator phase, without already assuming the temperature effect through an intrinsic model, is investigated and thereafter its impacts on electric vehicle performance using simulation tests are presented and discussed.*

Key words: *Backstepping control, Electric vehicle (EV), turn-to-turn-fault, Propulsion control structure.*

1. Introduction

A motor control system with high robustness is an important issue in research [1]. Thus, it is obvious that the monitoring and diagnosis of electrical machine constitute an economic and scientific challenge, combining safety and continuity of service for electrical drives. About 35% to 40% of the total failures of induction motor take place due to electrical faults [2]. The stator winding insulation failure due to a short-circuit known as inter turn short-circuit is one of the most common and severe kind of electrical faults affecting the electric motor [3-5]. This is mainly due to long term thermal aging and ultimately insulation failure [2]. If the turns of stator are shorted a large circulating current induced in shorted turn so the thermal overloading [6]. However, during operational phases, electric motors are continuously being exposed to thermal, mechanical and vibrational effects.

Therefore, it is important to detect and identify any incipient fault that occurs within the electrical motor at its earliest stage to avoid any unplanned outage, particularly in applications where safety is the primary concerns the global system. On the over side, it is common for any vehicle in urban traffic requires regime changes, frequent acceleration, deceleration, cruising, and stopping phases, which lead to serious breakdowns. In those applications where downtime isn't acceptable and where continuity of service is required, an unpredicted failure of a motor might result in higher maintenance costs or loss of life. However, understanding fault diagnosis is very important, because a good diagnosis is an early detection of the severity and location of faults, to reduce the downtime as well as the maintenance costs while ensuring continuity of operations for an EV. Therefore, modeling and identification of inter-turn short circuit fault at its earliest stage of an induction motor is the first major step in the motor health monitoring and fault diagnosis process. The main focus of the present work is on the influence of an incipient inter turn short circuit fault occurred at its earliest stage on electric vehicle performances and service continuity. The proposed control structure consists of an electric vehicle using dual-induction motors Backstepping control placed at the rear wheels, which propels electrically the vehicle, based on an electric differential assured by dual motors operating at different speed. For this purpose, a precise equivalent model of an induction motor (IM) taking into account the presence of the turn-to-turn fault resulting of a short-circuit winding in stator phase at several levels is described, and the consequences on electric vehicle performances in terms of service continuity where a fault occurred into one of both propulsion structure motors are analyzed.

Simulation tests were carried out for detecting fault occurrence and its impact on EV control, without already considering the temperature effect through an intrinsic model, for a faulty model. Also, note that the existence of the short-circuit in some turns on one phase could give an increase in temperature inside the machine leading to overheating which causes the insulation loss of the machine winding and the short circuit becomes rapid and total in such a small time.

The paper is organized as follows. Section 2 presents the Backstepping control for IM, using an accurate faulty model with turn-to-turn fault applied for an EV. In section 3, the dual-motor configuration of the proposed propulsion structure will be shown. To evaluate the performances and the failures effect caused by turn-to-turn fault in first stator phase of the right motor, series of simulation tests will be presented in section 4. Conclusion is done in section 5.

2. Backstepping control for IM

Backstepping control technique enables in a sequential and systematic manner to build stabilizing Lyapunov function. Thus, the main goal is to achieve the convergence of errors towards zero and stable operations of the system. The design of Backstepping control approach is to recursively select the appropriate state variables as virtual reference input, characterized by step-by-step interlacing. Each step generates a new virtual control variable and finally the process terminates when the final external control is reached [7-11].

Let us first given the equations of an IM for a healthy model, which includes both the mechanical and electrical dynamics, expressed in the (d,q) synchronous rotating frame obviously, after orientation of the rotor flux by [1][8]:

$$\begin{cases} \dfrac{d\Omega}{dt} = \dfrac{pM}{JL_r}\phi_r i_{sq} - \dfrac{T_L}{J} \\ \dfrac{d\phi_r}{dt} = \dfrac{M}{T_r} i_{sd} - \dfrac{1}{T_r}\phi_r \\ \dfrac{di_{sd}}{dt} = -\left(\dfrac{R_s}{\sigma L_s} + \dfrac{M^2 R_r}{\sigma L_s L_r^2}\right) i_{sd} + \omega_s i_{sq} + \dfrac{MR_r}{\sigma L_s L_r}\phi_r + \dfrac{1}{\sigma L_s} v_{sd} \\ \dfrac{di_{sq}}{dt} = -\left(\dfrac{R_s}{\sigma L_s} + \dfrac{M^2 R_r}{\sigma L_s L_r^2}\right) i_{sq} - \omega_s i_{sd} - \dfrac{MR_r}{\sigma L_s L_r}\phi_r + \dfrac{1}{\sigma L_s} v_{sq} \end{cases} \quad (1)$$

The objective of the Backstepping design is to synthesize the d-axis and q-axis voltage control input expressions (v_{sd}^*, v_{sq}^*), where the system must be able to follow the desired references. It mainly consists of the following two steps.

For the first step, the objective is the replacement of classical PI tracking controller by computing the reference values of stator current components (i_{sd}^*, i_{sq}^*). In our case, the tracking errors dynamics of speed $\dot{e}_\Omega$ and rotor flux $\dot{e}_\phi$, by using equations (1) are defined as follows:

$$\begin{cases} \dot{e}_\Omega = \dot{\Omega}^* - \dot{\Omega} = \dot{\Omega}^* - \dfrac{1}{J}\dfrac{pM}{L_r}\phi_r i_{sq} + \dfrac{T_L}{J} \\ \dot{e}_\phi = \dot{\phi}_r^* - \dot{\phi}_r = \dot{\phi}_r^* - \dfrac{M}{T_r} i_{sd} + \dfrac{1}{T_r}\phi_r \end{cases} \quad (2)$$

Then, with an appropriate choice of the Lyapunov function V_1 of the subsystem described above, such that:

$$V_1 = \frac{1}{2}\left(e_\Omega^2 + e_\phi^2\right) \quad (3)$$

For which its derivative $\dot{V}_1$ must be negative, we can write:

$$\begin{cases} \dot{e}_\Omega = -k_\Omega \cdot e_\Omega \\ \dot{e}_\phi = -k_\phi \cdot e_\phi \end{cases} \quad (4)$$

where k_Ω, k_ϕ are positives coefficients in order to guarantee the stable tracking. Thereby, the reference values of stator current components are given by:

$$\begin{cases} i_{sd}^* = \dfrac{JL_r}{pM\phi_r}\left(\dot{\Omega}^* + k_\Omega \cdot e_\Omega + \dfrac{1}{J} T_r\right) \\ i_{sq}^* = \dfrac{T_r}{M}\left(\dot{\phi}_r^* + k_\phi \cdot e_\phi + \dfrac{1}{T_r}\phi_r\right) \end{cases} \quad (5)$$

In the second step, the main goal is to achieve the final external control, by computing the reference stator voltage. To do so, we define the stator current errors terms. Expressed by their derivatives as follows:

$$\begin{cases} \dot{e}_{id} = \dot{i}_{sd}^* - \dot{i}_{sd} \\ \dot{e}_{iq} = \dot{i}_{sq}^* - \dot{i}_{sq} \end{cases} \quad (6)$$

Substituting (1) into (6), we find:

$$\begin{cases} \dot{e}_{id} = \dot{i}_{sd}^* - d_1 - \dfrac{1}{\sigma L_s} v_{sd} \\ \dot{e}_{iq} = \dot{i}_{sq}^* - d_2 - \dfrac{1}{\sigma L_s} v_{sq} \end{cases} \quad (7)$$

Where

$$\begin{cases} d_1 = -\left(\dfrac{R_s}{\sigma L_s} + \dfrac{M^2 R_r}{\sigma L_s L_r^2}\right) i_{sd} + \omega_s i_{sq} + \dfrac{MR_r}{\sigma L_s L_r}\phi_r \\ d_2 = -\left(\dfrac{R_s}{\sigma L_s} + \dfrac{M^2 R_r}{\sigma L_s L_r^2}\right) i_{sq} - \omega_s i_{sd} - \dfrac{MR_r}{\sigma L_s L_r}\phi_r \end{cases} \quad (8)$$

From the equations system (7), the stator voltage input, could be calculated through the definition of another Lyapunov function into the following form:

$$V_2 = V_1 + \frac{1}{2}\left(e_{id}^2 + e_{iq}^2\right) \tag{9}$$

To ensure that its derivative is always negative, such that

$$\dot{V}_2 = \dot{V}_1 - k_{id}e_{id}^2 - k_{iq}e_{iq}^2 \tag{10}$$

with k_{id}, k_{iq} are positives coefficients.

Finally, the input voltages components are chosen as follows:

$$\begin{cases} v_{sd}^* = \sigma L_s (i_{sd}^* - d_1 + k_{id}e_{id}) \\ v_{sq}^* = \sigma L_s (i_{sq}^* - d_2 + k_{iq}e_{iq}) \end{cases} \tag{11}$$

For a faulty model, different research works of mathematical models regarding inter-turn short-circuit faults in the stator of an induction motors can be found in literature [12-14]. As the need for greater accuracy in induction motor modeling, important physical characteristics have to be taken into account. An accurate model for an induction motor with stator winding turn fault in first phase was presented in [14].

Stator, rotor and short circuit equations in matrix form for an IM faulty model in coordinates referred to the stator frame, with a turn-to-turn fault in the first phase "a", is formulated as follows [14], given next by equation (12). Index sc denotes short circuit. Conventional used abbreviation of the induction motor will be defined next in nomenclature.

$$v = D_{1sc}\, I + \left[\omega D_{2sc} + D_{3sc}\frac{dI}{dt}\right] \tag{12}$$

with:

$$D_{1sc} = \begin{bmatrix} R_s & 0 & 0 & 0 & -\sqrt{\frac{2}{3}}x_{sc}R_s \\ 0 & R_s & 0 & 0 & 0 \\ 0 & 0 & R_r & 0 & 0 \\ 0 & 0 & 0 & R_r & 0 \\ \sqrt{\frac{2}{3}}x_{sc}R_s & 0 & 0 & 0 & -(R_s + x_{sc}R_s) \end{bmatrix}$$

$$D_{2sc} = \begin{bmatrix} 0 & 0 & 0 & 0 & 0 \\ 0 & 0 & 0 & 0 & 0 \\ 0 & M & 0 & L_r & 0 \\ -M & 0 & -L_r & 0 & \sqrt{\frac{2}{3}}mx_{sc} \\ 0 & 0 & 0 & 0 & 0 \end{bmatrix}$$

$$D_{3sc} = \begin{bmatrix} L_s & 0 & M & 0 & 0 \\ 0 & 0 & 0 & M & 0 \\ M & 0 & L_r & 0 & -\sqrt{\frac{3}{2}}mx_{sc} \\ 0 & M & 0 & L_r & 0 \\ x_{sc}\sqrt{\frac{2}{3}}L_s & 0 & mx_{sc}\sqrt{\frac{3}{2}} & 0 & -x_{sc}^2 L_s \end{bmatrix}$$

The voltage and current matrices are expressed as:

$$v = \left[v_{s\alpha}\ v_{s\beta}\ 0_{r\alpha}\ 0_{r\beta}\ 0_{sc}\right]^T,\ I = \left[i_{s\alpha}\ i_{s\beta}\ i_{r\alpha}\ i_{r\beta}\ i_{sc}\right]^T.$$

The short-circuited turn's index is:

$$x_{sc} = \frac{n_{sc}}{n} = \frac{\text{Number of interturns short - circuit windings}}{\text{Total number of interturns in healthy phase}}$$

Figure 1 shows a general block diagram implementation of Backstepping control intended to EV application. This is used to maintain stability and better performance capabilities of the system under disturbances, with at least two control loops. As shown in Fig. 1, n_{sc} represents a number of shortened turns in the first stator phase "a". R_{sc} is an equivalent resistance of the shortened turns.

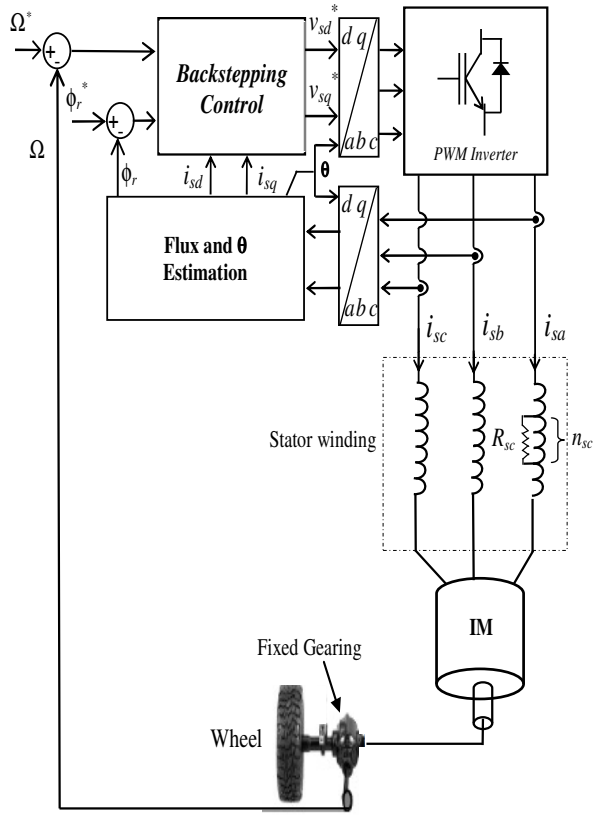

Fig. 1. Backstepping structure of IM with turn-to-turn fault on phase a.

When the short circuit fault is negligible ($x_{sc} = R_{sc} = 0$) the previous formulation gives exactly the same as in the healthy model.

3. Electric vehicle dual induction motor's structure

Figure 2 presents the proposed control structure in which two identical induction motors drive, separately the rear wheels of the vehicle via fixed gearing. The left and right induction motors are fed through power converters and driven by Backstepping strategy.

The differential action assured by dual motors operating at different speed enables the wheels to be driven at different speeds when cornering the outer wheel covering a greater distance than the inner wheel. Then the propulsion control structure placed at the rear wheels propels electrically the vehicle and assures the required differential speed Ω_{diff} according to [15]:

$$\begin{cases} \Omega_1^* = \Omega_o^* + \Omega_{diff}^* \\ \Omega_2^* = \Omega_o^* - \Omega_{diff}^* \end{cases} \quad (13)$$

where:

Ω_1^*, Ω_2^*: Speeds of left motor 1 and right motor 2.

Ω_o^*, Ω_{diff}^* : EV speed command, speed difference.

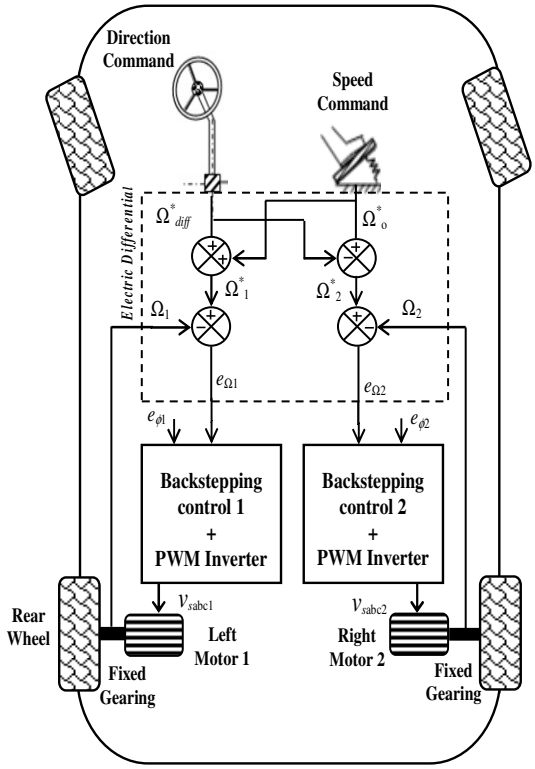

Fig. 2. EV propulsion control structure.

4. Simulation results and discussion

Numerical simulations have been carried out, in order to assess the effect of initial turn-to-turn fault on electric vehicle structure performances propelled by dual induction motors which rated data are summarized in the appendix.

Figures 3(a,b,c) and their respective zoom on Figures 3(a_1, b_1) also, Figures 3(a_2, b_2, c_2) depict and compare the main characteristics (speed, electromagnetic torque, stator currents and copper losses responses) of an EV propulsion structure using dual inductions motors driven by Backstepping control where the turn-to-turn fault resulting of a short-circuit winding may be occurred in the first stator phase into one of both propulsion motors structure (the right motor) at several short-circuited turns index levels: x_{sc} = 20%, 50% and 100%.

The simulation tests were used considering the selected route defined as illustrated in figures 3 by the vehicle speed reference drawn in dashed line.

From scratch, the vehicle starts with a constant acceleration until attains the speed of 157 rad/s then it will be maintained constant. In fact, in this propulsion structure each of both motors is associated with a fixed mechanical gearing, which enables the reduction of the motor speed to the desired wheel speed and high substantial torque.

At t = 0.5s, a load torque is applied on each motor. This last case might be occurred for example when EV wheels are stopped by a strong obstacle. After there, at t = 1s the vehicle accomplishes its turn maneuvers, by turning left.

The electric differential action allows the inner wheel to rotate slower than the outer one, i.e $\Omega_{Right} > \Omega_{left}$. Further, to test severely the propulsion structure performances, at t = 1.5s the turn-to-turn fault resulting of a short-circuit winding in the first stator phase has been activated on the right motor when the vehicle accomplishes its turn maneuvers.

Finally, the vehicle maintains a constant cruising speed, which results in equality of both motors speeds, i.e $\Omega_{Right} = \Omega_{left}$.

Figure 3a and its zoom in figure 3a1 show before and after the shorted turns faulty case for x_{sc} =20%, introduced at t = 1.5sec, the simulated EV speed, electromagnetic torque and stator currents waveforms.

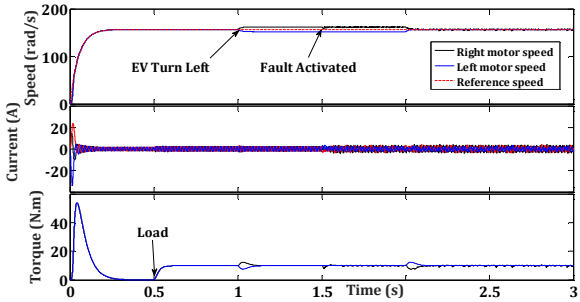

Fig. 3a. Turn-to-turn fault effect for x_{sc} = 20 %.

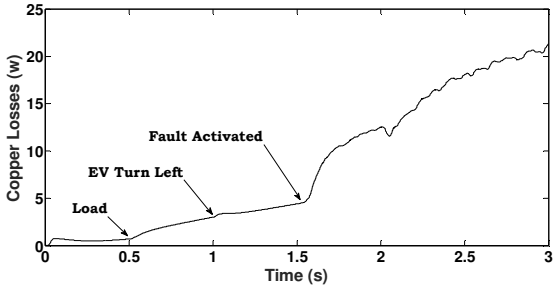

Fig. 3a$_2$. Cooper losses evolution for x_{sc} = 20 %.

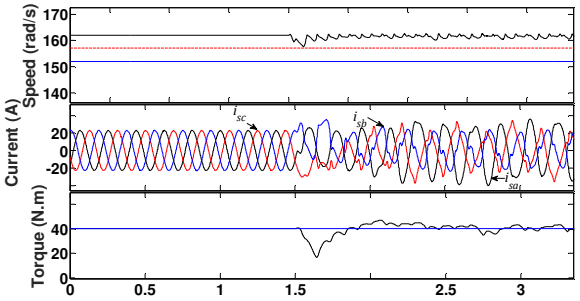

Fig. 3a$_1$. Zoom of turn-to-turn fault effect for x_{sc} = 20 %.

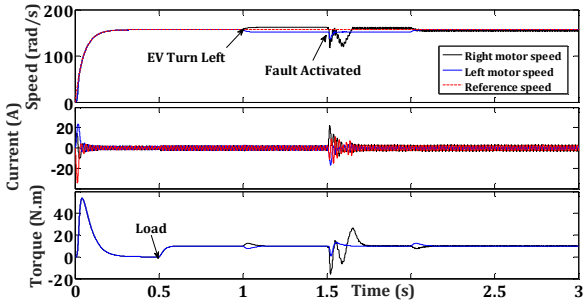

Fig. 3b. Turn-to-turn fault effect for x_{sc} = 50 %.

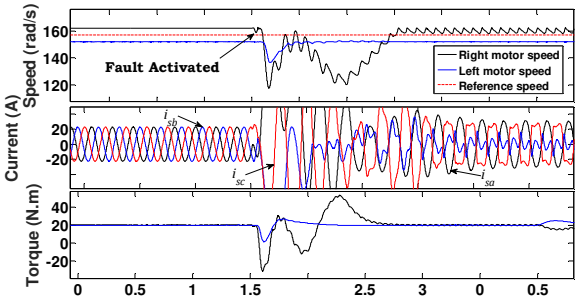

Fig. 3b$_1$. Zoom of turn-to-turn fault effect for x_{sc} = 50 %.

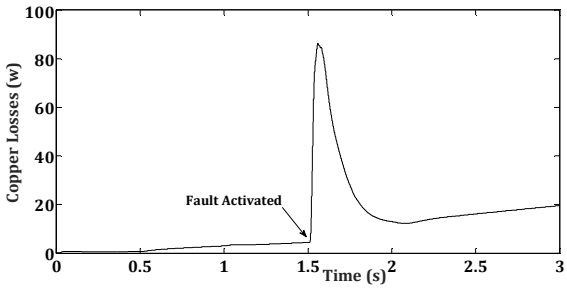

Fig. 3b$_2$. Cooper losses evolution for x_{sc} = 50 %.

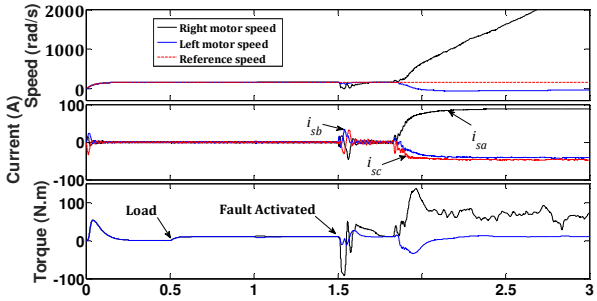

Fig. 3c. Turn-to-turn fault effect for x_{sc} = 100 %.

It can be seen that the fault effect in this case, isn't noticeable on the EV speed and electromagnetic torque responses, expect for the stator currents amplitudes, which increase slightly after fault occurs. So, in this case, the incipient winding fault will not impose great influences on EV performances.

Figure 3a$_2$ shows with the same above shorted turns faulty case for x_{sc} = 20%, the evolution of stator copper losses versus time. It is well known that copper losses dependent on the square of stator current in RMS value and the stator resistance. These losses result from Joule heating are caused by stator current induced in the stator windings, which generates the heat, and therefore the temperature of the motor rises with time. Indeed, as can be seen from Figure 3a$_2$ as the stator currents amplitudes increase, the copper losses increase also with time particularly when the fault occurs.

On the other hand, as shown in figures 3(b-c) and 3(b$_1$) the fault effect is more noticeable as the fault severity increases. For x_{sc} = 50%, and in particular, for x_{sc} = 100%, while the stator current amplitude of the faulty phase current becomes higher.

The increase in RMS stator currents may have a serious damage, such as total short-circuit of the stator winding, the degradation of the insulation of the windings due to the resulting overheating, which potentially shortening its lifespan and even fire.

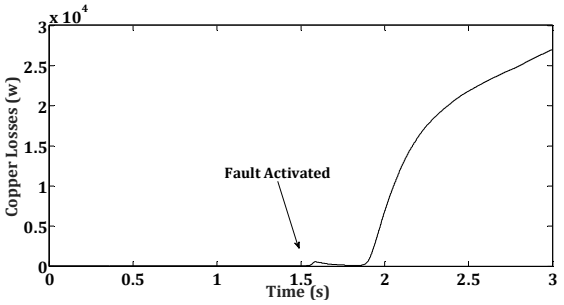

Fig. 3c$_2$. Cooper losses evolution for x_{sc} = 100 %.

At the same time, the occurred fault cited above might influence one of the dual induction motors which could be conducted an unbalance in the dual used motors and from which the vehicle leaves its reference trajectory, so the control of the differential action is gravely lost accompanied by the loss of the aim control vehicle direction. Finally, as depicted in figures 3(b$_2$, c$_2$) with rising amplitude currents the copper losses increase also.

5. Conclusion

In this paper, we focused on the incipient turn-to-turn fault influence on EV dual induction motor's structure performances and service continuity. An accurate model for an induction motor with inter-turn fault in the first phase of stator winding occurred into one of both motors has been presented for detecting fault occurrence and its impact on EV control, without already considering the temperature effect through an intrinsic model, for a faulty model. Simulation tests performed under a fault severity index at several levels show that the incipient turn-to-turn short fault has a small effect for a lower-level fault on EV operation. In this case, the vehicle continued to function even in the presence of fault. But for the high fault levels, the results show a very significant change, particularly for the currents wave forms. The stator currents amplitude raised significantly where the fault has occurred and a relative height that is lower for the other phases.

Thus, if no coping measures are applied, this will result in the temperature increase in the stator winding, which will lead to the failure of the entire phase eventually. That's means unfortunately the loss of the systematic control on the EV driven by the propulsion structure.

Nomenclature

v_s , i_s	Stator voltage, stator current αβ-vector
ϕ_s	Stator flux αβ-vector
R_s , R_r	Stator and rotor resistances
L_s , L_r	Global Stator and rotor self-inductances of each armature
M	Global Mutual inductance between stator and rotor armatures
m	Mutual inductance between two phases stator and rotor, where, $m = \frac{2}{3}M$
T_r	Rotor time constant where, $T_r = \frac{L_r}{R_r}$
ω_s	Synchronous angular speed
j	Imaginary unit, satisfying $j^2 = -1$
θ	Flux stator angle
p	Number of pole pairs
T_e , T_L	Electromagnetic torque, Torque Load
(.)*	Input command variable
i_s	Current flowing through the short circuit winding
Ω	Mechanical speed
Ω_1, Ω_2	Speeds of left motor and right motor
Ω^*_o, Ω_{diff}	EV speed command, speed difference
J	Rotor Inertia
PI	Proportional Integral controller

Appendix

Table 1 Induction motor parameters

Parameters	Values
Power	4 [kW]
Voltage	220/380 V
Frequency	50 Hz
+ Eventual three-phase boost transformer with ratio 1/20 adapted to voltage battery	
R_s	1.2 [Ω]
R_r	1.8 [Ω]
L_s=L_r	0.1564 [H]
M	0.15 [H]
J	0.07 [Kg.m2]
p	2

References

1. Roubache, T., Chaouch, S., Naït-Saïd, M.S.: *Backstepping design for fault detection and FTC of an induction motor drives-based EVs*. In: Automatika, (2016), Vol. 57, N° 3, p. 736–748.
2. Gangsar, P., Tiwari, R.: *Signal based condition monitoring techniques for fault detection and diagnosis of induction motors: A state-of-the-art review*. In: mechanical systems and signal processing, (October 2020), Vol. 144, p. 1–37.
3. Mazzoletti, M.A., Bossio, G.R., De Angelo, C.H., Espinoza-Trejo, D.R.: *A Model-Based Strategy for Inter turn Short-Circuit Fault Diagnosis in PMSM*. In: IEEE Transactions on Industrial Electronics, (September 2017), Vol. 64, N° 9, p. 7218–7228.
4. Wu, Y., Jiang, B., Wang, Y.: *Incipient winding fault detection and diagnosis for squirrel-cage induction*

motors equipped on CRH trains. In: ISA Transactions, (2020), Vol. 99, p. 488–495.

5. Teguia, J.B., God promesse Kenne, G.C.F.: *Induction Motor Windings Faults Detection Using Active and Reactive Power Based Model Reference Adaptive System Estimator*. In: International Journal of Progressive Sciences and Technologies (IJPSAT), (2 November 2020), Vol. 23, N°2, p. 66–86.
6. *Dhamal, S.S., Bhatkar, M.V.: Modelling and Simulation of Three-Phase Induction Motor to Diagnose the Performance on Inter-Turn Short Circuit Fault in Stator Winding*. In: International Conference on Computing, Power and Communication Technologies (GUCON), Sep 28-29, 2018, Greater Noida, UP, India, p. 1166–1172.
7. El Kharki, A., Boulghasoul, Z., Et-Taaj, L., Kandoussi, Z., Elbacha, A.: *Real Time Implemntation of Backstepping Control for High Performances Induction Motor Drive*. In: 4th World Conference on Complex Systems (WCCS), 22-25 April, 2019, Ouarzazate, Morocco.
8. Trabelsia, R., Khedher, A., Mimouni, M.F., M'sahli, F.: *Backstepping control for an induction motor using an adaptive sliding rotor-flux observer*. In: Electric Power Systems Research, December 2012, Vol. 93, p. 1–15.
9. Vaidyanathan, S., Azar, A.T.: *Backstepping Control of Nonlinear Dynamical Systems*, 1st edition, Academic Press, 15th august 2020, p. 1–515.
10. Horch, M., Boumediene, A., Baghli, L.: *Backstepping approach for nonlinear super twisting sliding mode control of an induction motor*. In: 3rd International Conference on Control, Engineering & Information Technology, IEEE CEIT'2015, 26 may 2015, Tlemcen, Algeria.
11. Ameid, T., Menacer, A., Romary, R., Pusca, R., Talhaoui, H.: *DWT for rotor bars fault detection applied to Backstepping control induction motor drive in low-speed*. In: 43th Annual Conference of the IEEE Industrial Electronics Society, Oct.-1 29 Nov. 2017, p. 8059–8064.
12. Dhamal, S.S., Bhatkar, M.V.: *Modelling and Simulation of Three-Phase Induction Motor to Diagnose the Performance on Inter-Turn Short Circuit Fault in Stator Winding*. In: International Conference on Computing, Power and Communication Technologies (GUCON), 28-29 Sept. 2018, p. 1166–1172, Greater Noida, India.
13. Hamoudi, A., Kouadri, B.: *On-Line Stator Winding Inter-Turn Short-Circuits Detection in Induction Motors Using Recursive Levenberg-Marquardt Algorithm*. In: International Journal on Electrical Engineering and Informatics, March 2017, Vol. 9, N°1, p. 42–57.
14. Bouakoura, M., Naït-Saïd, M.S., Naït-Saïd, N.: *Incipient Inter-Turn Short Circuit Fault Estimation Based on a Faulty Model Observer and ANN-Method for Induction Motor Drives*. In: Recent Advances in Electrical & Electronic Engineering, 2019, Vol. 12, p. 1–7.
15. Benoudjit, D., Nait-Said, N., Nait-Said, M-S.: *Differential Speed Control of a Propulsion System using Fractional-Order Controller*. In: Electromotion Journal, April-June 2007, Vol. 14, N° 2, p. 91–98.

High Power Voltage Multiplier (VM) PFC Converter with Inherent ZCS Characteristics and High Step-Up Gain for Enhanced Low-Line Efficiency

Pratap Ranjan Mohanty[1],Anup Kumar Panda[2], *Senior Member, IEEE*, Nishant Patnaik[3]
[1] Madanapalle Institute of Technology & Science, Madanapalle, Chittor, AP, India
[2] National Institute of Technology, Rourkela, Odisha, India
[3] Anil Neerukonda Institute of Technology & Sciences,Vishakapatnam, AP, India

***Abstract*—In this paper, a Voltage Multiplier (VM) converter configuration has been designed for high Power PFC application, ensuring reduced losses and high system efficiency.The conventional PFC system is improved with adding VM circuit configuration that enhances the static gain features with moderate duty ratio (D), and hence, the reverse recovery (RR) issue is resolved. The VM section inherently adds two main specific features of clamping behavior and ZCS phenomenon to the PFC system. An experimental prototype of $2\ kW$, $600\ V$ VM PFC converter configuration is designed and its effectiveness is validated under low line input of $100\ V$, operating at a high duty ratio, $D = 0.67$. The Real-Time Interface (RTI) feature of dSPACE1104 and MATLAB/Simulink are used to give the control signal for the verification of the system. Always, less than half of the output voltage ($300\ V$) appears across the switches of the converter, hence, voltage stress of the switch is minimized. Also, ZCS phenomenon is evident during switching commutations due to the snubber circuit behavior of the resonant tank, included in the proposed PFC converter. Hence, the overall system efficiency is improved. Furthermore, higher system efficiency is maintained for different rating which has been tested in this research work.**

I. Introduction

The rapid growth of Power Supply Units (PSUs) in industrial and commercial power distribution system demands high efficiency with the high quality of power in many aspects [1], [2]. Also, high power and high voltage AC-DC system is required for many applications [3]. However, it is hard to achieve high output voltage and high efficiency simultaneously at low AC input [4], [5], [6].

The boost Power Factor Correction (PFC) converter is most popular due to its superior performance. It controls the shape of input current to obtain high quality power [7], [8], [9], [10]. Generally, the input side injected harmonics, input power factor (pf), output voltage ripple, efficiency, size of the converter/filter etc. are considered as the fundamental performance index for power quality improvement while designing PFC converter [3]. However, the converter should essentially operate at high switching frequency for achieving high power density and small converter size [11]. However, this high switching operation results in higher switching losses and hence, converter efficiency is reduced. Furthermore, the high duty cycle operation of Voltage-Doubler (VD) or Voltage-Multiplier (VM) converter gives rise to reverse recovery problem, which in turn limits the voltage gain and efficiency of the converter system [12], [13], [14]. The implementation of proper soft-switching concept helps to attain desired high efficiency [13], [15], [16]. Also, the high output voltage could be obtained with modification in conventional converter configuration which helps to attain high static gain even at moderate duty ratio. These ideas motivated for integrating these two concepts to design a high static voltage-gain Boost Voltage Multiplier (VM) PFC circuit which is having inherent soft switching feature.

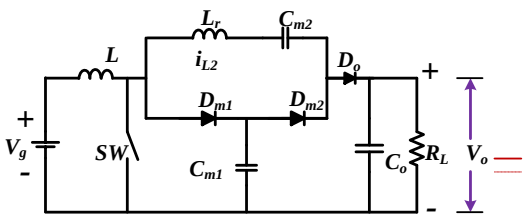

Fig. 1. Circuit configuration of high step-up Voltage Multiplier (VM)

In recent years, several novel high step-up PFC converter configurations have been developed for high voltage and power applications. Whereas, the reverse recovery issue during switching of devices isn't being considered to limit the switch losses. On the contrary, in many other research articles, several passive snubber circuits for implementation of suitable soft switching concept have been developed. But, the usability of such converters for high power and voltage applications aren't being discussed. Furthermore, the recently developed novel high step-up converters and multiplier converters [17], [18], [19], [20], [21], [22], [23], [24], [25], [26] are tried for PFC applications. Also, these aren't suitable for heavy loading as they give large input current ripple and higher conduction losses [27]. Furthermore, researchers are interested in designing high static voltage gain multiplier circuit which not only has the enhanced performance in high voltage and power application but also has inherent features to alleviate the reverse recovery losses. The popular CockcroftWalton (CW) Voltage Multiplier (VM) is improved to resolve certain practical limitations [28]. However, it suffers due to the non-ideal characteristics poor output voltage regulation with high output

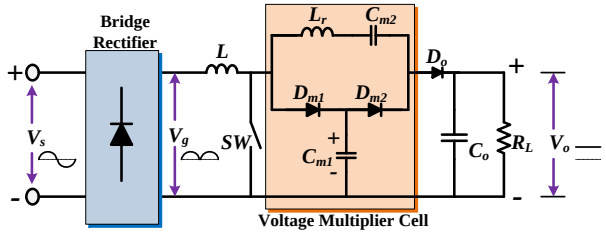

Fig. 2. Circuit configuration of VM PFC Converter system

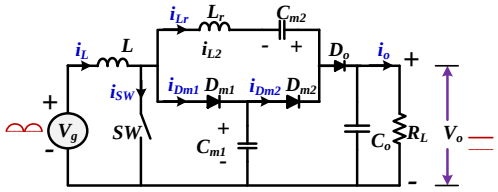

Fig. 3. Simplified equivalent circuit configuration of VM PFC converter

ripple at heavy loading conditions [28]. In [29], compromising circuit complexity, high power and high voltage PFC converter is designed with enhanced ZCS technique. Again, the VM having presented in [30] has inherent ZCS technique and is performing satisfactorily, but this has't been tried for PFC application. This idea motivated to implement the VM circuit configuration, (reported in [17], [25]) presented in Fig. 1 for designing high power PFC system which ensures limited losses and high system efficiency.

In this paper, the VM circuit configuration (reported in [17], [25]) presented in Fig. 1 has been designing for high power PFC system which ensures reduced losses and high system efficiency. The proposed PFC system includes a voltage multiplier (VM) unit embedded in the conventional PFC configuration to enhance the static gain features with moderate duty ratio (D), and hence, the reverse recovery issue is resolved. The VM section inherently adds two main specific features of clamping behavior and ZCS phenomenon to the PFC system. To examine the usability of the proposed system, an experimental prototype of 2 kW, 600 V VM PFC converter configuration is designed and validated under low line input of 100 V, operating at a high duty ratio, $D = 0.67$. The Real-Time Interface (RTI) feature of dSPACE1104 and MATLAB/Simulink are used to give the open loop control signal for the verification of the system.

II. Proposed VM PFC Converter

The proposed VM PFC Converter is presented in Fig. 2. The conventional boost converter is appended with a VM cell without losing its inherent property as pf corrector in PFC system. The VM cell composes a multiplier diode pair (D_{m1}, D_{m2}), multiplier capacitor pair (C_{m1}, C_{m2}) and a resonant inductor (L_r). The boost inductor, switch, output diode and the output capacitor are denoted as L, SW, D_o and C_o respectively.

The simplified VM PFC system is presented in Fig. 3. The inclusion of resonant inductor, L_r is to obtain ZCS turn-on behavior and, hence, the negative effects of reverse recovery current of all diodes is minimised. Thus, the current transitions in all components happen in a resonant way with low $\frac{di}{dt}$. The multiplier capacitor, C_{m1} operates as clamping capacitor and eliminates the switching over voltage. Both the multiplier capacitors work in such a manner that half of the energy consumed by the load is transferred through them and the second half is transferred directly.

A. Characteristics of VM PFC Converter

The main characteristics of the VM converter are as follows;

1) The input current is naturally continuous while the converter includes only one inductor for energy storage.
2) The VM also operates as a regenerative clamping circuit, reducing problems with layout and the EMI generation.
3) Due to the clamp circuit behavior, large output voltage gain is achieved without high duty ratio compared to the conventional PFC converter.
4) The clamped circuit is used to minimize the voltage stress across switches. Every switching device blocks a similar voltage. Consequently, low voltage rating and low on-state resistance ($R_{DS(ON)}$) switching devices can be used which leads to minimization of the cost.
5) The VM operates with inherent ZCS turn-on feature and hence, minimizes the effects of the reverse recovery current of all diodes with the inclusion of a small inductance, L_r.

B. Operation of VM PFC Converter

In this paper, continuous conduction mode (CCM) operation of proposed converter have been considered. For the simplicity in operational analysis, certain initial assumptions have been considered as:

- The switch, SW is considered in OFF state.
- The multiplier capacitor, C_{m1} is initially fully charged with a voltage, $V_{Cm1} = \frac{V_o}{2}$.
- The system is operating with high static gain, i.e. ($Q > 5$, where, $Q = \frac{V_o}{V_g} = \frac{2}{1-D}$. Therefore, $V_g < V_{Cm1}$, where, V_g is the boost multiplier input voltage.
- Hence, D_{m1} and D_{m2} are in blocking state to attain ZCS commutation.
- The resonant inductor current, i_{Lr} is equal to input inductor current, i_L. i.e. $i_L = i_{Lr} = i_o$.
- The energy of the input inductor is transferred to the load, R_L through the diode, D_o.

The CCM operation of the proposed converter is analyzed by five switching stages, as illustrated in Fig. 4. The Stage I, Stage II and Stage III describe the ON state of the switch, SW whereas, Stage IV and Stage V describe the OFF state. The ideal currents and voltages of each switching state are displayed in Fig. 5.

1) Stage I [T_0, T_1]: The Fig. 4(a) describes the operation of proposed converter in switching State I [T_0, T_1]. Also, the direction of circuit current with voltage polarity is presented. The ideal current and voltage waveforms of the circuit during the state, [T_0, T_1] are displayed in Fig. 5.

This state starts at $t = T_0$ and ends at $t = T_1$. At T_0, the switch, SW is turned with ZCS commutation. The inductor, L

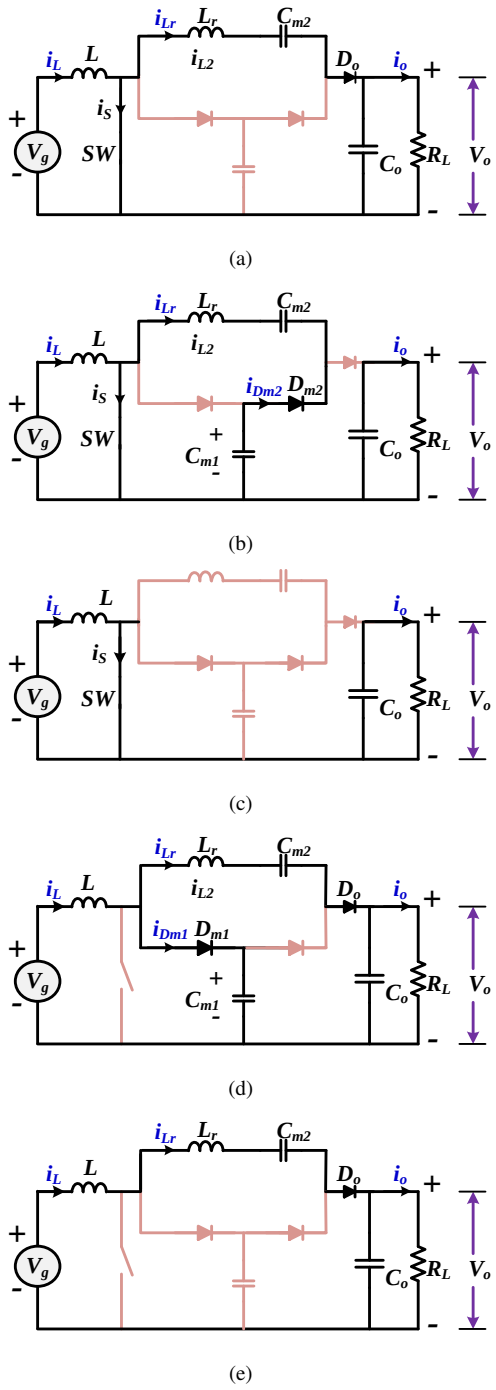

Fig. 4. Circuit diagram: (a) Stage I [T_o to T_1], (b) Stage II [T_1 to T_2], (c) Stage III [T_2 to T_3], (d) Stage IV [T_3 to T_4], and (e) Stage V [T_4 to T_5]

starts charging linearly whereas, the resonant inductor current, i_{Lr} and output diode current, i_{Do} are reduced linearly to zero at $t = T_1$. Thus, the output diode, D_o becomes OFF, and its reverse recovery current is also minimised.

The capacitor, C_{m1} is initially charged with $\frac{V_o}{2}$ i.e.

$$V_{Cm1} = \frac{V_o}{2} \tag{1}$$

Therefore, applying KVL to the circuit, Fig. 4(a);

$$V_{Dm1} = \frac{V_o}{2} \tag{2}$$

$$V_{Dm2} = -\frac{V_o}{2} \tag{3}$$

2) Stage II [T_1, T_2]: This switching state starts when the resonant current becomes zero at $t = T_1$ and ends at $t = T_2$ as the operational circuit is shown in Figure 4(b). The ideal currents and voltages of the VM PFC circuit during this switching state, [T_1, T_2] are shown in Fig. 5.

The switch, SW remains in ON state and the inductor, L is in progress to stores energy. Whereas, the output diode, D_o is blocked at $t = T_1$ (end of $StageI$) and the multiplier diode, D_{m2} starts conducting. The capacitor, C_{m1} transfers energy to the capacitor, C_{m2} in a resonant manner. At $t = T_2$, the diode D_{m2} is blocked with low $\frac{di}{dt}$, when the energy between both the multiplier capacitors C_{m1} and C_{m2} are balanced.

Applying KVL to the circuit, Fig. 4(b);

$$v_{Dm1} = v_{Cm2} \tag{4}$$

3) Stage III [T_2, T_3]: The Fig. 4(c) describes the State III operating condition. The figure indicates the direction of circuit current with voltage polarity. Further, the ideal currents and voltages of the PFC circuit for this switching state [T_2, T_3] are presented in Fig. 5.

The proposed converter goes into this stage during $t = [T_2, T_3]$. When both the multiplier capacitors are reached to balanced energy state, then this stage starts. The multiplier section completely isolates both input section and output section, since it behaves as dead-circuit during this period. The input inductor is still in charging state and hence, the increasing current flows through the switch only. The output capacitor supplies to the load during this period.

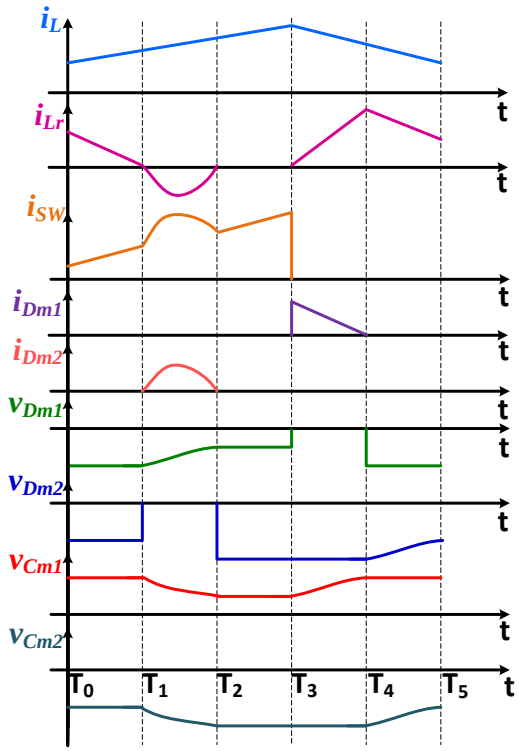

Fig. 5. Switching state voltages and current of the VM PFC converter

The capacitors C_{m1} and C_{m2} are at the same energy level. Therefore, applying KVL to the circuit, Fig. 4(c);

$$v_{Dm1} = -v_{Cm1} \tag{5}$$

And,

$$v_{Dm2} = v_{Cm2} \tag{6}$$

4) Stage IV [T_3, T_4]: At the end of $StageIII$. i.e. at $t = T_3$, the switch, SW turns OFF. At the same time, the diode, D_{m1} starts conduction, since the capacitor, C_{m1} is completely discharged in previous stage. During this stage, the stored energy of inductor, L is transferred to the capacitor, C_{m1} through diode, D_{m1} until $i_{Dm1} = 0$ at $t = T_3$.

The Fig. 4(d) describes the operation of the proposed converter in State IV. The direction of circuit current with voltage polarity is also presented. Also, the ideal currents and voltages of the VM PFC converter during the operating state, [T_3, T_4] are displayed in Fig. 5.

Applying KVL to the circuit, Fig. 4(d);

$$v_{SW} = v_{Cm1} \tag{7}$$

And,

$$v_{Dm2} = v_o - v_{Cm1} \tag{8}$$

The resonant inductor current, i_{Lr} rises from zero and charges the output capacitor, C_o through diode, D until $i_{Lr} = i_L$ at $t = T_3$.

5) Stage V [T_4, T_5]: The switch, SW remains in OFF state as before. At $t = T_4$, the diode, D_{m1} is blocked with low $\frac{di}{dt}$, minimising the diode reverse recovery current. During this stage, both the inductors L and L_r are in series i.e. $i_{Lr} = i_L$ and the inductor, L remains in discharging state. The stored energy is transferred to the load, R_L through diode D_o.

This stage is nothing but the initial assumption state of the proposed converter for operational analysis. After this stage, the circuit further enters the $StageI$ and continues the CCM operation.

The Fig. 4(e) describes the switching State V of the proposed converter. The direction of the circuit current with voltage polarity is also presented in the figure. The ideal currents and voltages during the state, are shown in Fig. 5 [T_4, T_5].

Applying KVL to the circuit, Fig. 4(e)

$$v_{Dm1} = -(v_{SW} + v_{Cm1}) \tag{9}$$

And,

$$v_{Dm2} = v_{Cm1} - v_o \tag{10}$$

$$v_{SW} = -(v_{Dm1} + v_{Cm1}) \tag{11}$$

III. Experimental Result Analysis

A 2 kW, 600 V output hardware prototype of proposed VM PFC Converter is designed in our laboratory. The block diagram presented in Fig. 7 describes about the Real-time implementation (RTI) of the proposed system. The experimental set-up is presented in Fig. 6 The set-up includes mainly a VM PFC power circuit and switch driving circuit. The power

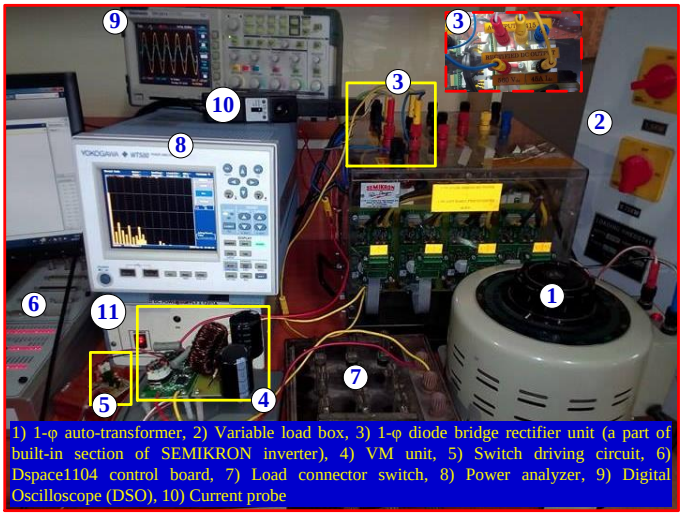

Fig. 6. Experimental Set-Up of proposed VM PFC system

circuit incorporates a $1-\phi$ auto-transformer, $1-\phi$ diode bridge rectifier followed by the proposed VM unit and DC dynamic load. The $1-\phi$ rectifier unit is a part of built-in rectifier section of SEMIKRON inverter, which is discussed briefly in Appendix A. The proposed VM PFC converter system, operating in open loop control is modeled in the MATLAB/Simulink and downloaded to the dSPACE, which delivers the required regulating signals to the driver section. The switching driver circuit receives the analog switching signal from dSPACE1104 board and is used to drive the switch. In addition, to process the control algorithm on VM PFC prototype, the RTI feature is enabled. The essential driving pulse is generated by the master bit I/O. For the designing of the prototype, ferrite core type inductor and plain polyester type capacitor are used. The components, used for the experimental designing of proposed PFC converter are enlisted in TABLE I.

A. Design Consideration of VM PFC Converter

The design consideration of proposed VM PFC converter includes;

Selection of Duty Ratio (D): For the proposed VM configuration, the relationship between rectified input voltage, output voltage, duty ratio (D) and voltage gain is given by:

TABLE I
Experimental Design Parameters of VM PFC Converter

System Parameters	Specification	Rating
Boost Inductor (L)	Ferrite Core Type	0.83 mH
Output Capacitor (C_0)	Electrolytic type	680 μF
Resonant Inductor (L_r)	Ferrite Core Type	37 μH
Multiplier Capacitor (C_{m1}, C_{m2})	Ceramic Type	45 μF
Multiplier Switch (SW)	MOSFET:FCP20N60	20 A, 600 V
Multiplier Diodes (D_{m1}, D_{m2}), Output Diode (D_0)	VS-20ETF06FPPBF	20 A, 600 V
Load	Resistive Load Box	Maximum Load upto 5 kW
Switching Frequency (f_{SW})		40 kHz
Duty Ratio (D)		0.67

$$Q = \frac{V_o}{V_g} = \frac{2}{1-D} \tag{12}$$

From the Equation (12), the value of D can be selected depending on the desired voltage gain (Q) ratio.

Selection of Switch Voltage Rating: The voltage across multiplier capacitors decide the voltage rating of the switching devices which includes FET switch (SW) and circuit diodes. Thus, the maximum rating of voltage for these devices can be selected as:

$$V_{SW} = V_{Dm1} = V_{Dm2} = V_{Do} = V_{Cm2} = \frac{V_g}{1-D} \tag{13}$$

Selection of Front End Inductor: The allowable ripple content of the input inductor current mainly decides its minimum inductance value and is expressed as:

$$L = \frac{V_g D}{\triangle I_L f_{SW}} \tag{14}$$

Selection of VM Capacitors: The rating selection of VM capacitors is decided by the VM capacitor voltage, the maximum output power (P_o) and the switching frequency (f_{SW}). The energy stored in the multiplier capacitor governs the maximum output power ($P_{o_{max}}$). Thus, the value of the VM capacitors is given by:

$$C_{m1} \geq \frac{P_{o_{max}}}{V_{Cm1}^2 f} \tag{15}$$

Selection of Resonant Inductor (L_r): The commutation losses across the switches can be reduced with the help of resonant inductor (L_r). It limits the rate of change of current which can be expressed as:

$$\frac{di}{dt} = \frac{V_o - V_{Cm2}}{L_r} \tag{16}$$

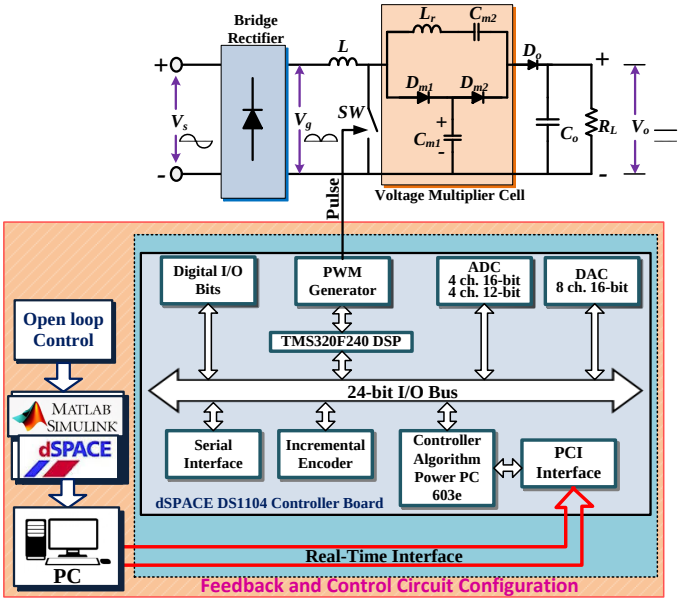

Fig. 7. Block diagram representation of Real-time implementation of VM PFC converter system

B. Comparative Analysis of Theoretical Losses and Efficiency

Switch conduction loss: The RMS value of switch current $I_{SW_{rms}}$ mainly decides the switch conduction loss and can be expressed as (neglecting the current ripple):

$$I_{SW_{rms}} = \frac{P_g}{V_g}\sqrt{D} \tag{17}$$

Hence, the power loss during switch conduction is given by:

$$P_{SW(cond)} = I_{SW_{rms}}^2 R_{DS_{on}} \tag{18}$$

For high power application, the RMS value of switch current (I_{SW}) comparatively very high in Boost PFC converter than the the proposed VM PFC converter.

Switch Commutation Loss: The operation of such systems is greatly effected by the commutation loss across the controlled switching device. The current flowing through the switch during commutation is a combination of current flowing through the switch and the reverse recovery current of diode. The commutation loss is expressed as:

$$P_{SW(off)} = (\frac{1}{2} V_s I_s T_{off}) f_{SW} \tag{19}$$

The traditional Boost PFC system suffers due to large reverse recovery current. However, the commutation loss for the proposed system is negligible, as the reverse recovery current is limited due to its inherent ZCS mode of operation.

Diode Conduction Loss: The diode average current decides its conduction loss which is equivalent to the output current for the proposed system. For high power rating with low output voltage, the output current rises to a high value. This causes an increase in diode conduction loss which in turn affects the system efficiency.

The conduction loss of boost diode is expressed as:

$$P_D = \frac{P_o}{V_o} V_f \tag{20}$$

where, V_f is forward blocking voltage of the diode. The conduction loss of multiplier (three) diodes is expressed as:

$$P_D = 3\frac{P_o}{V_o} V_f \tag{21}$$

The forward blocking voltage in For high power, high voltage (say ($600 V_{DC}$)) system is comparatively larger than the equal rating of proposed PFC converter system. Thus, the diode conduction loss is noticeably reduced and maintaining high system efficiency in proposed system.

Theoretical Efficiency:

Hence, based on the losses calculated, the system efficiency of the PFC converter system is estimated:

$$\eta = \frac{P_o}{P_o + P_{SW(cond)} + P_{SW(off)} + P_D + P_{Lin}} \tag{22}$$

The efficiency of the proposed VM PFC converter is higher than the boost PFC system as the theoretical losses in the proposed converter is comparatively quit low.

C. Result Analysis

In this paper, the proposed system has been examined for its inherent ZCS phenomenon and static gain response at low input level. The ZCS characteristic is validated with voltage-current characteristics of the switching devices and the multiplier capacitors. The static gain of the proposed system is compared with the conventional PFC configuration with respect to duty cycle at different loads. Also, the efficiency and $\%THD$ with respect to load for both conventional and proposed converter have been discussed.

1) Switch Voltage and Current Characteristics: The voltage across the switch and current flowing through it during turning ON and OFF instants are as shown in Fig. 8(a). In case of a conventional boost PFC converter, the voltage across the switch during OFF condition is same as the output voltage. Whereas, for the proposed configuration switch voltage is reduced to below 50% of the output voltage as evident from the waveform. Thus, the switching loss is also reduced to a great extent comparatively. Also, due to the snubber circuit behavior of the resonant tank, ZCS phenomenon is evident during switching commutations. Hence, conduction loss is also minimized, enhancing the overall system efficiency. The reduction in commutation loss of the switch is also supported by low di/dt factor in RR current of diodes.

2) Diode Voltage and Current Characteristics: The voltage across the diodes and current flowing through them during turning ON and OFF instants are as shown in Fig. 8(c) , Fig. 8(d) and Fig. 8(b) All the diodes of the proposed configuration have a small RR area of current with very low di/dt. The RR portion of Diode, D_{m1} occurs during the OFF state of the switch. Hence, it doesn'tt quite affect the commutation loss of the switch, SW. However, negligibly small RR zones with low di/dt of multiplier diode, D_{m2} and output diode, D_o coincide with the ON state of the switch, SW. Thus, the switch is quite unaffected due to the RR current of these diodes. Hence, the switch commutation loss is significantly reduced. Also, as evident from the waveforms, the diode voltages are always observed below fifty percentage (50%) of the output voltage. This is highly advantageous in terms of low power loss, voltage stress reduction and selecting diodes with low rating.

3) VM Static Gain Analysis: The input current and output voltage of the proposed VM PFC converter is displayed in Fig. 9. The system is operating at a low line supply of $100\ V$ and duty cycle $D = 0.67$. It is evident from the waveforms that nearly $600\ V$ (double of conventional output) is obtained at the output terminals. The input current (I_s) is in phase with the line voltage and sinusoidal in shape. Also, its $\%THD$ content with spectrum analysis of the VD PFC systems is presented in Fig. 10.

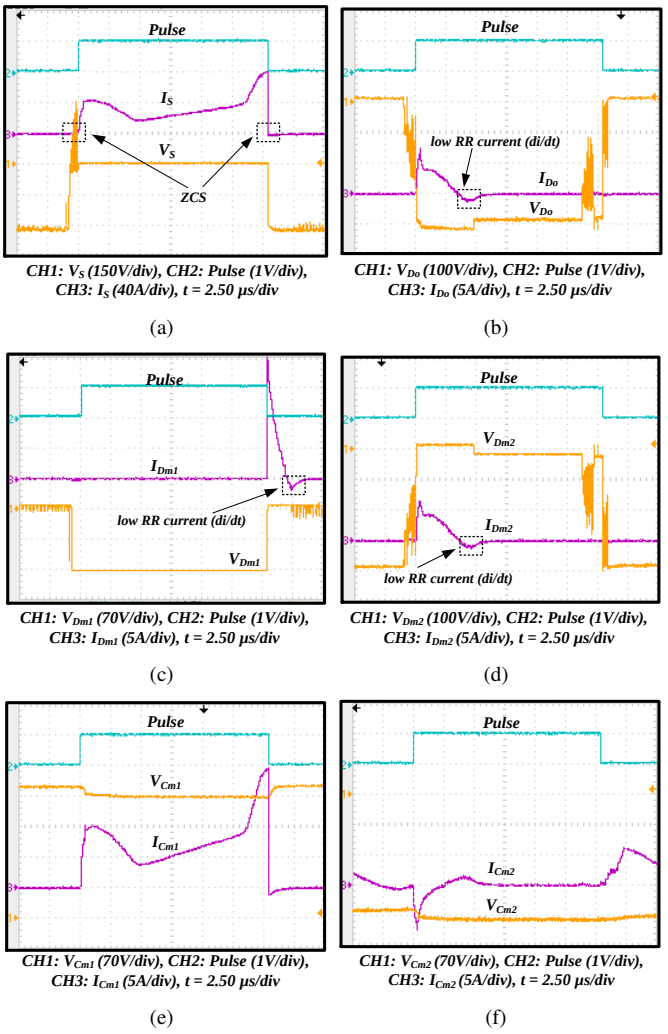

Fig. 8. Voltage and Current Characteristics of proposed system: (a) Converter Switch, S (b) Multiplier Diode, D_{m1} (c) Multiplier Diode, D_{m2} (d) Output Diode, D_0 (e) Multiplier Capacitor, C_{m1} (f) Multiplier Capacitor, C_{m2}

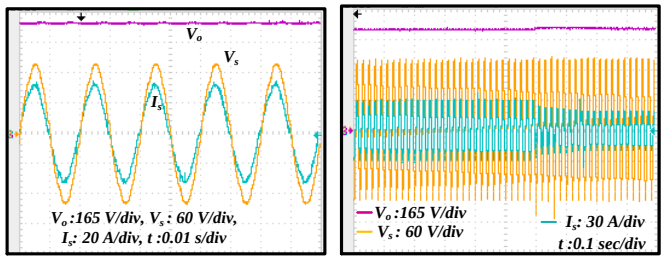

Fig. 9. Input Voltage, Input Current and Output Voltage Waveforms of Proposed VM PFC system: (a) Steady loading condition, (b) Load variation condition

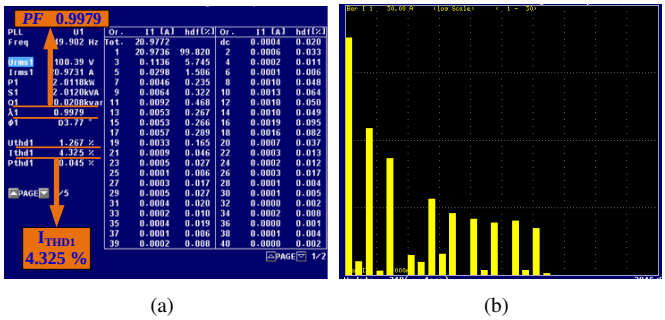

Fig. 10. Power analyser results of Proposed VM PFC system, illustrating: (a) power consumption, input power factor and %THD, (b) harmonics spectrum

TABLE II
COMPARATIVE PERFORMANCE ANALYSIS BASED ON LOAD VARIATION

S.N.	Load (W)	Conventional PFC System			VM PFC System		
		Efficiency (%)	THD (%)	pf	Efficiency (%)	THD (%)	pf
1	400	97.31	3.06	0.996	97.92	4.14	0.986
2	600	97.01	3.94	0.998	97.52	4.22	0.988
3	800	96.41	4.11	0.989	97.73	3.96	0.99
4	1000	96.02	4.26	0.987	97.81	3.80	0.992
5	1200	95.00	4.35	0.987	97.54	3.91	0.996
6	1400	94.42	4.49	0.983	97.81	3.88	0.997
7	1600	93.94	5.33	0.982	97.91	3.01	0.998
8	1800	93.13	5.73	0.983	98.26	3.16	0.998
9	2000	93.10	6.16	0.981	98.30	3.16	0.999
10	2200	92.31	6.56	0.982	98.22	3.22	0.997
11	2400	92.11	6.72	0.981	98.26	3.04	0.998
12	2600	92.17	6.82	0.980	98.29	3.15	0.999
13	2800	92.19	7.01	0.980	98.29	3.11	0.997

TABLE III
COMPARATIVE PERFORMANCE ANALYSIS BASED ON INPUT VARIATION

S.N.	Input RMS Voltage (V)	Conventional PFC System		VM PFC System	
		Efficiency (%)	pf	Efficiency (%)	pf
1	80	90.13	0.983	97.02	0.992
2	100	91.91	0.989	97.23	0.996
3	120	93.14	0.992	98.14	0.997
4	140	94.32	0.996	98.05	0.998
5	160	96.11	0.990	98.17	0.999
6	180	96.14	0.998	98.17	0.998
7	200	96.17	0.999	98.25	0.998
8	220	96.19	0.998	98.26	0.999
9	240	96.23	0.997	98.29	0.998

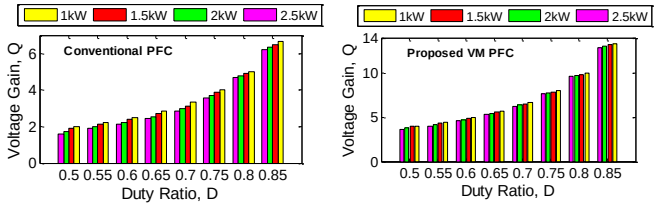

(a) (b)

Fig. 11. Voltage Gain vs Duty Ratio for different Load Ratings: (a) Conventional system (b) Proposed VM PFC system

The performance of the proposed converter has been tested under load variation, and the relevant result waveforms are displayed in Fig. 9(b). The presented waveforms are captured for a load decrement of 50%. The output voltage is regulated, and the input voltage is sinusoidal, as presented in the figure.

In this research work, the proposed PFC system is tested under various operating conditions to validate its performance and compared with that of a conventional system of equal rating. A comparative analysis on the efficiency,%THD and pf of proposed system with the conventional system for various load conditions are presented in Table II. The efficiency of both conventional and proposed PFC systems is nearly equal at a lower level of loading. However, the efficiency of the conventional system decreases linearly with the increase of load. On the contrary, the system efficiency of the proposed system is comparatively very high at heavy loading conditions. Furthermore, the input current %THD for conventional system exceeds the IEC 61000-2-2 standard, while operating under heavy loading condition. Whereas, the input current %THD level of the proposed PFC system is under the standard limit irrespective of load rating.

Furthermore, the Table **??** describes the behavior of efficiency with respect to changes in input voltage. Although, the system efficiency increases for both the systems with an increase in supply voltage, but the VM PFC converter efficiency is comparatively very high at any input level.

The variation in static voltage gain (Q) with respect to duty ratio (D) at individual load ratings for both the systems are described in Fig. 11. For the performance analysis, a constant supply voltage of 100 V is given to both the systems. The value of D is varied within a range of $D = (0.5\ to\ 0.85)$ for each value of load (P) i.e. $P = (1\ kW, 2\ kW, 3\ kW\ and\ 4\ kW)$. The static voltage gain of proposed VM PFC system is nearly double to that of the conventional system for each D value under each specified load.

IV. CONCLUSION

A high power VM PFC converter with inherent ZCS feature and high static gain is proposed in this paper to obtain enhanced efficiency at low line input. The system is validated with an experimental prototype of 2 kW, 600 V rating, operating at a high duty ratio, $D = 0.67$. The performance of the proposed system is tested at low line input of 100 V. It is observed that always less than half of the output voltage (300 V) appears across the switches, hence, voltage stress of the switch is minimized. Furthermore, the switch conduction loss and diode commutation loss are minimized, and hence, the overall system efficiency is improved. The proposed PFC system includes a voltage multiplier (VM) unit embedded in conventional PFC configuration to enhance the static gain features with moderate duty ratio (D), and hence, the reverse recovery issue is resolved. The VM section inherently adds two main specific features of clamping behaviour and ZCS phenomenon to the PFC system. For both the steady state and transient loading condition unity pf and regulated output voltage are evident. The performance of the proposed converter in term of efficiency, pf, %THD under different input voltage and load is examined and compared with that of the conventional system. The system efficiency of the proposed system is maintained high for different load ratings with a slight variation of around 1%. Whereas, the efficiency variation increases upto 6% for the conventional system. Also, with respect to different line voltages, the system efficiency is maintained high and steady for the proposed system. For the proposed system, the input current %THD is maintained within the standard limit, even at higher load ratings. However, with the conventional system, it increases gradually above the limit at higher ratings. The voltage gain for the proposed system is also observed to be almost double as compared to the conventional system for different load ratings. Moreover, the presented experimental results infer that the proposed VM PFC converter offers enhanced low-line-efficiency and is a better choice for high power with high voltage applications.

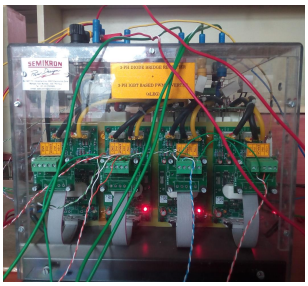

Fig. A1. SEMIKRON built power electronics teaching kit

APPENDIX

A. 1-ϕ DIODE BRIDGE RECTIFIER (A BUILT-IN SECTION OF SEMIKRON POWER ELECTRONICS TEACHING KIT)

A pictorial view of the SEMIKRON power electronics teaching kit is presented in Figure A1. It consists of an isolated $3-\phi$ diode bridge rectifier and $3-\phi$ inverter section. The rectifier section can be used both for $1-\phi$ and $3-\phi$ AC-DC conversion system, as per the requirement. The specification of the rectifier section is presented in Table A1.

TABLE A1
SPECIFICATION OF THE SEMIKRON BUILT $1-\phi$ DIODE BRIDGE RECTIFIER

Input AC voltage (V_s)	415 $Volt$
Output DC voltage (V_o)	600 $Volt$
Input AC current (I_s)	30 Amp
Fundamental frequency	50 Hz
Diode bridge module	SKD 160/18 (1 Nos)

REFERENCES

[1] H. Sarnago, . Luca, A. Mediano, and J. M. Burdo, "Design and Implementation of a high-efficiency multiple-output resonant converter for induction heating applications featuring wide bandgap devices," *IEEE Transactions on Power Electronics*, vol. 29, no. 5, pp. 2539–2549, May 2014.

[2] "*Limits for Harmonics Current Emissions (Equiptment Input Current* $< 16A$ *per Phase*," IEC International Standard 1000-3-2, Tech. Rep., 2001.

[3] B. Singh, B. N. Singh, A. Chandra, K. Al-Haddad, A. Pandey, and D. P. Kothari, "A review of single-phase improved power quality ac-dc converters," *IEEE Transactions on Industrial Electronics*, vol. 50, no. 5, pp. 962–981, Oct 2003.

[4] Y. Jang and M. M. Jovanovic, "Interleaved boost converter with intrinsic voltage-doubler characteristic for universal-line pfc front end," *IEEE Transactions on Power Electronics*, vol. 22, no. 4, pp. 1394–1401, July 2007.

[5] J. P. Hong and G. W. Moon, "A digitally controlled soft valley change technique for a flyback converter," *IEEE Transactions on Industrial Electronics*, vol. 62, no. 2, pp. 966–971, Feb 2015.

[6] P. R. Mohanty, A. K. Panda, V. Y. Kumar, and T. Penthia, "Small-signal analysis for designing a stable voltage-doubler pfc system," in *TENCON 2017 - 2017 IEEE Region 10 Conference*, Nov 2017, pp. 980–985.

[7] P. R. Mohanty, A. K. Panda, and D. Das, "An active pfc boost converter topology for power factor correction," in *2015 Annual IEEE India Conference (INDICON)*, Dec 2015, pp. 1–5.

[8] P. R. Mohanty and A. K. Panda, "Fixed-frequency sliding-mode control scheme based on current control manifold for improved dynamic performance of boost pfc converter," *IEEE Journal of Emerging and Selected Topics in Power Electronics*, vol. 5, no. 1, pp. 576–586, March 2017.

[9] ——, "A nonlinear control scheme based on dynamic evolution path theory for improved dynamic performance of boost pfc converter working on nonlinear features," *ISA Transactions*, vol. 65, pp. 254 – 261, 2016.

[10] A. K. Panda, P. R. Mohanty, T. Penthia, and N. Patnaik, "Dual output interleaved pfc for alleviating mutual interference between loads during transients," in *2016 IEEE Uttar Pradesh Section International Conference on Electrical, Computer and Electronics Engineering (UPCON)*, Dec 2016, pp. 289–294.

[11] B. Akn and H. Bodur, "A new single-phase soft-switching power factor correction converter," *IEEE Transactions on Power Electronics*, vol. 26, no. 2, pp. 436–443, Feb 2011.

[12] L. S. Yang, T. J. Liang, H. C. Lee, and J. F. Chen, "Novel high step-up dc-dc converter with coupled-inductor and voltage-doubler circuits," *IEEE Transactions on Industrial Electronics*, vol. 58, no. 9, pp. 4196–4206, Sept 2011.

[13] K. S. B. Muhammad and D. D. C. Lu, "Zcs bridgeless boost pfc rectifier using only two active switches," *IEEE Transactions on Industrial Electronics*, vol. 62, no. 5, pp. 2795–2806, May 2015.

[14] A. K. Panda, P. R. Mohanty, N. Patnaik, and T. Penthia, "Closed-loop controlled cascaded current controlled dynamic evolution control (cc-dec) based voltage doubler (vd) pfc converter for improved dynamic performance," *IEEE Journal of Emerging and Selected Topics in Power Electronics*, pp. 1–1, 2017.

[15] C.-M. Wang, "A novel zcs-pwm power-factor preregulator with reduced conduction losses," *IEEE Transactions on Industrial Electronics*, vol. 52, no. 3, pp. 689–700, June 2005.

[16] M. Mahesh and A. K. Panda, "Increase of efficiency of an ac-dc power factor correction boost converter by a novel soft-switching technique," *Electric Power Components and Systems*, vol. 40, no. 1, pp. 57–73, 2011.

[17] M. Prudente, L. L. Pfitscher, G. Emmendoerfer, E. F. Romaneli, and R. Gules, "Voltage multiplier cells applied to non-isolated dc-dc converters," *IEEE Transactions on Power Electronics*, vol. 23, no. 2, pp. 871–887, March 2008.

[18] Q. Zhao and F. C. Lee, "High-efficiency, high step-up dc-dc converters," *IEEE Transactions on Power Electronics*, vol. 18, no. 1, pp. 65–73, Jan 2003.

[19] K. C. Tseng and T. J. Liang, "Novel high-efficiency step-up converter," *IEE Proceedings - Electric Power Applications*, vol. 151, no. 2, pp. 182–190, Mar 2004.

[20] C. L. Shen and P. C. Chiu, "Buck-boost-flyback integrated converter with single switch to achieve high voltage gain for pv or fuel-cell applications," *IET Power Electronics*, vol. 9, no. 6, pp. 1228–1237, 2016.

[21] L. S. Yang, T. J. Liang, and J. F. Chen, "Transformerless dc-dc converters with high step-up voltage gain," *IEEE Transactions on Industrial Electronics*, vol. 56, no. 8, pp. 3144–3152, Aug 2009.

[22] R. J. Wai, C. Y. Lin, R. Y. Duan, and Y. R. Chang, "High-efficiency dc-dc converter with high voltage gain and reduced switch stress," *IEEE Transactions on Industrial Electronics*, vol. 54, no. 1, pp. 354–364, Feb 2007.

[23] J. C. Rosas-Caro, J. C. Mayo-Maldonado, A. Valderrabano-Gonzalez, F. Beltran-Carbajal, J. M. Ramirez-Arredondo, and J. R. Rodriguez-Rodriguez, "Dc-dc multiplier boost converter with resonant switching," *Electric Power Systems Research*, vol. 119, pp. 83 – 90, 2015.

[24] J. K. Park, W. Y. Choi, and B. H. Kwon, "A step-up dc-dc converter with a resonant voltage doubler," *IEEE Transactions on Industrial Electronics*, vol. 54, no. 6, pp. 3267–3275, Dec 2007.

[25] M. Prudente, L. Pfitscher, and R. Gules, "A boost converter with voltage multiplier cells," in *2005 IEEE 36th Power Electronics Specialists Conference*, June 2005, pp. 2716–2721.

[26] "Soft-switched non-isolated high step-up multi-port dc-dc converter for hybrid energy system with minimum number of switches," *International Journal of Electrical Power & Energy Systems*, vol. 106, pp. 511 – 519, 2019.

[27] K. C. Tseng and C. C. Huang, "High step-up high-efficiency interleaved converter with voltage multiplier module for renewable energy system," *IEEE Transactions on Industrial Electronics*, vol. 61, no. 3, pp. 1311–1319, March 2014.

[28] C. M. Young, M. H. Chen, S. H. Yeh, and K. H. Yuo, "A single-phase single-stage high step-up ac-dc matrix converter based on cockcroft-walton voltage multiplier with pfc," *IEEE Transactions on Power Electronics*, vol. 27, no. 12, pp. 4894–4905, Dec 2012.

[29] C. Li and D. Xu, "A family of enhanced zcs single-stage single-phase isolated ac-dc converter for high power high voltage dc supply," *IEEE Transactions on Industrial Electronics*, vol. PP, no. 99, pp. 1–1, 2017.

[30] K. C. Tseng, C. C. Huang, and W. Y. Shih, "A high step-up converter with a voltage multiplier module for a photovoltaic system," *IEEE Transactions on Power Electronics*, vol. 28, no. 6, pp. 3047–3057, June 2013.

GLAUCOMA BASED DETECTION OF CUP TO DISC RATIO FROM RETINAL FUNDUS IMAGE: AN IMAGE PROCESSING TECHNIQUE

Anitha Duraisamy[1] and Suganthi M[2]

[1]*Research scholar, Anna university, Chennai, Tamilnadu, India. mail:assvanitha@gmail.com*

[2]*Professor, Mahendra College of Engineering, Salem, Tamil Nadu, India.*

mail:msuganthib@gmail.com

**Corresponding mail*: *assvanitha@gmail.com*

Abstract

This work proposes a method for the detection of glaucoma using fundus image based on the optic disc and cup size. The ratio of the optic cup to disc (CDR) in retinal fundus images is one of the primary physiological parameter for the diagnosis of glaucoma. Using SVM classifier the dataset is trained. The CDR values are considered as features for the prediction. Also, the advantages of using electriucal stimulation for the treatment of glaucom are prosed in this study. The mechanism underlying the electrical stimulation for the positive effects are outlined in connection with their effects on increased production of neurotrophic agents. Therefore through work, we aim to provide insight on the applications CDR and the advantages of electrical stimulation and its importance as a potential therapy for improving vision and treating various eye diseases.

Keywords: Glaucoma, fundus image, Cup to disc ratio. SVM classifier, Electrical Simulation.

Introduction

Glaucoma is a leading cause of irreversible blindness that occurs with progressive damage of optic nerve and retinal ganglion cells with concomitant visual field (VF) loss [1]. It is the second leading cause of blindness worldwide and in 2025 it is estimated that approximately 11 million individuals will be blind from glaucoma [2]. Currently, glaucoma can be treated. Glaucoma is considered as age-related disease and the top most cause of permanent visual impairment [3]. The complications in glaucoma disease pathology have significantly suggested that its diagnosis is very important at its early stages to prevent the permanent visual loss [4]. This is a multifactorial ocular disease and is diagnosed by increased intra-ocular pressure (IOP), a crucial factor in the disease progression. The optic nerve head is distinguished as a brightest yellow oval

shape containing a central optic cup surrounded by an optic disc is seen in 2D images of retinal images (Figure.1)

\

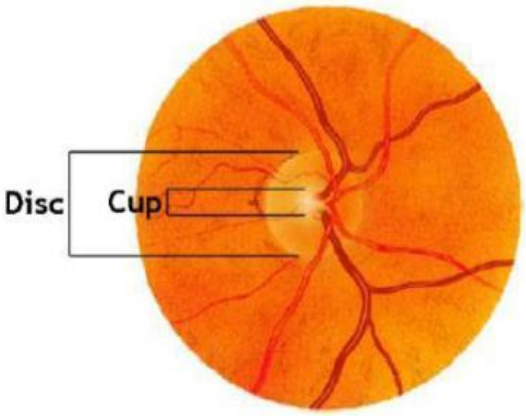

Figure 1. Optic cup and disc in retinal images

An increase in the IOP above the normal ranges (10-21 mmHg); create a pressure against optic nerves and leads to the degeneration of retinal ganglion cells [5]. However, the glaucomatous loss of visual field can be seen in some patients with normal IOP which significantly suggests that keeping low IOP alone is not enough to inhibit the glaucomatous optic neuropathy [6]. However, cup-disk ration (CDR) has become important in detection of glaucoma from the fundus image. The CDR value of 0.65 is considered to be suspicious for glaucoma [7]. This can be done by calculating the ratio of optic cup to disc area or ratio of cup-disc vertical diameter. However the physical detection and diagnosis of glaucoma is quite laborious and depends on professional expertise. From the last few decades several Machine Learning techniques are used to prediction of glaucoma based on the fundus images [8]. Some of the techniques which have been used are neural networks, decision tree based on ID3 algorithms, Support Vector Machine, Naive Bayesian classifier, k- nearest neighbor, Thresholding, CDR and ISNT [9]. In this proposed work a novel algorithmic based based on Cup to Disc Ratio approach for the identification of glaucoma from fundus images was proposed.

Statement of Problem

An early detection of glaucoma is very crucial as it allows timely treatment to prevent major visual field loss. The diagnosis of glaucoma can be done through measurement of CDR (cup-to-disc ratio). Currently, CDR evaluation is very laborious and is performed manually by ophthalmologists. Thus, this paper proposes an intuitive, efficient and objective method for automatically classifying digital fundus images into either normal or glaucomatous types in order to facilitate ophthalmologists.

Methodology

In flowchart of proposed methodology for detection of glaucoma based on cup-to-disc ratio from fundus

images is shown in Figure 2. First step, pre-processing is intend to change of the picture for next investigation and processing. Here the image is resized to a color space changes and specific size in view of necessity. Second step, is segmentation procedure to concentrate on the Cup and Disc shapes from the input picture. Third is to measure the area of cup to disc ration of image and Finally trained with the SVM classifier.

ROI Determination

In this small portion of an image that was extracted and necessary operations are performed on it. ROI is defined as a binary image that has the same size as of the image we want to process. In the mask image, pixels which lie in ROI has been set to 1 and all other pixels has been set to 0. In retinal fundus image, the optic disc has been traced out as optic disc occupies less than 5% of pixels are extracted [10]. By localizing the ROI, it reduces the computational cost and also improves accuracy of segmentation .it is defined as a rectangle around the ROI centre with dimensions of twice the typical optic disc diameter, and has been used as the initial boundary for the optic disc segmentation.

Algorithm

Input: RGB fundus image

[1] Colored fundus image

[2] Region propping and Bounding box

[3] Crop the image in the bounded box

[4] Perform ISNT Mask Generation

[5] Extract the ROI of the image.

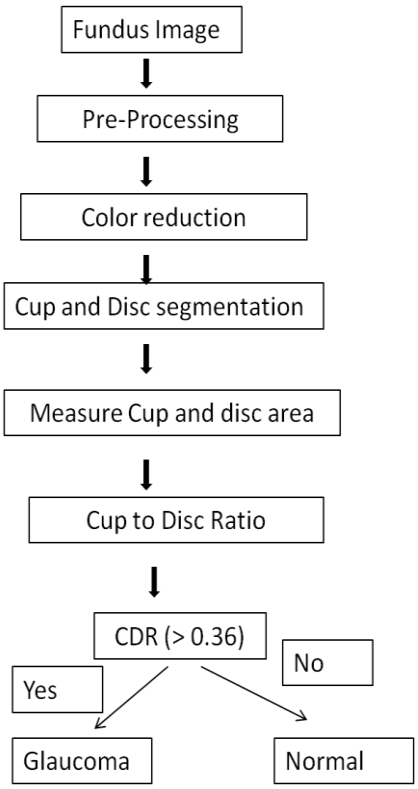

Figure. 2: Flow chart of this study

Optic Disc Segmentation and Smoothening

The disadvantages of Optic Nerve Head (ONH) will be eliminated by the segmentation process of optic disc and optic cup evaluation methods. For calculating the vertical cup to disc ratio firstly the optic cup and disc segmented from the retinal images [11]. There are various techniques for segmentation based on template matching, machine learning, active contour model, level sets and Hough transform. ellipse fitting has been applied in

order to reshape the disc boundary for smoothing.

Optic Cup Segmentation and Smoothening

Optic cup segmentation is bit harder than optic disc extraction since the cup-disc boundary is less measurable than that of disc region and besides combines with increased visibility of blood vessels across the cup-disc boundary. Ellipse fitting is an important tool especially when portions of the blood vessels in the neuro-retinal rim which is outside the cup are included within the detected boundary [12]. Based on the height of detected optic disc and cup, the cup to disc ratio (CDR) has been obtained.

Cup To Disc Ratio

The segmented cup and disc that consists of white pixels are counted to calculate the area of the cup and disc. Calculate the CDR and compare the ratio for normal cup to disc ratio. For normal eye CDR is 0.3, if the input image CDR exceeds more than 0.3, then it is to be considered as an image affected by glaucoma. If the Value is <0.36 the prediction is normal, If it is 0.36 and 0.5 Stage 1, 0.5 to 0.7 stage 2 and <0.7 stage 3 or advancved stage [13].

After finding normal or abnormality of fundus images (glaucoma), then SVM is used as classifier.

CDR is calculated as

CDR = (Cup area ÷ Disc area) x 2 …(1)

Cross validation

In this study, normal fundus image and glaucoma are defined as positive and negative respectively. Therefore, TP stands for True Positives, TN - True Negatives, FP - False Positives and FN - False Negatives..

Sensitivity (Sn): sensitivity measures the ability of the process to predict correct results

$$Sn = \frac{tp}{tp+fn} \times 100\% \quad ..(2)$$

Specificity (Sp): specificity measures the ability of a process to predict incorrect results. **..**

$$Sp = \frac{tn}{tn+fp} \times 100\% \quad \ldots. (3)$$

Accuracy (Acc): accuracy measures the degree of correctness of the predicted results to its actual value or the experimental value

$$Acc = \frac{tp+tn}{tp+fn+tn+fp} \times 100\% \quad \ldots.. \quad (4)$$

Results and Discussion

The cup to disc ratio (CDR) is an important indicator of the risk of the presence of glaucoma in an individual. The proposed algorithm is tested on 8 normal fundus images and 8 glaucoma fundus images. SVM classifier are used to analyze the performance of the proposed system. The noise handling, large dataset and large feature space abilities of SVM has put forth

its usage as a successful machine learning (ML)-technique [14]. SVM classification can separate the positive instances from negative instances with high margin. The parameters and kernels (linear, polynomial, radial base function (RBF) and sigmoid) were optimized for the best performance of SVM classifiers and trained with CDR as features. In statistical prediction, the jackknife cross-validation, also known as the Leave-One-Out Cross-Validation (LOOCV), is regarded as an objective and effective method to evaluate a classifier for its effectiveness in practical application. Thus a ten-fold cross-validation was used to evaluate the performance of SVM classifiers.

The SVM classifier was trained and optimized with CDR features. Various kernels such as linear, quadratic, polynomial, radial basis function (RBF), MLP and RBF_sigma were optimized for the best performance of the SVM classifiers. The kernel parameters (C and gamma) corresponding to maximum accuracy were optimized as best parameter values. The accuracy, sensitivity and specificity of normal fundus images were shown in figure.3. The AAC-SVM classifier optimized with RBF kernel has the highest accuracy of 79.13% followed by Polynomial kernel with 78.54%. The lowest accuracy of 52.38 % was exhibited by MLP kernel. The average accuracy was considered for the best performance of a kernel. Thus in the present study, RBF kernel was considered as the most suitable kernel for the SVM classifiers-training and testing with normal fundus image features.

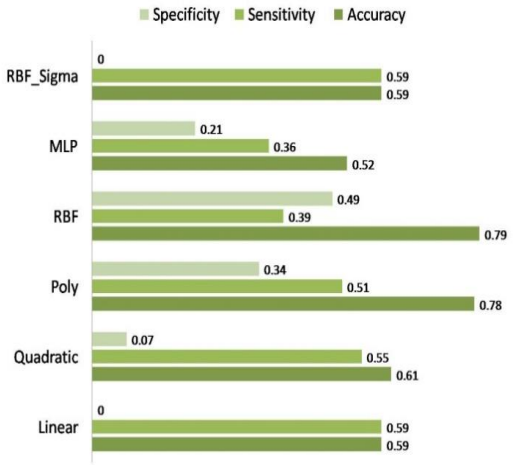

Figure.3: The performance evaluation of SVM classifier for CDR with various kernels

Cup to disc ratio of normal and abnormal images

To find the disc area of input image with different threshold values are applied and related to the cup areas. After finding disc area keep disc area as constant for all the different images of the eye and cup area varied by applying threshold values for different regions. In the present technique the author measures the cup area and disc area keeping the structureing element on it and do the segmentation for required region, which gives the more accurate result compare to previous result

The normal cup to disc ratio is 0.3. The increase in cup ratio may imply glaucoma or other pathology. The cup-to-disc ratio compares the diameter of the "cup" portion of the optic disc with the total diameter of the optic disc. The cup-to-disc ratio of normal subjects is typically around 0.2 to 0.3. While there is no one cup-to-disc ratio that separates normal from glaucoma, the cup-to-disc ratio greater than 0.6 or 0.7 is suspicious of glaucoma and often requires further testing to rule out glaucoma.

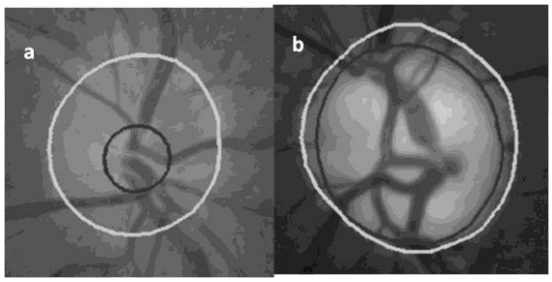

Figure4: cup to disc ratio fundus retinal images (a) normal (CDR<0.36) (b) glaucoma (CDR >0.36)

Table. 1: Prediction of SVM classifier of Normal and Glaucoma fundus images based on CDR

S.no	CDR	Prediction
1.	0.328	Normal
2.	0.38	Glaucoma
3.	0.304	Normal
4.	0.410	Glaucoma
5.	0.319	Normal
6.	0.329	Normal
7.	0.443	Glaucoma
8.	0.216	Normal
9.	0.169	Normal
10.	0.498	Glaucoma
11.	0.392	Glaucoma
12	0.216	Normal
13	0.501	Glaucoma
14	0.455	Glaucoma
15	0.272	Normal
16	0.389	Glaucoma

Currently, to treat and improve the patients' vision, the electrical stimulations are being applied as epiretinal, subretinal, transchoroidal, transcorneal, transorbital, transpalpebral and direct stimulation of brain or eye. In early methods that are simple to implement and non invasive, the electrical stimulations targets retinal cells alone, while direct method targets higher visual cells. In advanced glaucoma patients, where the connections between the eye and brain are affected, the later direct method that stimulates the brain is very useful therapeutic strategy.

The methods such as epiretinal, subretinal, transchoroidal electrical stimulations are known as retinal implants or chips or prostheses. These retinal prostheses mimic photoreceptor activities by using electricity generated by energy converters. The ganglion cells are targeted by epiretinal prostheses and inner nuclear layer of the retina are targeted by subretinal implants while transchoroidal implants stimulate the retina from the outer region. In retinal pigmentosa patients, the defective pigment epithelium and photoreceptors are observed while the inner retina and ganglion cell layer are kept intact. The retinal prostheses must activate the retinal neurons by detecting the light when converting light energy into electricity in order to restore the visual function.

Conclusions

In this study, we have presented a method to calculate the CDR automatically from fundus images. First step, pre-processing is intend to change of the picture for next investigation and processing. Here the image is resized to a color space changes and specific size in view of necessity. Second step, is segmentation procedure to concentrate on the Cup and Disc shapes from the input picture. Third is to measure the area of cup to disc ration of image and Finally trained with the SVM classifier.. Using 16 images the performance of our approach is evaluated using SVM. The results indicate that our approach provides 89% accuracy in glaucoma analysis. Conversly, this study has a good potential in automated screening systems for the early detection of glaucoma based on CDR. In this scenario, currently the usage of electrical stimulation for the treatment of glaucoma and vision restoration has moved into clinical practice. Its favorable safety profile is key advantage and is likely to boost the progress of electrical stimulation in the treatment of various eye diseases. However, there is a urgent need for a deeper understanding of the underlying mechanisms of this electrical stimulations restoring the vision.

References

[1] Cheng JW, Cheng SW, Ma XY, Cai JP, Li Y, Lu GC, Wei RL. Myocilin polymorphisms and primary open-angle glaucoma: A systematic review and meta-analysis. PloS one. 2012; 7: e46632.

[2] Quigley HA, Broman AT. The number of people with glaucoma worldwide in 2010 and 2020. Br. J. Ophthalmol. 2006; 90: 262–267.

[3] Coleman AL, Miglior S. Risk factors for glaucoma onset and progression. Surv. Ophthalmol. 2008; 53: S3–10.

[4] Wang SK, Chang RT. An emerging treatment option for glaucoma: Rho kinase

inhibitors. Clin. Ophthalmol. 2014; 8: 883–890.

[5] Tang M, Fu Y, Fan Y, Fu MS, Zheng Z, Xu X. In-silico design of novel myocilin inhibitors for glaucoma therapy. Trop. J. Pharm. Res. 2017;16: 2527-2533.

[6] Chen J, Runyan SA. Robinson MR. Novel ocular antihypertensive compounds in clinical trials. Clin. Ophthalmol. 2011; 5: 667–677.

[7] R. Chrastek a, M. Wolf a, K. Donath, "Automated segmentation of the optic nerve Medical Image Analysis in Elsevier, Functional Imaging and Modeling of the Heart, August 2005, pp 297-314.

[8] Ahmed Wasif Reza & C. Eswaran & Subhas Hati, "Automatic Tracing of Optic Disc and Exudates from Color Fundus Images Using Fixed and Variable Thresholds", Journal of Medical Systems, Feb 2009, pp 73 -80.

[9] J. Liu, D. W. K. Wong, J.H. Lim, X. Jia, "Optic Cup and Disk Extraction from Retinal Fundus Images for Determination of Cup-to-Disc Ratio", IEEE third conference on Industrial Electronics and Applications, June 2008, pp 1828 -1832.

[10] Koen A. Vermeer, Frans M. Vos, Barrick Lo, Images of the Human Retina for Progression Detection of Glaucoma", IEEE Transactions On Medical Imaging, May 2006, pp 517-528.

[11] T. Walter and J. C. Klein, "Automatic analysis of color fundus photographs and its application to the diagnosis of diabetic retinopathy," in Handbook of Biomedical Image Analysis, vol. 2, pp. 315-368, 2005.

[12] Prasad Maldhure, N. and Dixit, V. V. Glaucoma Detection Using Optic Cup and Optic

Disc Segmentation. *International Journal of Engineering Trends and Technology,* **20**(2),

2015, pp. 52-55.

[13] Ann mary babu and Hanis, S. Segmentation of optic disc boundary in digital Fundus images.

International journal of biomedical signal processing, **2**(1), 2012, pp. 1-6.

[14] U. Rajendra Acharya, Sumeet Dua, Xian Du, "Automated Diagnosis of Glaucoma Using Texture and Higher Order Spectra Features", IEEE Transactions On Information Technology In Biomedicine, May 2011, pp 449-455.

vol 21 / 2021

University "Politehnica"
Timișoara Romania
Faculty of Electrical and Power
Engineering

"Politehnica" Publishing House
ISSN 1582-4594

No 3